

**Study of the B -Meson Lifetime
and
the Performance of the Outer Tracker
at LHC b**

Cover design: Mariyana Vankova.

Printed by PrintPartners IJskamp B.V., Amsterdam.
Copyright © 2008 by Peter Vankov. All rights reserved.

The work described in this dissertation is part of the research programme of the "Stichting voor Fundamenteel Onderzoek der Materie (FOM)", which is financially supported by the "Nederlandse Organisatie voor Wetenschappelijk Onderzoek (NWO)".

VRIJE UNIVERSITEIT

**Study of the *B*-Meson Lifetime
and
the Performance of the Outer Tracker
at LHCb**

ACADEMISCH PROEFSCHRIFT

ter verkrijging van de graad Doctor aan
de Vrije Universiteit Amsterdam,
op gezag van de rector magnificus
prof.dr. L.M. Bouter,
in het openbaar te verdedigen
ten overstaan van de promotiecommissie
van de faculteit der Exacte Wetenschappen
op woensdag 5 november 2008 om 10.45 uur
in de aula van de universiteit,
De Boelelaan 1105

door

Peter Hristoforov Vankov

geboren te Sofia, Bulgarije

promotor: prof.dr.ing. J.F.J. van den Brand

copromotoren: dr. A. Pellegrino
dr. H.G. Raven

*Information is not knowledge.
Knowledge is not wisdom.
Wisdom is not truth.
Truth is not beauty.
Beauty is not love.*

Frank Zappa.

На баща ми.

Contents

Introduction	1
1 B Mesons and Their Lifetime	5
1.1 Standard Model	5
1.2 Weak Interaction	7
1.2.1 CKM Matrix	8
1.2.2 B Mesons	10
1.3 CP Violation in B -Meson Decays	13
1.4 Importance of Proper-Time Resolution	14
1.5 B Lifetimes and the Heavy Quark Expansion	17
1.5.1 Spectator Model	17
1.5.2 Heavy Quark Expansion Model	19
2 The LHCb Experiment	23
2.1 The Large Hadron Collider	23
2.2 The LHC b Detector	26
2.2.1 Design Considerations	26
2.2.2 General Structure	27
2.2.3 Vertex Locator	29
2.2.4 Trigger Tracker	31
2.2.5 Inner Tracker	32
2.2.6 RICH Detectors	33
2.2.7 Calorimeters	34
2.2.8 Muon System	35
2.2.9 Trigger System	35
2.3 Outer Tracker	36
2.3.1 General Layout of the OT system	36
2.3.2 OT Module Design	38
2.3.3 OT Working Principle	41
2.3.4 OT Readout Electronics	42

3 Outer Tracker Quality Assurance	45
3.1 Introduction	45
3.2 Wire Selection	48
3.3 Friction Force of Wire-Locators	49
3.4 Wire Position Measurements	52
3.5 Wire Tension	56
3.5.1 Tensioning of the Anode Wires	56
3.5.2 Wire Tension Meter	56
3.5.3 Measurement of the Wire Tension	57
3.5.4 Single Tension per Wire, Derivation of the Segment Lengths	60
3.5.5 Variation of the Wire Tension	60
3.6 Currents in Air	62
3.7 Gas Tightness Measurements	65
3.7.1 Overpressure Decay Test	65
3.7.2 Leak Rate Measurement with Flow Meter	66
3.7.3 Gas Tightness Comparison between F and S Modules	69
3.8 Water Content Measurements	70
3.8.1 Setup and Method	70
3.8.2 Drying of a Newly-Built Module	71
3.8.3 Water Content in Gas-Tight and Leaky Modules	71
3.9 High Voltage Training	73
3.10 Scanning with Radioactive Source	76
3.10.1 The Experimental Setup	76
3.10.2 Results	77
3.11 Summary	79
4 Beam Tests of OT Modules	81
4.1 Beam Test Setup	81
4.1.1 The Test Setup	81
4.1.2 The Silicon Strip Telescope	84
4.2 Analysis of the OT Beam Tests Data	85
4.2.1 Si-telescope track reconstruction	85
4.2.2 Space - Drift Time Relation	87
4.2.3 Spatial Resolution	89
4.2.4 Multiple Scattering	90
4.2.5 Efficiency	91
4.2.6 Noise	93
4.2.7 Cross Talk	94
4.3 Results of the Beam Tests	95
4.3.1 Resolution	95
4.3.2 Efficiency	97
4.3.3 Noise	97
4.3.4 Cross Talk	97

4.4	Summary	99
5	Proper-Time Resolution Modeling	101
5.1	Introduction	101
5.2	Software and Data	102
5.3	Event Selection	103
5.4	Resolution Model	107
5.4.1	Proper-Time Reconstruction	107
5.4.2	Resolution Model	108
5.4.3	The Per-Event-Errors	109
5.4.4	Determination of the Resolution Model Parameters	110
5.4.5	Validation of the Model	114
5.5	Determination of the Parameters on Real Data	120
5.5.1	Method	120
5.5.2	Results	121
5.6	Dependence on t_{true}	124
5.6.1	Test for Dependence on t_{true}	124
5.6.2	Explanation of the t_{true} Dependence	127
5.6.3	Primary Vertex Re-Definition	131
5.7	Summary and Conclusions	139
6	Extraction of the Lifetime Ratio τ_{B^+}/τ_{B^0}	141
6.1	Event Selection	141
6.1.1	Background Scaling	142
6.2	Background and Signal Modeling	146
6.2.1	Modeling the Background	146
6.2.2	Modeling the Signal	147
6.2.3	Modeling the Signal and Background Simultaneously	147
6.3	Determination of Lifetime with Signal Only	148
6.4	Results	153
6.4.1	Maximum-Likelihood Fit including Background	153
6.4.2	Dependence of the Resolution Model Parameters on the Background	159
6.4.3	τ_{B^+}/τ_{B^0}	160
6.4.4	Conclusion	163
Bibliography		165
Summary		169
Samenvatting		171
Acknowledgements		173

Introduction

By convention sweet and by convention bitter; by convention hot, by convention cold, by convention color; but in reality atoms and void.

Democritus of Abdera [1, 2].

The idea that all matter is made of indivisible, structureless entities is not new. It dates from antiquity and is connected with the names of Greek philosophers Leucippus (c. 500 - 450 B.C.) and Democritus (460 - 371 B.C.). However, this idea remained just a conjecture until 1897, when the first elementary particle, the electron, was discovered by J.J. Thomson. This moment can be considered as the birth date of particle physics - the science of the fundamental structure of matter.

Enormous progress has been made in particle physics during the last century: experiments with high-energy particle beams have revealed that, besides atomic-shell electrons, other types of leptons exist as well; it has been found that protons and neutrons, which were at first thought to be elementary, have a complex structure and are made of smaller objects, called quarks; the existence of a corresponding antiparticle partner of each kind of quarks and leptons has been predicted and verified; in addition to gravitation and electromagnetism, two new fundamental forces have been discovered: the strong and the weak nuclear interaction.

At present, the fundamental constituents of matter are thought to be the quarks, leptons and their antiparticles. The interactions amongst them are governed by the fundamental forces listed above and are well described (excluding gravity) in the theoretical framework of particle physics: the Standard Model.

The imbalance between matter and antimatter is one of the biggest mysteries in modern cosmology. Equal amounts of matter and antimatter must have been created during the Big Bang, when the Universe formed 13.73 ± 0.12 billion years ago [3]. However, today's world is predominantly composed of matter; the antimatter is almost absent. For example, the results from the AMS-01 experiment [4] show that the ratio of the numbers of antihelium to helium nuclei, measured in the cosmic rays, 400 km above the Earth surface, is smaller than one in a million. In 1967 it was realized (by A. Sakharov [5]) that the violation of the Charge-Parity (CP) symmetry is a necessary requirement to explain this disproportion. Therefore, the study of CP violation is of key importance for understanding the dynamics of the early Universe.

The breaking of CP invariance by the weak interaction was for the first time observed in the decay of neutral kaons in 1964 [6]. The kaon system remained the only known system where this effect had been seen until 2002, when CP violation was also detected in the decays of neutral B mesons (particles including the massive b (\bar{b}) quark in their composition) [7, 8]. Despite of these discoveries, CP violation is still one of the least explored phenomena in particle physics.

Beside allowing precise tests of the reliability and consistence of the theoretical predictions, exploring CP violation also provides an opportunity to probe "new physics", i.e. physics beyond the Standard Model. Typically, this is connected with searches for new¹ sources of CP violation.

This year in the European Laboratory for Particle Physics (CERN) in Geneva, Switzerland, a new particle accelerator, the Large Hadron Collider (LHC), will be put in operation. LHC will collide beams of protons at a center-of-mass energy of $\sqrt{s} = 14$ TeV at luminosities up to 10^{34} cm $^{-2}$ s $^{-1}$. Physics at the LHC requires high performance detectors. One of the four experiments operating with LHC is LHCb, which will perform precision measurements of CP violation in the B -meson system and study rare B decays.

The tracking system is an essential element of the LHCb detector, providing a precise and efficient determination of the momenta of the charged particles in the final state. In order to efficiently reconstruct the trajectories of charged particles, the LHCb Outer Tracker (OT) is equipped with gaseous straw-tube detectors. The OT system comprises three stations, each consisting of multiple layers of drift tubes. The basic unit of the OT stations is the module, a self-contained detector unit filled with a counting-gas mixture.

The OT module production was carefully monitored by a variety of tests. The overall performance of the OT detector as shown during the quality assurance tests and the beam tests is one of the topics of this dissertation.

The precise measurement of the time-dependent CP asymmetry requires a high resolution of the proper lifetime of the B mesons. The second part of this dissertation is a study of the resolution of the proper lifetime of the B mesons at LHCb. The study is carried out using the decay modes $B^+ \rightarrow J/\psi K^+$ and $B^0 \rightarrow J/\psi K^0$. Subsequently, the ratio of the lifetimes of B^+ and B^0 mesons, τ_{B^+}/τ_{B^0} , is derived; the value of this ratio can be used as an important indication for the validity of the Heavy Quark Expansion model [10]. The sensitivity of LHCb to τ_{B^+}/τ_{B^0} is investigated.

Outline

This dissertation can be divided in three main parts: theory and description of the experiment, testing of the OT detector performance and physics analysis. Two chapters are devoted to each of these parts.

¹The amount of CP violation present in the Standard Model is too small to generate the observed matter-antimatter asymmetry in the Universe [9].

Chapter 1 gives an overview of the theoretical framework of our study. A summary of the basic concepts of the Standard Model of particle physics is presented, followed by descriptions of the characteristics of weak interaction, the properties of B mesons, and the mechanism of CP violation in the Standard Model. The importance of high resolution measurements of the B proper-time is discussed. The Heavy Quark Expansion model is introduced.

The properties of the LHC accelerator and the design of the LHCb experiment are discussed in Chapter 2. Special attention is given to the architecture and operational principle of the Outer Tracker system.

Chapter 3 focuses on the quality monitoring and validation of the Outer Tracker modules, while Chapter 4 is devoted to the beam tests of the OT modules at DESY. Results of these tests, illustrating the detector efficiency, spatial resolution, noise and cross-talk are presented.

Chapter 5 reports on a study of the resolution of the proper lifetime of the B^+ and B^0 mesons. The study is performed with $B^+ \rightarrow J/\psi(\mu^+\mu^-)K^+$ and $B^0 \rightarrow J/\psi(\mu^+\mu^-)K^*(K^+\pi^-)$ decay modes and their conjugates. A resolution model based on proper-time residuals and corresponding per-event errors is developed and results are presented.

Finally, Chapter 6 illustrates a method for the determination of B^+ and B^0 lifetimes in the presence of backgrounds, and reports on the sensitivity of LHCb for measuring the lifetime ratio τ_{B^+}/τ_{B^0} .

Chapter 1

B Mesons and Their Lifetime

Science is built of facts the way a house is built of bricks; but an accumulation of facts is no more science than a pile of bricks is a house.

Henri Poincaré (1854-1912)

This chapter outlines the theoretical basis and the motivation of the study of B -meson lifetimes.

In Sec. 1.1 a summary of the Standard Model (SM) of particle physics is presented. An overview of the weak interaction and the properties of B mesons are given in Sec. 1.2. The mechanism of the violation of the combined Charge-Parity (CP) symmetry in the framework of SM is described in Sec. 1.3. In Sec. 1.4, the importance of the resolution of the B -mesons proper lifetime measurement for determining time dependent (CP) asymmetries is substantiated. Finally, the Heavy Quark Expansion model¹ and its prediction for the ratio of lifetimes of B^+ and B^0 mesons are introduced in Sec. 1.5.

1.1 Standard Model

The *Standard Model* of particle physics [12] is a theoretical framework which describes the interactions between the fundamental constituents of matter. Within the SM description, matter in the universe is made up of elementary (structureless) particles, *fermions*, with intrinsic angular momentum, spin = $\frac{1}{2}$. These elementary fermions appear as two types: *leptons* and *quarks*, grouped in three generations with increasing mass. Each fermion generation contains a quark and lepton pair as indicated in Table 1.1. For every particle there is a corresponding antiparticle, with the same mass and spin, but with opposite magnetic moment and opposite "charges"².

¹The Heavy Quark Expansion model is a method for computation of *inclusive* decay rates of heavy (B) hadrons, by using the heavy-quark limit $m_b \gg \Lambda_{QCD}$. Not to be confused with Heavy Quark Effective Theory (HQET), which is applicable to *exclusive* heavy hadron decays [10, 11].

²Except the electric charge, the fermions carry also other charge-like quantum number labels, such as color charge, flavor, lepton or baryon number.

Fermions	I	II	III	El. charge
Quarks	u (up) 1.5 - 3.0 MeV/c ²	c (charm) (1.25 ± 0.09) GeV/c ²	t (top) (174.2 ± 3.3) GeV/c ²	$+\frac{2}{3}$
	d (down) 3.0 - 7.0 MeV/c ²	s (strange) (95 ± 25) MeV/c ²	b (bottom) (4.20 ± 0.07) GeV/c ²	$-\frac{1}{3}$
Leptons	e (electron) 0.511 MeV/c ²	μ (muon) 106 MeV/c ²	τ (tau) 1.78 GeV/c ²	-1
	ν_e (e neutrino) < 3 eV/c ²	ν_μ (μ neutrino) < 0.19 MeV/c ²	ν_τ (τ neutrino) < 18.2 MeV/c ²	0

Table 1.1. Three generations of fermions. The values of the masses are taken from Particle Data Group (PDG) 2006 [13].

Interaction	Mediator (bosons)	Relative Strength
Strong	g_α , $\alpha = 1, \dots, 8$ (gluons) $m_{g_\alpha} = 0$	$\alpha_s \sim \mathcal{O}(1)$
Electromagnetic	γ (photon) $m_\gamma = 0$	$\alpha = 1/137 \sim \mathcal{O}(10^{-2})$
Weak	W^\pm, Z^0 (weak bosons) $m_{W^\pm} = 80.4$ GeV/c ² , $m_{Z^0} = 91.2$ GeV/c ²	$\alpha_w \sim \mathcal{O}(10^{-6})$
Gravitational	graviton - if exists	$\alpha_g \sim \mathcal{O}(10^{-39})$

Table 1.2. Fundamental interactions and their mediator particles.

The elementary particles interact with each other through four fundamental forces (interactions): *strong*, *electromagnetic*, *weak* and *gravitation*. The weak interaction acts on all quarks and leptons. The electromagnetic interaction acts on all electrically charged particles (all quarks and charged leptons), while the strong interaction (also called color force) acts only on the quarks. To each fundamental interaction, a mediator (carrier) particle is associated, a *boson*, with spin = 1, see Table 1.2.

The Standard Model is a quantum field theory based on the principle of gauge invariance, with symmetry group $SU(3)_C \times SU(2)_I \times U(1)_Y$. It describes the strong, weak, and electromagnetic interactions.

The $SU(3)_C$ group describes the strong interaction. In addition to the electric charge, the quarks carry a *color* charge, or simply color. The color can be of three different types, normally denoted as red, green and blue. The antiquarks carry anticolor. The interactions between quarks in which the color changes are subject of the strong interaction and are connected through gluon exchange. Quarks are always bound in groups, forming colorless objects, called *hadrons*. These hadrons can be subdivided into two groups: *mesons*, consisting of a quark-antiquark pair

and *baryons*, containing three quarks of different color.

The $SU(2)_I \times U(1)_Y$ group describes the weak and the electromagnetic interactions, which, in the SM, are unified into a single *electroweak* interaction. However, the observations show that the carriers of the weak and the electromagnetic interactions are of quite different nature - γ , the carrier of the electromagnetic interaction, is massless, while W^\pm and Z^0 , the carriers of the weak interaction, are massive. To explain this, in the SM it is postulated that, for energies below the electro-weak scale, the electro-weak $SU(2)_I \times U(1)_Y$ symmetry is spontaneously broken to $U(1)_{\text{EM}}$. This breaking of the electro-weak symmetry is accommodated in the SM by introducing a new scalar field, the Higgs field. The quantum of this field, the Higgs boson particle, is so far unobserved and is the last component of the SM to be experimentally confirmed. By interacting with the Higgs field, W^\pm and Z^0 (as well as all the elementary fermions) acquire their mass, while γ remains massless.

Although the predictions of the SM have been tested to a remarkable accuracy in many experiments around the world, the SM is not a final theory, mainly because it does not include gravity. In addition, the Standard model contains an arbitrary number of fermion generations with 26 free parameters (like the masses of the particles) that do not follow from the theory. Finally, a disturbing aspect of the model is the large difference between the Planck scale and the electroweak scale, leading to large radiative corrections to the Higgs mass, known as the hierarchy problem.

1.2 Weak Interaction

The weak interaction is responsible for changing the flavor of the quarks and leptons. Furthermore, the down-type quark mass (flavor) eigenstates differ from the weak interaction eigenstates, resulting in the effect of *quark-mixing*: the weak interaction couples to down-type quark states that are not flavor specific, but are a linear combination of the latter. The Cabibbo-Kobayashi-Maskawa (CKM) matrix, proposed in 1973 [14] describes this effect, summarizing the quark couplings to the weak charged current. An example of a process where quark flavor changes is given in Fig. 1.1.

Strong and electromagnetic interactions conserve three basic discrete symmetries in Nature - *parity* (P), *charge conjugation* (C) and *time reversal* (T). Parity is the discrete symmetry under which the space coordinates are inverted, $\vec{x} \rightarrow -\vec{x}$. As a result, a *left-handed* (with the spin direction opposite to the momentum) particle is changed into a *right-handed* one. Charge conjugation is the discrete symmetry which transforms a particle into its antiparticle. Time reversal is the discrete symmetry under which the time coordinate is inverted, $t \rightarrow -t$ ³.

³More precisely, the time reversal is a symmetry under the combined operation: $T = \mathcal{T}^*$, where \mathcal{T} is the simple time reversal operator ($\mathcal{T} : t \rightarrow -t$), and $*$ is complex conjugation.

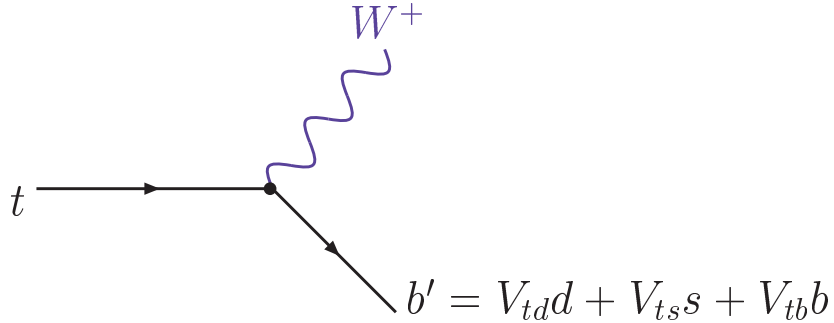


Figure 1.1. An example of quark flavor changing transition. A top quark changes flavor by emitting a W^+ boson. The final state, b' , is not a pure b -quark mass state, but a superposition (mix) of b , s and d quarks states. The coefficients in the linear combination of the final state are elements of the CKM matrix.

A distinguishable feature of the weak interaction is the violation of parity, charge conjugation and also the combined *charge-parity*⁴ (CP) symmetries. Moreover, the P and C symmetries are maximally violated. The combined CP symmetry was thought to be conserved by the weak interaction until a small violation ($\sim \mathcal{O}(10^{-3})$) was discovered in neutral kaon decays in 1964 [6].

1.2.1 CKM Matrix

The complex, unitary 3×3 quark-mixing matrix V_{CKM} , relates the electroweak eigenstates of the down-type quarks, (d', s', b') , with their mass eigenstates, (d, s, b) ,

$$\begin{pmatrix} d' \\ s' \\ b' \end{pmatrix} = \underbrace{\begin{pmatrix} V_{ud} & V_{us} & V_{ub} \\ V_{cd} & V_{cs} & V_{cb} \\ V_{td} & V_{ts} & V_{tb} \end{pmatrix}}_{V_{\text{CKM}}} \begin{pmatrix} d \\ s \\ b \end{pmatrix}. \quad (1.1)$$

The coupling constants, V_{ij} (i, j are generation indices) define the strength of the flavor-changing weak decays and are fundamental SM parameters. The postulated unitarity of V_{CKM} ($V_{\text{CKM}}^\dagger V_{\text{CKM}} = \mathbb{1}$) implies nine constraints (six orthogonality and three normalization conditions) on its complex elements,

$$\sum_{k=1}^3 \underbrace{V_{ki}^* V_{kj}}_{\text{orthogonality conditions}} = 0 \quad (i, j = 1, 2, 3 \text{ and } i \neq j), \quad \sum_{k=1}^3 \underbrace{|V_{kj}|^2}_{\text{normalization conditions}} = 1 \quad (j = 1, 2, 3), \quad (1.2)$$

which reduce the 18 real parameters defining the matrix to nine, namely three mixing angles and six complex phases. Redefining the quark fields allows five of the

⁴Consecutive application of P and C operations.

phases to be absorbed. Consequently, the CKM matrix is completely defined in terms of four real parameters - three mixing angles and one phase. A non-zero value of this phase makes the CKM matrix complex and is a necessary ingredient for CP violation in the Standard model⁵.

One of the most widely used representations of the CKM matrix, allowing to express the observed hierarchy in the magnitudes of the matrix elements, is the one suggested by Wolfenstein [15]. The V_{CKM} is expanded in powers of $\lambda = \sin \theta_C$, where θ_C is the Cabibbo angle,

$$V_{\text{CKM}} = \begin{pmatrix} 1 - \frac{1}{2}\lambda^2 & \lambda & A\lambda^3(\rho - i\eta) \\ -\lambda & 1 - \frac{1}{2}\lambda^2 & A\lambda^2 \\ A\lambda^3(1 - \rho - i\eta) & -A\lambda^2 & 1 \end{pmatrix} + \mathcal{O}(\lambda^4) . \quad (1.3)$$

The experimental measurements have revealed that $\lambda \approx 0.22$, and $A \approx 0.8$ [13]. CP-violation implies that $\eta \neq 0$.

The orthogonality conditions (see Eq. (1.2)) can be represented graphically as triangles in the complex plane, called *unitarity triangles*. In Fig. 1.2 the unitarity triangle corresponding to the following orthogonality relation:

$$\underbrace{V_{ud}V_{ub}^*}_{\mathcal{O}(\lambda^3)} + \underbrace{V_{cd}V_{cb}^*}_{\mathcal{O}(\lambda^3)} + \underbrace{V_{td}V_{tb}^*}_{\mathcal{O}(\lambda^3)} = 0 , \quad (1.4)$$

is shown.

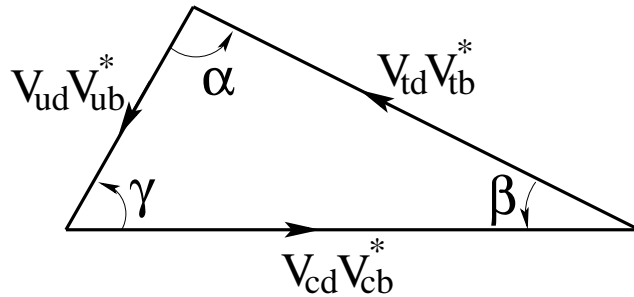


Figure 1.2. The unitarity triangle.

This is one of the two triangles⁶ that have sides of comparable size (since all three terms in Eq. (1.4) are of the same order of magnitude). The other four triangles that

⁵The amplitude of a given decay and its CP conjugate can have different magnitudes (which is a sign of violation of the CP symmetry), due to the opposite sign of this weak phase under CP transformation. In addition, a relative strong phase between the two amplitudes that does not change sign is required.

⁶The other unitarity triangle having all sides of comparable magnitude corresponds to $V_{tb}V_{ub}^* + V_{ts}V_{us}^* + V_{td}V_{ud}^* = 0$.

can be constructed are squashed and thus, high experimental precision is needed to resolve them. The depicted triangle, however, has angles which are not extremely large or small. It is often referred to as "the" unitarity triangle and can be measured in the B -meson system. For example, the angle β is probed through $B^0 \rightarrow J/\psi K_s$, where the phase of V_{td} enters in the mixing of the B^0 and \bar{B}^0 (see Sec. 1.2.2), and the angle γ can be probed through $B_s^0 \rightarrow D_s K$, where the phase of V_{ub} enters [16]. The angles α , β and γ of the unitarity triangle are defined as

$$\alpha \equiv \arg\left(-\frac{V_{td}V_{tb}^*}{V_{ud}V_{ub}^*}\right) , \quad \beta \equiv \arg\left(-\frac{V_{cd}V_{cb}^*}{V_{td}V_{tb}^*}\right) , \quad \gamma \equiv \arg\left(-\frac{V_{ud}V_{ub}^*}{V_{cd}V_{cb}^*}\right) , \quad (1.5)$$

with $\alpha + \beta + \gamma = \pi$. Under rephasing these angles remain invariant, and hence can be measured. Using the Wolfenstein parametrization it can be seen that $-\gamma$ and $-\beta$ are the phases of V_{ub} and V_{tb} respectively, which means that these two quantities are responsible for CP violation.

In the SM, all six unitarity triangles have the same area, which in the Wolfenstein parametrization is given by

$$S = \frac{1}{2} A^2 \lambda^6 \eta = \mathcal{O}(10^{-5}) . \quad (1.6)$$

The size of this area can be interpreted as a measure of the amount of CP violation in the SM [17, 18]; consequently, CP violation in the SM is small.

The over-constraining of the unitarity triangle through independent precision measurements of its sides and angles is an important test for the internal consistency of the Standard Model. Any observed inconsistency in these measurements would be a sign for *new physics*, i.e. physics mechanisms that go beyond the Standard Model.

1.2.2 B Mesons

B mesons are pseudoscalar mesons which include a \bar{b} or b quark. They can be charged or neutral,

$$B^+ = u\bar{b} , \quad B^0 = d\bar{b} , \quad B_s^0 = s\bar{b} , \quad B_c^+ = c\bar{b} , \quad \Upsilon = \bar{b}b , \quad (1.7)$$

plus the corresponding charge-conjugated states. The top quark is too heavy to produce hadrons and thus B mesons are the heaviest mesons. The masses and the lifetimes of the various B mesons are given in Table 1.3.

B mesons are characterized by a relatively long lifetime, $\sim \mathcal{O}(\text{ps})$, due to the small value of the coupling constant V_{cb} , which defines the strength of the primary decay of the b -quark, namely $b \rightarrow c$, and which happens to be $\sim \mathcal{O}(\lambda^2)$.

The large mass and the long lifetime of B mesons facilitate their experimental detection because their decay vertex is displaced from the primary interaction vertex, and their decay products possess high transverse momenta.

B meson	Mass [MeV/c ²]	Lifetime (τ_B) [ps]
B^+	5279.0 ± 0.5	1.638 ± 0.011
B^0	5279.4 ± 0.5	1.530 ± 0.009
B_s^0	5367.5 ± 1.8	1.466 ± 0.059
B_c^+	6286 ± 5	$0.46^{+0.18}_{-0.16}$

Table 1.3. B -mesons masses and lifetimes as reported by PDG 2006 [13].

Another interesting and useful property for CP-violation measurements of the neutral B mesons is that they can fluctuate into their antiparticles, see Fig. 1.3. This phenomenon, known as B oscillation (B mixing) was first experimentally confirmed in the B_d system in 1987 [19]. These B oscillations happen as a result of the difference between the flavor ($|B^0\rangle$ and $|\overline{B}^0\rangle$) and the mass eigenstates of the neutral B meson. There are two mass eigenstates, often denoted as *heavy* ($|B_H\rangle$) and *light* ($|B_L\rangle$), which can be expressed as a linear combination of the flavor eigenstates,

$$|B_{H,L}\rangle = p|B^0\rangle \mp q|\overline{B}^0\rangle . \quad (1.8)$$

The time evolution of the $|B_H\rangle$ and $|B_L\rangle$ is given by

$$|B_{H,L}(t)\rangle = e^{-(im_{H,L}+\Gamma_{H,L}/2)t}|B_{H,L}(0)\rangle , \quad (1.9)$$

where $\Gamma_{H,L}$ and $m_{H,L}$ are the corresponding widths and masses. The B mesons are typically created in the strong interaction as pure flavour eigenstates. At time t the state of a B meson produced at $t = 0$ as a B^0 or \overline{B}^0 is defined as

$$|B_{phys}^0(t)\rangle = g_+(t)|B^0\rangle + \frac{q}{p}g_-(t)|\overline{B}^0\rangle , \quad |\overline{B}_{phys}^0(t)\rangle = g_+(t)|\overline{B}^0\rangle + \frac{p}{q}g_-(t)|B^0\rangle , \quad (1.10)$$

where

$$g_{\pm}(t) = \frac{1}{2} (e^{-(im_L+\Gamma_L/2)t} \pm e^{-(im_H+\Gamma_H/2)t}) . \quad (1.11)$$

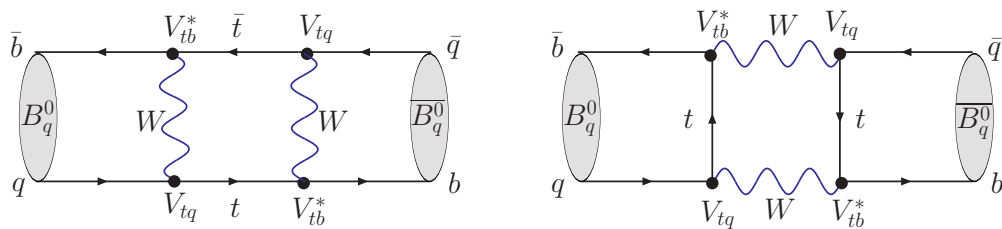


Figure 1.3. The dominant Standard Model Feynman box diagrams for $B_q^0 - \overline{B}_q^0$ oscillations. The index q stands for d or s quarks. The phase of the B_q^0 mixing amplitude is $\phi_q \equiv 2 \arg(V_{tq}V_{tb}^*)$.

Therefore, the probabilities of finding a $|B^0\rangle$ and a $|\overline{B^0}\rangle$ at time t , starting from a pure $|B^0\rangle$ state, are

$$\begin{aligned} P(B^0 \rightarrow B^0; t) &= |\langle B^0 | B_{phys}^0(t) \rangle|^2 = |g_+(t)|^2 \\ P(B^0 \rightarrow \overline{B^0}; t) &= |\langle \overline{B^0} | B_{phys}^0(t) \rangle|^2 = \left| \frac{q}{p} g_-(t) \right|^2 \end{aligned} \quad (1.12)$$

with

$$|g_{\pm}(t)|^2 = \frac{1}{4} (\mathrm{e}^{-\Gamma_L t} + \mathrm{e}^{-\Gamma_H t} \pm 2\mathrm{e}^{-\Gamma t} \cos(\Delta m t)) . \quad (1.13)$$

In the above equation $\Gamma = (\Gamma_H + \Gamma_L)/2$, and $\Delta m = (m_H - m_L)$ is the quantity that determines the frequency of the oscillations. For the B^0 system $\Delta m_d = 0.5 \text{ ps}^{-1}$ [13], and for the B_s^0 system $\Delta m_s = 17.3 \text{ ps}^{-1}$ [20]. This means that the B_s^0 oscillates much more rapidly.

The time-dependent decay rates for the neutral B^0 and $\overline{B^0}$ mesons to a common final state f are given by

$$R_f(t) = \frac{|A_f|^2}{2} \mathrm{e}^{-\Gamma t} [I_+(t) + I_-(t)] , \quad \overline{R_f}(t) = \frac{|\overline{A}_f|^2}{2|\lambda_f|^2} \mathrm{e}^{-\Gamma t} [I_+(t) - I_-(t)] , \quad (1.14)$$

where A_f and \overline{A}_f are the instantaneous decay amplitudes for the process $B^0 \rightarrow f$ and $\overline{B^0} \rightarrow f$. The functions $I_+(t)$ and $I_-(t)$ are defined through

$$I_+(t) = (1 + |\lambda_f|^2) \cosh\left(\frac{\Delta\Gamma t}{2}\right) + 2\Re\{\lambda_f\} \sinh\left(\frac{\Delta\Gamma t}{2}\right) \quad (1.15)$$

$$I_-(t) = (1 - |\lambda_f|^2) \cos(\Delta m t) + 2\Im\{\lambda_f\} \sin(\Delta m t) ,$$

where $\Delta\Gamma = (\Gamma_H - \Gamma_L)$ is the decay width difference, and the quantity

$$\lambda_f = \frac{q}{p} \frac{\overline{A}_f}{A_f} \quad (1.16)$$

is a complex parameter. Analogous equations can be written for the time-dependent decay rates $R_{\bar{f}}(t)$ and $\overline{R}_{\bar{f}}(t)$ for B^0 and $\overline{B^0}$ transiting to a common final state \bar{f} . Then, the following time-dependent decay rate asymmetries can be constructed:

$$\mathcal{A}_f(t) = \frac{R_f(t) - \overline{R}_f(t)}{R_f(t) + \overline{R}_f(t)} , \quad \mathcal{A}_{\bar{f}}(t) = \frac{R_{\bar{f}}(t) - \overline{R}_{\bar{f}}(t)}{R_{\bar{f}}(t) + \overline{R}_{\bar{f}}(t)} , \quad (1.17)$$

where $\mathcal{A}_f(t)$ and $\mathcal{A}_{\bar{f}}(t)$ are CP-violating observables.

A particularly interesting case is the decay of the B to a CP final state, f_{CP} , since it can decay both directly to f_{CP} , $B \rightarrow f_{CP}$, and by first oscillating to a \overline{B} and then

decay, $B \rightarrow \bar{B} \rightarrow f_{CP}$. When the final state f is a CP eigenstate $f = \bar{f}$ and hence, the time-dependent decay rate asymmetries are identical $\mathcal{A}_f(t) = \mathcal{A}_{\bar{f}}(t) = \mathcal{A}_{CP}(t)$. The time-dependent CP-asymmetry, $\mathcal{A}_{CP}(t)$, can be expressed as⁷

$$\mathcal{A}_{CP}(t) = \frac{I_-(t)}{I_+(t)} = \frac{(1 - |\lambda_f|^2) \cos(\Delta mt) + 2\Im\{\lambda_f\} \sin(\Delta mt)}{(1 + |\lambda_f|^2) \cosh\left(\frac{\Delta\Gamma t}{2}\right) + 2\Re\{\lambda_f\} \sinh\left(\frac{\Delta\Gamma t}{2}\right)} . \quad (1.18)$$

In the B^0 system ($B^0 \equiv d\bar{b}$, $\bar{B}^0 \equiv \bar{d}b$), $\Delta\Gamma$ is small and can be neglected, therefore

$$\mathcal{A}_{CP}(t) = \frac{2\Im\{\lambda_f\}}{1 + |\lambda_f|^2} \sin(\Delta mt) + \frac{1 - |\lambda_f|^2}{1 + |\lambda_f|^2} \cos(\Delta mt) . \quad (1.19)$$

1.3 CP Violation in B -Meson Decays

Three types of CP violation can occur in B -meson decays:

- *Direct CP violation.* It is detected when the decay rate of $B^0 \rightarrow f$ is different from the decay rate of $\bar{B}^0 \rightarrow \bar{f}$, with \bar{f} the CP-conjugated state of f :

$$|A_f| \neq |\overline{A}_{\bar{f}}| ; \quad (1.20)$$

- *CP violation in mixing.* It is generated when

$$|q/p| \neq 1 , \quad (1.21)$$

which means that the oscillation probability for $B^0 \rightarrow \bar{B}^0$ is different from that for $\bar{B}^0 \rightarrow B^0$ (see Eq. (1.12));

- *CP violation in the interference between a decay with and without mixing.* This type of CP violation is a reflection of the fact that B^0 can either directly decay to a state f or first oscillate to \bar{B}^0 and then decay to the same state f . An example of such a decay is given in Fig. 1.4. For this to occur, it is necessary that:

$$\Im\{\lambda_f\} \neq 0 . \quad (1.22)$$

⁷Under the assumption that $|q/p| \approx 1$, which is a good approximation for the B^0 and B_s^0 mesons (as reported in Ref. [21]).

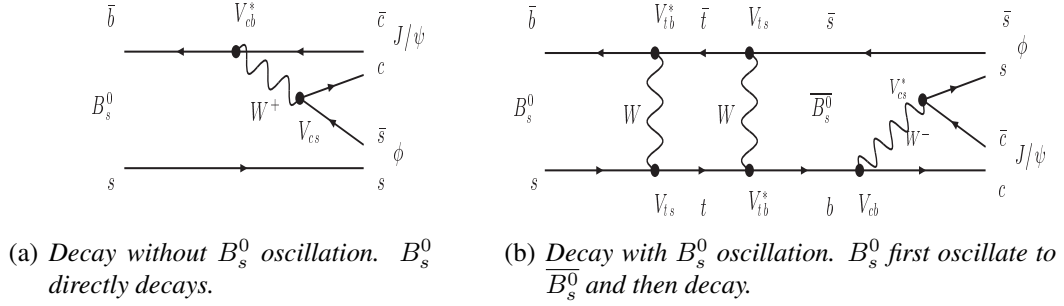


Figure 1.4. The $B_s^0 \rightarrow J/\psi \phi$ decay can proceed through both ((a) and (b)) diagrams.

1.4 Importance of Proper-Time Resolution

Whereas the B^0 system has been the subject of many experiments so far (BaBar, Belle, CDF, D0), the heavier B_s system is not yet fully explored. The next-generation hadron-collider experiment LHCb (see Sec. 2) will be able to produce and study the B_s mesons in greater detail, due to the large luminosity and large cross section at the LHC. One of main topics in the LHCb experimental program is the precise measurement of the CP-violation parameters in B_s decays. The precise measurement of the time-dependent CP asymmetry (Eq. (1.18)) requires a high resolution of the lifetime of the B meson (σ_τ). The importance of σ_τ for the estimation of $\mathcal{A}_{CP}(t)$ is much stronger in the rapidly oscillating B_s^0 system, than it is in the B^0 system, as will be demonstrated next. In Fig. 1.5, $\mathcal{A}_{CP}(t)$ is plotted for two of the most interesting decay modes of B^0 and B_s^0 , namely $B^0 \rightarrow J/\psi K_s$ and $B_s^0 \rightarrow J/\psi \phi$. In the case of $B^0 \rightarrow J/\psi K_s$, the time-dependent CP-asymmetry, Eq. (1.19), can be simplified to

$$\mathcal{A}_{CP}^{B^0}(t) = \Im\{\lambda_f\} \sin(\Delta m_d t) , \quad (1.23)$$

since $|\lambda_f| \approx 1$, because $|A_f/\bar{A}_f| = 1$ and $|q/p| \approx 1$. The decay amplitudes A_f and \bar{A}_f are controlled by a single weak phase, $\Phi_D \equiv \arg(V_{cb}V_{cs}^*) = \mathcal{O}(\lambda^6) \sim 0$, and thus their ratio $A_f/\bar{A}_f = -\eta_f e^{i2\Phi_D} \approx -\eta_f$ [22]. Combining the latter expression with $q/p = -e^{-i\phi_d}$, yields (see Eq. (1.16)) $\lambda_f \approx \eta_f e^{-i\phi_d}$, where ϕ_d is the phase of the B_d^0 mixing amplitude (see Fig 1.3). The factor η_f accounts for the eigenvalue of the final CP eigenstate⁸. Since for $B^0 \rightarrow J/\psi K_s$ the final state is CP odd, $\eta_f = -1$. Then, Eq. (1.23) can be transformed into

$$\mathcal{A}_{CP}^{B^0}(t) = \sin(\phi_d) \sin(\Delta m_d t) , \quad (1.24)$$

Similarly, the time-dependent asymmetry in the B_s^0 system, Eq. (1.18), can be approximated as

⁸ $|\bar{f}\rangle = (CP)|f\rangle = \eta_f|f\rangle$.

$$\mathcal{A}_{CP}^{B_s^0}(t) = -\frac{\eta_f \sin(\phi_s)}{\cosh\left(\frac{\Delta\Gamma_s t}{2}\right) - \eta_f \cos(\phi_s) \sinh\left(\frac{\Delta\Gamma_s t}{2}\right)} \sin(\Delta m_s t) , \quad (1.25)$$

with ϕ_s the phase introduced by the B_s^0 mixing amplitude (see Fig 1.3), and $\eta_f = \pm 1$. The amplitude of the time-dependent CP asymmetry in Eq. (1.24) and Eq. (1.25) is given by $\sin(\phi_d)$ and $\sin(\phi_s)$, respectively. In the Standard Model, $\phi_d \approx 2\beta$ (see Eq. (1.5)) and $\phi_s \approx -2\beta_s$, with⁹ $\beta_s \approx \arg(V_{ts}) - \pi$. The value of $\sin(2\beta)$ has been measured and equals 0.725 ± 0.037 (PDG 2006 [13]), while the value of ϕ_s is not yet precisely measured. In the beginning of this year, the D0 collaboration at Fermilab reported $\phi_s = -0.57^{+0.24}_{-0.30}(\text{stat})^{+0.07}_{-0.02}(\text{syst})$ [23]. The Standard Model prediction amounts to $\phi_s^{SM} \approx -0.04$ rad. Any established deviation from the SM value would signal New Physics (NP) contributions to $\phi_s = \phi_s^{SM} + \phi_s^{NP}$.

The rapid $B_s - \overline{B}_s$ oscillations and the expected small value of the amplitude of $\mathcal{A}_{CP}^{B_s^0}(t)$, $\sim \mathcal{O}(0.04)$, make the precise measurement of this amplitude difficult and demanding. The two main factors that impede the measurement due to unavoidable detector imperfections are *flavour mistagging*¹⁰ and the finite B_s^0 proper lifetime resolution. Therefore, the actual experimentally observed CP-asymmetry will be diluted,

$$\left[\mathcal{A}_{CP}^{B_s^0}(t) \right]^{obs} = D_{tag} D_{res} \mathcal{A}_{CP}^{B_s^0}(t) . \quad (1.26)$$

The mistagging dilution factor is represented by $D_{tag} = (1 - 2\omega)$, where ω is the wrong tag fraction. It is apparent that if for example $\omega = 50\%$, $D_{tag} = 0$ and $\left[\mathcal{A}_{CP}^{B_s^0}(t) \right]^{obs}$ vanishes.

The factor $D_{res} = D_{res}(\sigma_{\tau_{B_s}})$ incorporates the smearing of the time-dependent asymmetry due to the finite resolution of the proper-time measurement, $\sigma_{\tau_{B_s}}$. Explicitly D_{res} can be expressed as [24]

$$D_{res} = \exp\left(-\frac{1}{2}(\Delta m_s \sigma_{\tau_{B_s}})^2\right) . \quad (1.27)$$

Hence, knowledge on $\sigma_{\tau_{B_s}}$ is needed to extract $\mathcal{A}_{CP}^{B_s^0}(t)$. Secondly, the proper time resolution needs to be high enough to accurately resolve the fast oscillations of the B_s^0 meson, in contrast to the B^0 . As can be seen from Fig. 1.5, the resolution should be much better than the period of the oscillations. In order to have $D_{res} \rightarrow 1$, from Eq. (1.27) follows that $(\Delta m_s \sigma_{\tau_{B_s}})^2 \ll 1$, and thus $\sigma_{\tau_{B_s}} \ll 1/\Delta m_s$.

⁹The angle β_s is the corresponding angle in the so called *sb*-unitarity triangle, constructed by using the relation $V_{us}^* V_{ub} + V_{cs}^* V_{cb} + V_{ts}^* V_{tb} = 0$.

¹⁰Misidentification of the initial flavour of the B_s^0 -meson.

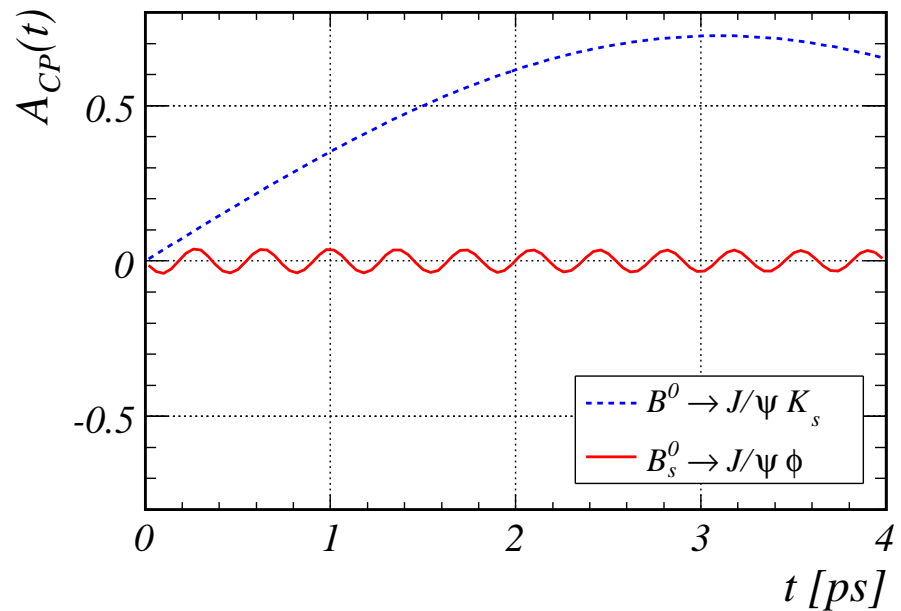


Figure 1.5. The predicted CP asymmetry, $A_{CP}(t)$, in decay channels $B^0 \rightarrow J/\psi K_s$ and $B_s^0 \rightarrow J/\psi \phi$. For $\sin(\phi_s)$ the value predicted by the SM of -0.04 is used. For $\Delta\Gamma_s$ the predicted value $0.088 \pm 0.017 \text{ ps}^{-1}$ as given in Ref. [25] is used. The values of the oscillation frequencies are $\Delta m_d = 0.5 \text{ ps}^{-1}$ and $\Delta m_s = 17.3 \text{ ps}^{-1}$, respectively.

1.5 B Lifetimes and the Heavy Quark Expansion

The measurement of the various B -meson lifetimes is of particular significance for some theoretical models. The simple *Spectator model* assumes equal lifetimes for all B species. The more advanced *Heavy Quark Expansion* (HQE) model predicts a difference in the lifetimes and also predicts the magnitude of this difference. Accordingly, measuring the B lifetimes and their ratios probes the extent to which the naive picture of the spectator model is adequate and tests the correctness of the HQE.

1.5.1 Spectator Model

The spectator model [26] suggests that the decay rate of B mesons is fully dominated by the decay of the heavy b quark and that the lighter (u , d , s or c) quark does not participate nor influence that decay; it is just a "spectator" of the b decay, Fig. 1.6.

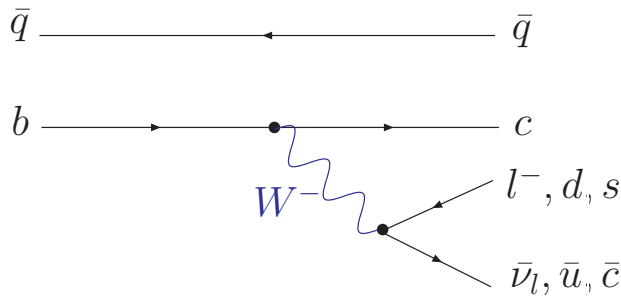


Figure 1.6. Spectator B -decay diagram. The quark q (u,d,s,c) is the "spectator". It is assumed passive and does not participate in the decay.

Thus, the expected lifetime of the B -meson can be reduced to the lifetime of a "free" b -quark, which (calculated relative to the muon decay) is given by

$$\tau_B = \frac{1}{\Gamma_0} \approx \frac{1}{N_c^2 |V_{cb}|^2} \left(\frac{m_\mu}{m_b} \right)^5 \tau_\mu \approx 1.3 \text{ ps} - 1.6 \text{ ps}, \quad (1.28)$$

where $V_{cb} = 0.039 - 0.044$ [27], $\tau_\mu = 2.197 \mu\text{s}$ [27] is the muon lifetime, m_b and m_μ are the b -quark and muon masses (see Table 1.1), and $N_c = 3$.

However, measurements revealed that there is a non-negligible difference in the lifetime of the various B -mesons, which follows the hierarchy (see Table 1.3)

$$\tau_{B^+} > \tau_{B^0} \approx \tau_{B_S^0} > \tau_{B_c}. \quad (1.29)$$

To explain this hierarchy in the B lifetimes, the spectator model is modified to include the presence of *non-spectator effects*. In other words, the light quark component of the B meson can no longer be considered passive, but is also involved in

the decay. Examples of spectator and non-spectator diagrams which contribute to the B decay and which are responsible for the B lifetime differences are shown in Fig. 1.7.

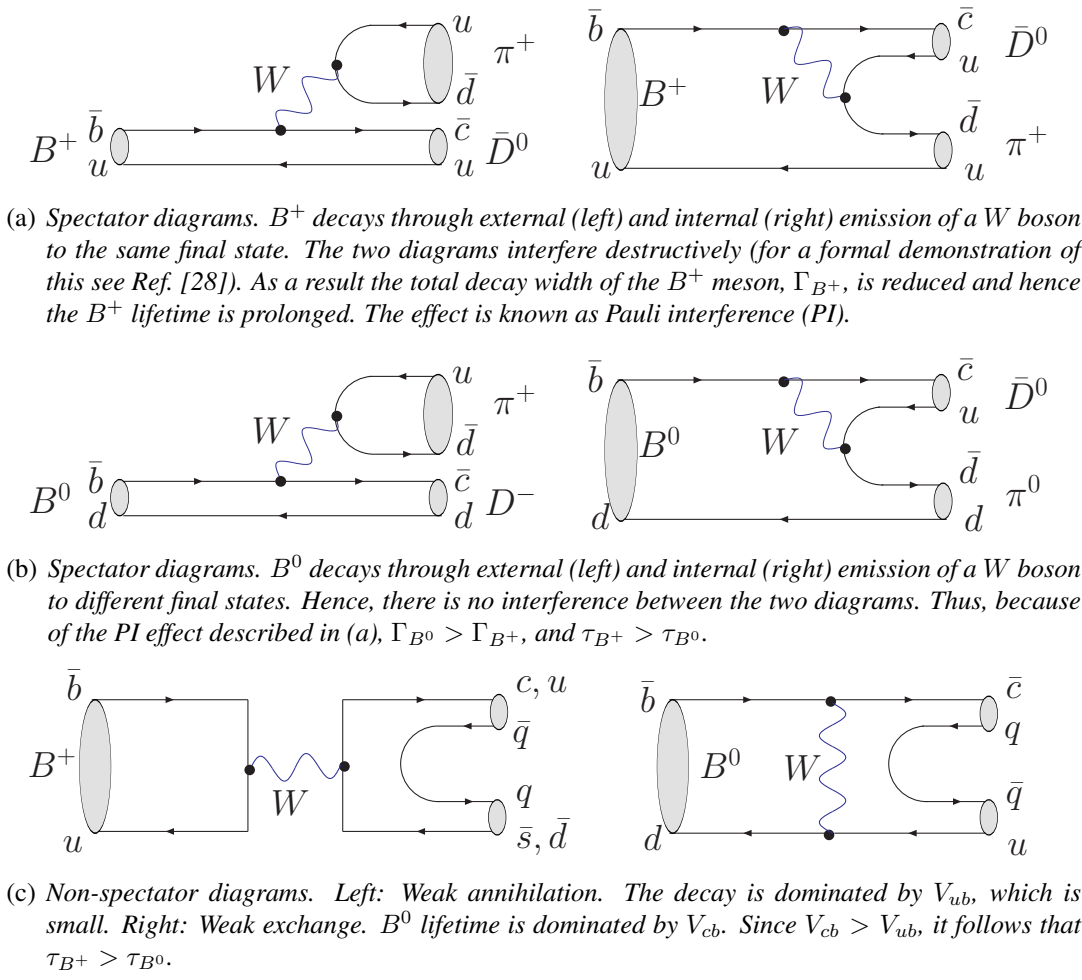


Figure 1.7. Spectator and non-spectator diagrams contributing to the B decay.

In spite of the fact that the spectator model can phenomenologically explain the B -lifetimes hierarchy (see the above diagrams), it cannot make precise lifetime predictions nor scale the range of the lifetime corrections with respect to the heavy quark mass. Presently, one of the most actual theoretical approaches for the study of the b -flavoured hadrons is the heavy quark expansion model. It allows for calculations of the B lifetimes within the Standard Model.

1.5.2 Heavy Quark Expansion Model

The HQE [10] is based on the *operator product expansion*, which is a method to separate the non-perturbative, long-distance QCD contributions to the decay amplitude from the short-distance electroweak contributions. In the HQE model, the total decay width of the B meson is expressed as an expansion in inverse powers of the b -quark mass ($1/m_b^n$) as

$$\Gamma = \Gamma_0 \left[1 + A_2 \left(\frac{\Lambda_{QCD}}{m_b} \right)^2 + A_3 \left(\frac{\Lambda_{QCD}}{m_b} \right)^3 + \cdots + A_n \left(\frac{\Lambda_{QCD}}{m_b} \right)^n \right], \quad (1.30)$$

where Γ_0 is the free b -quark decay width, as given in the spectator model (see Eq. (1.28)), Λ_{QCD} is the QCD scale parameter, and A_n are calculable coefficients. The following conclusions can be drawn from Eq. (1.30):

- At the lowest (leading) order, $1/m_b$, the total decay width of the B -meson is equal to the decay width of a free b quark, $\Gamma = \Gamma_0$. At this order the decay proceeds as in the spectator model, with no interaction with the light quark;
- At order $1/m_b^2$, the first correction term appears. The effects described by this term arise from time dilatation due to the recoil motion of the heavy b quark, and from spin interactions between the light and heavy quarks [10]. For example, baryons, which are surrounded by two light quarks with a total spin 0 decay faster than the mesons, which have a light quark partner with spin 1/2. As a result, the baryon lifetime is decreased by about 2% relative to the meson lifetime [29];
- At order $1/m_b^3$, Pauli interference in the B^+ decay (see Fig. 1.7a) and spectator effects, such as weak annihilation and weak exchange in both B meson decays (see Fig. 1.7c), start taking place. These effects are mainly responsible for the lifetime difference between the B^+ and B^0 mesons. Out of them, the effect of Pauli interference is strongest and contributes most in the prolongation of the lifetime of the B^+ relative to the B^0 meson [29].

The HQE prediction for the ratio of the lifetimes of B^+ and B^0 mesons, together with the experimentally measured value are listed in Table 1.4.

Lifetime ratio	Theoretical prediction	Measured Value
τ_{B^+}/τ_{B^0}	1.06 ± 0.02	1.071 ± 0.009

Table 1.4. Comparison of the measured value [13] of the lifetime ratio of B^+ and B^0 mesons with the HQE prediction [30].

For completeness, in Fig. 1.8, Fig. 1.9 and Fig. 1.10 comparisons of the results for τ_{B^+}/τ_{B^0} , τ_{B^+} and τ_{B^0} obtained from various high-energy physics experiments, are shown.

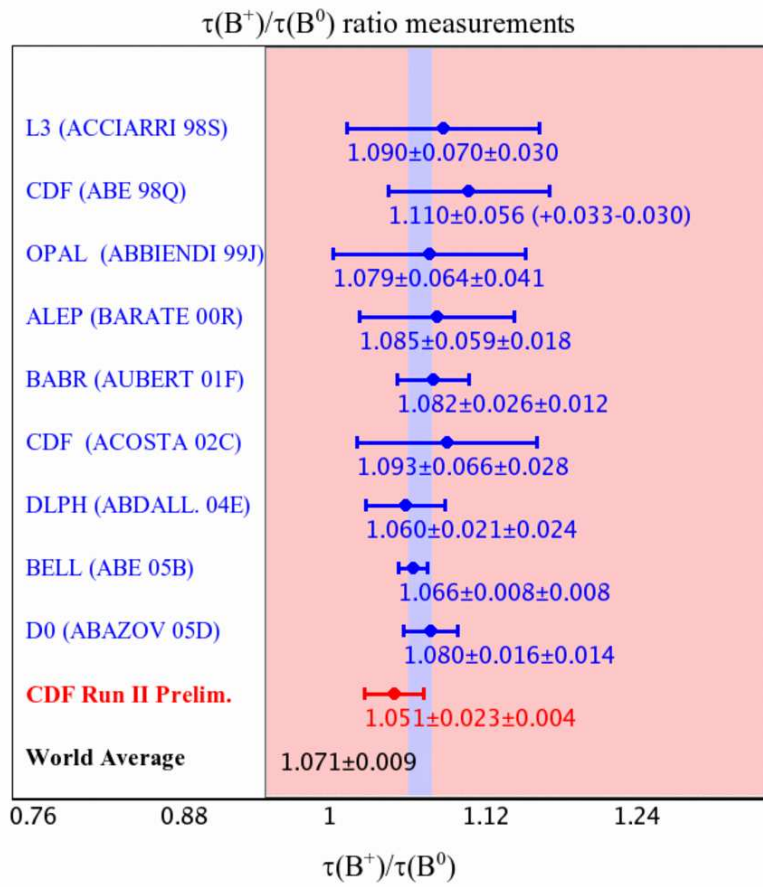


Figure 1.8. τ_{B^+}/τ_{B^0} , as measured from different experiments. The world average value [13] does not include the CDF preliminary result. The plot is taken from Ref. [29].

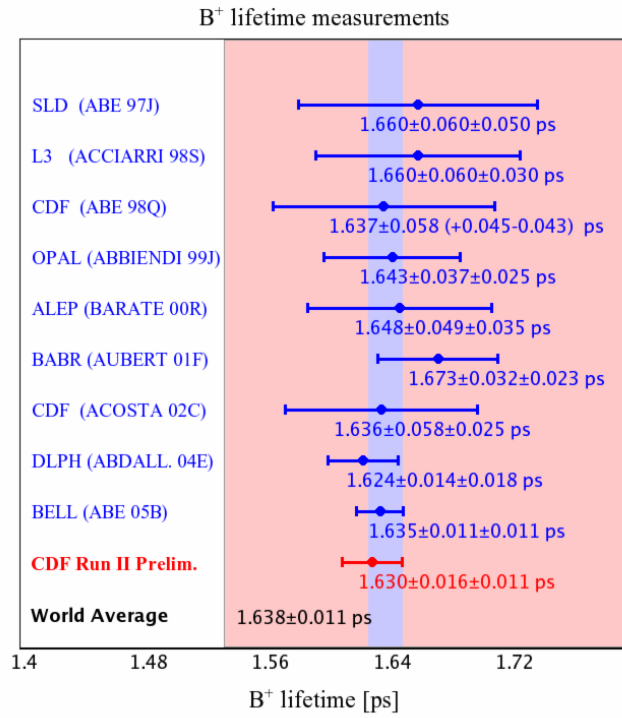


Figure 1.9. B^+ lifetime, τ_{B^+} , as measured from different experiments. The world average value [13] does not include the CDF preliminary result. The plot is taken from Ref. [29].

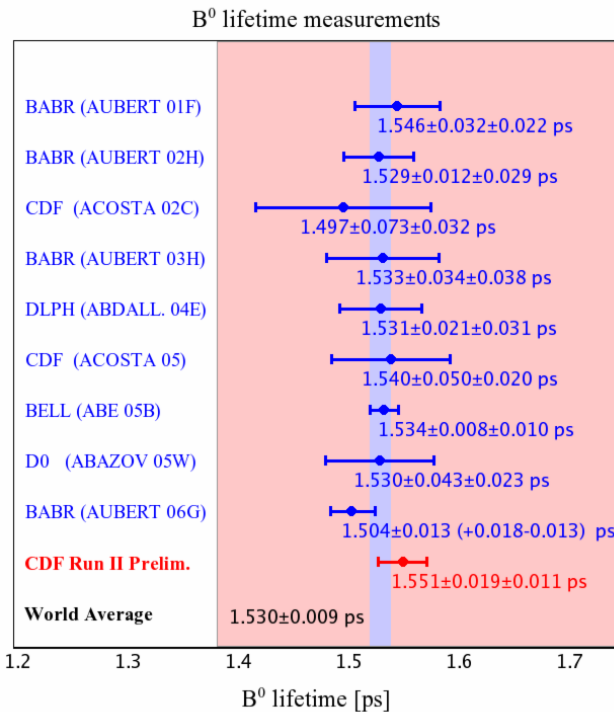


Figure 1.10. B^0 lifetime, τ_{B^0} , as measured from different experiments. The world average value [13] does not include the CDF preliminary result. The plot is taken from Ref. [29].

Chapter 2

The LHC b Experiment

..., a race of hyperintelligent pan-dimensional beings once built themselves a gigantic supercomputer called Deep Thought to calculate once and for all the Answer to the Ultimate Question of Life, the Universe, and Everything.

"The Restaurant at the End of the Universe", **Douglas Adams**
(1952-2001)

LHC b is an experiment at the proton-proton (pp) Large Hadron Collider (LHC) accelerator in CERN, Geneva. It is designed to make precision measurements of CP violation in the B -meson system and to study rare B -decays.

In what follows, the LHC accelerator (see Sec. 2.1), and the layout of the LHC b detector (see Sec. 2.2) are described. The Outer Tracker subdetector system is presented in more detail in Sec 2.3.

2.1 The Large Hadron Collider

The LHC [31] at the European Laboratory for Particle Physics (CERN) in Geneva, Switzerland, will be the world's most powerful particle accelerator, exceeding the present energy limits. Placed about 100 m underground, in the 27 km tunnel of the old LEP¹ accelerator, LHC will collide protons with a center-of-mass energy of $\sqrt{s} = 14$ TeV at a maximum luminosity of the order of 10^{34} cm $^{-2}$ s $^{-1}$.

LHC consists of two separate, parallel vacuum pipes in which two proton beams will be guided and accelerated in opposite directions. To keep the rotating protons in orbit a high magnetic field of ~ 8 T is required, provided by 1232 superconducting dipole magnets operating at a temperature of 1.9 K. The dipoles are built into a single 2-in-1 housing around the beam pipes, and will supply magnetic fields with reversed directions for the oppositely moving particles.

¹Large Electron-Positron collider at CERN, closed in November, 2000.

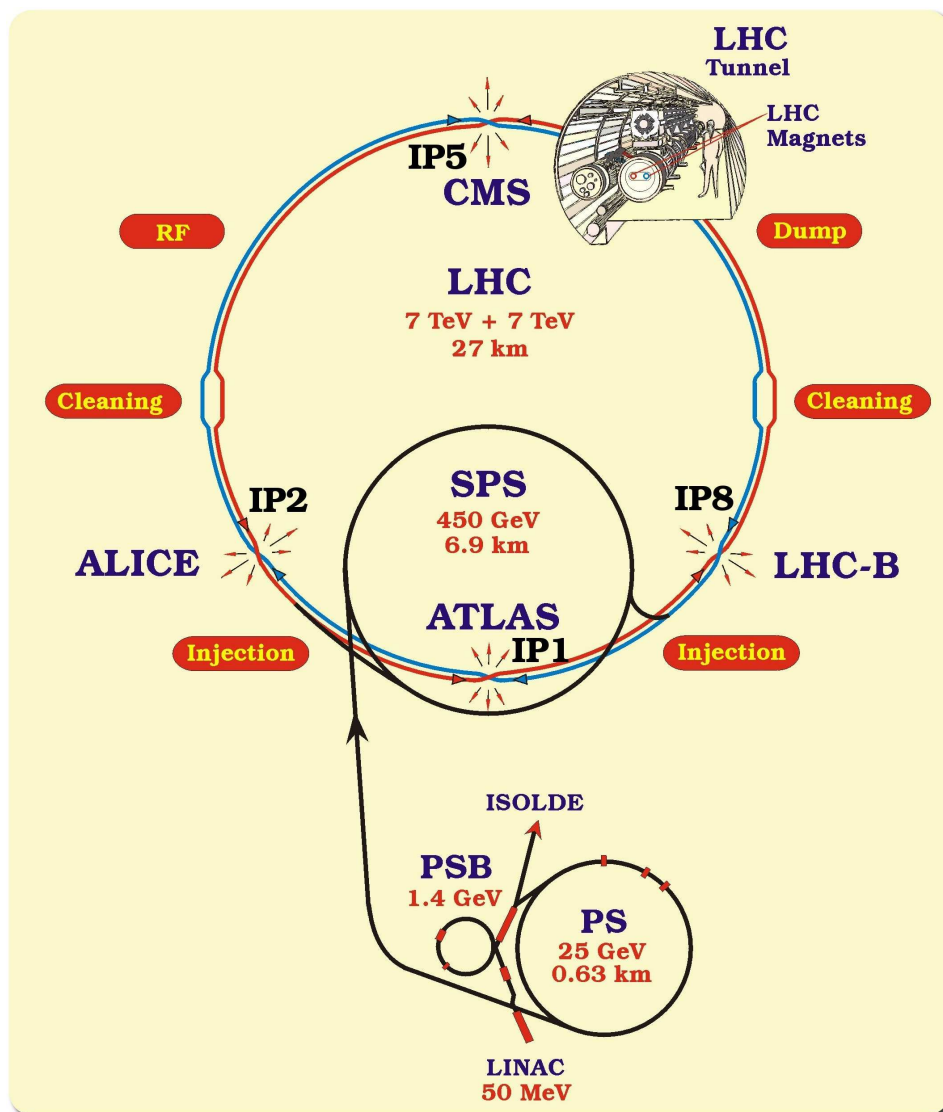


Figure 2.1. A sketch of the LHC accelerator, together with the system of pre-accelerators. The four LHC experiments are located at the interaction points IP1 (ATLAS), IP2 (ALICE), IP5 (CMS) and IP8 (LHCb).

The two proton beams, each containing 2808 bunches with about 10^{11} protons, will be collided in the center of the detectors, after reaching their final energy of 7 TeV. The bunch crossing rate of the pp collisions will be 40 MHz, corresponding to a 25 ns time window between two consecutive bunch intersections. On average² 27 pp inelastic interactions per beam crossing are expected at the nominal design luminosity of $10^{34} \text{ cm}^{-2}\text{s}^{-1}$ at ATLAS and CMS.

Before being injected in LHC, the proton beams will pass through a series of preliminary accelerations. A linear proton accelerator (Linac) will ensure the initial particle energy of 50 MeV. It is followed by the PS Booster increasing the energy to 1.4 GeV and subsequently by the Proton Synchrotron (PS) upgrading it to 26 GeV. The pre-accelerator phase will finish with the Super Proton Synchrotron (SPS) boosting the energy to 450 GeV, from where the protons will be transmitted into the LHC, Fig. 2.1.

The proton-proton collisions in LHC occur at four interaction points along the ring, namely IP1, IP2, IP5 and IP8, as indicated in Fig. 2.1. At these locations the LHC experiments are positioned. The main LHC parameters are summarized in Table 2.1.

Physics at the LHC requires high performance detectors. Four large-scale experiments will explore the products of the LHC collisions. Two of them - A Torroidal apparatus (ATLAS) [32] and Compact Muon Solenoid (CMS) [33] are general purpose detectors (designed to perform a broad spectrum of physics research). The remaining two - A Large Ion Collider Experiment (ALICE) [34] and LHCb are specialized in heavy ion³ collisions and b -quark physics, respectively.

In the next section the LHCb experiment is described in detail.

proton beam energy	7	[TeV]
ring circumference	26.66	[km]
dipole field	8.33	[T]
revolution frequency	11.2	[kHz]
bunch-crossing frequency	40	[MHz]
number of bunches per beam	2808	
number of particles per bunch	10^{11}	
nominal luminosity	10^{34}	$[\text{cm}^{-2}\text{s}^{-1}]$

Table 2.1. *LHC design parameters [31].*

²Under the assumption that the inelastic cross section for pp collision is $\sigma_{inel} = 80 \text{ mb}$.

³For ALICE, gold nuclei will be accelerated and collided at a center-of-mass energy of $\sqrt{s} = 5 \text{ TeV}$.

2.2 The LHCb Detector

2.2.1 Design Considerations

The purpose of the LHCb detector is to study the production of B mesons and their subsequent decays. In the proton-proton collisions at LHC, the b quarks, from which the b -hadrons originate, will be produced in $b\bar{b}$ -pairs [35]. The correlation of the polar angle θ (the angle between the beam axis and the direction of moving) of the b and the \bar{b} quarks, created in a pp event at $\sqrt{s} = 14$ TeV, as simulated with PYTHIA [36], is shown in Fig. 2.2 a). The formation of the b -hadrons (both b and \bar{b}) is concentrated at small (forward direction) or large (backward direction) angles along the beam. On that basis LHCb has been designed as a single-arm forward spectrometer, with an acceptance covering a large fraction of the phase-space of the created B mesons (within the acceptance of LHCb (see Sec. 2.2.2) about one third of the produced $b\bar{b}$ -pairs will decay [16]).

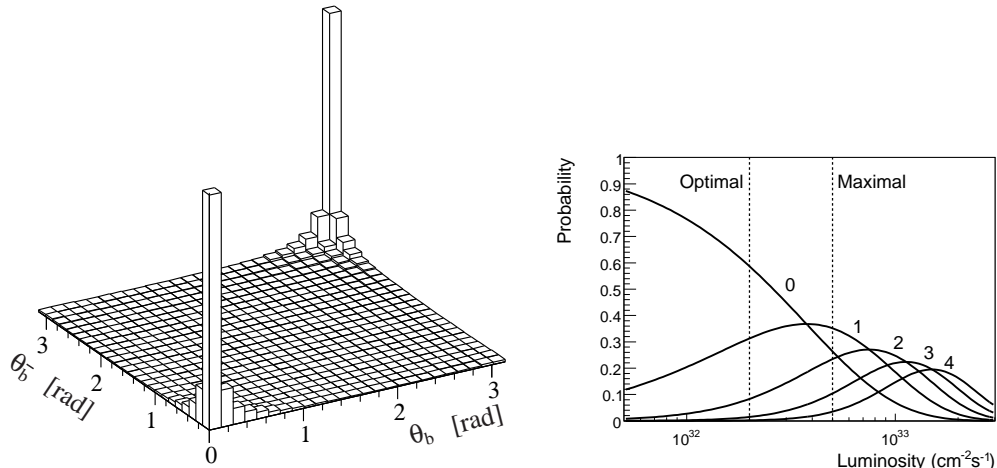


Figure 2.2. (a) PYTHIA simulation of the correlation between the polar angles of the b and the \bar{b} quarks produced simultaneously in a single pp event at $\sqrt{s} = 14$ TeV. (b) Probability for 0, 1, 2, 3 and 4 proton-proton inelastic interactions per bunch crossing as function of the luminosity at $\sqrt{s} = 14$ TeV.

Another important design aspect of LHCb is the lower luminosity than the nominal $10^{34} \text{ cm}^{-2}\text{s}^{-1}$. The reason for this is the necessity of avoiding multiple primary interactions per bunch crossing (the so called *pile-up* effect), which would hamper the track reconstruction and the B -decay vertex finding. The desirable operating luminosity for LHCb is the one at which the probability of having a single pp interaction per bunch crossing is maximal, as at the same time the probabilities of having zero

or more than one interaction are minimized. The optimal solution is found [37] at $\mathcal{L}_{\text{LHC}b} = 2 \times 10^{32} \text{ cm}^{-2}\text{s}^{-1}$, as marked in Fig. 2.2 b). This value of the luminosity is chosen to be the LHCb working luminosity. It will be achieved by defocusing the proton beams at IP8. At $\mathcal{L}_{\text{LHC}b}$, in one nominal year of LHCb running (10^7 s) $10^{12} b\bar{b}$ -pairs are expected to be produced⁴. The maximal luminosity that LHCb can work with is $\mathcal{L}_{\text{LHC}b}^{\text{MAX}} = 5 \times 10^{32} \text{ cm}^{-2}\text{s}^{-1}$. All subdetectors of LHCb, as well its trigger and data-acquisition systems are designed to withstand the radiation levels and to operate properly at $\mathcal{L}_{\text{LHC}b}^{\text{MAX}}$.

2.2.2 General Structure

A cross section of the LHCb spectrometer can be seen in Fig. 2.3. The acceptance of the detector covers a region from 15 to 300 mrad in the horizontal x - z plane (the bending plane of the magnet) and from 15 to 250 mrad in the vertical y - z plane.

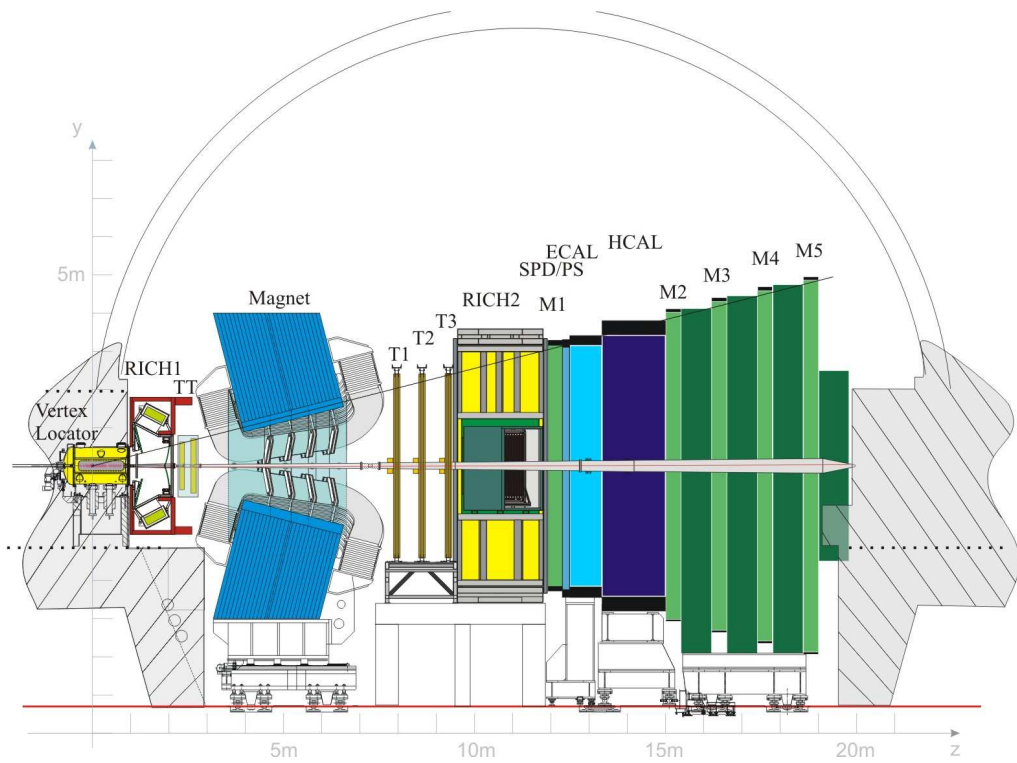


Figure 2.3. Cross section of the LHCb detector (y - z plane).

⁴The $b\bar{b}$ cross section $\sigma_{b\bar{b}}$ is assumed to be $500 \mu\text{b}$.

LHCb contains the following detector systems:

- Tracking detectors
 - Vertex locator - for precise determination of the B primary vertex;
 - Trigger tracker (TT) - used in making the trigger decision and for specific particle tracks reconstruction;
 - Outer Tracker (T1, T2, T3) - for reconstruction of the tracks of the charged particles;
 - Inner Tracker (IT) - embodied in the center of the T-stations; used to reconstruct the particle tracks close to the beam pipe, where high event occupancy is foreseen;
- Particle Identification (PID) detectors
 - Ring Cherenkov detectors (RICH1 & RICH2) for achieving K^\pm/π^\pm separation;
 - Calorimetry system
 - * Scintillator pad / Preshower detector (SPD/PS) - for charged particles identification, $e - \gamma$ separation and electron-hadron discrimination;
 - * Electromagnetic calorimeter (ECAL) - for reconstruction of the energy and the position of the electrons (positrons);
 - * Hadronic calorimeter (HCAL) - for identification and reconstruction of the energy and the position of the hadrons;
 - Muon system (M1, M2, M3, M4 and M5) - for identification and reconstruction of the muon tracks.

The construction and the working principle of the LHCb detectors listed above will be described in the following sections.

A central element in the LHCb detector is its warm-coil dipole magnet [38], located between the TT and T-stations. The purpose of the magnet is to deflect the paths of the traversing charged particles. The momenta of the charged particles will be determined from the curvatures of their reconstructed trajectories. The magnetic field created by the dipole magnet will be oriented vertically. The total integrated magnetic field will be $\int B dl = 4.2$ Tm. A plot representing the y-component of the magnetic field as a function of distance is presented in Fig. 2.4, with the position of the tracking detectors indicated.

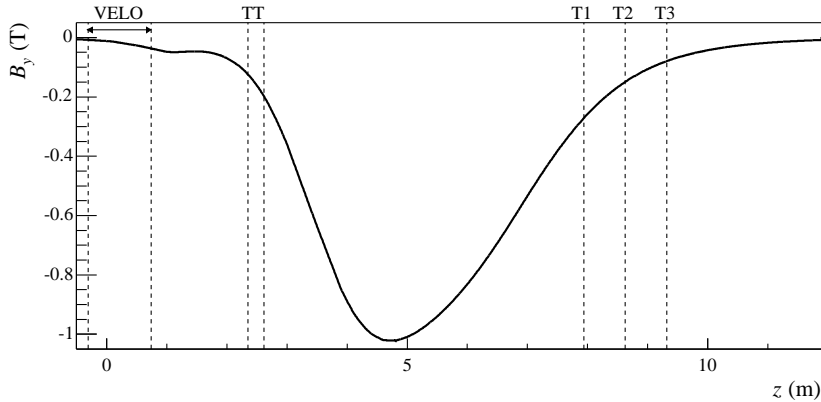


Figure 2.4. The y -component of the magnetic field as a function of z -position.

2.2.3 Vertex Locator

The VErtex LOcator (VELO) [39] will measure the track coordinates close to the pp interaction point. It will be used for the reconstruction of the primary interaction vertex (PV) as well as for the reconstruction of the secondary B meson decay vertex (SV).

The VELO contains 21 stations of silicon detectors, placed perpendicularly along the beam axis z , encompassing the interaction region; see Fig. 2.5. One station consists of 2 modules positioned on both sides of the beamline. Figure 2.6 shows that each module is constructed of two types of $200\text{ }\mu\text{m}$ thick silicon sensors, separated by 2 mm in z and having a half-circle shape. The r -type sensor, built of circular, concentric silicon strips around the beam axis will measure the r -coordinate of the particle tracks, while the ϕ -type sensor, with its straight, radial silicon segments will measure the ϕ -coordinate.

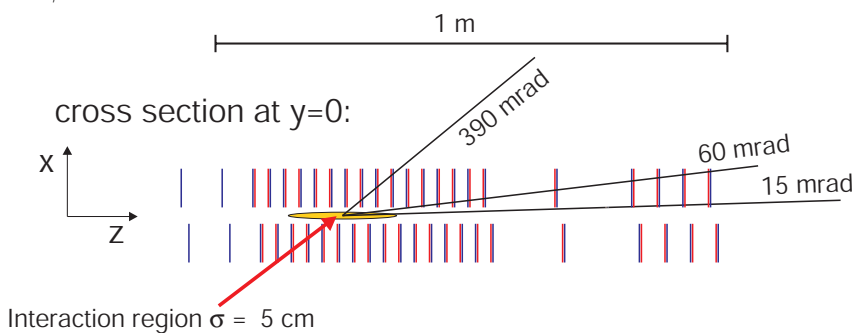
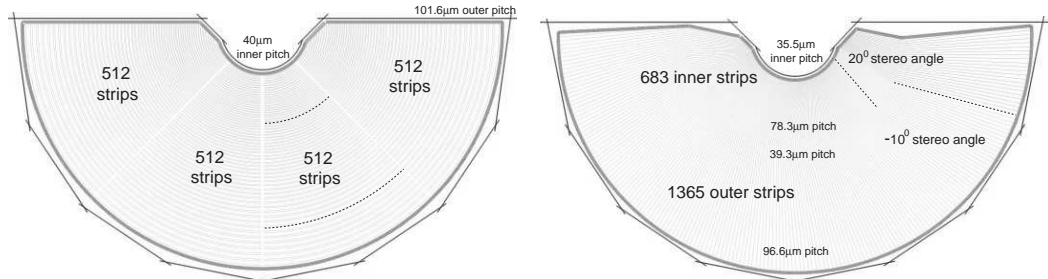


Figure 2.5. Top view of the VELO system. The IP has a spread $\sigma_{IP} = 5.3\text{ cm}$ along the beam axis, due to the width and the small crossing angle of the proton bunches. The arrangement of the VELO stations ensures that 99.9% of the tracks will traverse at least 3 stations within the acceptance from 15 to 390 mrad for any IP in the range $[-\sigma_{IP}, \sigma_{IP}]$, [40].



(a) *r*-measuring sensor. It is divided into 4 sectors of 45° . The pitch between the strips is 40 μm for the inner strips and 101.6 μm for the outer strips.

(b) ϕ -measuring sensor. It consists of an inner section with stereo angle of 20° and of an outer section with stereo angle of -10° . The strip pitch varies from 35.5 μm to 78.3 μm for the inner section, and from 39.3 μm to 96.6 μm for the outer section.

Figure 2.6. Layout of the two silicon sensors that make up one VELO module, [40].

The first two stations at the VELO upstream side consist of single *r*-type sensors. These 4 sensors will be used as a Pile-Up trigger detector, suppressing events with multiple pp interactions.

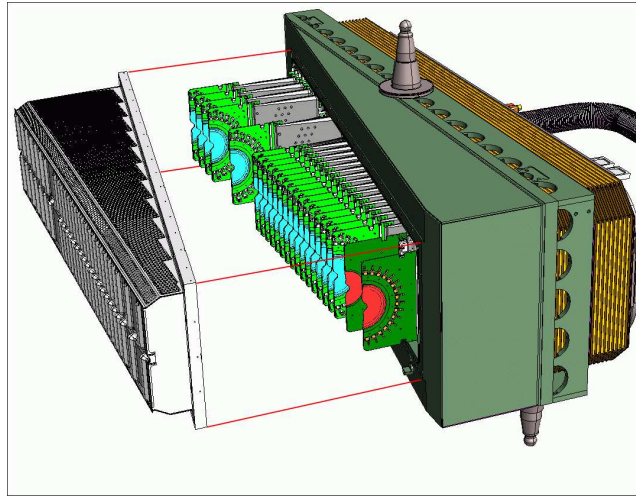


Figure 2.7. A drawing of one half of the VELO stations. The aluminum container that will encapsulate the modules is also shown. The first two sensors belong to the Pile-Up detector.

To obtain maximum resolution in the reconstruction of the primary vertex, the VELO modules have to be put as close as possible to the interaction point. To realize this, both the left and the right modules are set into a vacuum environment in two separate containers of thin-walled aluminum foil, which also will act as wake field suppressor and will protect the sensors electronics from RF pickup from the

beams, Fig 2.7. The proton beams will be collided in the gap between the two VELO containers. This way the two module halves can maximally approach the beamline (up to 7 mm), while the LHC primary vacuum will be preserved.

2.2.4 Trigger Tracker

The Trigger Tracker (TT) [40] is positioned after the RICH1, just in front of the magnet. It incorporates four detection layers of silicon micro strip sensors, combined in two stations - TTa and TTb. Each sensor has dimensions of $94.4 \text{ mm} \times 94.6 \text{ mm}$ and thickness of $500 \mu\text{m}$ and contains 512 silicon strips arranged at a pitch of $183 \mu\text{m}$ [41]. The silicon strips in the TT layers are oriented differently with respect to the y -axis. The first and the fourth layers are equipped with vertical strips (x -layers), while the strips in the second and in the third layers are rotated in $+5^\circ$ (u -layer) and -5° (v -layer), respectively, Fig. 2.8. This stereo configuration of the layers will allow a 3D reconstruction of the tracks. The sensitive area of the TT covers the full LHCb acceptance.

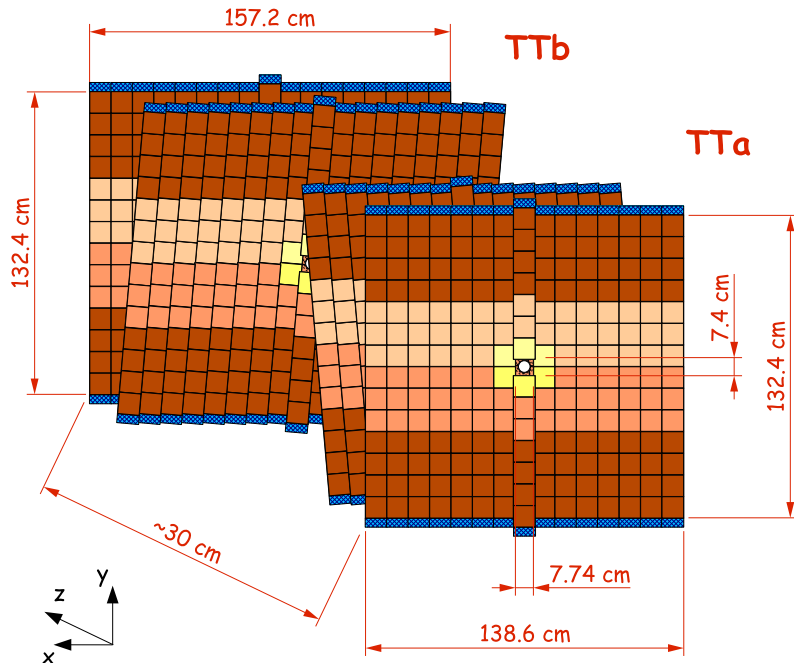


Figure 2.8. The layout of the TT system is shown. The strips in the sensors at a given layer that are colored identically are connected in vertical direction. Depending on the expected event occupancy, at maximum 4 sensors are connected (at the outer region) and read out with a single preamplifier channel, [42].

The tasks of the TT stations are first, to supply the trigger with information about

the transverse-momentum p_t of the tracks and second, to reconstruct the trajectories of the long-lived neutral particles decaying outside the VELO (such as K_s for instance). It can also be used for reconstruction of the tracks of low-momentum particles that are bent out of the LHCb acceptance before reaching the T-stations. For the determination of p_t , the presence of a low magnetic field between the VELO and the TT is used (see Fig. 2.4). Together with the good spatial resolution of the TT of $\sim 50 \mu\text{m}$ [43], this field ($\int B_y dl = 0.15 \text{ Tm}$) is sufficient to achieve momentum resolution of 20%-40% for high-momentum tracks with $0.5 < p_t < 4 \text{ GeV}/c$ [44].

2.2.5 Inner Tracker

The Inner (IT) and the Outer (OT) Trackers (a description of the OT is given in Sec. 2.3) compose the T1, T2 and T3 tracking stations, placed after the magnet; see Fig. 2.3.

The Inner Tracker [45] covers a 120 cm wide and 40 cm high cross-shaped region in the center of the T stations, around the beam pipe, where the highest particle flux is expected. Each of the 3 IT stations, consists of 4 layers of silicon micro strip sensors with $x-u-v-x$ stereo topology (see Sec. 2.2.4). The arrangement of the sensors and the overall dimensions of the layers are given in Fig. 2.9. The sensors are 7.6 cm wide and 11 cm long, with thickness of $320 \mu\text{m}$ for the single sensors above and below the beam pipe, and of $410 \mu\text{m}$ for the double sensors aside the beam pipe. They accommodate 384 readout strips with a strip pitch of $198 \mu\text{m}$ [46].

Although the IT occupies only 1% of the sensitive area of the T stations it will detect almost 20% of all charged particles that enter the tracking system.

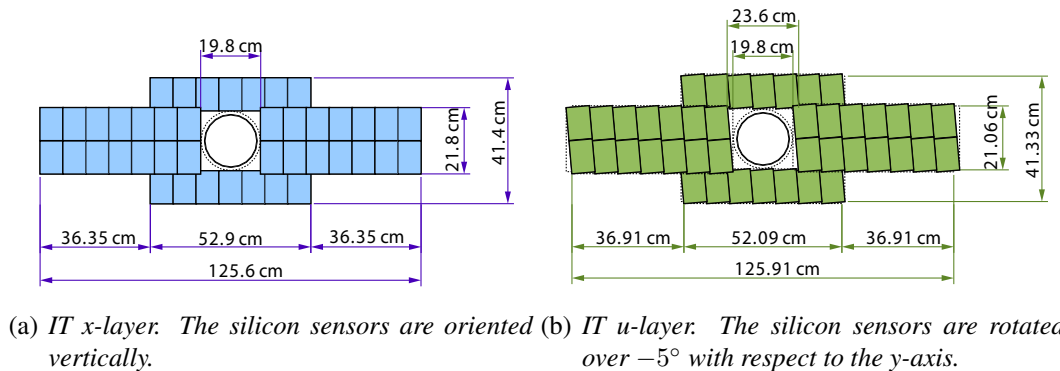


Figure 2.9. View of IT x and u layers in the $(x-y)$ plane. The circle at the center of the cross-shaped regions corresponds to the beam pipe, [45].

2.2.6 RICH Detectors

Two Ring Imaging CHerenkov detectors [40, 47] - RICH1 and RICH2 will operate in LHC b . Their purpose is to provide particle identification, and in particular to distinguish between different charged hadrons. The analysis of various decay channels, for instance $B_q^0 \rightarrow h^+ h^-$ ($h^\pm = \pi^\pm, K^\pm$), strongly relies on efficient $\pi - K$ separation, which will be achieved with the RICH detectors. Simulations show [40] that the kaon identification efficiency provided by the RICH system is $\sim 90\%$ with a pion misidentification rate of the order of 10% for tracks with momenta up to 100 GeV/c.

The RICH detectors make use of the Cherenkov effect - a charged particle moving in a medium emits electromagnetic radiation if its velocity v is greater than the speed of light in that medium. If n is the refractive index of the medium and $\beta = v/c$, then the Cherenkov light is emitted if $n\beta \geq 1$. The light is radiated at an angle θ_c with respect to the direction of motion and satisfies the relation

$$\cos \theta_c = \frac{1}{\beta n} . \quad (2.1)$$

The particle's velocity can be determined by measuring the angle θ_c , and when the momentum is known, the mass can be extracted.

The RICH1 is positioned between the VELO and the trigger tracker and RICH2 is placed between the T-stations and calorimeters, see Fig. 2.3. RICH1 will be used to identify low momenta particles with $1 < p < 60$ GeV/c, while RICH2 will cover momenta up to 100 GeV/c. The main parameters of the radiators of the two RICH detectors are listed in Table 2.2.

	RICH1		RICH2
	Silica Aerogel	C ₄ F ₁₀	CF ₄
n	1.03	1.0014	1.0005
θ_{max} [mrad]	242	53	23
p range [GeV/c]	1 - 10	10 - 60	60 - 100

Table 2.2. Values of the refractive index n , the saturation angle θ_{max} and the working momentum range of the radiator media used in RICH1 and RICH2.

The Cherenkov light emitted in the radiators will be collected on a plane of photodetectors. They consist of cylindrical pixellated HPD⁵ tubes with an overall diameter of 83 mm.

⁵Hybrid Photon Detectors.

2.2.7 Calorimeters

The calorimetric system [48] of LHCb will be used to identify hadrons, electrons and photons and to measure their energy and position. It is located between the first and the second muon stations, as indicated in Fig. 2.3. In addition, the information from the calorimeters will be exploited by the trigger system to select events with high E_T (transverse energy), which are typical for the B -decays. All calorimeters in the system are of the sampling type, with a "sandwich"-like structure, made of separate layers of active and passive (absorber) materials. An incident particle loses its energy due to a cascade of interactions with the absorber material of the calorimeter. In this process *showers* of secondary particles are produced. The total energy of all showers absorbed in the active material is measured and related to the initial energy of the particle.

A brief description of the different LHCb calorimeters, in the order of their position, is given below.

Scintillation Pad Detector (SPD) / Preshower (PS)

Made of 15 mm thick scintillator pads the SPD will distinguish between electrons and photons (photons will traverse the scintillator without interaction, and therefore will not create a signal). A 12 mm lead wall, called lead converter, positioned after the SPD and before the preshower detector induces electromagnetic showers. The PS, also made of scintillator pads, will detect these showers, discriminating this way between electrons and hadrons.

Electromagnetic Calorimeter (ECAL)

The ECAL has a modular design and will be used to measure the energy of the electrons and photons. Each ECAL module is constructed of alternating slices of 4 mm thick scintillator tiles and lead sheets with thickness of 2 mm. In total 66 layers of lead/scintillator are accommodated in a module, corresponding to a total radiation length of 25 X_0 . The modules are installed with layers oriented perpendicularly to the z -axis. The energy resolution of the ECAL is given by

$$\frac{\sigma(E)}{E} = \frac{10\%}{\sqrt{E}} \oplus 1.5\% , \quad (2.2)$$

where \oplus means summation in quadrature and E is in GeV.

Hadronic Calorimeter (HCAL)

The energy of the charged hadrons will be measured by the HCAL, which consists of alternating 16 mm thick iron plates and 4 mm thick scintillating tiles oriented in

parallel to the z -axis. The HCAL energy resolution (E in GeV) is

$$\frac{\sigma(E)}{E} = \frac{80\%}{\sqrt{E}} \oplus 10\% . \quad (2.3)$$

2.2.8 Muon System

Muons are expected to provide clean signatures for many CP-sensitive B decays. For example, muons are among the final states in the two "gold-plated" CP decays $B_d^0 \rightarrow J/\psi(\mu^+\mu^-)K_s^0$ and $B_s^0 \rightarrow J/\psi(\mu^+\mu^-)\phi$. The only particles (except the neutrinos) that can traverse the calorimeters are the muons. In LHCb the identification and measurement of muons are assigned to a dedicated muon system, consisting of five muon stations [49]. The first muon station, M1, is located before the SPD, and the other four, M2 - M5, are placed behind the HCAL, separated by 80 cm thick iron plates, see Fig. 2.3. The iron plates together with the calorimeters play the role of *muon filter*, rejecting the background of hadrons. The muon stations are mainly built of multi-wire proportional chambers, which are characterized by a high level of radiation hardness and fast response (25 ns). The latter is an important feature, since the muon system is also included at the earliest trigger level (Level-0). The innermost region of M1 will be covered with gaseous electron multiplier detectors (triple-GEM), which will be able to handle the higher particle flux rates expected in that area.

2.2.9 Trigger System

Given the relatively low luminosity at LHCb of $2 \times 10^{32} \text{ cm}^{-2}\text{s}^{-1}$, only 10 MHz will contain *visible interactions*, i.e. interactions producing at least two reconstructible tracks in the detector. From these visible interactions, approximately 100 kHz will contain $b\bar{b}$ -pairs. Moreover, the branching ratios of the B decays of interest are of the order of 10^{-4} . Therefore, a trigger to filter out the B -decays of interest from the background collisions is of substantial importance for the experiment.

The trigger system of LHCb [44, 50] is structured in two levels - Level-0 Trigger and High Level Trigger. They will reduce the initial event rate to the acceptable 2 kHz. The design of the two trigger levels is outlined briefly below.

Level-0 Trigger

The B -hadrons are relatively heavy and long-lived, and their decay products possess high transverse energy, E_T . The Level-0 (L0) trigger exploits this fact and selects particles with high E_T . At the same time, L0 rejects high-multiplicity events and events with multiple pp interactions. The L0 trigger is fully implemented in hardware with a fixed latency of 4 μs . The trigger decision generated by the L0 decision unit (L0DU) is based on the dedicated trigger outputs from the calorimeter system, the muon system and the VELO pile-up system.

The calorimeter system supplies the L0DU with information about the candidates (h, e^-, γ, π^0) with highest E_T . It also gives to L0DU the total HCAL E_T and the SPD multiplicity. The muon system sends the two highest- p_T candidates from each of its four quadrants. Finally, the VELO pile-up system provides the number of tracks from the second vertex and the pile-up system hit multiplicity.

The L0 will reduce the initial rate of 16 MHz of inelastic pp collisions (at the nominal luminosity of $2 \times 10^{32} \text{ cm}^{-2} \text{s}^{-1}$) to 1 MHz.

Hadronic, electronic and muonic channels are typically selected with efficiencies of approximately 50%, 70% and 90%, respectively.

High Level Trigger

The events accepted from L0 are transmitted to the High Level Trigger (HLT). The HLT is based on software algorithms, running on a computer farm with ~ 1800 CPU nodes. The HLT algorithms exploit the fact that B-mesons are characterized by large lifetimes. First, partial event reconstruction is performed. Depending on the L0 decision, few tracks are selected based on their transverse momenta and impact parameters. After a significant decrease of the event rate, full reconstruction is done.

The HLT will decrease the input event rate of 1 MHz to 2 kHz, which is finally sent for mass storage. After optimization, it is expected that the HLT efficiencies will reach a level of 60% - 80% [51].

2.3 Outer Tracker

In this section the layout and the operation principle of the Outer Tracker is explained, which is of particular relevance for Chapters 3 and 4.

2.3.1 General Layout of the OT system

The Outer Tracker (OT) system [52] of the LHCb experiment has a modular design. It is constructed of stand-alone, gas-tight detector units, which are built out of drift cells with straw tube geometry. As in the IT case, the modules in the 3 OT stations are organized in detection layers, arranged in a $x-u-v-x$ stereo view, i.e. the drift cells in each of the 4 detection layers of an OT station are oriented with respect to the y -axis in 0° , -5° , $+5^\circ$ and 0° . In Fig. 2.10 the order of the modules in a station is shown. Two main type of modules can be distinguished - long (F-type) ones, situated adjacent to each side of the IT and short ones (S-type), placed above and below the IT. Each layer contains 14 F-modules and 8 S-modules.

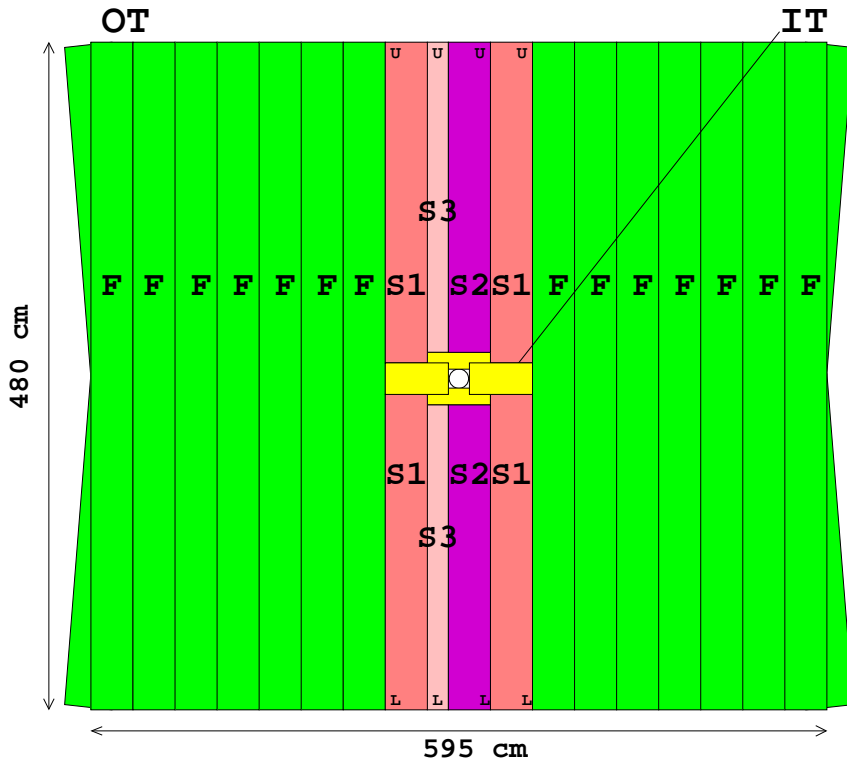


Figure 2.10. Arrangement of the OT modules in a T-station (x - y plane). In the center, the modules of the silicon Inner Tracker (IT), surrounding the beam pipe are indicated.

The overall parameters of the different OT module types are listed in Table 2.3.

The Outer Tracker is a joint project. The three major contributing sites are NIKHEF, Heidelberg Physikalisches Institute and Warsaw University. NIKHEF is responsible for the building of 135 F-modules out of a total of 207 (including the spares).

Module type	dimensions [mm ³]	# channels	quantity
F	4900×340×31	256	168
S1	2375×340×31	128	24
S2	2275×340×31	128	12
S3	2275×170×31	64	12

Table 2.3. Design parameters of the OT modules.

2.3.2 OT Module Design

An OT F-module consists of two, staggered mono-layers of 64 straws, see Fig 2.12. The channels are electrically disconnected at the center of the module to limit the hit occupancy. The straws are glued on a *panel*, manufactured of 10 mm thick polymethacrylimide rigid foam (Rohacell) sandwiched between two carbon-fiber skins. The inside part of each panel is covered with 25 μm kapton foil to ensure gas tightness, followed by 12 μm aluminum layer providing common grounding of the straws. Photographs of a panel with wired straws are displayed in Fig. 2.11. The material of the straws is composite and includes two layers, as is shown in Fig. 2.13. The outer layer, with a thickness of 12 μm is made of aluminum-laminated kapton foil and has shielding functions whereas the inner layer, which acts as a cathode, is produced out of Kapton-XC foil with a 25% doping of carbon. The straw tubes have an inner diameter of 4.9 mm, a length of \sim 2.4 m and are arranged with a pitch of 5.25 mm, Fig. 2.14. The anode is centered along the straw axis and consists of gold-plated tungsten wire with diameter of 25 μm . The wire is supported every 80 cm by small plastic wire locators, inserted in the straw tube.

Two panels with straws, packed together, form a gas-tight detector box with 256 channels, which are read out from both modules ends.

The S1 and S2 modules are designed to have 64 straw tubes per mono-layer and are half the length of an F-module. This results in 128 channels per module. The S3 modules are the smallest. They have half the normal width, corresponding to 32 straw tubes per mono-layer, or 64 channels in total for the module.

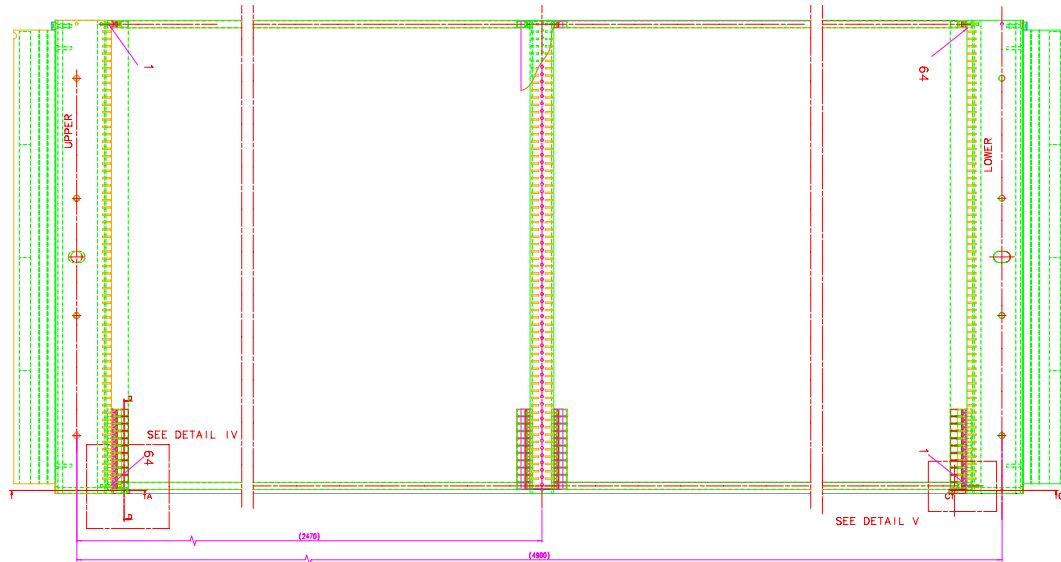
The baseline counting gas that will be used for the OT detector is a mixture of Ar (70%) and CO₂ (30%). This assures a fast signal collection time of <50 ns - 2 LHC bunch crossings. The gas volume of the modules will be continuously exchanged at the rate of one module volume every two hours.



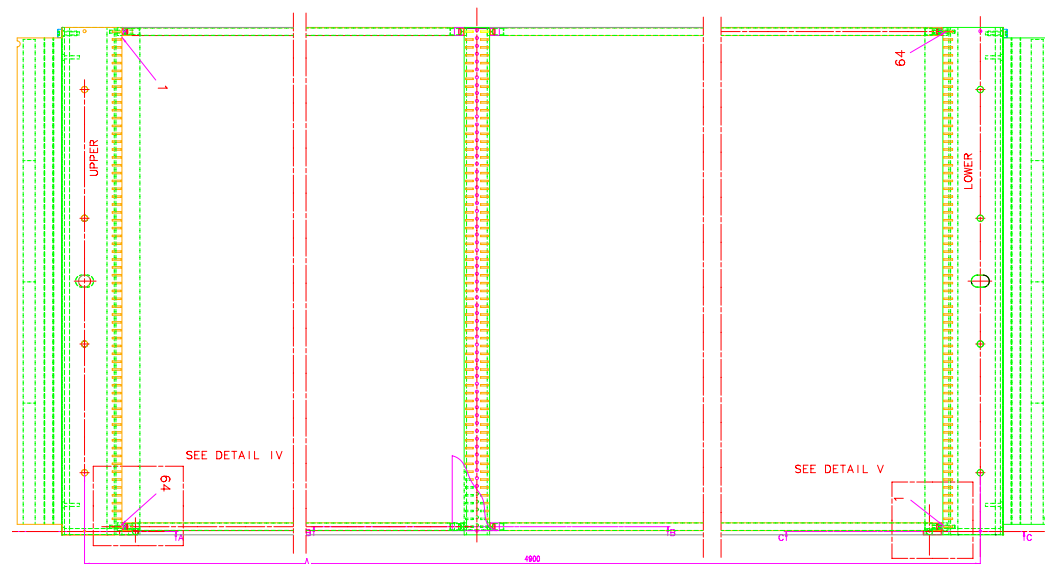
(a) *Panel with straw tubes. In the middle the straws are separated and the wires are electrically disconnected.*

(b) *Close view of the straw tubes with wires at the end of the panel.*

Figure 2.11. *Photographs of a panel with wired straws.*



(a) Top view drawing of mono-layer A with indications of the positions of the cathode straws and anode wires. Two sections of long and short 64 straws can be distinguished.



(b) Top view drawing of mono-layer B. The long and short straw tube sections are with swapped places in comparison with mono-layer A.

Figure 2.12. Drawings of the two mono-layers (A and B) that compose an OT F-module. Both mono-layers are built of 64 long and 64 short cathode straw tubes with corresponding number of anode wires. Note, that the mono-layers are not identical. The difference is in the exchanged positions of the long and short straws.

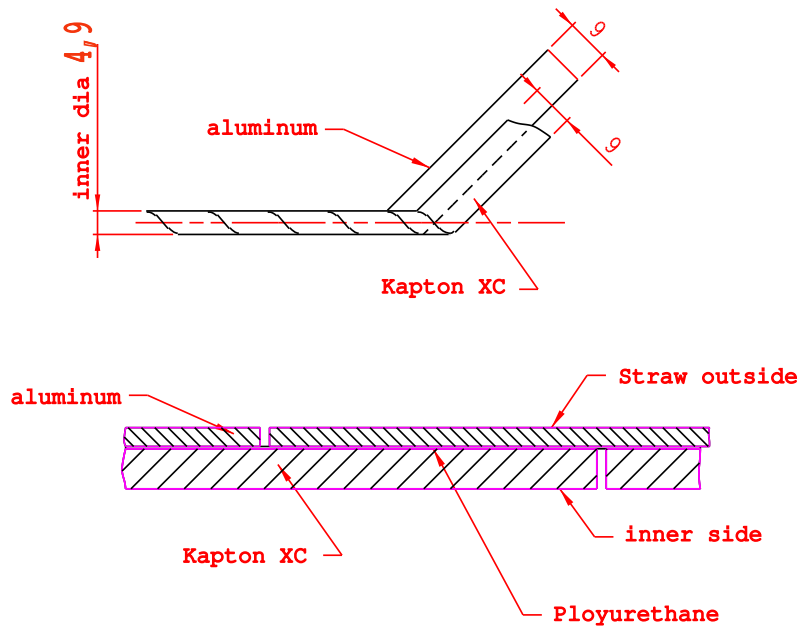


Figure 2.13. An illustration of the winding pattern of the straw tubes. The Kapton-XC and the aluminum layers are wound from 9 mm wide strips, staggered by a half winding cycle, [52].

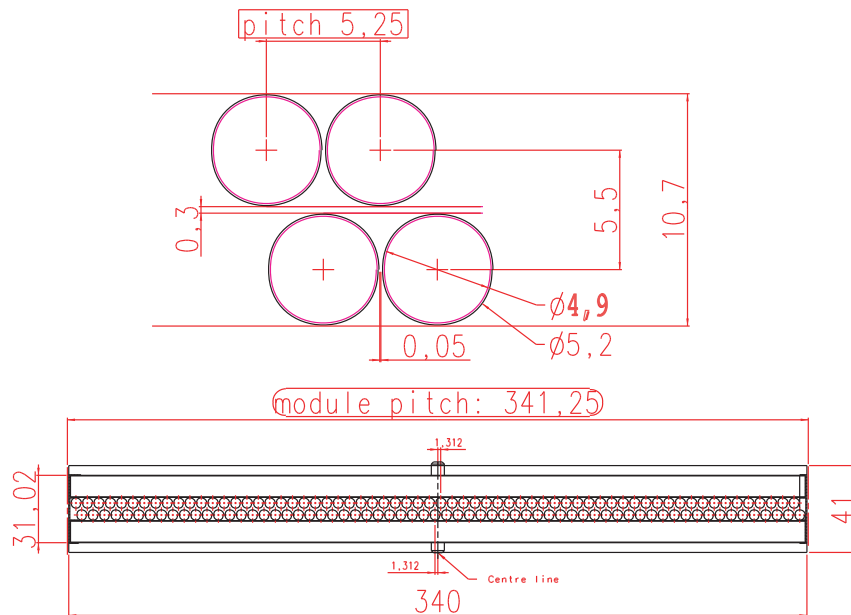


Figure 2.14. Cross section view of an OT F-module, [52].

2.3.3 OT Working Principle

In essence, the OT detector represents an array of fast drift chambers with cylindrical geometry, characterized by a high gas gain and good proportionality. This section will briefly describe the operation principle of a gaseous detector (drift tube) working in proportional mode.

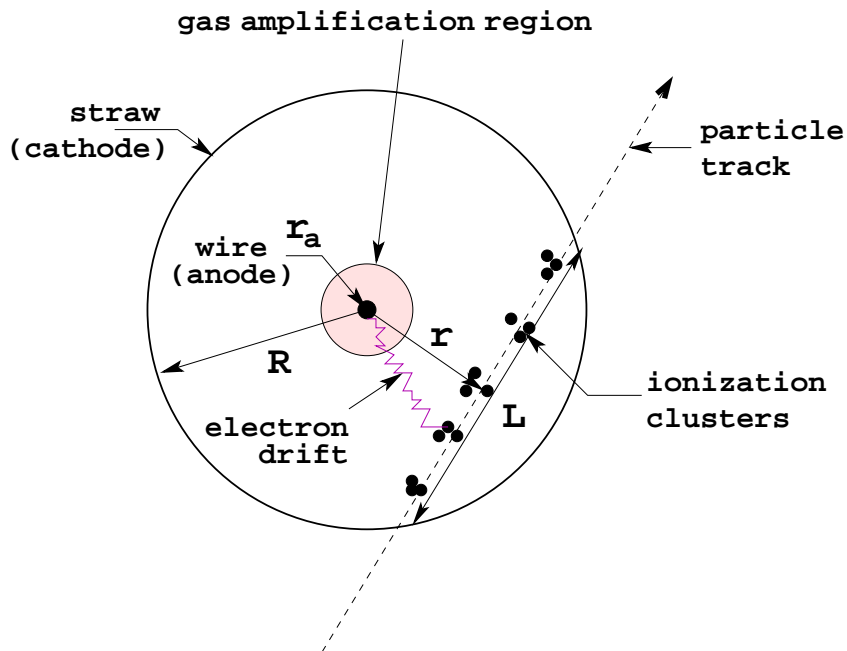


Figure 2.15. A sketch of the OT drift cell in action. L is the length of the path of the ionization particle, r is the distance of closest approach of the track to the wire and R is the cell diameter.

Each OT straw tube is a stand-alone drift chamber (cell) with a cathode - the conductive interior of the tube itself and an anode represented by the sense wire stretched along the tube's axis. The cell is filled with gas and an electrical potential difference between the cathode and the anode is created. When a charged particle traverses the gas volume of the chamber, it interacts electromagnetically with the gas constituents. As a result of these interactions, the particle will lose energy, which will be transferred to the gas molecules. Consequently, the gas becomes ionized, liberating electrons and ions, when the transferred energy is higher than the ionization potential of the gas. The number of primary ionization encounters or *clusters* that the charged particle leaves along its path, Fig 2.15, strongly depends on the nature of the used gas. For the baseline OT gas mixture of Ar(70%)-CO₂(30%) at standard temperature and pressure (0° and 101.325 kPa), a minimum-ionizing particle would produce every cm on average 31 clusters with, on average, 3 electron-ion pairs [53]. Because of the applied electric field, the detached electrons and the ions will start to drift towards the anode and the cathode, respectively. Since the ions are much

heavier than the electrons, they will drift slower⁶. Secondary electron-ion pairs might be produced from the primary electrons if the latter are energetic enough. Equation (2.4) expresses the dependence of the intensity of the electric field E on the distance to the anode r , for a straw tube with radius R :

$$E(r) = \frac{U}{r \ln \frac{R}{r_a}} . \quad (2.4)$$

U is the applied voltage and r_a is the diameter of the wire. It is clear that E increases close to the wire. This means that the energy of the electrons also will increase, and at some distance close to the wire it will be sufficient for ionization. In turn, the newly released electrons also will cause ionization and the process will result in an avalanche of ionizations. The region where this avalanche starts is called gas amplification region. The parameter that describes the gas amplification process is called gas amplification factor, or simply *gas gain* and is a basic characteristic of the gaseous detectors. It is normally defined as the ratio of the electrical charge deposited on the anode and the primary liberated electrical charge. The gas amplification process can lead to gas gains of up to 10^6 .

The OT straw tubes, operating at 1550 V, will have a gas amplification region starting at 50-100 μm from the anode and will reach a gas gain of 5×10^4 [54].

For the full reconstruction of the charged particle trajectory, the OT straw tubes have to provide the minimum distance of the particle track to the wire. This distance is determined simply by measuring the arrival time of the *first* cluster to the anode. Therefore, the detection of precisely the first cluster is extremely important for achieving a high spatial resolution.

2.3.4 OT Readout Electronics

The front-end electronics used for the readout of the straw tubes signals is based on specially designed ASICs⁷, mounted on service boards in a modular way. It consists of 8-channel ASDBLR amplifier chips, that amplify, shape and discriminate the charge pulses; 32-channels OTIS (Outer Tracker Time Information System) TDC chips for the drift time measurement; Gigabit Optical Link chips for the data serialization and optical transmission. A scheme of the OT front-end electronics is included in Fig 2.16. An anode pulse from the OT arrives at the ASDBLR amplifier. If the charge of the pulse is higher than a certain threshold, the signal is passed to the OTIS, where the measurement of the drift time is performed.

The amplifier threshold expressed in mV approximately corresponds to a charge

$$Q(\text{fC}) = e^{-1.25 + 0.0033 \text{Thr}(\text{mV})}, \quad (2.5)$$

The above relation (Eq. (2.5)) is shown graphically in Fig. 2.17.

⁶The drift velocity of the ions is a factor of ~ 1000 smaller than that of the electrons.

⁷Application-specific integrated circuits.

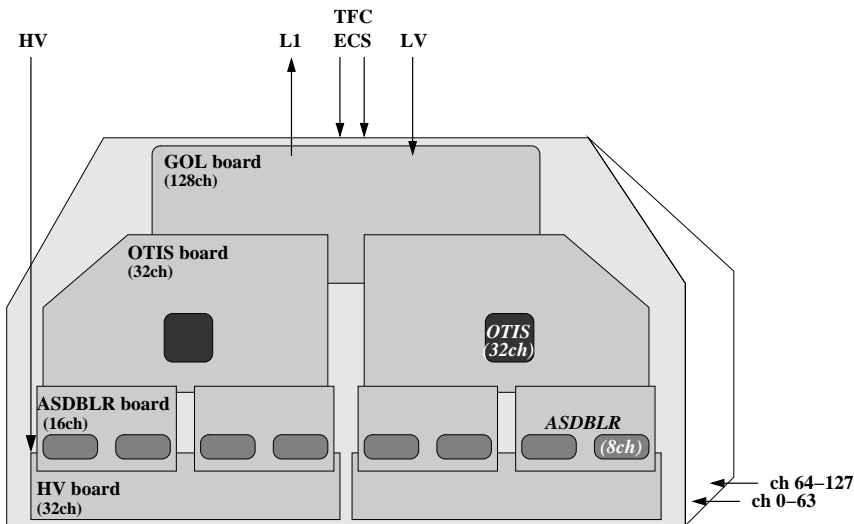


Figure 2.16. A scheme of the OT front-end electronics box.

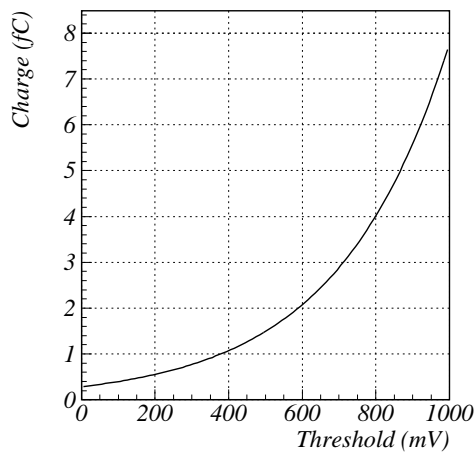


Figure 2.17. Correlation between the amplifier threshold in mV and the corresponding charge in fC.

Chapter 3

Outer Tracker Quality Assurance

Quality is never an accident; it is always the result of intelligent effort.

John Ruskin (1819-1900)

The construction of a highly reliable and well functioning detector implies systematic and precise quality control. LHCb Outer Tracker modules were inspected carefully during and after their production. The procedure of quality monitoring and validating of the modules is subject of this chapter.

3.1 Introduction

The Outer Tracker system of the LHCb experiment consists of 168 straw-tube detector F-modules (see Chapter 2). The overall performance of the system depends on the efficacy of each single module. To ensure that all the modules will meet the TDR [52] requirements, a special quality control program [54] is carried out in parallel with the production process. The program consists of a series of experiments designed to measure any possible deviation from the target specifications.

The mass production of the 5 meter long modules (or *F* type modules) passes through three major phases, as listed below (the procedure is described in detail in Ref. [55]):

Phase 1: Preparation of the straws, Fig. 3.1 a)

- Cutting the straws to the proper length
- Crimping of grounding contacts at the end of the straw tube
- Inserting and fixing wire supporters (locators)

Phase 2: Preparation of the monolayers (half-modules), Fig. 3.1 b), c)

- Alignment of the straw tubes with an external precision jig

- Soldering of the straw grounding contacts to the feedthrough boards
- Gluing the panel to the straws and feedthrough boards in the jig
- Anode wiring of the straw tubes

Phase 3: Module assembly, Fig. 3.1 d)

- Gluing of two monolayers
- Sealing with sidewall strips, creating a gas-tight unit

The performance at each phase is checked with dedicated quality control tests. When Phase 1 is completed the friction force of the wire locators with the straw is measured (Sec. 3.3). The anode wire quality is checked optically before usage (Sec. 3.2). After the straws are aligned and glued on the panel, the wire is placed and soldered at the ends. The position of the wire inside the straw is measured as explained in Sec. 3.4. The wire tension force (Sec. 3.5) and the currents under high voltage in air (Sec. 3.6) are examined at the end of Phase 2. In case bad wires are found, they are replaced and the process is continued in Phase 3. Gas tightness test is performed when the module is assembled at Phase 3 (Sec. 3.7). Finally, the module is filled with counting gas and put under high voltage (HV). Regular monitoring of the currents (also called "High voltage training") (Sec. 3.9) is applied, followed by scanning with radioactive source (Sec. 3.10) - for survey of the uniformity of module's response. An OT module is considered commissioned only if it successfully passed all quality tests.

In Sec. 3.8 we discuss on the measurements of the water content in the module. Summary is made and conclusions are drawn in Sec. 3.11.



Figure 3.1. Various phases in the module production.

3.2 Wire Selection

The anode of each straw drift-tube within an OT module is a thin gold-plated wire. The base material of the wire is tungsten (W), coated with 6% of gold (Au). The diameter of the wire is $25.4 \mu m$.

Tungsten is a standard material of choice for the anodes in the drift chambers because of its tensile strength that allows making wires with smallest diameters. It also has high electrical conductivity, enhancing the signal propagation, low thermal expansion and low outgassing - indication for strength and robustness. The last is a perfect property for long term operation. The gold-plating is done for two reasons. First, gold is inert, protecting the wire chemically. Second, it allows the wires to be soldered to the feed-through boards.

The nominal amount of wire needed to build all OT modules is 170 km. The production of the wire is assigned to California Fine Wire Company [56]. The wire is delivered to NIKHEF rolled up in spools. Each spool has a diameter of 10 cm, thickness of 1.7 cm and contains 1 km of wire.

Although the wire quality is guaranteed and certified by the producer, it is checked independently at NIKHEF. Wire samples of every spool are optically inspected for damages with the help of a microscope. Per spool, three different 10 cm long pieces of wire from the first 10, 20 and 30 meters are checked. The spool is rejected for use if in all three pieces consistently visible defects are found. Some of the typically monitored wire imperfections of the rejected spools are shown in Fig. 3.2. The gold layer is fully (Fig. 3.2 c) or partially (Fig. 3.2 a, b) damaged with chips, flakes, pores or cracks.

The samples are checked for abnormal curliness too, which could hamper the final usage. From the totally ordered 437 spools, 50 were discarded and returned for replacement, following our inspection. A total of 387 km of wire was used in the construction of the OT modules and 50 km was put aside as spare.

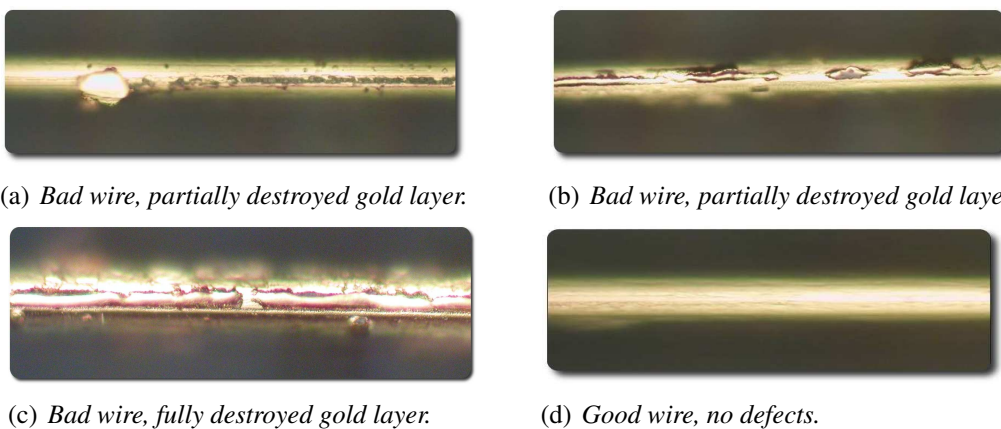


Figure 3.2. Microscope images (magnification look) of the anode wire.

As already mentioned, the wire consists of *W* and *Au*, with a 94/6 mass ratio and its mass density can thus be estimated as

$$\rho = 0.94 \times 19250 + 0.06 \times 19300 = 19253 \text{ [kg/m}^3\text{].} \quad (3.1)$$

The precise value of the wire's diameter is of great importance, given the strong dependence of the gas amplification on the anode wire radius. Verifying the stated value of 0.001 inches (0.00254 cm) given by California Fine Wire, an attempt of determining the wire's diameter is done. The mass of a $8.62 \text{ m} \pm 0.01 \text{ m}$ wire sample, is measured with an electronic balance, resulting in a value of $M = 84.2 \text{ mg} \pm 0.4 \text{ mg}$. Using the density of the wire in Eq. (3.1), its radius $r = 12.71 \mu\text{m} \pm 0.02 \mu\text{m}$ is obtained, in agreement with the nominal value of 0.0005 inches = $12.7 \mu\text{m}$.

3.3 Friction Force of Wire-Locators

Accurate positioning of the anode wires at the center of the straw tubes is crucial. Small displacements of the wire from the straw axis are subject to asymmetric electrical forces and lead to instabilities. In addition, the accuracy of the wire position directly affects the position resolution of the detectors.

The alignment of the wire with design precision of $100 \mu\text{m}$ is guaranteed by three factors:

- 2 small plastic supports inserted in the straw and 2 supports at the ends of the straw;
- applied mechanical tension of 75 g on the wire (see Sec. 3.5);
- aluminum jig with 64 grooves for alignment of the straws (see Sec. 3.4).

Two types of straws - short ones and long ones, differing only in length, are used in the building of the F-modules. To support the wire, two *wire-locators*, an *end-block* and a *middle-block* are used, as indicated in Fig. 3.3. Made of radiation hard NORYL¹ plastics, the wire supports have a complicated design providing minimal disturbance of the counting gas flow, Fig. 3.4. The wire-locators support the wire inside the straw and the end and middle blocks give support at the ends.

In the experiment the modules are installed vertically and in order to keep the wire-locators in place they must be fixed. While the end and middle blocks are partly larger than the straw diameter, the wire-locators should be prevented from shifting. Their fixation is done by crimping to the straws through pressing and heating the straw exterior. While the wire-locator weight is only $\sim 1 \text{ g}$, it is chosen to fix the locator to the straw by a much larger force ($\sim 200 \text{ g}$), in order to have a

¹A modified polyphenylene oxide with excellent electrical insulating properties, light weight and long term dimensional stability.

large safety margin for protection from mechanical shocks during the detector construction, transport and installation. In particular, wire-locators have to resist to the vacuum pressure resulting from the wiring technique during the module construction, which is estimated to be not more than 50 g.

The friction force of the wire-locators with the straw, i.e., the measure of how well the wire-locators are fixed, is checked regularly. During the straw preparation session, for every batch of 64 straws, a sample is taken and the force necessary to displace the wire-locator out of position is measured by a spring dynamometer. It must be larger than 200 g.

In Fig. 3.5 a) the results from the friction force tests are summarized. The maximum force that can be measured with the dynamometer is 1 kg, which explains the high number of entries in the last bin. Figure 3.5 b) illustrates the evolving in time of the measured value of the friction force. The purpose is to show that the test, nor the straw crimping device, is systematically biased from some moment on.

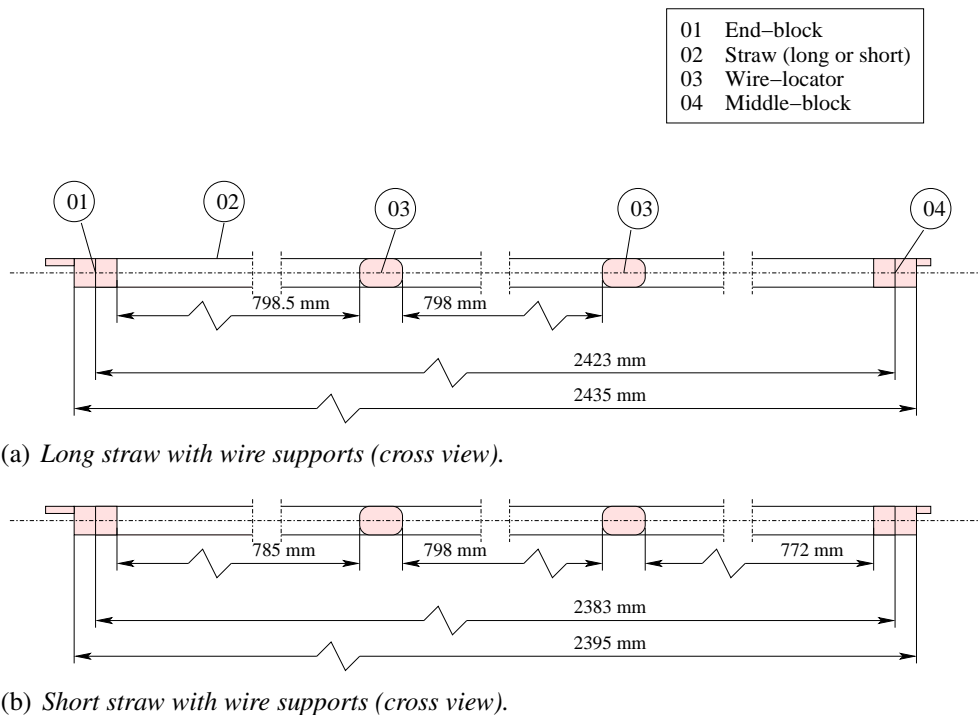


Figure 3.3. Straws for F-module.

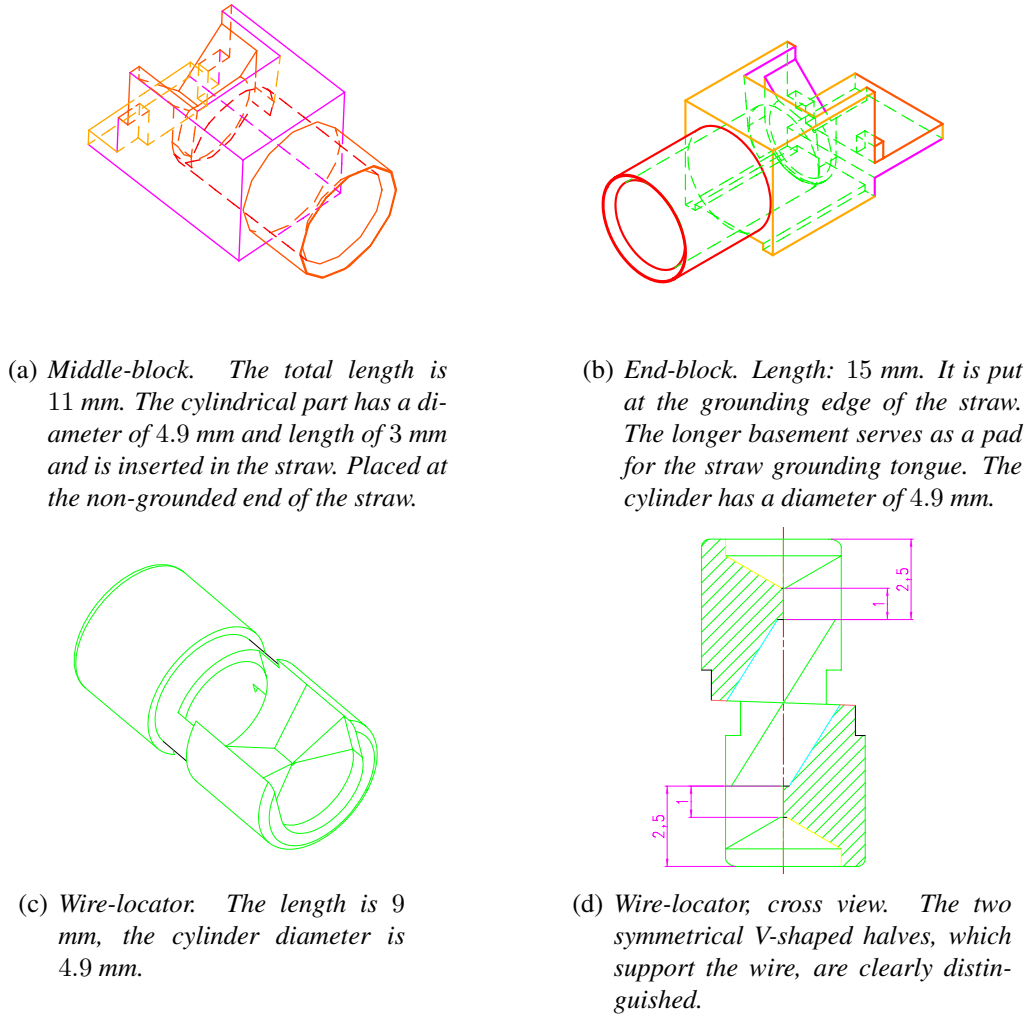


Figure 3.4. Wire supports (middle-block (a), end-block (b), wire-locator (c), (d)).

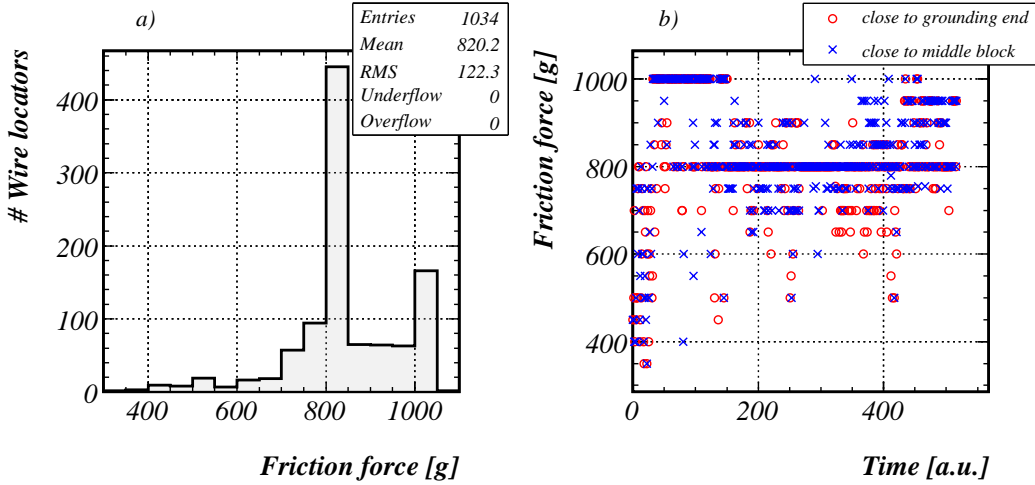


Figure 3.5. (a) Distribution of the measured friction force of the wire-locators (for both long and short straws). (b) Friction force of the wire-locators vs. time.

3.4 Wire Position Measurements

The momentum resolution of the LHCb tracks strongly depends on the precise knowledge of the x -position of the anode wires in the OT modules. As explained in the previous section, the wire is aligned to the straw axis with an accuracy of $18\ \mu\text{m}$, achieved with special wire supports and by applying mechanical tension to the wire. The arrangement of the straws themselves in the module, by using an external template with a pitch precision of $50\ \mu\text{m}$, assures accurate positioning of the wire with respect to the module. The straws are placed in the template before being glued to the panel and wired. The final OT position resolution is required to be $\leq 200\ \mu\text{m}$. This imposes the maximum deviation of the wire position with respect to the nominal to be within $100\ \mu\text{m}$, taking into account additional uncertainties from the drift time measurement.

To check whether the position of the wire is in the admissible margins of $\pm 100\ \mu\text{m}$, it is measured at the wires soldering pads² for the first few modules. The measurement is done for each module half (A and B) at four locations, named for convenience: Up-Up (UU), Up-Center (UC), Low-Center (LC) and Low-Low (LL). For every location the x -wire positions are measured with respect to the first wire, which is placed at point zero. The measurement is done with an (X,Y) micrometric positioning table equipped with a camera, see Fig. 3.6. The precision of the instrument is $1\ \mu\text{m}$. As an example we show in Fig. 3.7 the results of the measurement for Module 1, side B. The left column of plots represents the deviation from the nominal x -position versus the wire number. The dashed lines form the allowed $\pm 100\ \mu\text{m}$ band. The right column of plots show the $(x_{\text{meas}} - x_{\text{nominal}})$ distributions

²The reason is that only at the soldering pads the wire is visible and its position can be measured.

for the four sections. The distributions are fitted with gauss functions, whose standard deviations (σ) are in direct relation with the OT spatial resolution. In Table 3.1 the results for the measured modules are summarized. The number of wires that are dislocated more than $100 \mu\text{m}$ and the spread of the wires digressions are given. From the table one can see that the spread for all the measured modules is within the desired limits.

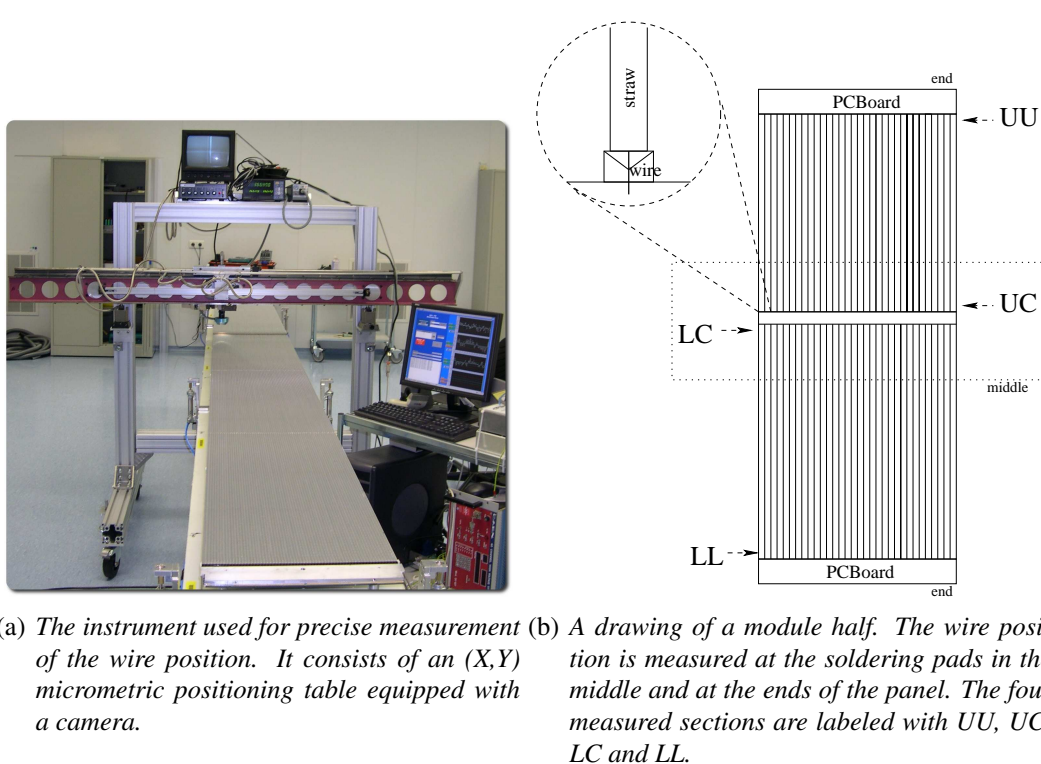


Figure 3.6. A tool for measurement of the wire position.

Module	Side	U/L	End		Middle	
			σ [μm]	# $ x > 100 \mu\text{m}$	σ [μm]	# $ x > 100 \mu\text{m}$
5012	A	L	46	1	59	8
5012	A	U	32	2	74	6
5012	B	L	53	0	51	2
5012	B	U	36	4	48	1
0	A	L	32	1	46	4
0	A	U	41	1	64	2
0	B	L	38	0	65	4
0	B	U	45	1	72	5
1	A	L	56	5	76	11
1	A	U	59	8	57	3
1	B	L	51	2	56	4
1	B	U	62	11	65	3
2	A	L	57	4	68	8
2	A	U	49	0	57	4
3	B	L	54	3	39	3
3	B	U	39	0	73	9
4	B	L	67	1	39	6
4	B	U	64	2	61	8

Table 3.1. Summary of the wire position measurements. The spread (σ) of the distribution of the difference between the measured wire position and the nominal one together with the number of wires per section with $|x_{\text{meas}} - x_{\text{nominal}}| > 100 \mu\text{m}$ are given.

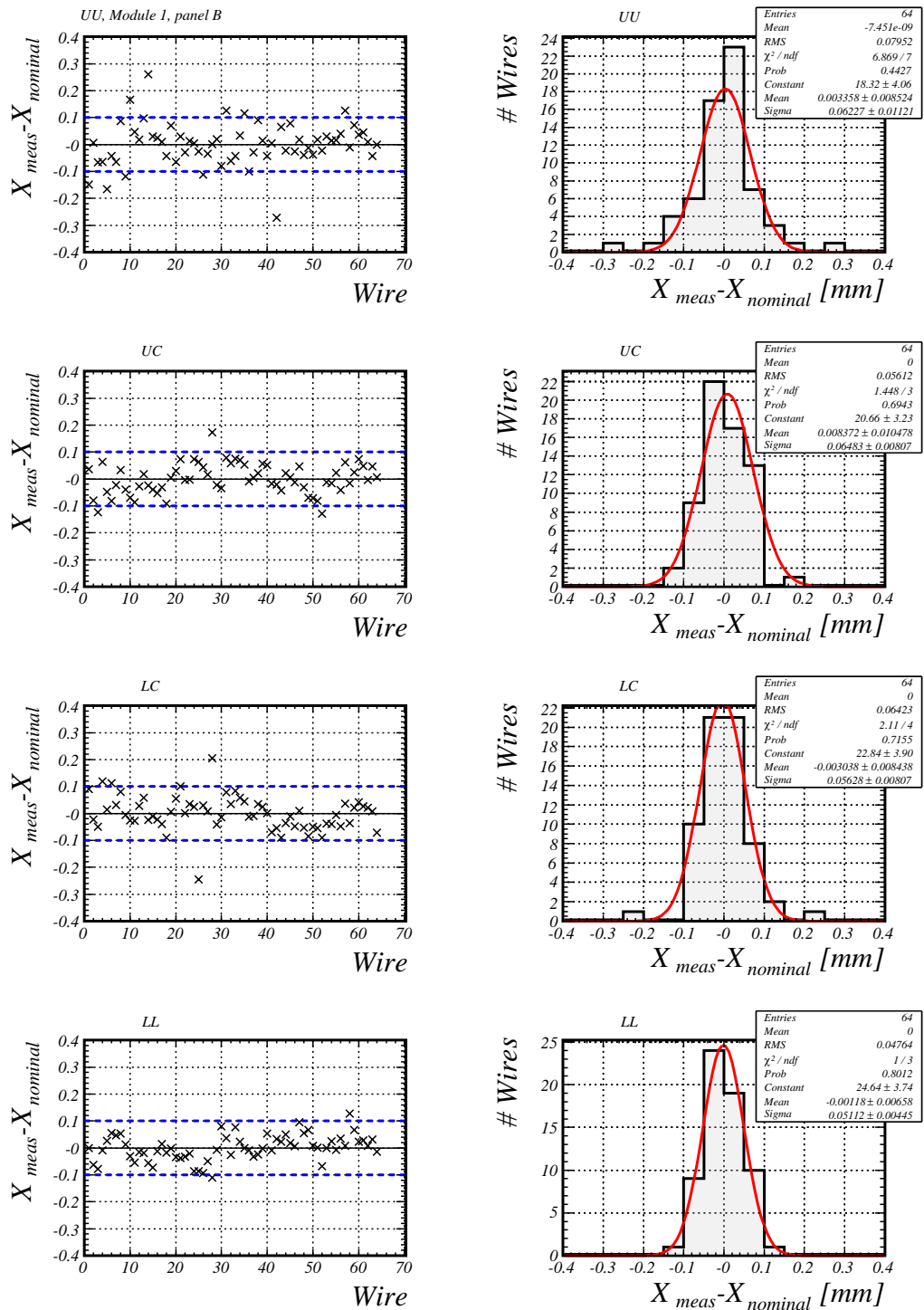


Figure 3.7. *Module 1, panel B. Left side: Deviation [mm] from the nominal x-position of the wire versus the wire number. Right side: Distribution of the deviation from the nominal position.*

3.5 Wire Tension

3.5.1 Tensioning of the Anode Wires

The anode wires inside the straw tubes have to be strung to a certain level of tension to keep the wire in the center of the straw. The value of the tension is carefully selected by finding the right balance of being sufficient to avoid gravitational sags and electrostatic instabilities³ and being not too large to avoid overloading and breakdown. The nominal magnitude of the tension is defined to be 75 ± 5 g, which is sufficiently far from the elastic limit of 140 g [54]. All the wires are stretched to that tension with the setup schematically shown in Fig. 3.8.

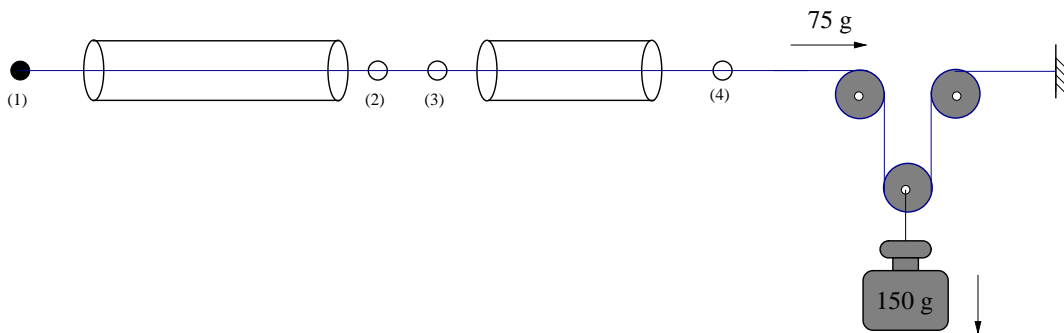


Figure 3.8. The wiring setup. The wire is inserted in both the long and short straws and is initially soldered at point (1). A fixed weight of 150 g connected to a system of spools is used for applying 75 g of tension. Then the wire is soldered at points (2), (3) and (4). Finally the connection between (2) and (3) is cut.

Before the modules are sealed all the wire tensions were measured to check if their values were in the required acceptance window of ± 5 g around 75 g. A special tool - Wire Tension Meter [57] was designed and produced to achieve this goal.

3.5.2 Wire Tension Meter

The Wire Tension Meter (WTM) is capable of detecting and displaying the resonance frequency of the anode wires in a magnetic field. A short (0.8 ms) current pulse of about 130 mA is sent by the WTM to the wire, which is placed in a perpendicular magnetic field $B = 0.05$ Tesla. Then the Lorentz force $\delta F_L = IB\delta L$, acting on a segment δL of the wire produces a mechanical oscillation $y(t) = y_0 \sin(\omega t)$. The oscillation of the wire in the magnetic field induces a current in the wire due

³Electrostatic instabilities may appear if the anode wire is displaced from its nominal position. In such case the wire is attracted to the cathode. Discharges or short circuit may happen if the wire is pulled too close to the straw.

to Faraday's law of electromagnetic induction: $I(t) = I_0 \cos(\omega t)$. The WTM analyzes the period of the induced current and determines the fundamental harmonics $f_1 = \omega/2\pi$. Once f_1 is determined, the tension of the wire, F , can be derived as

$$F = 4\mu f_1^2 L^2 , \quad (3.2)$$

where L is the wire length and μ is the wire mass per unit length. Taking into account that the radius of the wire r is 12.7×10^{-6} m, for the tension F expressed in grams we obtain the following expression

$$F = \frac{4\rho\pi r^2}{g} f_1^2 L^2 = 0.3979 f_1^2 L^2 = 0.3979 \frac{L^2}{T^2} , \quad (3.3)$$

where ρ is the mass density of the wire (see Eq. (3.1)), $T = (1/f_1)$ is in [ms] and L in [cm]. The full technical description of the WTM can be found elsewhere [58].

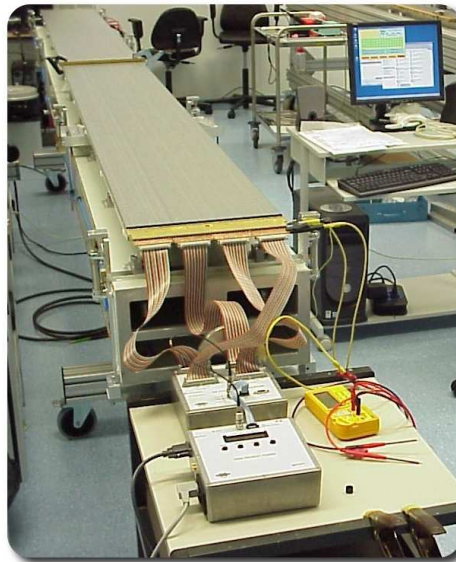


Figure 3.9. The Wire Tension Meter in action. The magnetic field is created by a permanent magnet put below the panel. Dedicated software automatizes and controls the measurement process.

3.5.3 Measurement of the Wire Tension

The wire oscillation frequency is measured with the WTM and translated into a tension (Eq. (3.3)) separately for each of the three wire segments between the wire supports. The reason is that the wire supports act as node points forcing the wire segments between them to oscillate independently. In general, per panel, six different wire sections are measured - three for each of the two staggered monolayers,

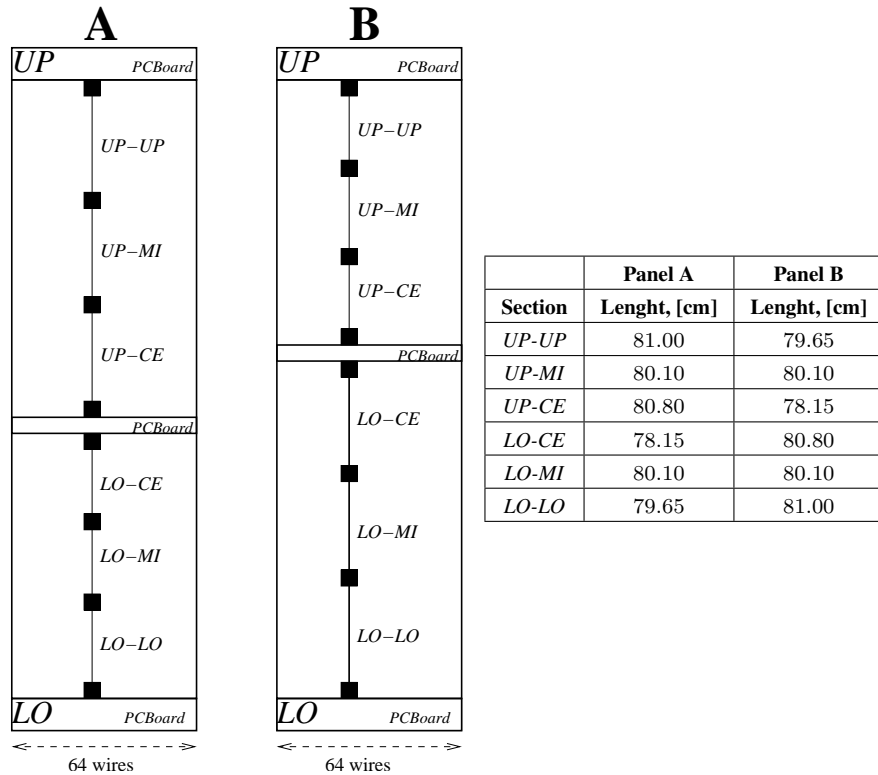


Figure 3.10. A drawing of the module halves illustrating the different wire segments for which the tension force is measured. These segments are defined by the wire supports (the black squares). During the wiring process the stretching weight is always put on the lower part of the panel. The table gives the nominal lengths of the wire segments for both panels; also see Fig. 3.3.

or in total: $2 \times 64 \times 3 = 384$ measurements/panel were done, (see Fig. 3.10). For the correct wire tension calculation knowledge of the precise length of the wire segments is crucial. The two panels (A and B) that compound the module are not symmetric in terms of the wire (straw) lengths. The nominal values of the wire lengths used for the tensions computation given the oscillation frequency are listed in the table given in Fig. 3.10.

Figure 3.11 shows the distribution of the wire tensions for module 30, panel B. The central value is approximately 74 g, which is less than the applied weight of 75 g. The difference can be attributed to friction in the wire supports. The RMS is typically less than 2 g. Wires with tension deviating more than 5 g from the nominal (75 g) are replaced. Usually one wire per panel is substituted. The panels are wired with homogeneous wire tension and no systematic aberrations are observed. The slightly smaller tension measured in the sections further from the stretching weight, compared with the one measured close to it, is attributed to the friction of the wire in the wire supports. Notice that the tension of the sections closer to the weight is more precise.

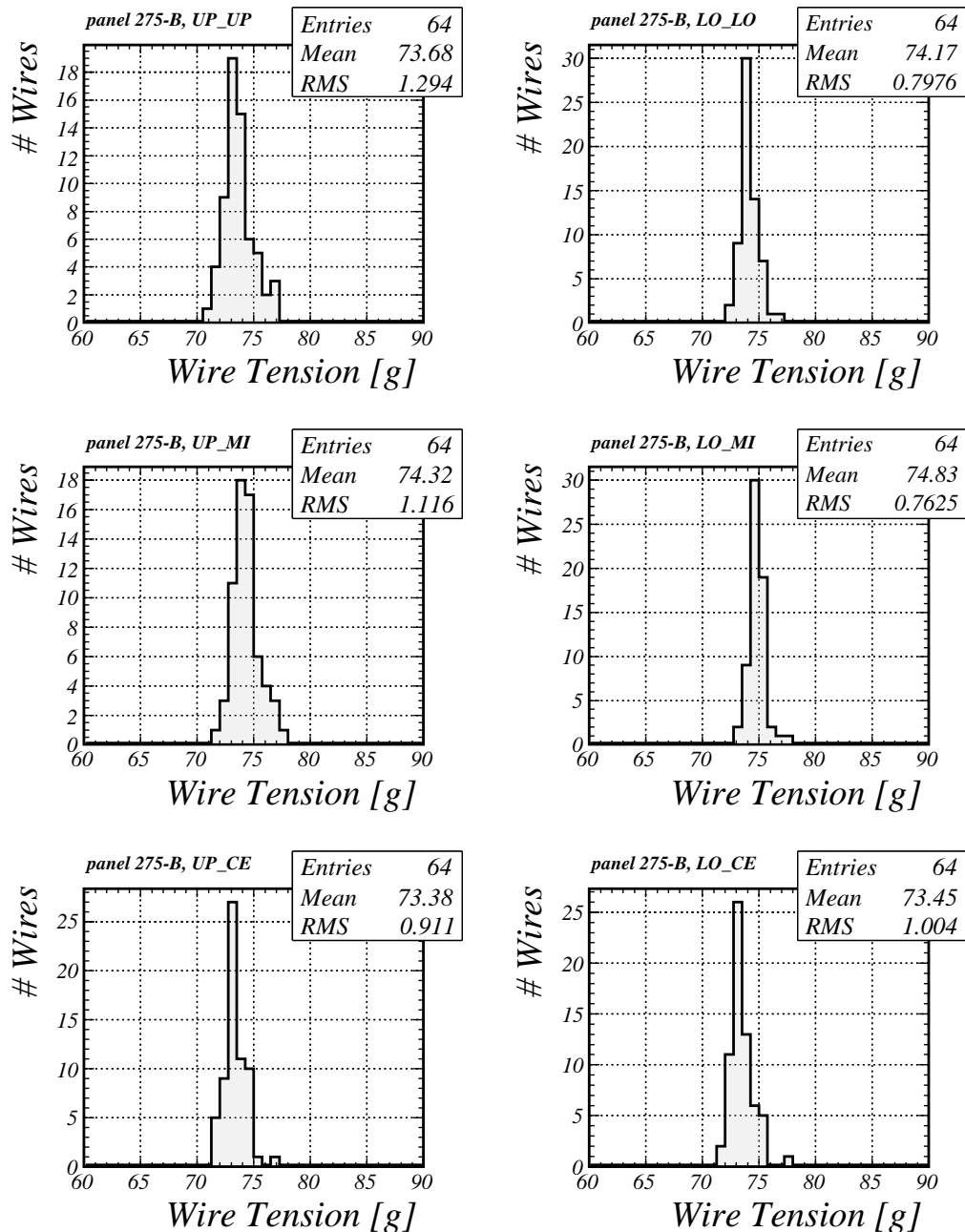


Figure 3.11. The distribution of the wire tension for the three measured sections of the upper and lower side of panel B of Module 30.

3.5.4 Single Tension per Wire, Derivation of the Segment Lengths

In the absence of friction in the wire supports the tension must be the same for all three wire segments of the lower or upper part of the panel. Assuming this, by assigning a single tension per wire, the wire segment lengths can be derived.

Let T_1 , T_2 and T_3 be the measured with the WTM periods of wire oscillations and L_1 , L_2 and L_3 the corresponding wire segments lengths. If the tension F is the same in the all three sections than we obtain the following relations,

$$F = k \frac{L_1^2}{T_1^2} = k \frac{L_2^2}{T_2^2} = k \frac{L_3^2}{T_3^2}, \quad (3.4)$$

$$L = L_1 + L_2 + L_3, \quad (3.5)$$

where L is the length of the whole wire and is very accurately known, and $k = 0.3979$ [$\text{g cm}^2/\text{ms}^2$], the factor from Eq. (3.3). Solving equations (3.4) and (3.5) with respect to F , L_1 , L_2 and L_3 we obtain the following results

$$F = k \frac{L^2}{T_1^2 + T_2^2 + T_3^2}, \quad (3.6)$$

$$L_1 = L \frac{T_1}{T_1 + T_2 + T_3}, \quad L_2 = L \frac{T_2}{T_1 + T_2 + T_3}, \quad L_3 = L \frac{T_3}{T_1 + T_2 + T_3}. \quad (3.7)$$

The lengths (Eq. 3.7) of the wire segments for module 30, panel B are shown in Fig. 3.12. The agreement with the nominal lengths is good, and differs by no more than 2 mm.

Summary plots showing the average wire tension (Eq. (3.6)) per panel per layer (upper or lower) and the corresponding spread (RMS) for all modules are presented in Fig. 3.13.

3.5.5 Variation of the Wire Tension

It is important to know how the wire tension varies with time. Does it decrease and how much, can the wire soldering points accommodate the (> 70 g) wire tension for 10 years?

To answer all these questions two panels (123A and 14A) were kept apart and their wire tension was monitored periodically. The results are presented in Fig. 3.14. Panel 123A showed no trend of a decrease of the wire tension for the whole observed period of ~ 1.3 years. The wire tension of Panel 14A however, decreased slightly (with ~ 1.5 g) in the first 40 days and then remained unchanged until the end of the monitoring.

After these tests, panel 14A was used for the construction of module 131, while panel 123A is still available for further wire tension checks, if necessary.

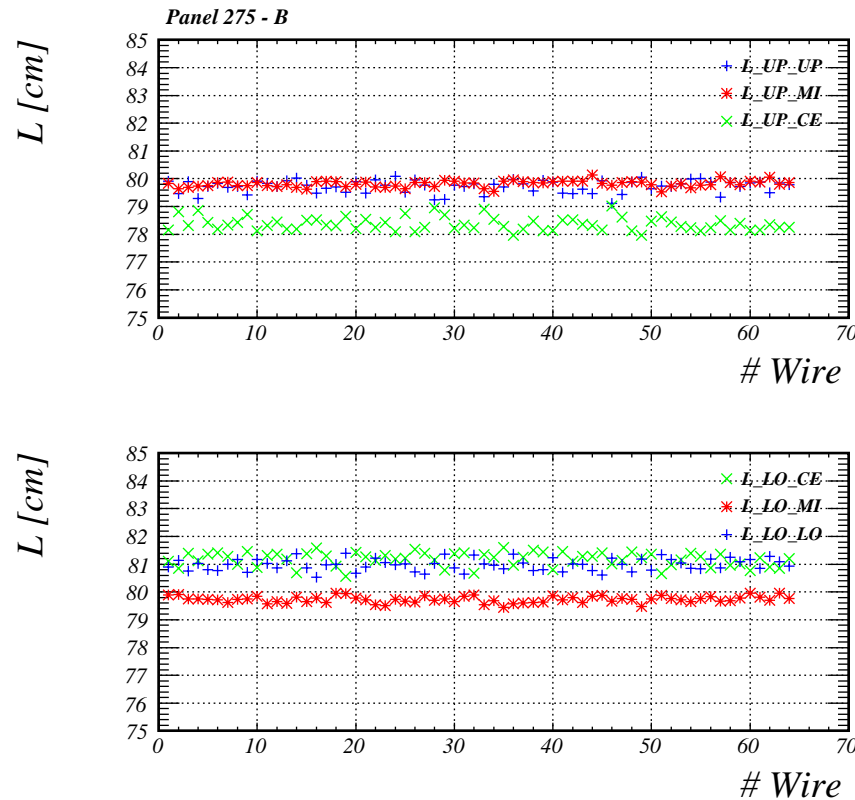


Figure 3.12. The pre-calculated lengths of the wire segments of Module 30, panel B, under the assumption of no friction between the wire and the wire supports.

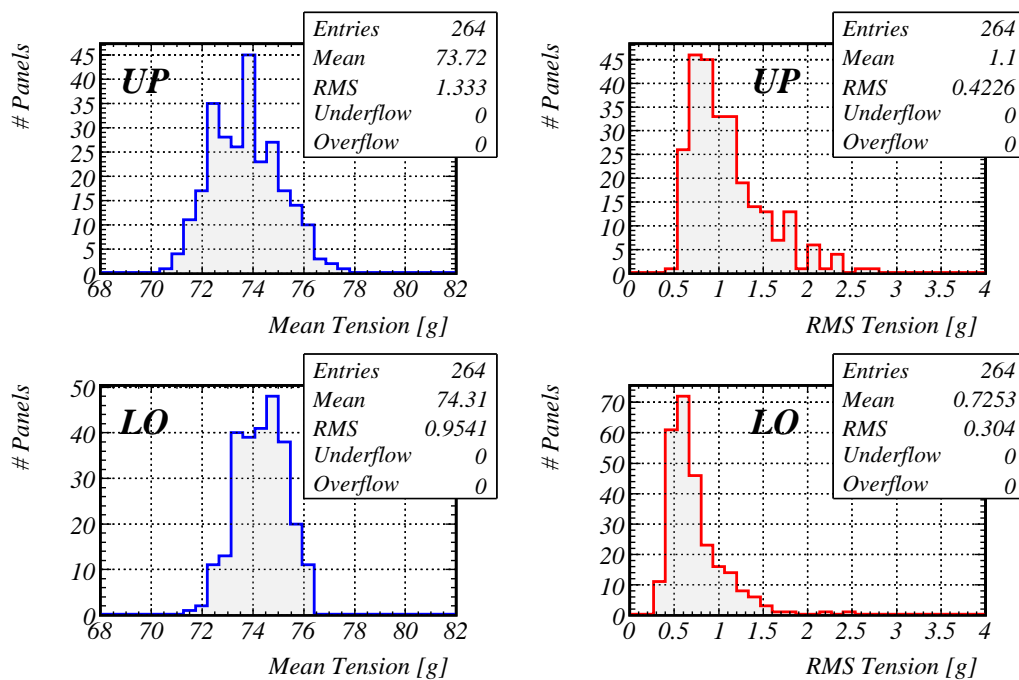


Figure 3.13. Distributions of the pre-calculated, averaged per layer wire tension and the corresponding RMS for all produced modules. Assumed no friction in the wire supports.

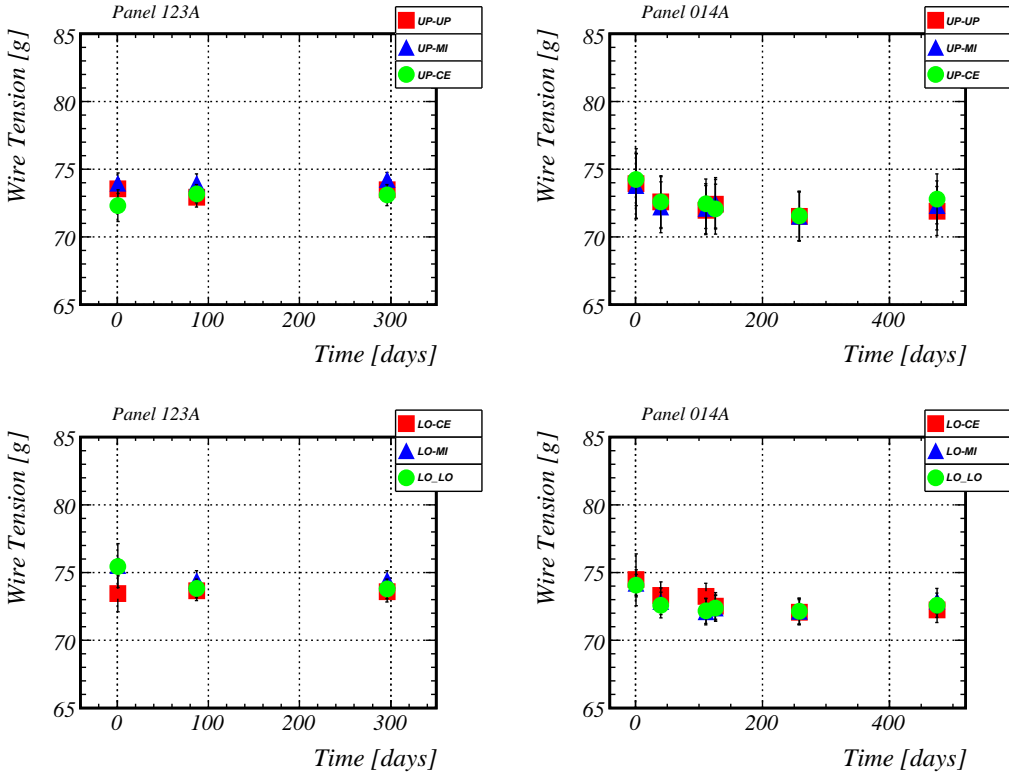


Figure 3.14. The mean wire tension per section as a function of the time for panels 14A and 123A. The error bars indicate the RMS values of the tension distribution per section.

3.6 Currents in Air

After passing the quality control on the wire tension, each channel is put under high-voltage and the current (*leakage current*) of each wire is measured in order to identify possible problems (shortcuts, wire defects, etc.). The measurement is done in an air environment, with a special 64 channel current meter, developed at NIKHEF. The accuracy of the current meter is 0.1 nA with a maximum detectable current of 500 nA per wire. A detailed description of the current meter is given elsewhere [54].

Starting from 50 V, the voltage is increased to 500 V if no large currents are observed, and subsequently to 1000 V, from where it is ramped up to the limit of 1600 V, in steps of 100 V. Through all this time, the current is carefully monitored and recorded. Figure 3.15 shows the current (I) as a function of the voltage (HV), for four example wires with different behavior, up to a HV of 1700 V.

The distribution of the wire currents at 1600 V for a typical module is presented in Fig. 3.16.

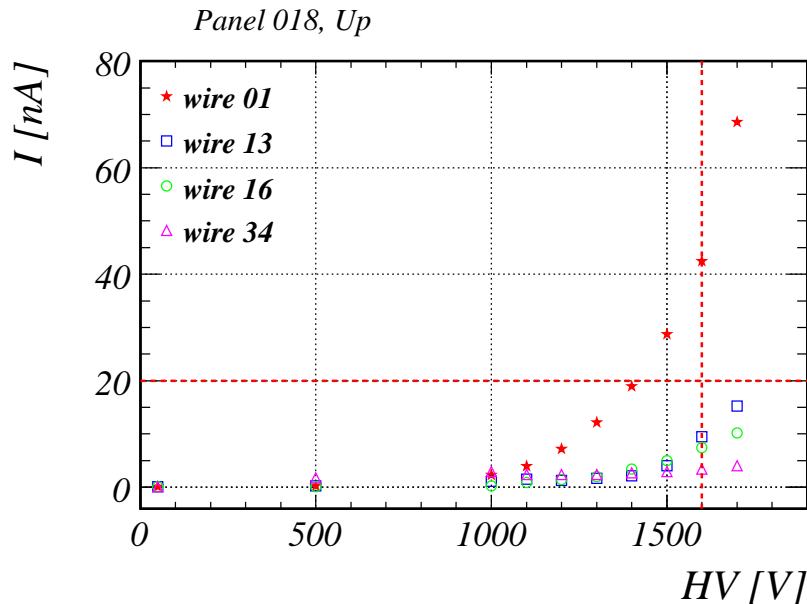


Figure 3.15. I - HV curves in an air environment for four wires from panel B (upper half) of module 007. Wire 01 is subject of replacement, since it does not meet the quality criterion.

While leakage currents of the order of few hundreds of nA pose no real threat to the detector performance, it was found by experience that wires showing no defects (bad plating, dirt, surface defects, etc.) would normally not exceed few nA of leakage current in air. A working level of 20 nA was set for the replacement of wires [54]. If at 1600 V the current in air of a given wire exceeds 20 nA, then the wire is not accepted and is replaced. The wire is kept however, when from multiple measurements at 1600 V at least one is below 20 nA.

The current limit of 20 nA was changed and restricted to 10 nA after the production of the first 40 modules. Typically one wire per panel was exchanged as a result of the leakage current monitoring during production.

Figure 3.17 gives the values of the mean panel current and the RMS for the two sections as a function of the module serial number. Since the modules were built chronologically, this plot represents the mean current and the RMS evolution during production. The visible improvement of the results over time is explained by

- ◊ increasing level of the experience of the operators;
- ◊ better wire quality; the wire-spools from the very first deliveries were proven to be of lower quality;
- ◊ inspection of wire samples from each wire-spool under microscope to check the wire quality and exclude the bad wire (see Sec. 3.2); this procedure was applied from module 008 onwards.

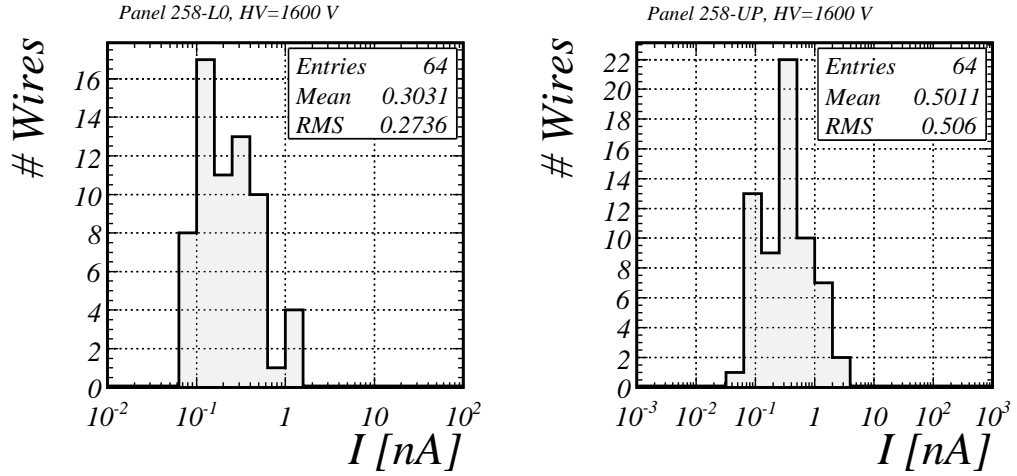


Figure 3.16. Distribution of the wire current for module 125, side B.

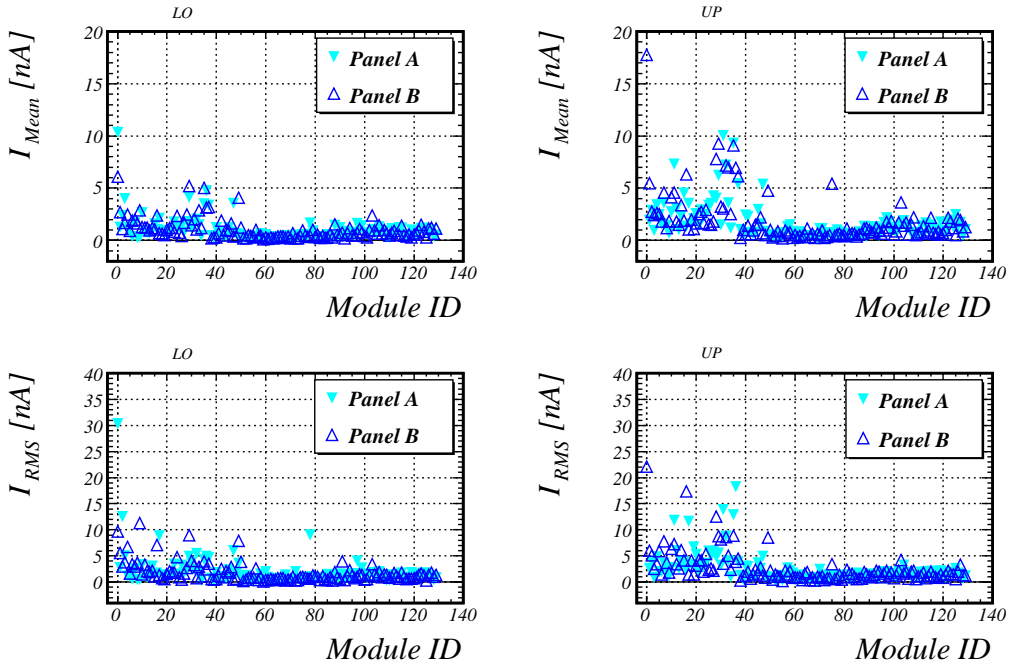


Figure 3.17. The mean panel current in air and the RMS of the current per panel for all produced modules. Note the improvement of the results with the progress of the module production.

3.7 Gas Tightness Measurements

The Outer Tracker modules must be gas tight in order to reduce the risk of contamination of the counting gas with impurities, which may enter the detector mostly by diffusion through leaks [59]. Each OT module forms a self-contained gas-detector unit. The straw tubes of the OT have an inner diameter of 4.9 mm and a length of approximately 2500 mm, resulting in a volume of about 47.1×10^{-3} l. A detector module of type "F" consists of 256 straw tubes, which leads to a total straw-tube volume of about 12 l. The total volume of the F-module gas box is about 18 l. During operation, the counting gas in the modules will be exchanged continuously. The gas-exchange rate will be half a detector volume per hour. The level of gas tightness of the OT modules must be such that the gas loss per volume exchange does not exceed 10% of the total gas volume [59]. For the five meter long F-modules a 10% gas loss per volume exchange corresponds to a leak rate of 2.5×10^{-4} l/s.

All F-modules constructed at NIKHEF are tested for gas tightness. An initial overpressure $H_0 = 7$ mbar is applied to the modules; the overpressure decay and the leak rate are measured in two separate steps:

- ◊ overpressure decay for a first coarse determination of the gas tightness and to aid repair actions (Argon is used), Sec. 3.7.1;
- ◊ a final direct leak rate measurement with a flow meter (N_2 is used), Sec. 3.7.2.

3.7.1 Overpressure Decay Test

The aim of this first test of the gas tightness of the OT modules, is to determine if there are large leaks and eventually seal them. The configuration of the setup used for the test is shown in Fig. 3.18.

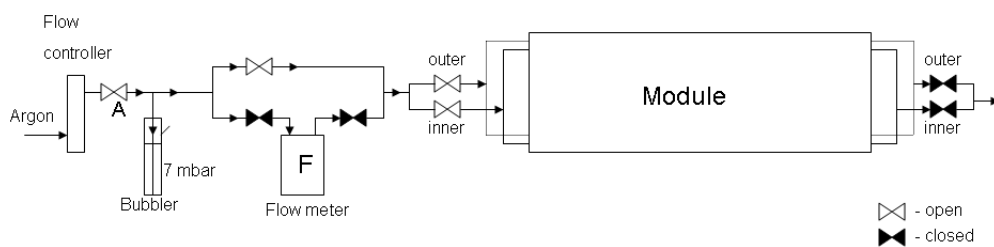


Figure 3.18. Experimental setup for overpressure decay test.

After reaching an initial overpressure of $7 \text{ mbar} \pm 0.1 \text{ mbar}$, valve A is closed. If the level change of the oil in the bubbler shows that the pressure drop exceeds 1 mbar

per 3 min (roughly corresponding to a leak rate of 10^{-4} l/s), then a gas-sniffler⁴ sensitive to Argon is used to locate the leaks. Unfortunately, experience showed that the gas tightness could only be improved marginally once a module is built.

Figure 3.19 gives the distribution of the measured values of the pressure drop per 3 minutes at 7 mbar overpressure for all F-modules produced at NIKHEF. One can see that there are a few modules that have $(dp/3\text{min}) > 1 \text{ mbar}$. Although the position of the gas leaks for these modules were found with the gas sniffler, the leaks could not be closed from the outside, due to the fact that the Rohacell and the carbon facing are not gas-tight by construction. As will be shown in Sec. 3.8, this is not so dangerous, since modules with leaks of the size of 1 mbar/min can still be accepted for use in LHCb, without the risk of considerable in-leak.

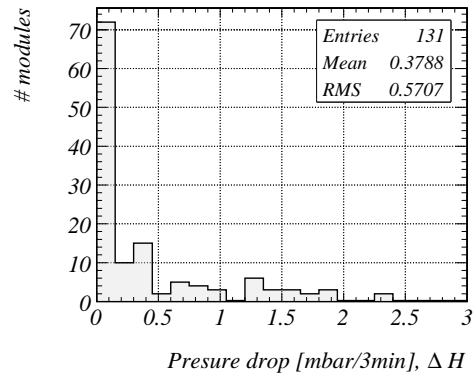


Figure 3.19. Distribution of the pressure drop per 3 minutes at 7 mbar overpressure for all F-modules produced at NIKHEF.

3.7.2 Leak Rate Measurement with Flow Meter

A second gas tightness test was performed with a flow meter. The configuration of the experimental setup used for the test is shown in Fig. 3.20.

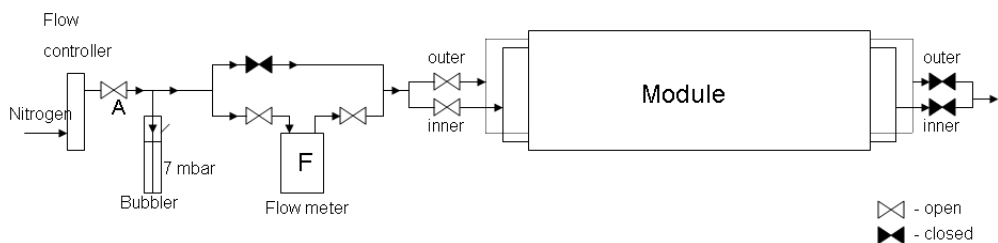


Figure 3.20. Experimental setup for leak rate test with a flow meter.

The questioned OT module is filled with N_2 until reaching an overpressure of 7 mbar ± 0.1 mbar, with the output closed. In typically 30 min the module is inflated and the gas flow measured with the mass flow meter directly corresponds to the module's leak rate.

⁴The used gas-sniffler model was *Gas Check 8500*, a product of Ion Science Ltd [60].

The gas flow measured with the mass flow meter during the test described above is shown in Fig. 3.21 for a leaky module (module 20) and for a gas tight module (module 23). The gas flow is fitted with exponential function $f(t) = p_0 + p_1 \exp(-|p_2|t)$, where t represents the time. The leak rate of the module is represented by the parameter p_0 , which is the value of the gas flow at $t \rightarrow \infty$, or in other words, when enough time has passed and the module is maximally inflated to its equilibrium state.

A histogram with the measured leak rates for all NIKHEF modules is shown in Fig. 3.22a). A graph of the leak rate versus the module number is given in Fig. 3.22b). Up to the construction of module 20 a single layer of glue for gluing the side-walls was used. Adding a second layer significantly decreased the leak rate and improved the modules gas tightness.

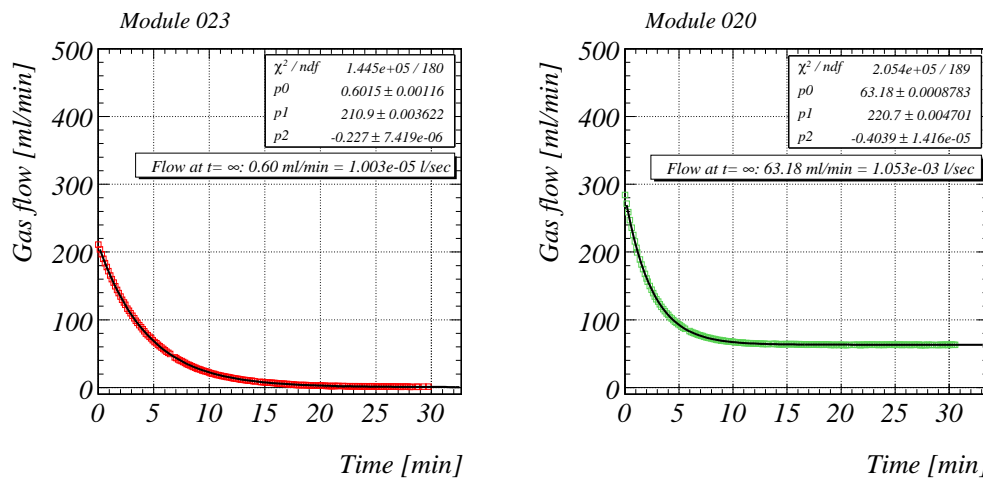
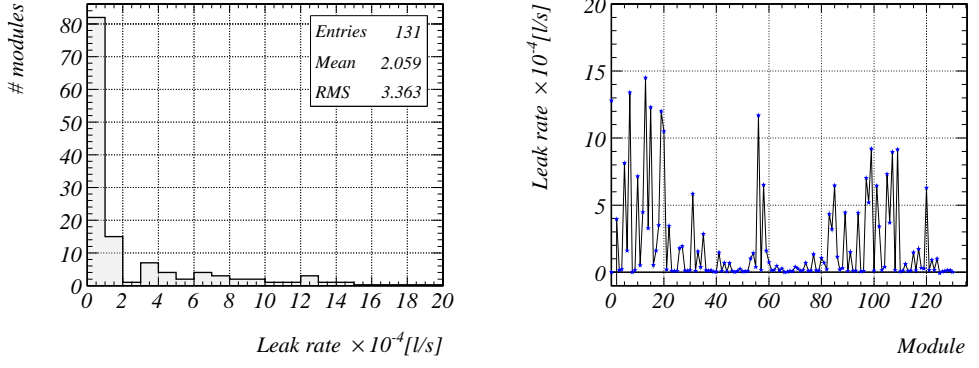


Figure 3.21. Leak rate measurement with a flow meter for a gas tight module, M023 and for a leaky module, M020. The value of the leak rate is defined by the parameter p_0 .

The correlation between the loss of overpressure in three minutes (see Sec. 3.7.1) and the leak rates for all NIKHEF modules is plotted in Fig. 3.23. A detailed discussion of the relation between the overpressure decay and the leak rate can be found in [61]; the curve in Fig. 3.23 denotes a fit to the data based on the following approximation:

$$R \approx \frac{V_0 H_0}{P_0} (1 + \lambda) \frac{\Delta H}{H_0 + \Delta H/2} \frac{1}{\Delta t}, \quad (3.8)$$

where P_0 , H_0 and V_0 are the initial atmospheric pressure, overpressure and volume, respectively; R is the leak rate at the initial overpressure H_0 ; Δt is the interval over which the overpressure drop is measured. Notice the importance of the correction factor $(1 + \lambda)$, accounting for the "bulging" of the module box with overpressure [61]: the value $\lambda = 4.1 \pm 0.1$ yielded by the fit (and corresponding to a deformation



(a) Distribution of the measured leak rates for all F-modules produced in NIKHEF.
(b) Leak rate vs. module ID for all NIKHEF F-modules.

Figure 3.22. Measured leak rates at overpressure of 7 mbar for all NIKHEF F-modules.

of each module face of the order of $20 \mu\text{m}/\text{mbar}$, roughly in agreement with direct measurements) shows that neglecting this effect would lead to a large underestimate of the leak rate deduced from the overpressure drop.

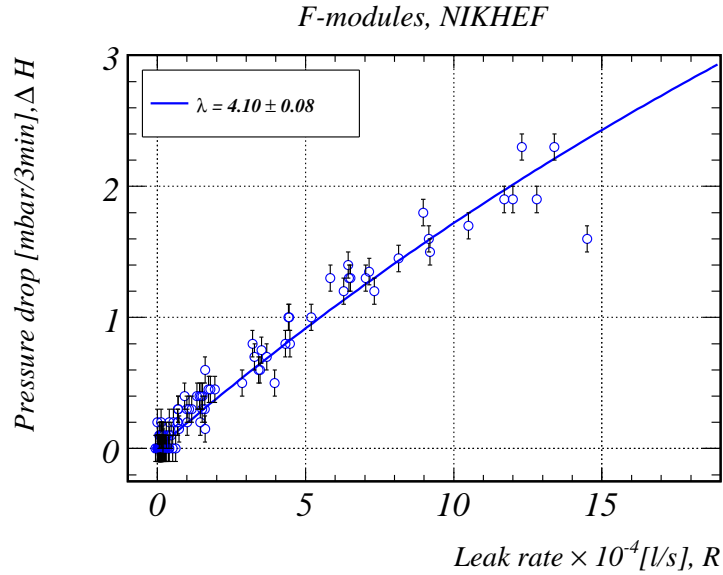


Figure 3.23. Correlation between the measured overpressure decays and the measured leak rates for all NIKHEF F-modules.

3.7.3 Gas Tightness Comparison between F and S Modules

The gas tightness of "S1", "S2" and "S3" types of modules, which will surround the beam pipe in the experiment, was tested at NIKHEF as well. The gas volume of the S1 and S2 modules is about 1/2 of the volume of the F-modules, and the gas volume of the S3-modules is 1/4 of the F-modules volume. The combined⁵ S1, S2 and S3 modules were re-tested after they were coupled in order to verify the gas tightness of the connection.

All gas tightness measurements performed at NIKHEF are summarized in Fig. 3.24. The curves denote fits to the data based on Eq. (3.8) (see Sec. 3.7.2). Notice that the values of the module expansion coefficient λ are comparable for the different types of modules, with the exception of the S3 modules, that show little significant bulging at 7 mbar of overpressure.

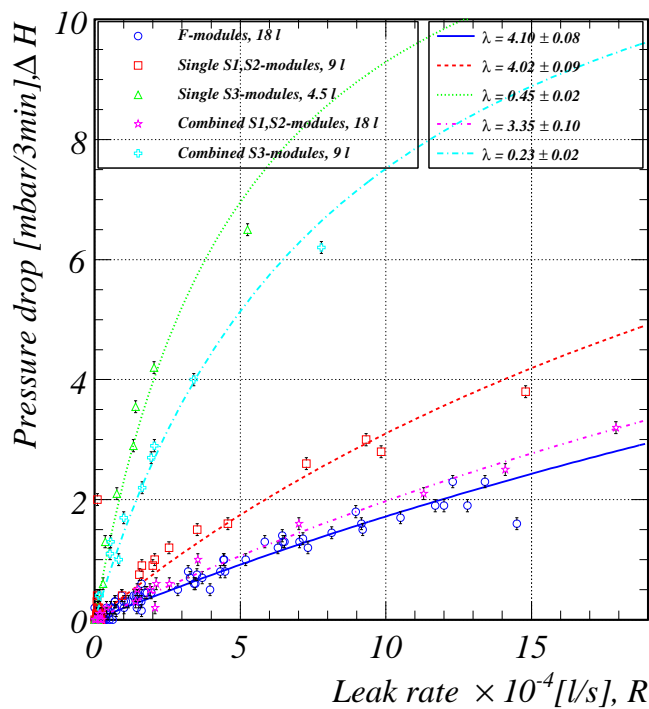


Figure 3.24. Correlation between the measured overpressure decays and leak rates for the S1-modules, S2-modules, S3-modules, combined S1-modules, combined S2-modules, combined S3-modules and F-modules.

⁵By design, the S1, S2 and S3 modules are installed on the experiment connected two by two, with special, stiff, non active couplings.

3.8 Water Content Measurements

Next, we studied the relation between the water content and the gas-tightness (see Sec. 3.7) of the OT modules. The purpose was to estimate the amount of in-leak and to establish a minimum requirement for the level of gas-tightness of a module. Small amounts of H₂O in the counting gas can have large implications on ageing effects, while the presence of N₂ reduces the gas gain significantly. For example, 500 ppm of H₂O in the OT gas mixture can cause $\sim 12\%$ drop of the gas gain due to deposits (C,O) on the anode wire [62], while adding 1% of N₂ leads to a loss of 17% of the gas gain [63].

The results and the analysis given here are based on the water content monitoring of several OT modules for a total period of half a year.

3.8.1 Setup and Method

The test setup used for the study is shown in Fig. 3.25.

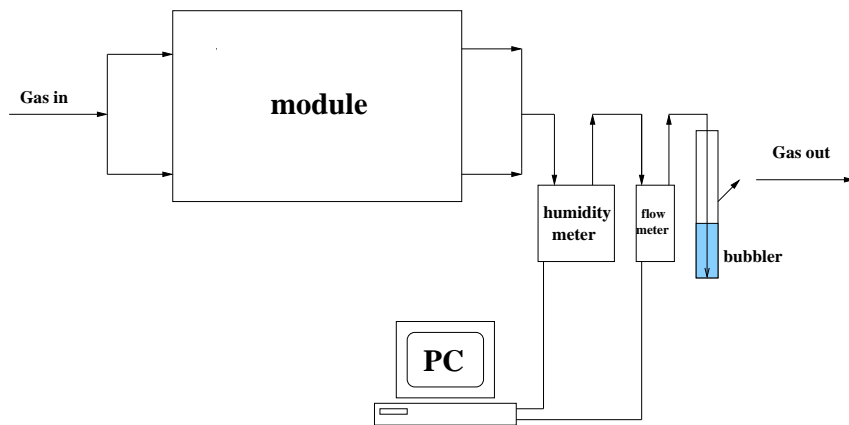


Figure 3.25. Test setup for measuring the water content of the OT modules.

The *absolute humidity* is the fraction of water with respect to the total amount of gas and is measured with a Mitchell dew point meter. The setup is closed with an oil bubbler, creating effectively a 1 mbar overpressure inside the module and sealing the exit of the system.

The dew point of a gas is a measure of its absolute humidity. It is defined as the temperature at which water vapors condense. The higher the dew point, the more water there is in the gas. The *water content* of a gas is conventionally defined as the ratio of the partial vapor pressure of water at the dew point, $P(t_{dew})$, over the total pressure P_{tot} ,

$$\text{Water content [ppm]} = \frac{P(t_{dew})}{P_{tot}} \times 10^6. \quad (3.9)$$

The relation between the saturation vapor pressure and the dew point, $P = P(t_{dew})$, is taken from Fig. 3.26.

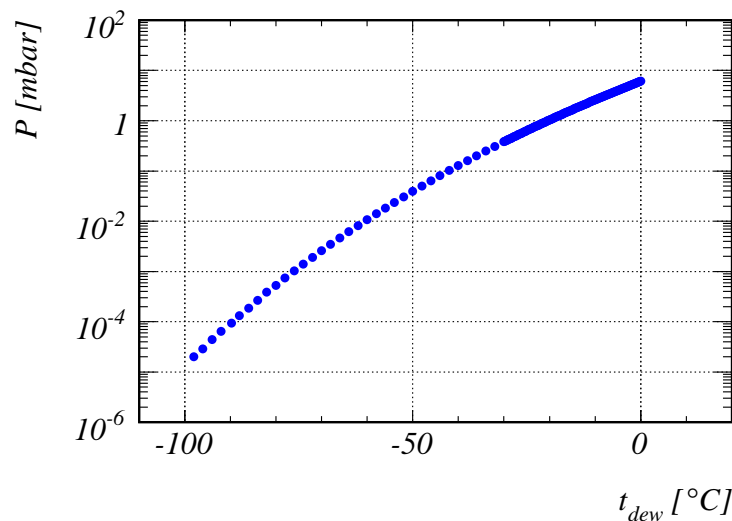


Figure 3.26. Vapor pressure of water versus dew temperature [64]. The saturation vapor pressure, $P(t_{dew})$, for a given dew point, t_{dew} , is determined by interpolation from the data displayed on this graph.

All the subsequent results are given in terms of water content.

3.8.2 Drying of a Newly-Built Module

After calibration of the humidity meter, the water content in the gas bottle was measured. After 40 hours, at a gas flow of 10 l/h, the humidity meter reached a plateau of -74°C , corresponding to 1.5 ppm of water content.

A newly built module contains a certain amount of humidity introduced by the glue, or by absorption of water by the various components of the module. The drying of a module has been monitored with module 045 (after it had been flushed for approximately 200 l.) The gas flow rate was set to 13.8 l/h. The result is shown in Fig. 3.27. After flushing with 2000 l, the water content of this module was 440 ppm. At the end of the measurement, after ~ 4000 l, the water content was 25 ppm.

3.8.3 Water Content in Gas-Tight and Leaky Modules

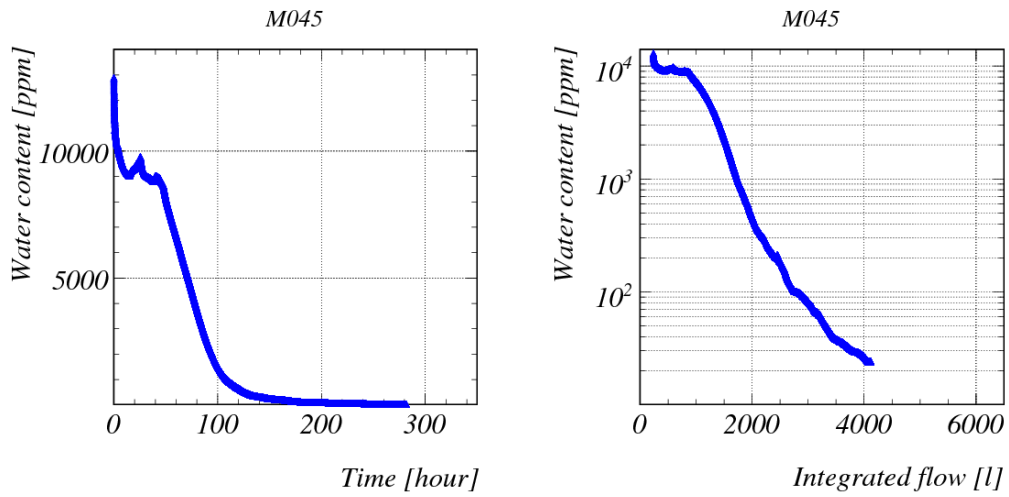
The absolute humidity has been measured in both a leaky (007) and a gas-tight module (008) in order to compare the amount of in-leak of water in the two modules. The results are shown on Fig. 3.28 and are summarized on Table 3.2. Both modules have been flushed with N_2 for 2.5 months before the test started at a flow rate of

8.8 l/h resulting in a total flush volume of ~ 16000 l. During the measurement the gas flow was set to 15.6 l/h for module 8, and for most of the time for module 7.

One can see that both the gas-tight and the leaky module have low absolute humidities, below 10 ppm. Surprisingly, the leaky module shows a lower absolute humidity, which is attributed to unknown systematic effects in the measurements. The environmental conditions were equivalent for both of the modules: constant ambient temperature of $20^\circ C$ and controlled ambient relative humidity of 50%.

The measurement is repeated for a second leaky module (015). The test was performed with a flow rate of 9.6 l/h. Before this test the module was flushed for approximately 200 hours. After 5800 l, at the end of the data taking the humidity of module 15 was 26 ppm, which is similar to the result shown from the non-leaky module (045) after 4000 l.

The two gas-tight modules do not show a significant lower water content than the leaky modules, indicating that the in-leak of pollution through the leaks is limited, see Table 3.2. Consequently, modules with leaks of the size of 1 mbar/min can still be accepted for use in LHCb, without the risk of considerable in-leak of H_2O , and possibly other pollutants.



(a) *The water content as a function of the time.* (b) *The water content as a function of the integrated gas flow.*

Figure 3.27. *Drying of the newly built module 045.*

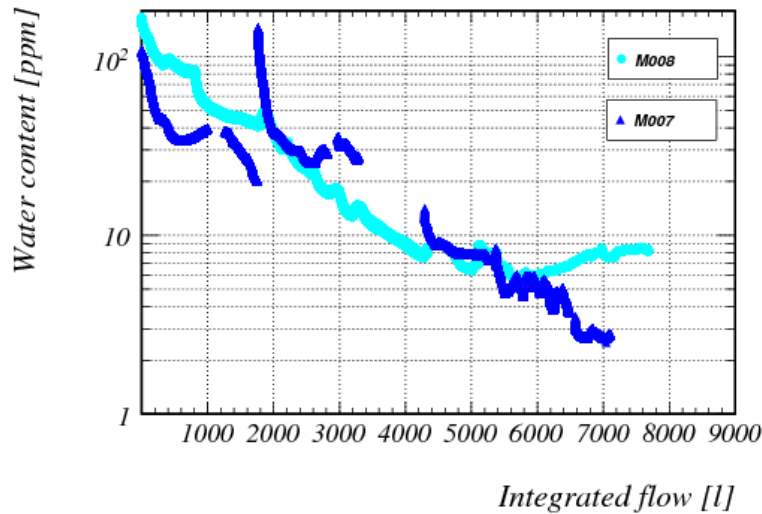


Figure 3.28. Water content of module 8 (gas tight one) and module 7 (leaky one). The spike at ~ 1700 l in module 7 was due to a disconnected gas tube. The gaps indicate missing data, while the modules were flushed at that time. Note that both modules were flushed already with 16,000 l before these measurements began.

Module	Gas Tightness		Int. flow [l]	Humidity [ppm]
	Leak rate [10^{-4} l/s]	dp/3min [mbar]		
M007	13.7	2.3	~ 20000	3.
M008	0.23	0.0	~ 20000	8.
M045	0.68	0.2	4000	25.
M015	12.30	2.3	6000	26.

Table 3.2. The humidity in a module does not significantly depend on the gas-tightness of the module.

3.9 High Voltage Training

The High Voltage (HV) training [54] of the OT modules is an integrated part of the OT quality assurance program at NIKHEF. It is performed after the modules have passed the tests for gas tightness (see Sec. 3.7). The objective of the HV training procedure is to achieve stable, constant in time current values in a counting gas environment, in presence of operational high voltage. When the HV is applied on the module initially, high wire currents are observed. With time the currents decrease, see Fig. 3.29, because all possible dust particles and any other pollutants

on the wire are slowly burned off.

The OT module is flushed with a counting gas mixture (Ar and CO₂ in ratio 70 : 30) at a gas flow rate of 10 l/h. High voltage of 1600 V is applied on the module after one night of flushing. The currents drawn by each single wire are measured every 20 s with a current meter [54]. The HV training is continued until the measured current of each channel is of the order of a few nA. This takes typically about 1.5 h. Occasionally, if the currents remained high (> 10 nA) and the time allowed it, the HV was kept on for a longer period.

As demonstrated in Fig. 3.29, the individual channels behave differently, but generally, after ~ 1.5 h there are very few wires that have currents larger than 2 nA. The drop of the total current (the sum of all currents in a given module section) in ~ 1.7 h for F-module 28-A, is shown in Fig. 3.30. One can see that the decrease of the total current for the lower and the upper sections of the module is ~ 10 and ~ 25 times, respectively.

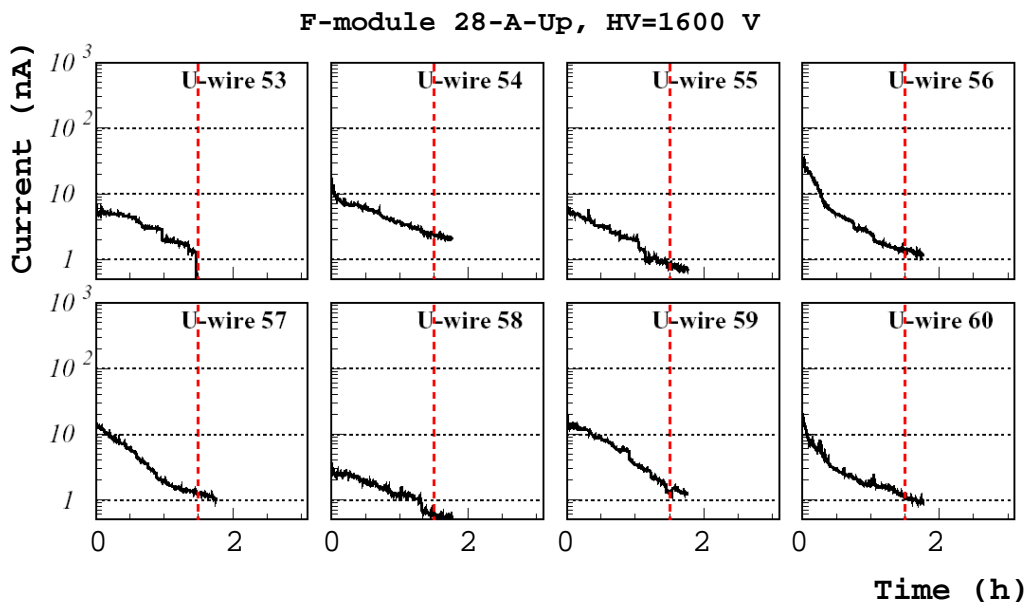


Figure 3.29. Current drop of 8 channels from F-module 28 during the HV training procedure. After about 1.7 h all channels have currents of the order of 1 – 2 nA.

The results from the HV training procedure for all the NIKHEF F-modules produced are illustrated in Fig. 3.31, where the number of wires with currents larger than 2 nA and 10 nA per module is plotted, in the beginning and at the end of the HV training. A significant decrease of these numbers is observed. We end up with only ~ 60 channels with currents larger than 10 nA (out of a total of about 34000 channels), which promises a stable high voltage operation for the detector. The modules constructed earlier⁶, have more wires with large currents. The reason is

⁶The numbering of the modules followed the order of their production.

the worse quality of the wire, as was detected when measuring the currents with HV in an air environment (see Sec. 3.6).

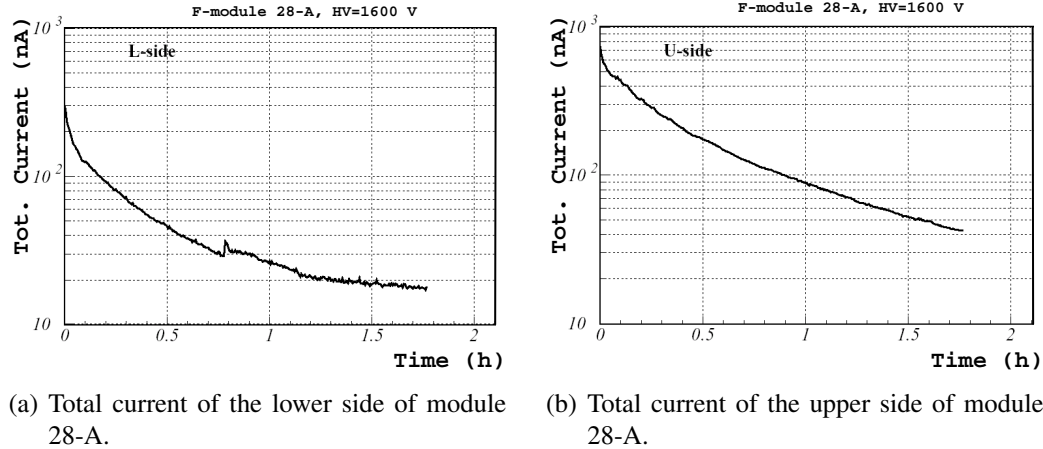


Figure 3.30. Total current of F-module 28-A during HV training at HV=1600 V.

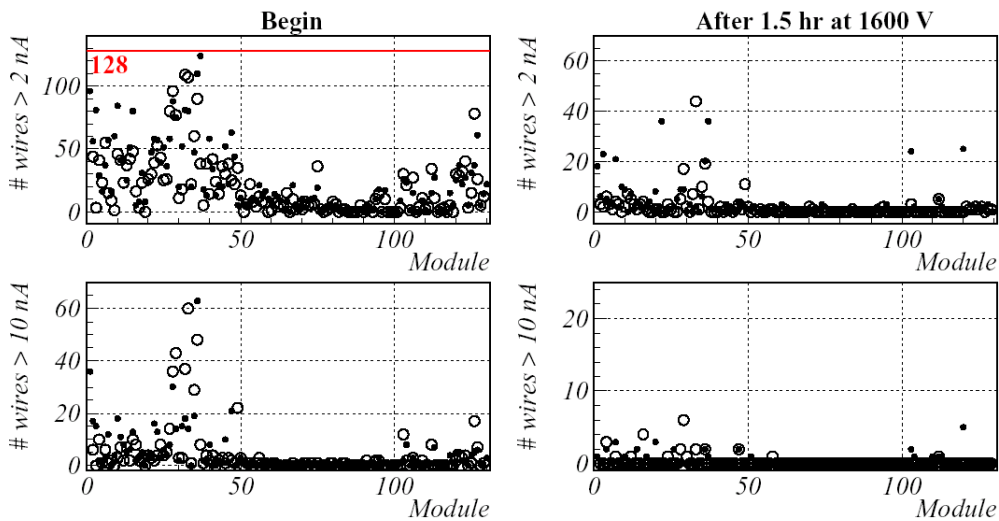


Figure 3.31. HV training results. Number of wires with currents larger than 2 nA (top) and 10 nA (bottom) per module, in the beginning (left) and at the end (right) of the HV training. The full circles correspond to side A of the module, and the empty circles to side B.

3.10 Scanning with Radioactive Source

The scanning of the OT modules with the radioactive β -source ^{90}Sr is the last quality assurance test. It is used for a final validation of the performance of the detectors during mass production. The electrons emitted by ^{90}Sr have energies up to 2.3 MeV and can traverse the straw tubes, causing ionization of the gas and creating a detectable electrical signal on the wire. A complete map of the current response of the modules is done by moving the source along the module's length in steps of 1 cm and by irradiating all the straws at the same time.

3.10.1 The Experimental Setup

A 20 mCi ^{90}Sr radioactive point source is mounted in the middle of a movable platform, 7 cm above the module's surface, as sketched in Fig. 3.32 a). The β -rays emitted from the source, irradiate the module through the 1 cm wide slit left, which is perpendicular to the direction of the wires.

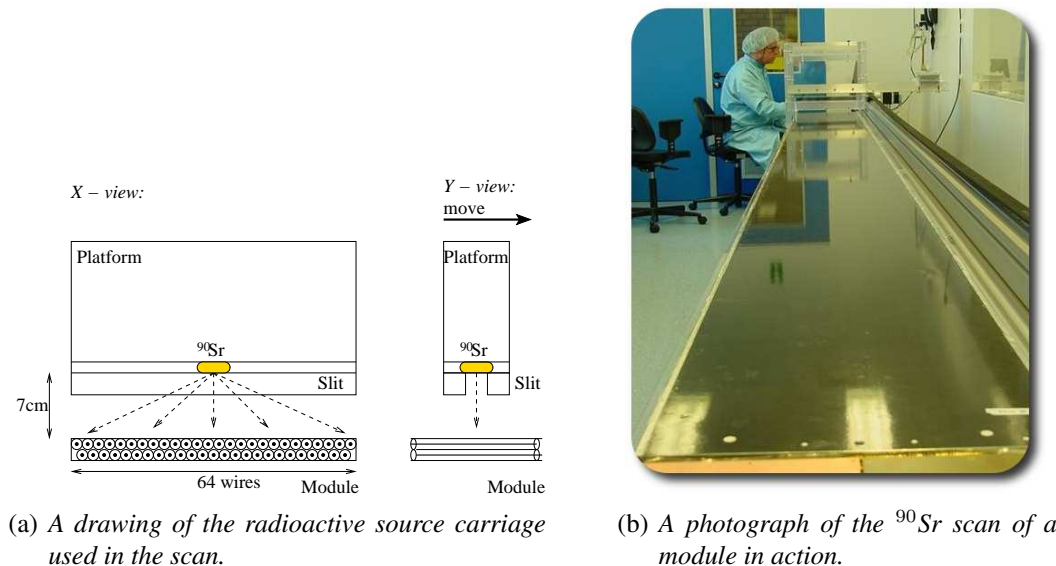


Figure 3.32. The setup used for a scan of the OT modules with a ^{90}Sr radioactive source.

The module is flushed with a counting gas mixture Ar(70%)-CO₂(30%) at a gas flow rate of 10 l/h, as the exposed to the source module-half is put under high-voltage of 1600 V. The platform is moved in steps of 1 cm along the length (y -axis) of the module, started from the lower, towards the upper end of the module. The current of each wire is measured⁷, when the source-carriage is at rest. Then, the module is turned and the other module-half is scanned the same way. The full module

⁷The current meter used for the measurement is described in Ref. [54].

scan lasts ~ 2 hours. A photograph of the ^{90}Sr -source scan test setup is given in Fig. 3.32 b).

3.10.2 Results

A typical profile of the ^{90}Sr -source is shown in Fig. 3.33, where one can see the measured current for each of the 64 wires at the same position along the length of the wires. The bell-shape of the current curve is determined by the fact that wires in the middle of the module (such as wires #31, #32, #33, etc.) are closer to the source, and therefore draw larger currents.

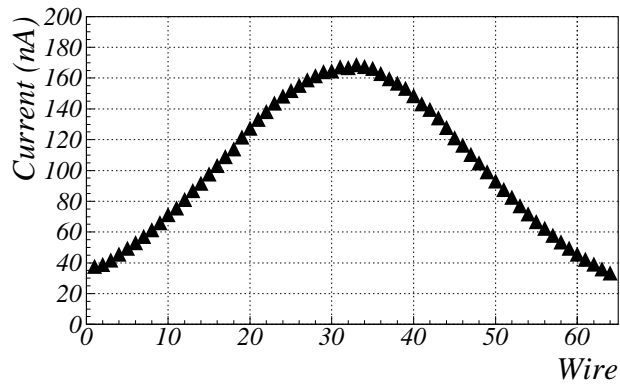


Figure 3.33. The current profile of the ^{90}Sr -source, measured with F-module 70-A, Up.

The ^{90}Sr scan is a powerful tool for discovering hidden module defects or imperfections, such as

- ◊ shifted or missing wire locators;
- ◊ curved straws;
- ◊ abnormally low or high currents, which can be caused by large amounts of glue, insufficient gas flow or instabilities that can produce high pulse rates.

For example, Fig. 3.34 demonstrates the response of two channels after their irradiation with the ^{90}Sr -source. The left plot illustrates the behavior of the current versus the y -position of the wire. The drop of the current on every ~ 80 cm is because of the presence of wire locators in these places and the zero current at ~ 270 cm is due to the straw tube separation. The right plot in the same figure shows an abnormally high current measured at $y = 80$ cm. The reason for this is a missing wire locator.

Results from the ^{90}Sr -scan for F-module 46-B are summarized in Fig. 3.35, showing the relative⁸ current deviation (in %) from the average response of the modules to the ^{90}Sr -source. For each wire and each position along the wire, the relative current is shown (in color code). The white strips indicate the places of the wire locators. The wider white strip in the middle is the straw tube separation region, which is non-active by construction. In general, as can be seen from the figure, the response of this module over its full surface is homogeneous within 10%. The same result is valid for most of our F-modules.

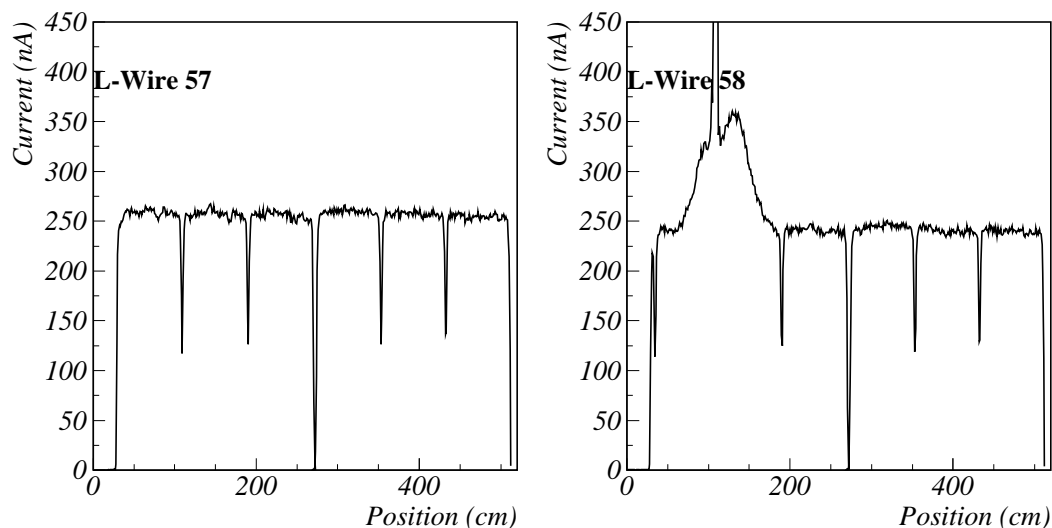


Figure 3.34. Examples of a "good" (wire #57) and a "bad" (wire #58) channel.

⁸The gas gain strongly depends on the variations of the atmospheric pressure and the ambient temperature, and hence the measured wire currents depend on these factors too. Therefore, we compare not the absolute, but the relative module response, corrected for temperature and pressure fluctuations.

F-module 46-B, HV=1600 V

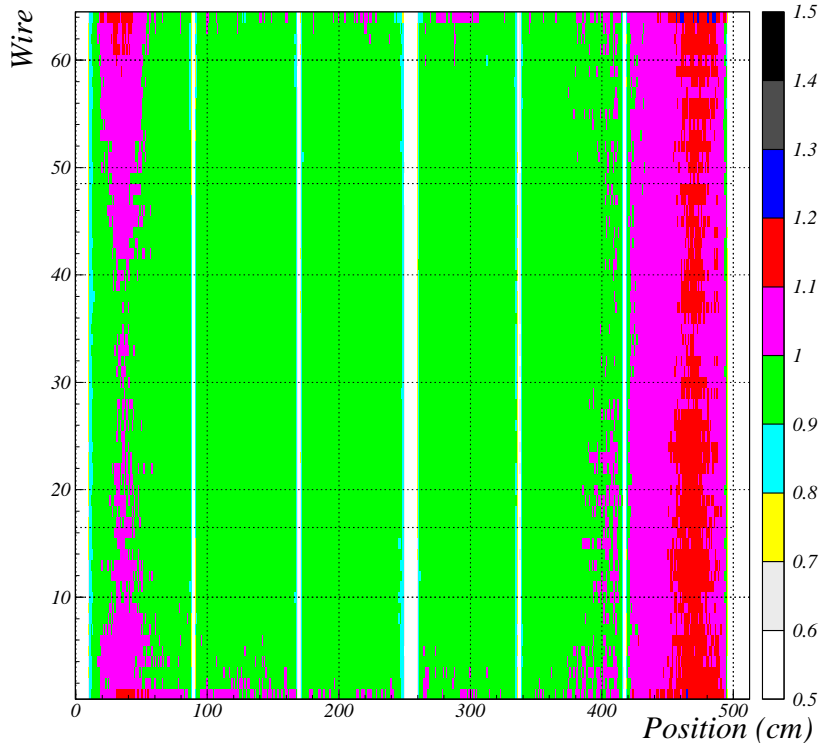


Figure 3.35. The relative current response of F-module 46-B to the ^{90}Sr -source as a function of wire number and position along the wire. The current is corrected according for the ^{90}Sr -source profile.

3.11 Summary

The performance of the OT modules produced at NIKHEF is closely watched during their construction. A variety of tests is carried out to verify the proper functioning of the detectors. The results of the quality assurance tests are summarized below.

1. The quality of the anode wire is checked by optical inspection of samples of the wire spools for damages. Fifty spools from a total of 437 are rejected for use because of low quality of the wire.
2. The friction force of the wire locators with the straw is regularly monitored and completely fulfill the requirement of being larger than 200 g.
3. The position of the anode wire inside the straw was initially checked. The results show an average (minimum) accuracy of $54 \mu\text{m}$ ($76 \mu\text{m}$), which is well within the desired limit band of $\pm 100 \mu\text{m}$.

4. The wire tension is measured systematically for each wire to check if it is in the required acceptance window of ± 5 g around 75 g. The measurements reveal that the averaged wire tension of the 64 wires per panel per layer (upper or lower) varies between 70 and 78 g with a spread between 0.3 and 2.8 g.
5. The current of each wire is measured in an air environment. No deviations from the required limit are allowed.
6. All modules are tested for gas tightness. Most of them suit the chosen gas tightness criterion.
7. HV training of the channels in a counting gas is performed in order to stabilize the measured currents in constant values of the order of a few nA.
8. Final validation of the modules with ^{90}Sr radioactive source is undertaken in a presence of a counting gas mixture and an operational high voltage. The scanning with ^{90}Sr show homogeneous current response of the OT modules over their active surface within $\pm 10\%$.

Based on the results of the quality assurance tests it is possible to conclude that the OT detectors show a satisfactory performance, which will guarantee their successful operation in the LHCb experiment.

Chapter 4

Beam Tests of OT Modules

It is a capital mistake to theorize before one has data.

Arthur Conan Doyle (1859-1930)

In the beginning of 2005, four LHCb Outer Tracker modules have been tested with a particle beam [65]. The purpose was to study the performance of the final mass-production modules, equipped with the final version of the frontend electronics, in the presence of a beam of minimum ionizing particles, and to determine the main detector performance parameters, such as efficiency, spatial resolution and noise. This chapter is devoted to these beam tests. In Sec. 4.1 the setup is described. The analysis of the collected data is explained in Sec. 4.2. The results are presented in Sec. 4.3. Conclusions are drawn in Sec. 4.4.

4.1 Beam Test Setup

4.1.1 The Test Setup

The beam tests were done in February-March 2005 in the experimental area 22 of DESY, Hamburg, at the DESY II testbeam facility, which provided an electron beam with energies from 1 to 6 GeV. The beam was obtained after two conversions from the main DESY II electron beam, as sketched in Fig 4.1.

The test setup configuration is shown in Fig. 4.2. It consisted of four OT modules of type S1U (see Chapter 2), a silicon strip telescope and trigger scintillators. The modules were installed vertically, perpendicular to the beam (z) direction. Since each OT chamber contained two straw layers, the beam irradiated in total eight straw layers. The modules are referred according to their z -position, starting from 1, i.e module 1 - 4 (or M1 - M4). The straw layers inside the modules are named layer 1 and layer 2 (or L1 and L2), where layer 1 is the one with smaller z . All modules were equipped with a frontend box (FEB) containing final readout electronics.

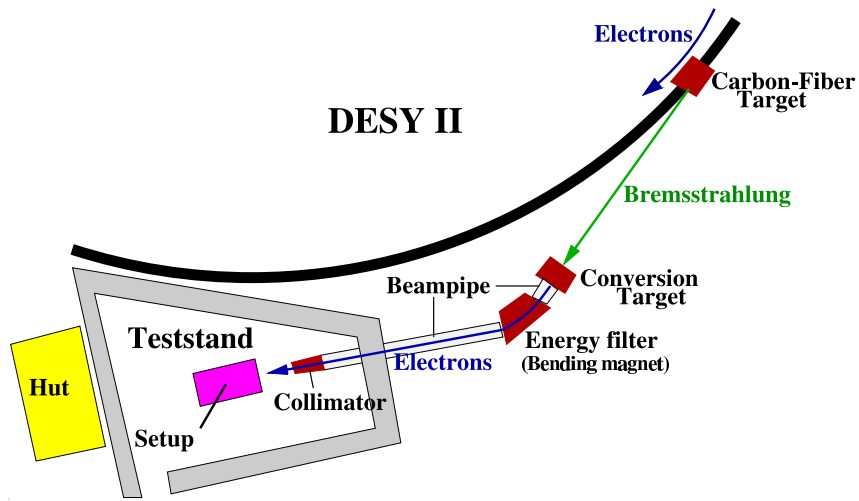


Figure 4.1. The DESY II electron beam is intercepted with a $10 \mu\text{m}$ thick carbon-fiber target, producing bremsstrahlung. The bremsstrahlung beam is converted into electron-positron pairs through a copper target with a radiation length of 0.1 g/cm^{-2} . A bending magnet and a collimator slit are used to filter the energy of the particles (from 1 to 6 GeV) and to deliver the electron test beam into the experimental hall [66].

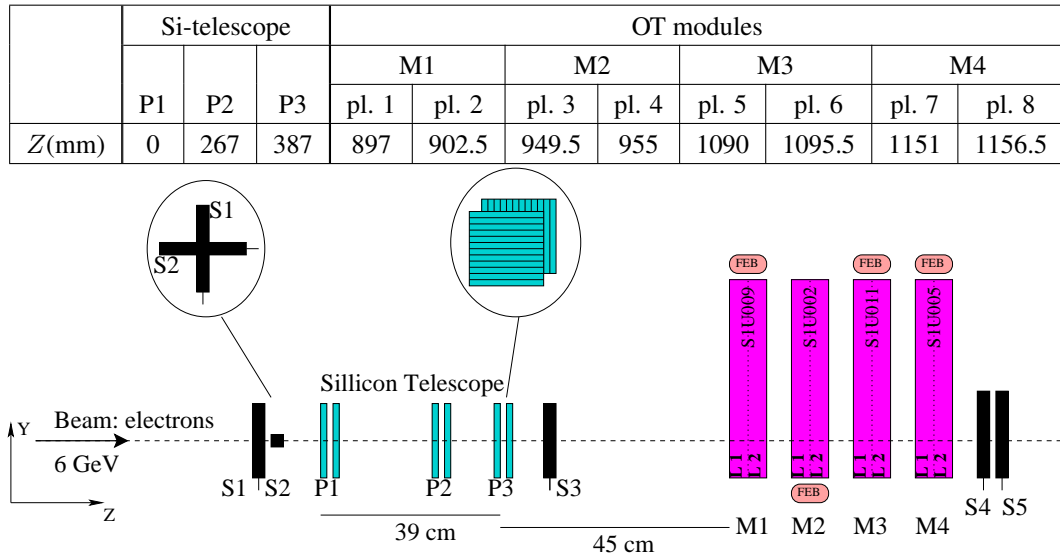


Figure 4.2. Schematic drawing of the beam test setup. The trigger signal is an AND-product of the signals from $S1$, $S2$, $S3$, $S4$ and $S5$ scintillators. The time reference, t_{ref} , for measuring the OT drift times is provided by $S4$ and $S5$.

Module 2 was positioned upside-down with respect to the other modules, with the FEB close to the beam, in order to get results also for particles passing the detector close to the readout electronics. As counting gas, a mixture of 70% Ar and 30% CO₂ was used.

The trigger signal was produced by coincidence of all five scintillator counters S1, S2, S3, S4 and S5.

The first two scintillators S1 and S2 with thickness of 2 mm and width of 9 mm were put perpendicularly to each other and defined the beam spot area in the *xy* plane ($9 \times 9 \text{ mm}^2$). The S3 counter was found to cause significant multiple scattering of the beam particles and was excluded from the setup for most part of the data taking. Except for trigger input, the signals from the S4 and S5 counters were used also as a time reference for measuring the OT drift times. This was necessary, since the beam and the OTIS chip were not synchronized (the beam particles arrived randomly with respect to the OTIS 40 MHz clock). The drift time was obtained by subtraction of the average arrival time of the scintillator signals from the OT arrival time, both measured by the OTIS TDCs,

$$t_{\text{drift}} = t_{\text{raw TDC}} - t_{\text{ref}} , \quad (4.1)$$

with $t_{\text{ref}} = (t_{S4} + t_{S5})/2$. The precision of the time reference, given by the width of the distribution of $\Delta t = (t_{S5} - t_{S4})/2$, shown in Fig. 4.3 a), was about 0.4 ns. The distribution of the OT raw times at HV=1600 V is shown in Fig. 4.3 b). It can be seen that the OT time window of 75 ns comprises the full width of OT raw times. Finally, the OT drift time spectrum on a random background at HV=1600 V can be seen in Fig. 4.3 c) after subtraction per event of t_{ref} , the average S4 and S5 raw time.

A drawing of the OT readout system used in the beam tests is presented in Fig. 4.4.

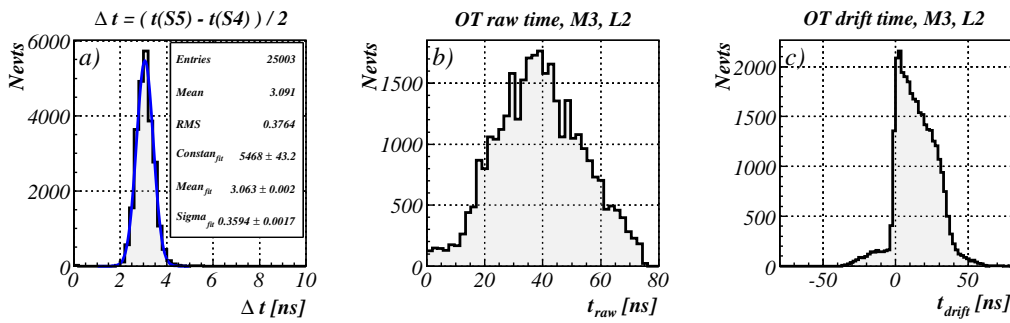


Figure 4.3. a) Precision of the time reference; b) OT raw time distribution; c) OT drift time distribution. HV=1600 V.

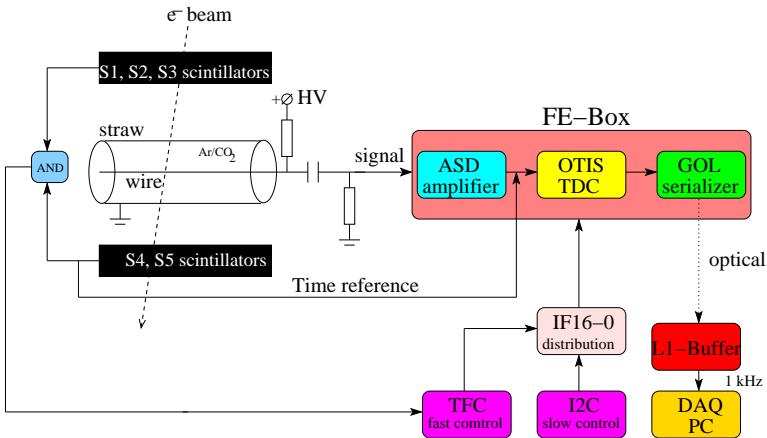


Figure 4.4. Scheme of the beam test readout. The FE-Box is modified for the purpose of this beam test with three external timing inputs (S_4 , S_5 and trigger) in order to obtain a time reference. Both fast (TFC) and slow (I2C) control systems were used to distribute the LHC 40 MHz clock together with the trigger decision and to manage the bunch and event counters.

4.1.2 The Silicon Strip Telescope

A silicon strip telescope [66, 67, 68] was used as an instrument providing an independent measurement of the beam tracks coordinates. It consisted of three pairs of single-sided silicon strip planes, put orthogonally to each other, with a strip pitch of $25\ \mu\text{m}$ and a readout pitch of $50\ \mu\text{m}$, measuring the vertical (y) and the horizontal (x) position (see Fig. 4.2). The high resolution ($< 3\ \mu\text{m}$) silicon strips sensors had a size of $32 \times 32\ \text{mm}^2$ and thickness of $0.3\ \text{mm}$. Each of the three detector pairs was mounted in a metal box with thin ($30\ \mu\text{m}$ thick) aluminum windows. A photograph of the Si-telescope system is displayed in Fig. 4.5. Distributions of the beam x -coordinates and slopes, measured with the Si-telescope, are shown in Fig. 4.6.

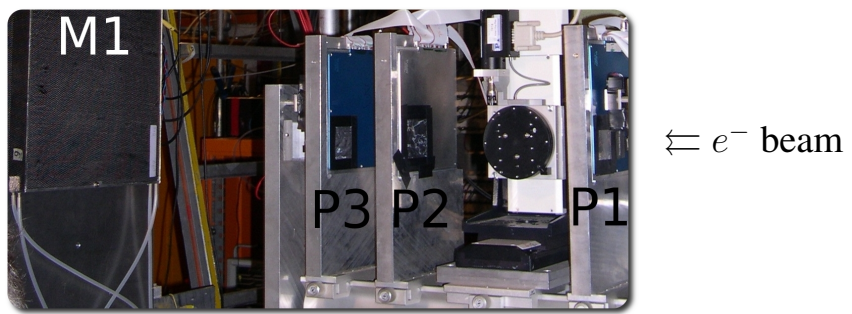


Figure 4.5. Photograph of the testbeam telescope setup (P_1 , P_2 , P_3). The electron beam enters from the right. At the left-side of the picture, the lower half with gas tube connections of the first OT module (M_1) is visible.

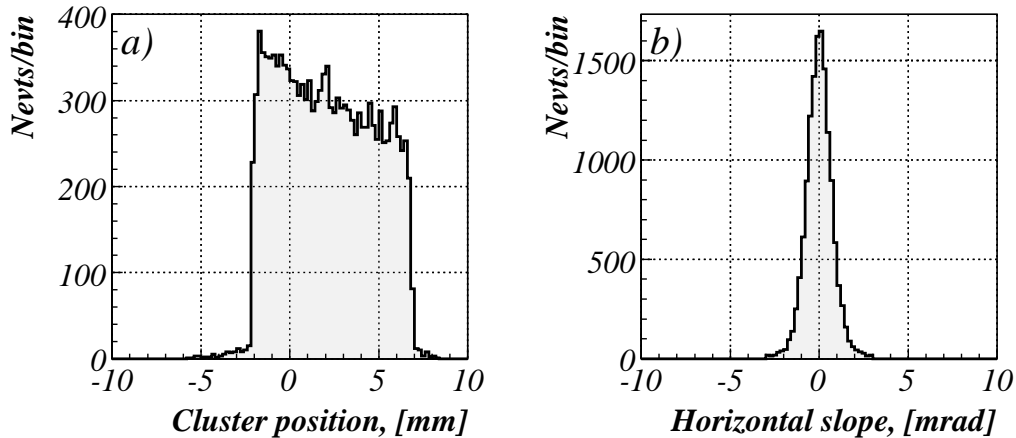


Figure 4.6. a) Distribution of x -coordinates of the triggered beam tracks measured with the Si-telescope; b) Horizontal slopes of the beam tracks measured with the Si-telescope.

4.2 Analysis of the OT Beam Tests Data

Next, we will review the data analysis. We determined the detector efficiency, spatial resolution, noise and cross talk. Most of the data were taken with a beam energy of 6 GeV, and unless otherwise noted, this beam energy value is considered throughout the analysis.

4.2.1 Si-telescope track reconstruction

During the beam tests, the two external OT modules (M1 and M4), were kept under constant conditions of high-voltage (HV) and amplifier threshold (Thr), while the operational mode of the internal modules (M2 and M3) was varied. Thus, M1 and M4 were acting as a *reference* of the two *test* chambers M2 and M3 (see Fig 4.7). The beam area of $9 \times 9 \text{ mm}^2$, pre-defined by the S1 \times S2 scintillators, results in two or three illuminated straws per layer.

The OT hit map for the two straw layers of the two test modules is shown in Fig. 4.8. In the analysis of the data, a single track in the Si-telescope per event was required. The events were selected according to the number of clusters reconstructed in the Si-telescope planes (P1, P2 and P3). The total number of clusters had to be 5 or 6. One and only one cluster in each of the three planes measuring the x -coordinate was demanded, and 0 or 1 in the planes measuring the y -coordinate. This cut reduced the number of events with 44%. A second cut concerning the track slopes t_x and t_y , was applied in addition: $-3 < t_x < 3 \text{ mrad}$ and $-3 < t_y < 3 \text{ mrad}$. As a result, the number of events was reduced with another 3%.

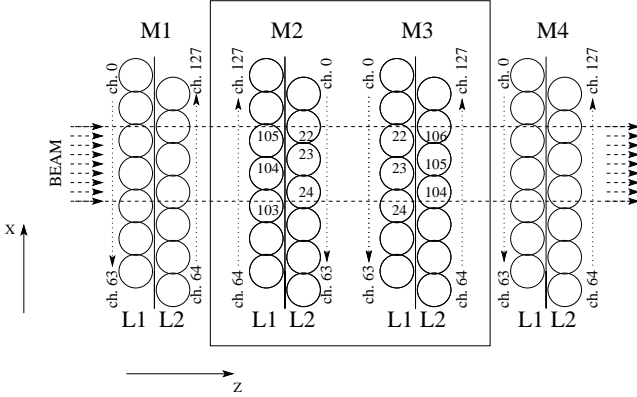


Figure 4.7. Top view of the layout of the tested OT modules. M1 and M4 were used as a reference for the test of M2 and M3. The counting of the channels is different for M2 and M3, since M2 is turned upside-down with respect to the other chambers.

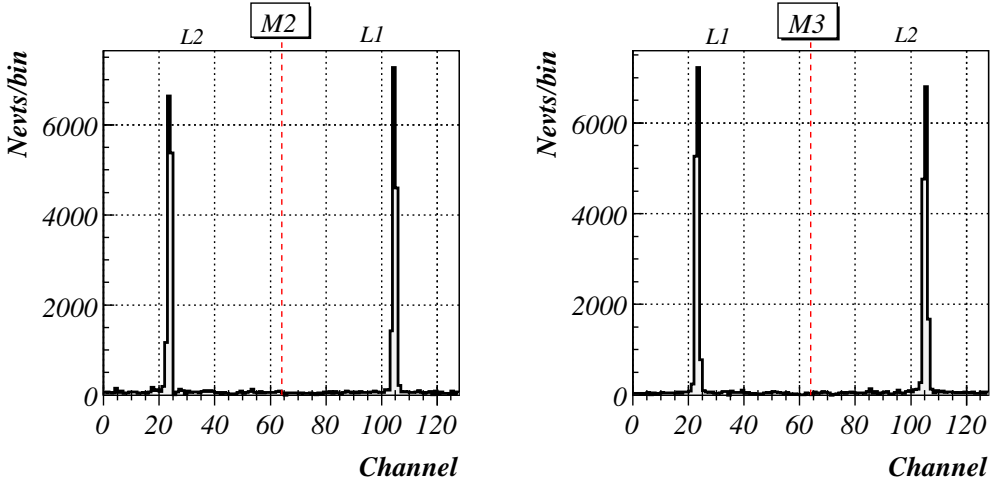


Figure 4.8. The hit pattern for the OT test modules M2 and M3 for HV=1600 V. The two peaks correspond to hits in the two layers.

As a measure of the accuracy of the tracks reconstructed in the Si-telescope, the distribution of the track residuals is plotted in Fig 4.9. The track residual is the difference between the coordinate of the track (x_{track}) and the coordinate of the cluster ($x_{tel,Pi}$) measured at a given Si-telescope plane ($P_i, i = 1, 2, 3$). The track residuals are not unbiased, since the clusters were also used for the reconstruction of the track. As can be seen from Fig 4.9, the width of the x -residuals distribution is $5 \mu\text{m}$ for P1, $16 \mu\text{m}$ for P2 and $11 \mu\text{m}$ for P3. The two outer planes have smaller residuals by construction, because the clusters themselves are used in the straight line fit. The residuals of P1 and P3 differ, since P2 is closer to P3 than to P1.

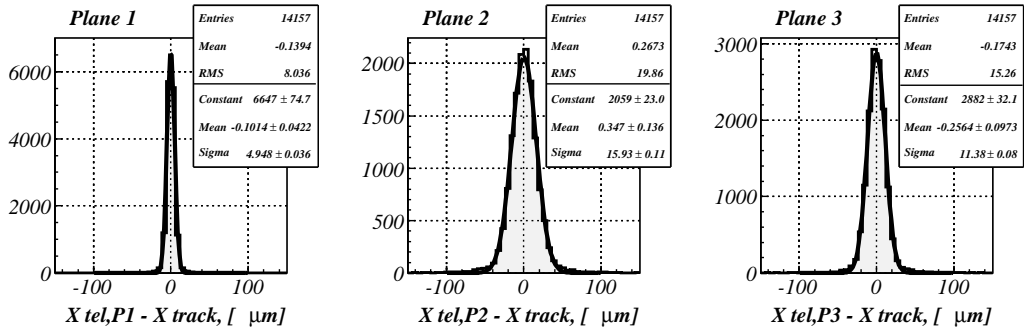


Figure 4.9. Distributions of the track residuals in the Si-telescope X planes.

4.2.2 Space - Drift Time Relation

An OT drift tube allows the measurement of the time between the trigger and the arrival of the first electrons of a nearby ionization cluster at the wire. The main contribution to this time is the drift time inside the straw tube. However, to reconstruct the trajectory of the particle, the shortest distance to the wire at which the charged particle has passed needs to be known [35]. This means, that the drift time has to be converted into a distance of closest approach of the particle to the wire. The conversion, also known as *space-drift time relation*, or simply *r(t)-relation*, is non trivial, and depends on many factors, such as the cell geometry, the gas mixture and the HV applied.

In our analysis, the *r(t)*-relation is determined by using the information provided by the Si-telescope. The tracks reconstructed in the Si-telescope are extrapolated to the OT layers, predicting the particles path within the straw. The predicted *x*-position in the OT is calculated by using the Si-telescope track parameters (the horizontal position of the track at P3 - $x_{tel,P3}$, and the horizontal slope of the track at the *xz*-plane - t_x),

$$x_{OT} = x_{tel,P3} + t_x(z_{OT} - z_{tel,P3}) . \quad (4.2)$$

Figure 4.10 shows the correlation between the measured drift time and the distance between the extrapolated Si-telescope track and the wire, for both layers of the test modules. The characteristic V-shapes patterns, expected for a cell with a drift tube geometry are clearly outlined.

The *r(t)*-relation was obtained with the following procedure.

1. The three distinct V-shapes, observed in each straw layer (see Fig 4.10) were superimposed into a single two dimensional *t(r)* histogram, Fig 4.12, in such a way, that the wire position is set at $r = 0$.
2. The resulting V-shape, was sliced in bins of the predicted track position. The mean drift time of each bin is determined with a Gaussian fit limited to drift times within 2σ from the peak time.

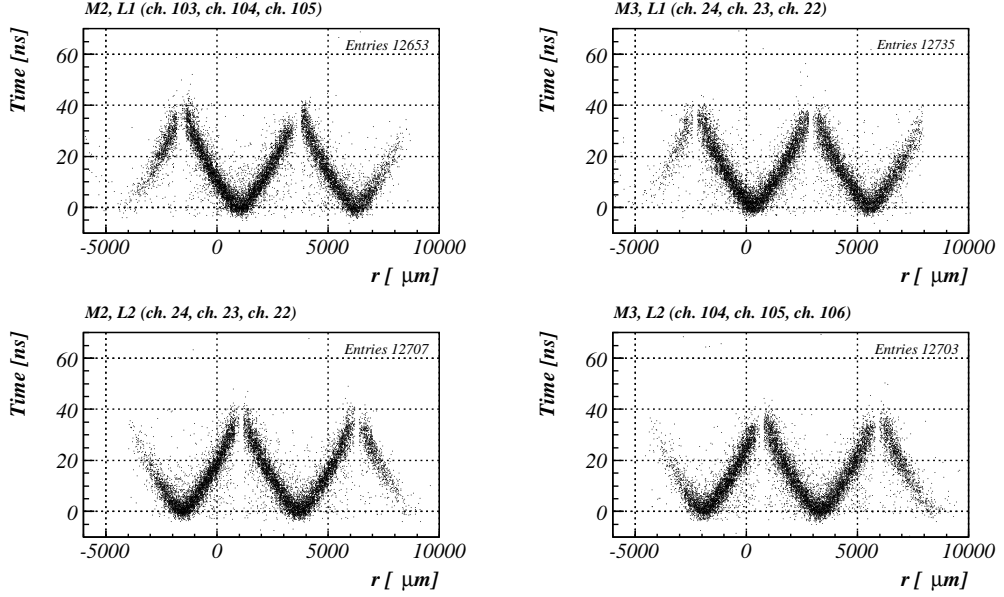


Figure 4.10. Drift time versus distance between the wire and extrapolated track coordinate from the Si-telescope for OT HV=1600 V and Thr=700 mV.

3. The $t(r)$ -relation was determined with a quadratic fit through the mean drift times per slice. The fitting function was parametrized as (see Fig 4.11)

$$\begin{aligned} t(r) &= p_0 + p_1(r - p_2)^2 \quad \text{for } r > 0 \\ t(r) &= p_0 + p_1(r - p_3)^2 \quad \text{for } r < 0, \end{aligned} \quad (4.3)$$

representing two parabolas, left and right of the wire position.

4. The parameters p_0 , p_1 , p_2 and p_3 were extracted from the fit (see Fig. 4.12).
5. Finally, solving Eq. (4.3) with respect to r , the $r(t)$ -relation was obtained,

$$\begin{aligned} r(t) &= p_2 + \sqrt{\frac{t - p_0}{p_1}} \quad \text{for } r > 0 \\ r(t) &= p_3 - \sqrt{\frac{t - p_0}{p_1}} \quad \text{for } r < 0. \end{aligned} \quad (4.4)$$

The above described procedure, provided a well defined, single $r(t)$ -relation for each layer of the test OT modules, allowing to fully map the drift time hits onto space coordinates. The next step is then the determination of the OT spatial resolution.

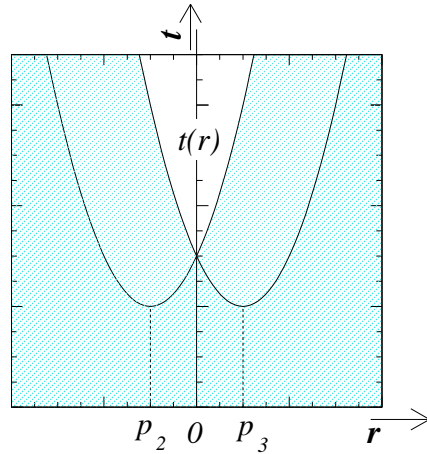


Figure 4.11. The $t(r)$ fitting function (the curve surrounding the non-shaded region). It is built from two parabolas, cut at $r = 0$.

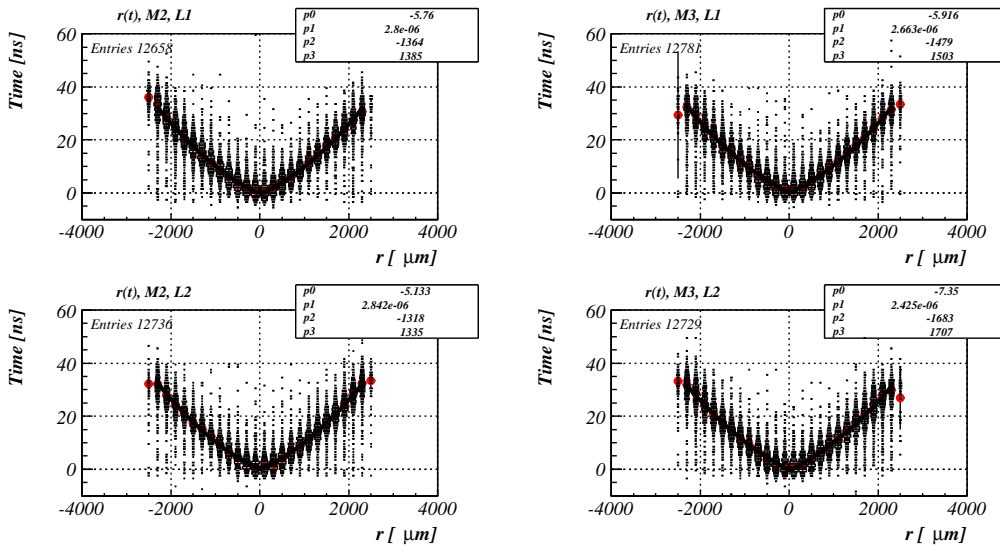


Figure 4.12. The $t(r)$ -relation for HV=1600 V and Thr=700 mV.

4.2.3 Spatial Resolution

The OT coordinate resolution can be obtained from the comparison of the predicted track position x_{tel} , and the position x_{OT} , determined via the measured drift time, converted into distance to the wire with the help of the developed $r(t)$ -relation (see Sec. 4.2.2). Thus, the resolution is defined as the width σ , of the *residual* distribution, where the *residual* is the difference $x_{tel} - x_{OT}$, assuming high accuracy for

x_{tel} .

Figure 4.13 represents the residual distributions for three values (1450 V, 1550 V, 1650 V) of the applied high voltage setting. The resolution ($407 \mu\text{m}$, $240 \mu\text{m}$, $207 \mu\text{m}$) in all three cases is overestimated, since the multiple scattering in the Si-telescope planes and for some of the runs, in the S3 scintillator counter, was not taken into account. The evaluation of the effect of multiple scattering is discussed in the next section.

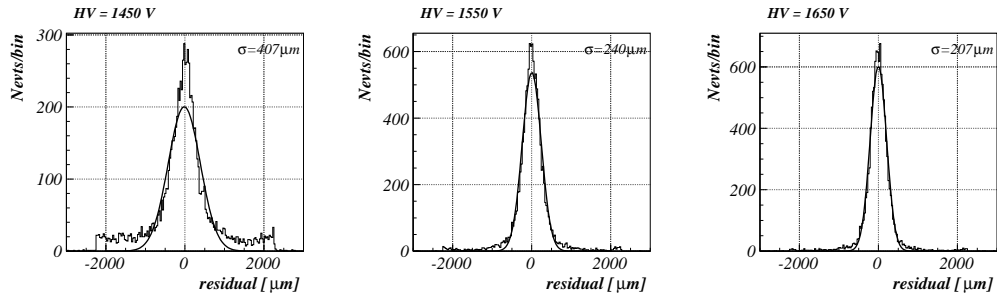


Figure 4.13. Residual distributions for $HV=1450$ V, 1550 V and 1650 V and with $Thr=700$ mV. The coordinate resolution is represented by the width σ of the Gaussian fit.

4.2.4 Multiple Scattering

Of particular importance for a correct estimate of the OT coordinate resolution (see Sec. 4.2.3) is to ensure that multiple scattering of the beam particles in the Si-telescope planes and in the S3 scintillator is properly taken into account.

The effect of multiple scattering was studied by taking runs at different beam energies and measuring the resolution with and without the S3 counter¹. Figure 4.14 shows the obtained spatial resolution σ_{tot} , as a function of the electron energy, E .

The multiple scattering contribution, $\sigma_{MS} = \sqrt{\sigma_{tot}^2 - \sigma_{OT}^2}$, to the total observed resolution, was extracted by fitting the data with

$$\sigma_{tot} = \sqrt{\sigma_{OT}^2 + (\sigma_{MS,1\text{GeV}}/E)^2} , \quad (4.5)$$

with $\sigma_{MS,1\text{GeV}}$ and the intrinsic OT spatial resolution σ_{OT} being free parameters of the fit. The multiple scattering contribution at 6 GeV was retrieved by using

$$\sigma_{MS,6\text{GeV}} = \sigma_{MS,1\text{GeV}}/6 . \quad (4.6)$$

The results for the multiple scattering contribution to the residuals for both OT modules are listed in Table 4.1. The values of the corresponding scattering-angle width σ_θ are consistent for both layers M2 and M3.

The final resolution, corrected for multiple scattering is given in Sec. 4.3.1.

¹Note that S3 was positioned between the Si-telescope and the OT modules, (see Fig 4.2).

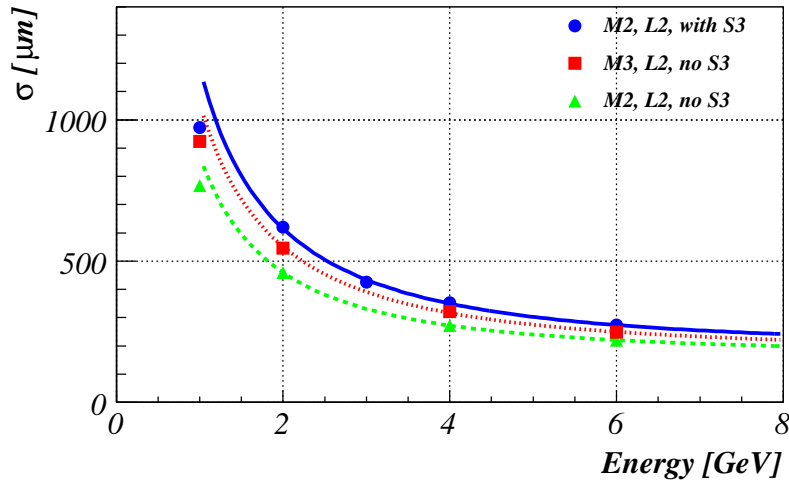


Figure 4.14. Resolution versus beam energy for HV=1600 V and Thr=700 mV. The data are fitted with the function in Eq. (4.5). The data point at 1 GeV is not used in the fit because of the relatively large multiple scattering compared to the OT cell size.

OT Module	without S3		with S3	
	$\sigma_{\text{MS}, 6\text{GeV}} [\mu\text{m}]$	$\sigma_\theta [\text{mrad}]$	$\sigma_{\text{MS}, 6\text{GeV}} [\mu\text{m}]$	$\sigma_\theta [\text{mrad}]$
M2 (L1,L2)	143	0.253	195	0.345
M3 (L1,L2)	176	0.249	246	0.348

Table 4.1. Multiple scattering contribution to the residual at 6 GeV and the angular width σ_θ are given for both OT test modules, in both cases with and without S3 scintillator.

4.2.5 Efficiency

Plateau Efficiency

In our analysis the efficiency was defined by its plateau value in the center of the straw, in a range of $[-1.6, +1.6]$ mm around the anode wire.

The straw efficiency profile, shown in Fig. 4.15 c) is obtained by dividing the x_{tel} distribution of "accepted" OT hits (Fig. 4.15 b)), to the one of the predicted hits (Fig. 4.15 a)). An OT hit is accepted if its x_{OT} position is within a 2 mm window around the extrapolated x_{tel} position. The quoted plateau efficiency in Sec. 4.3.2 is the ratio of the two histogram integrals over a range of 3.2 mm.

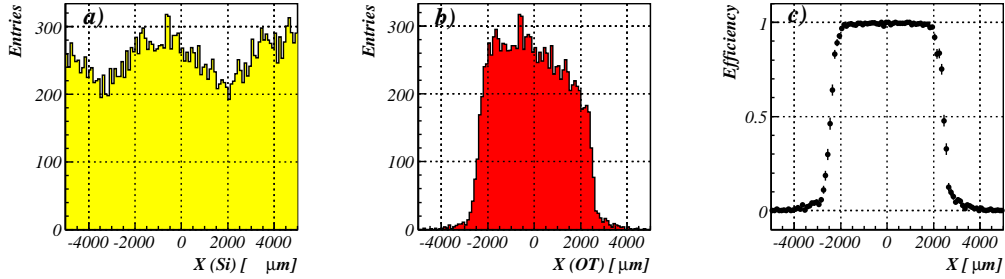


Figure 4.15. a) Distribution of the predicted x_{tel} positions in M3, L1. b) Distribution of the accepted x_{tel} positions in M3, L1 at $HV=1600$ V and $Thr=700$ mV. c) Straw efficiency profile obtained through division of the histograms in b) and a).

Plateau Efficiency Modeling

The probability $P(n; l)$ to observe n primary ionizations (clusters), when a charge particle traverses an OT straw tube, is given by Poisson statistics,

$$P(n; l) = \frac{\left(\frac{l}{\lambda}\right)^n \exp\left(-\frac{l}{\lambda}\right)}{n!}, \quad (4.7)$$

where l is the traversed path within the cell, and λ is the average ionization cluster length. In a gas mixture of Ar/CO₂ - 70/30, $\lambda = 325$ μm [53]. Assuming ideal detector response (fully efficient readout, and no loss of primary electrons), the single drift cell efficiency is given by

$$\epsilon(l) = 1 - P(0; l) = 1 - \exp(-l/\lambda). \quad (4.8)$$

For X being the shortest distance to the wire, and R the straw internal diameter, $l = 2\sqrt{R^2 - X^2}$, and Eq. (4.8) is transformed to

$$\epsilon(x) = \epsilon_{plateau} (1 - \exp(-2\sqrt{R^2 - x^2}/\lambda)), \quad (4.9)$$

expressing the drift cell efficiency as a function of the distance to the wire. The coefficient $\epsilon_{plateau}$ represents the plateau efficiency. The straw efficiency profile, Fig. 4.16 a), is deformed at the edges due to the smearing of the predicted x -position by multiple scattering. In the same figure the theoretical curves of the predicted efficiency (Eq. (4.9), with $\epsilon_{plateau} = 1$) are shown, under the assumption of zero and finite (with $\sigma = 200$ μm) multiple scattering contributions. In Fig. 4.16 b) a zoom-in of the plateau region is shown, from which it is clear that the plateau efficiency is greater than 99% (for $x \in [-1.6, 1.6]$ mm, $HV=1600$ V and $Thr=700$ mV).

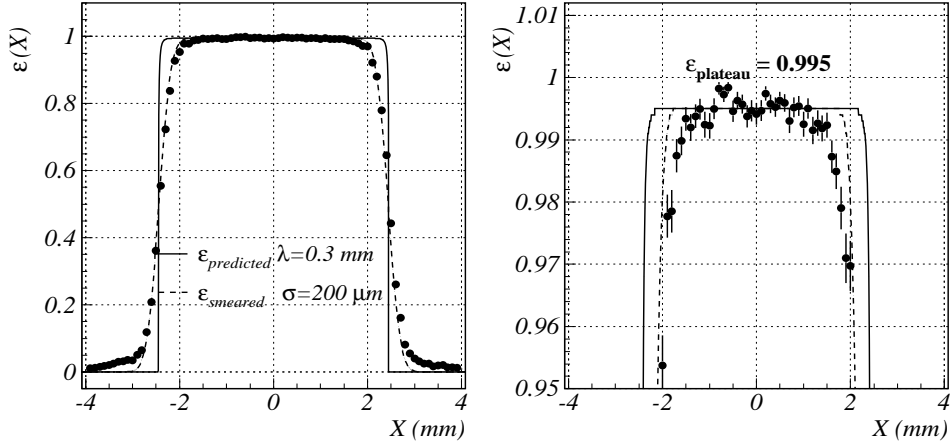


Figure 4.16. a) Straw efficiency profile, averaged for M2 and M3, with superimposed curves of the predicted efficiency (Eq. (4.9)) with infinite and finite ($\sigma = 200 \mu\text{m}$) spacial resolutions. b) A zoom-in of the plateau region.

4.2.6 Noise

Another important OT quantity that has been studied in the presence of the beam was the amount of *electronic noise*. For its estimation, the number of the OT hits in the channels remaining outside the beam coverage was monitored. More precisely, as Fig. 4.17 shows, 33 wires per straw layer outside the beam region were taken into account in the study². The number of hits per channel is shown, for a total number of ~ 14000 events, revealing uniform and modest level of noise. Assuming that none of these hits originated from the beam, the average noise occupancy per wire, \mathcal{O} , is defined as

$$\mathcal{O} = \frac{\left[(\sum_{ch}^{33} \text{hit}) / 33 \right]}{N_{\text{Si tracks}}}, \quad (4.10)$$

with $N_{\text{Si tracks}}$ the total number of tracks reconstructed in the Si-telescope and extrapolated to the given OT layer.

Knowing the average noise occupancy per wire \mathcal{O} (Eq. (4.10)), one can estimate the noise hit rate per wire, f , as follows

$$f = \frac{\mathcal{O}}{75\text{ns}} \quad (4.11)$$

In Sec. 4.3.4, the results for \mathcal{O} and f are given for different settings of high voltage and amplifier threshold.

²Although, only about 2 – 3 straws were directly exposed to the beam, for the noise study we excluded not only them, but yet another 15 channels from their both sides, which might be affected from scattered secondary particles.

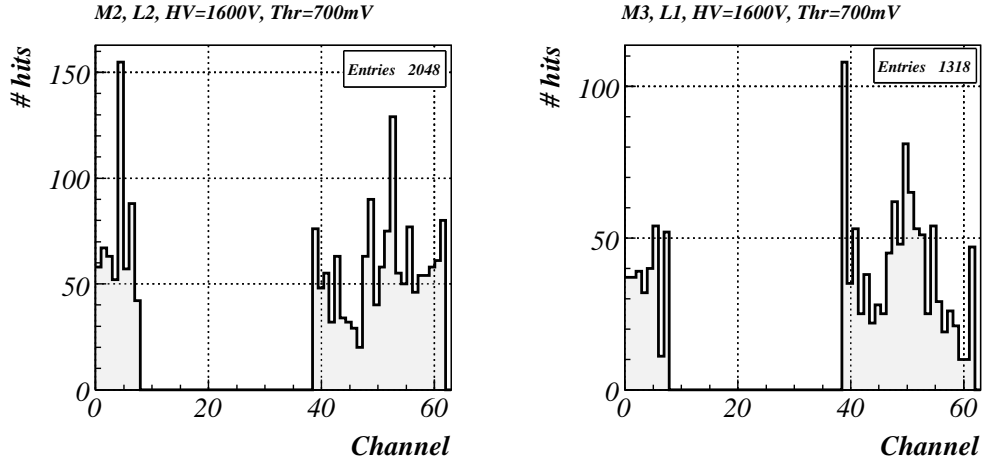


Figure 4.17. Noise maps of M2, L2 and M3, L1, representing the number of noise hits for the channels outside the beam region. The empty (beam) region is excluded from the noise study. The noise occupancy, \mathcal{O} , is of the order of 0.3% - 0.5%.

4.2.7 Cross Talk

Cross talk is a parameter that characterizes the signal coupling between adjacent channels (anode wires). Production of undesirable signals due to cross talk between the channels has to be minimized in order to ensure optimal performance of the detector. The cross talk per wire $P_{\text{cross},i}$ is the sum of the probabilities that when a straw i produces a hit caused by a beam particle, either of the two adjacent straws in the layer also produces a hit,

$$P_{\text{cross},i} = \frac{N_{i-1} + N_{i+1}}{N_i} . \quad (4.12)$$

Figure 4.18 shows the hit distribution of M3, L2, in the case that wire 104 has encountered a particle hit³. It is visible that the amount of hits collected by the two neighboring wires is an order of magnitude higher than the rest. This effect is attributed to cross talk.

The cross talk per layer was obtained by averaging the cross talk values of all the channels in the layer.

Results for the cross talk per layer as a function of the HV and amplifier threshold (Thr) are presented in Sec. 4.3.4 .

³The straw was considered hit by a particle, when in addition, a track reconstructed in the Si-telescope pointed to it.

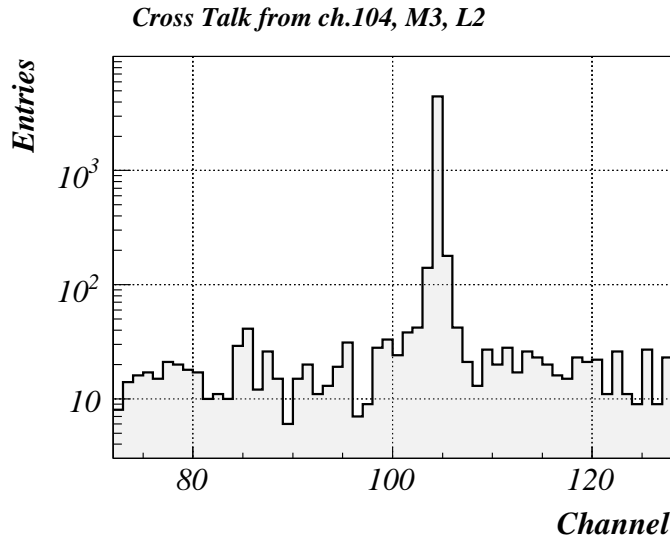


Figure 4.18. The straw hit map of M3, L2, for Si-telescope tracks pointing to wire 104, for HV=1600 V and Thr=700 mV. The two neighboring channels are subject to cross talk, resulting in an enhanced amount of encountered hits.

4.3 Results of the Beam Tests

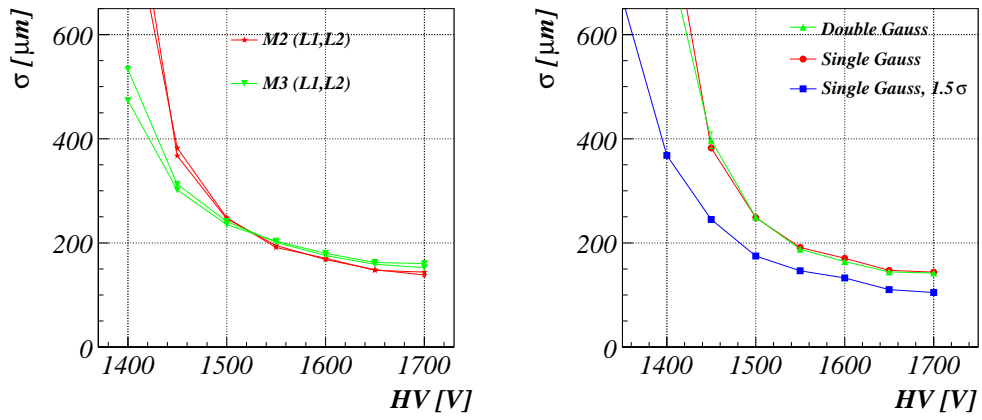
Here, we present the beam test results for the OT coordinate resolution, efficiency, noise and cross talk as a function of the applied high voltage (HV) and ASDBLR amplifier threshold setting (Thr).

4.3.1 Resolution

The coordinate resolution of the test OT modules, corrected for multiple scattering (see Sec. 4.2.4) is shown in Fig. 4.19a as a function of the HV. The resolution was obtained by fitting the residuals with a Gaussian function. At HV=1400 V, the resolution is large, due to large tails in the distribution, (see Fig. 4.13). This can be understood since the use of a single Gaussian function is not appropriate for fitting the residuals. The presence of these tails is probably due to the fact of forming the hit not from the first electron cluster, arriving to the anode. In Fig. 4.19b the resolution curves are shown, when using alternative fitting functions, namely, a single Gaussian fitted around the core of the residual within $\pm 1.5\sigma$ and a double Gaussian with $\sigma_{\text{double Gaussian}} \equiv \frac{c_1\sigma_1 + c_2\sigma_2}{c_1 + c_2}$ (with $c_{1,2}$ and $\sigma_{1,2}$, the heights and the widths of the constituent single Gaussians).

At high voltages (HV>1550 V) the OT coordinate resolution is better than the required value of 200 μm [52], independently of the choice of residual fitting function. Figure 4.20 shows the coordinate resolution as a function of amplifier threshold in

the working region 600 mV - 900 mV, roughly corresponding to 2.0 fC - 5.5 fC. The moderate worsening of the resolution ($\leq 50 \mu\text{m}$) is of negligible consequence for the physics performance.



(a) *OT resolution obtained fitting the residuals with a single Gaussian function.* (b) *OT resolution for M2, L1, obtained fitting the residuals with different functions.*

Figure 4.19. *OT coordinate resolution versus applied high-voltage, HV, at an amplifier threshold value of Thr=700 mV.*

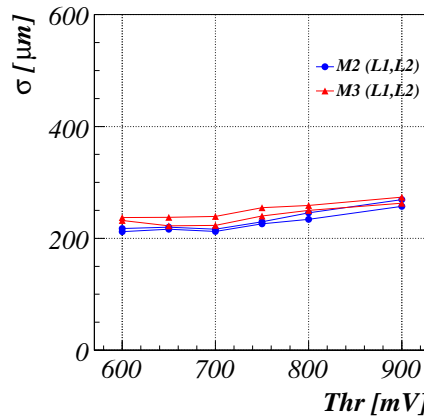
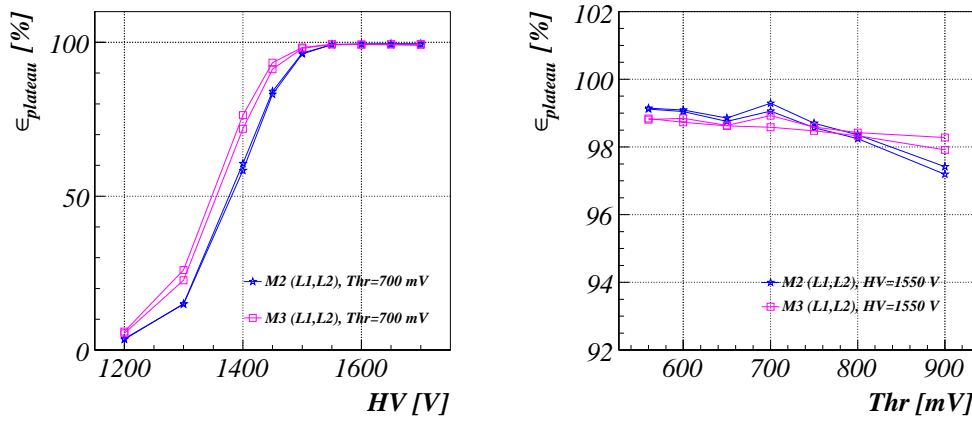


Figure 4.20. *OT coordinate resolution versus amplifier threshold, Thr, for high-voltage setting of HV=1550 V.*

4.3.2 Efficiency

The plateau efficiency of the OT test modules is shown in Fig. 4.21 as a function of HV and Thr. As expected, the efficiency slightly drops with increasing amplifier threshold. Full efficiency is reached at 1550 V and remains higher than 97% for threshold settings up to 900 mV.



(a) *OT efficiency versus HV at Thr=700 mV.* (b) *OT efficiency versus Thr for HV=1550 V.*

Figure 4.21. *OT efficiency as a function of the applied high-voltage, HV, and as a function of the amplifier threshold, Thr.*

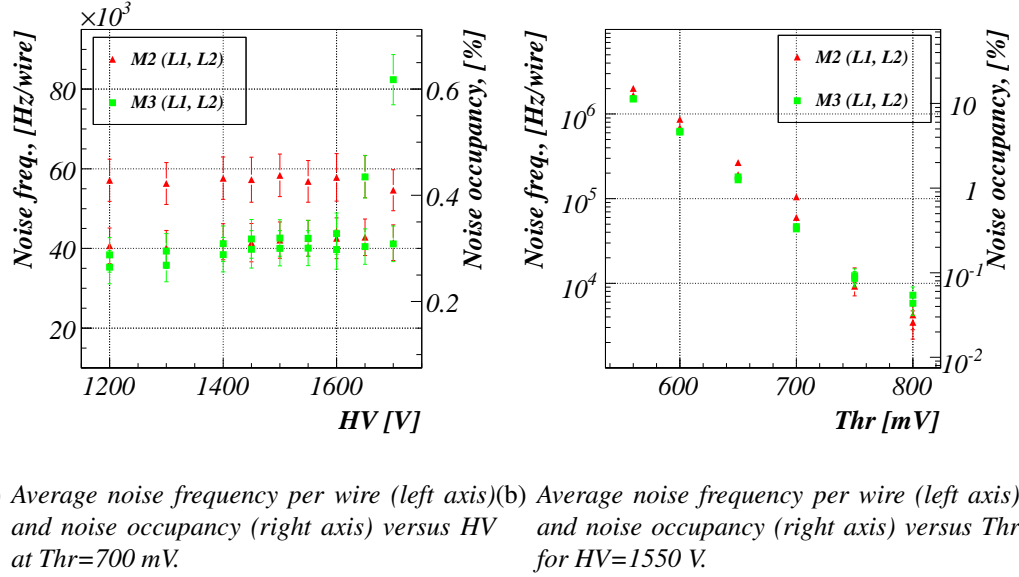
4.3.3 Noise

The average noise frequency per wire f , as a function of the applied high voltage is shown in Fig. 4.22a. The scale of the noise occupancy \mathcal{O} , is given at the right side of the plot. Both \mathcal{O} and f are constant and do not depend on HV. Module 2, L1 showed higher noise levels than the other straw layers.

Figure 4.22b shows f and \mathcal{O} values depending on the ASDBLR threshold setting. The observed dependence is exponential. At thresholds higher than 700 mV the noise level is acceptable [69].

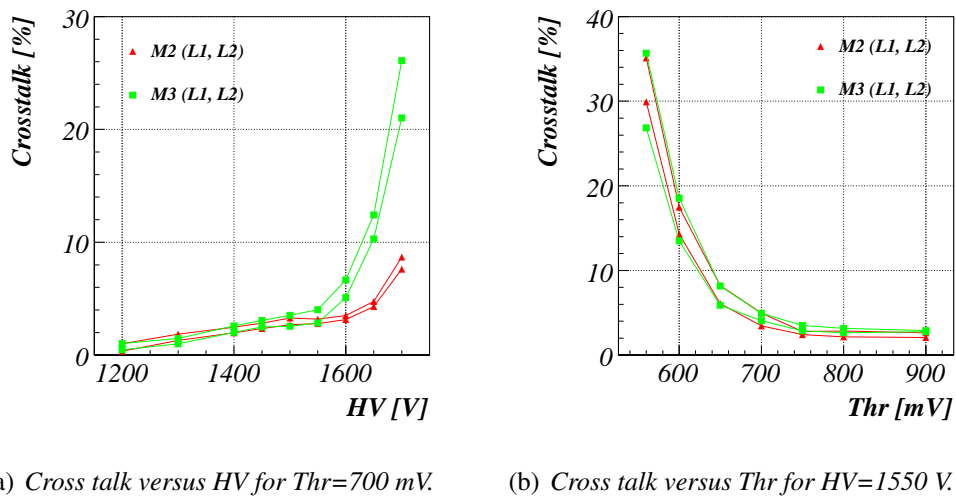
4.3.4 Cross Talk

The cross talk measured for different values of high voltage and amplifier threshold setting is presented in Fig. 4.23. According to the specifications [52], the acceptable cross talk level is below 10%. From the plots it is visible that this value is achieved at voltages below 1630 V and thresholds higher than 600 mV.



(a) Average noise frequency per wire (left axis) and noise occupancy (right axis) versus HV at $\text{Thr}=700$ mV.
(b) Average noise frequency per wire (left axis) and noise occupancy (right axis) versus Thr for $\text{HV}=1550$ V.

Figure 4.22. OT average noise frequency per wire, f , and noise occupancy, \mathcal{O} , as a function of applied high-voltage and amplifier threshold.



(a) Cross talk versus HV for $\text{Thr}=700$ mV.
(b) Cross talk versus Thr for $\text{HV}=1550$ V.

Figure 4.23. OT crosstalk as a function of applied high-voltage and amplifier threshold.

4.4 Summary

OT beam tests were carried out in the beginning of 2005 at DESY laboratory, with an electron beam of 6 GeV. OT modules of type S1U were used, equipped with the final version of the front-end electronics. Four basic detector macro parameters, namely the spatial resolution, the efficiency, the noise level and the cross talk were measured for different values of the applied high voltage and amplifier threshold settings. The examined OT modules showed satisfactory performance, as the values of the measured parameters were within the desired specifications limits.

1. Coordinate resolution better than $200 \mu\text{m}$ for $\text{HV} \geq 1550 \text{ V}$ and $\text{Thr} = 700 \text{ mV}$;
2. High efficiency $\sim 98\%$, reached at $\text{HV} \geq 1550 \text{ V}$ for $\text{Thr} \in [550, 800] \text{ mV}$;
3. Admissible noise level $\leq 10 \text{ kHz/wire}$ for $\text{Thr} > 750 \text{ mV}$, independent of the HV;
4. Acceptable cross talk $< 10\%$ for $\text{HV} < 1630 \text{ V}$ and $\text{Thr} > 600 \text{ mV}$.

The reported results evidence that the OT performance is optimal, and meets the design criteria, when the applied high voltage is in the range $1550 - 1650 \text{ V}$ and the ASDBLR threshold setting is in the range $700 - 800 \text{ mV}$.

An alternative analysis performed on the same beam test data (see Ref. [65, 70]) confirmed the results exposed here.

Chapter 5

Proper-Time Resolution Modeling

All models are wrong. Some are useful.

George E. P. Box (1919)

This chapter reports on a study [71] of the resolution of the proper-time of the B^0 and B^+ mesons. The decay modes used are $B^+ \rightarrow J/\psi(\mu^+\mu^-)K^+$ and $B^0 \rightarrow J/\psi(\mu^+\mu^-)K^*(K^+\pi^-)$ and their conjugates. A resolution model based on the proper-time residuals and the corresponding per-event error is proposed and results are presented on the two decay modes studied.

5.1 Introduction

The main goal of the study presented here is to derive a reliable *resolution model*, which is able to describe with sufficient precision the distribution of the decay time residuals: $t_{rec}^i - t_{true}^i$, taking into account the B mesons proper-time per-event-errors, $\sigma_{t_{rec}}^i$, measured with the LHCb experiment. The resolution of the proper-time is an important ingredient in the measurement of time-dependent (CP) asymmetries, especially in the decay of the rapidly oscillating B_s meson. Thereby, we need to model its behavior as good as possible.

The parameters of our model are first determined with "Monte-Carlo truth" information for $t_{rec}^i - t_{true}^i$. Then, later in this chapter, the parameters are determined in a manner that can be applied to real data by using t_{rec}^i and $\sigma_{t_{rec}}^i$.

Two b -flavored mesons (B^+ and B^0) are chosen to be analyzed. The B^+ is selected and reconstructed in the mode $B^+ \rightarrow J/\psi(1S)K^+$, where $J/\psi(1S)$ decays into μ^+ and μ^- . The B^0 meson is reconstructed in the mode $B^0 \rightarrow J/\psi(1S)K^*(892)$, with $J/\psi(1S) \rightarrow \mu^+\mu^-$, and $K^*(892) \rightarrow K^+\pi^-$. The complex conjugated modes are also considered¹. Both B mesons decay through a tree-level diagram, as is shown

¹ $B^- \rightarrow J/\psi(1S)K^-$ with $J/\psi(1S) \rightarrow \mu^+\mu^-$ and $\overline{B^0} \rightarrow J/\psi(1S)\overline{K^*(892)}$ with $J/\psi(1S) \rightarrow \mu^+\mu^-$, $\overline{K^*(892)} \rightarrow K^-\pi^+$; Unless otherwise noted, charge conjugated modes are implicitly considered throughout this chapter.

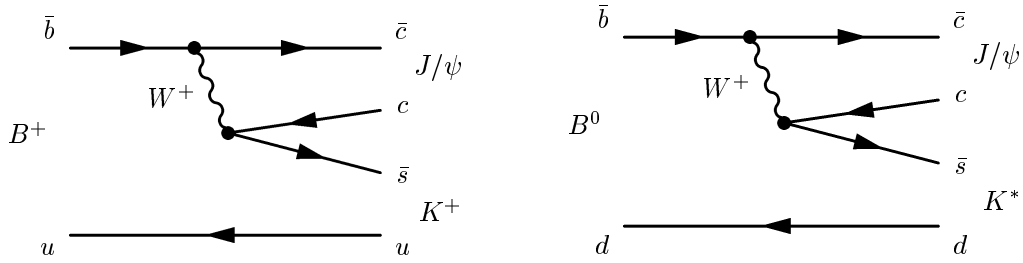


Figure 5.1. Feynman diagrams for the $B^+ \rightarrow J/\psi K^+$ and $B^0 \rightarrow J/\psi K^*$ decays.

in Fig. 5.1. The reason to explore these particular channels is two-fold:

- ◊ Among the interesting B meson decay channels, these channels have the highest expected annual signal yield [40]. The high event statistics ensures fast data collection. Therefore, the two decay modes will be among the first ones to be reconstructed once the LHCb detector is operational.
- ◊ The di-muon pair in the final state allows these channels to be efficiently triggered and selected. Accordingly, there is no need for impact parameter cuts, which distort the proper-time distribution.

As a result, these channels are expected to be excellent *control channels* to study the detector response, and to obtain a resolution model which, hopefully, can also be used for other B meson decay modes.

The chapter is organized as follows:

Section 5.2 contains a brief description of the software framework and the data set used. In Sec. 5.3 the method to select $B^+ \rightarrow J/\psi K^+$ and $B^0 \rightarrow J/\psi K^*$ is discussed. In Sec. 5.4 the construction of a resolution model is presented and applied to the data. The determination of the resolution model parameters on *real* data is described in Sec. 5.5 and results are presented. Section 5.6 focuses on the dependence of the resolution model on the true proper-time t_{true} . An explanation of this discovered effect is given and a way to resolve it is proposed. The solution is based on a redefinition of the primary vertex (PV) position by exclusion of the B decay products from the PV reconstruction. The chapter finishes in Sec. 5.7 with summary and conclusions.

5.2 Software and Data

The data used for the analysis are produced at the CERN's computer cluster *lxplus*, as a part of the so called Data Challenge 2004, also known as the DC'04 dataset. This dataset includes various event types, generated under the same conditions (detector geometry description, reconstruction algorithms, etc.). For the production of

the data GAUSS [72] v15r8, BOOLE [73] v5r8 and BRUNEL [74] v23r7 are used, while DAVINCI [75] v12r18 is used for the selection and analysis. The files with the reconstructed data are stored at CERN in the form of DST² files. These files are the input for the DAVINCI program. For the current study, only $B^+ \rightarrow J/\psi K^+$ and $B^0 \rightarrow J/\psi K^*$ signal samples are used. This implies that each event contains one B meson which decays into the signal modes. The effect of the inclusion of background is part of a follow-up study, presented in Chapter 6.

About 2×10^6 signal events were subject to selection and analysis.

5.3 Event Selection

The topologies of $B^+ \rightarrow J/\psi K^+$ and $B^0 \rightarrow J/\psi K^*$, shown in Fig. 5.2 are similar, with one distinguishable secondary vertex - the B meson decay vertex.

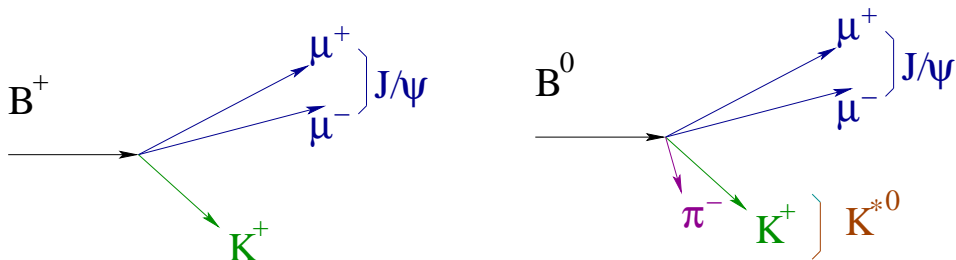


Figure 5.2. Topologies for $B^+ \rightarrow J/\psi K^+$ and $B^0 \rightarrow J/\psi K^*$ decays.

The J/ψ and K^* resonances have extremely short life-times ($\sim 10^{-23}$ seconds) and hence do not generate displaced vertices with respect to their production point.

The events are selected and reconstructed by first reconstructing the $J/\psi(1S) \rightarrow \mu^+ \mu^-$, then the $K^*(892) \rightarrow K^+ \pi^-$, and finally the $B^+ \rightarrow J/\psi(1S) K^+$ and $B^0 \rightarrow J/\psi K^*$ mesons. This is accomplished with the following procedure:

- ◊ The $J/\psi(1S)$ selection and reconstruction is identical for both channels. The $J/\psi(1S)$ candidates are reconstructed by combining two oppositely charged muons with $p_T > 1000$ MeV/c and requiring their invariant mass to be within a ± 50 MeV/c² window around the nominal $J/\psi(1S)$ mass. A quality criterion of $\chi^2 < 9$ for the J/ψ vertex fit is applied.

$B^+ \rightarrow J/\psi(1S) K^+$ decay:

- ◊ The B^+ candidates are reconstructed from the selected J/ψ candidates and the charged kaons. The B^+ candidate invariant mass is required to be within a ± 50 MeV/c² mass window around the nominal B^+ mass, see Fig. 5.3. A quality criterion of $\chi^2 < 20$ for the B^+ vertex fit is applied.

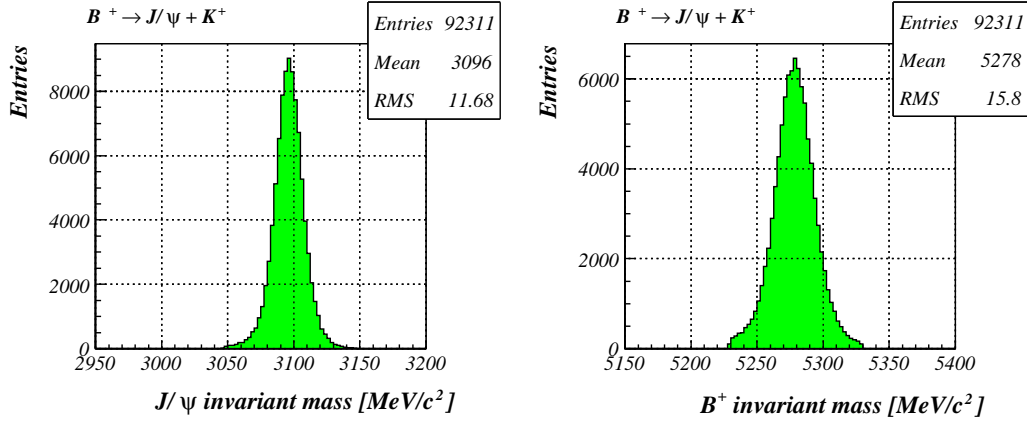


Figure 5.3. Reconstructed invariant mass distribution for $J/\psi(1S) \rightarrow \mu^+\mu^-$ and for $B^+ \rightarrow J/\psi K^+$.

$B^0 \rightarrow J/\psi(1S)K^*(892)$ decay:

- ◊ The $K^*(892)$ candidates are reconstructed from the identified K^+ and π^- . The $K^*(892)$ candidate must have a $p_T > 1000$ MeV/c, and its invariant mass is required to be within a ± 150 MeV/c² window around the $K^*(892)$ mass. A quality criterion of $\chi^2 < 9$ for the vertex fit is applied.
- ◊ The B^0 candidates are reconstructed based on the selected J/ψ and K^* candidates. The invariant mass of the B^0 candidate is required to be within ± 50 MeV/c² of the expected B^0 mass; see Fig. 5.4. A quality criterion of $\chi^2 < 27$ for the B^0 vertex fit is applied.

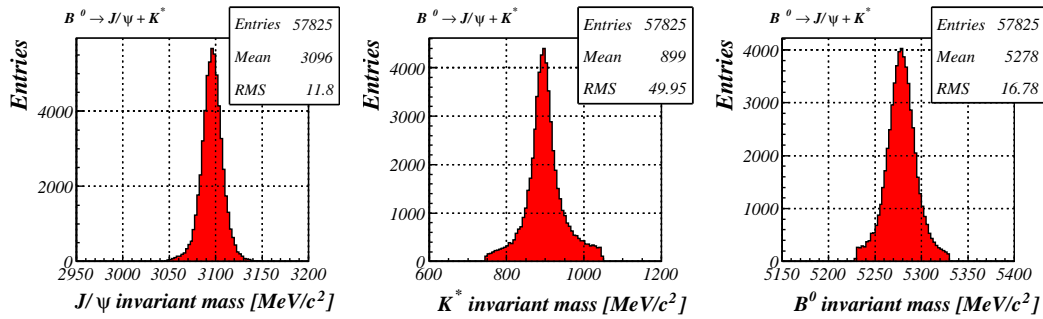


Figure 5.4. Reconstructed invariant mass distribution for $J/\psi(1S) \rightarrow \mu^+\mu^-$, for $K^* \rightarrow K^+\pi^-$ and for $B^0 \rightarrow J/\psi(1S)K^*(892)$.

²Data Summary Tapes.

Given that the signal yield is expected to be a limiting factor, we decided to keep the selection procedure simple and only accept those events which contain a single reconstructed B candidate. At the price of losing data by rejecting higher multiplicity events, better selection stability and a decreased number of mis-reconstructed B candidates are achieved. The results from the event selection are summarized in Table 5.1.

channel	# Generated Events	# Selected Events
$B^+ \rightarrow J/\psi K^+$	684000	92311
$B^0 \rightarrow J/\psi K^*$	960000	57825

Table 5.1. *Event Selection - Results.*

To check whether the selection introduces a bias on the proper-time distribution, we have plotted the Monte-Carlo true proper decay time for both channels and fitted these with the expected exponential distribution $e^{\Gamma_B t_{true}}$, as shown in Fig. 5.5 and Fig. 5.6. It is apparent that no large bias is present and the proper-time acceptance is flat to a good approximation. The values of the mean B lifetimes $\tau_B = -1/\Gamma_B$ are extracted from the fits and should match those of the input MC values, see Table 5.2.

MC inputs	Fit outputs
$\tau_{B^+}^{\text{MC}} = 1.671$ [ps]	$\tau_{B^+} = 1.695 \pm 0.006$ [ps]
$\tau_{B^0}^{\text{MC}} = 1.536$ [ps]	$\tau_{B^0} = 1.523 \pm 0.006$ [ps]

Table 5.2. *B^+ and B^0 mean lifetimes.*

The small discrepancy observed is not completely understood, but could be a hint of a small bias in either the event selection itself or in its inputs, *e.g.* the reconstruction efficiencies.

To indicate the quality of the exponential fit of the true proper-times in Fig. 5.5 and Fig. 5.6, the fit *Residuals* and the fit *Pulls* are given. The *Residual* and *Pull* from the fit are defined as

$$\text{Residual}(t_{true}) = \text{data}(t_{true}) - \text{fit}(t_{true}) , \quad (5.1)$$

$$\text{Pull}(t_{true}) = \frac{\text{data}(t_{true}) - \text{fit}(t_{true})}{\text{data}(t_{true})_{\text{error}}} . \quad (5.2)$$

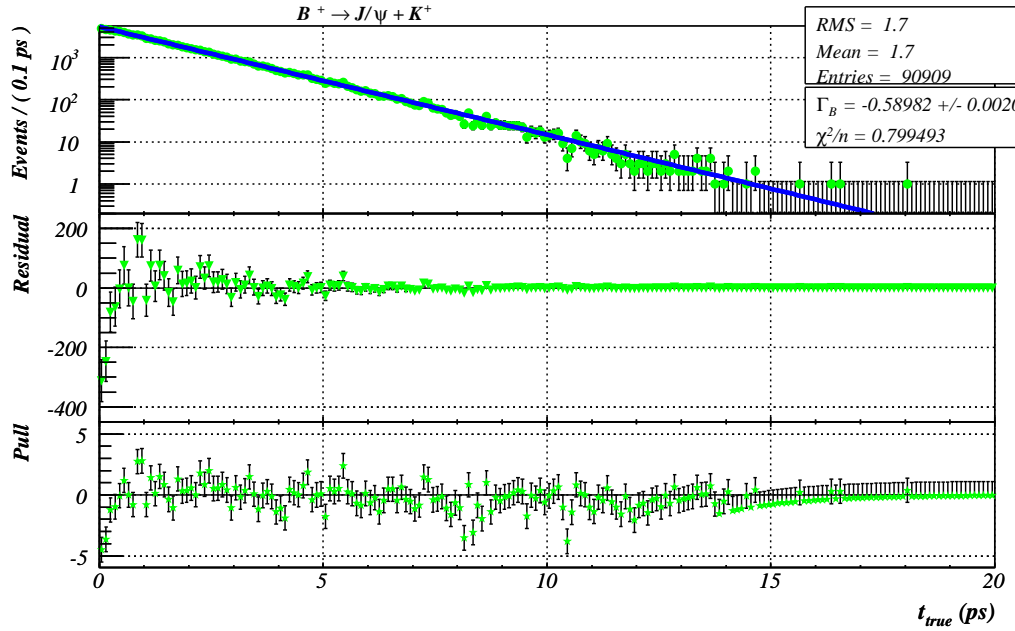


Figure 5.5. The MC true proper decay times fitted with an exponential function, the corresponding fit residuals and pulls for channel $B^+ \rightarrow J/\psi(1S)K^+$.

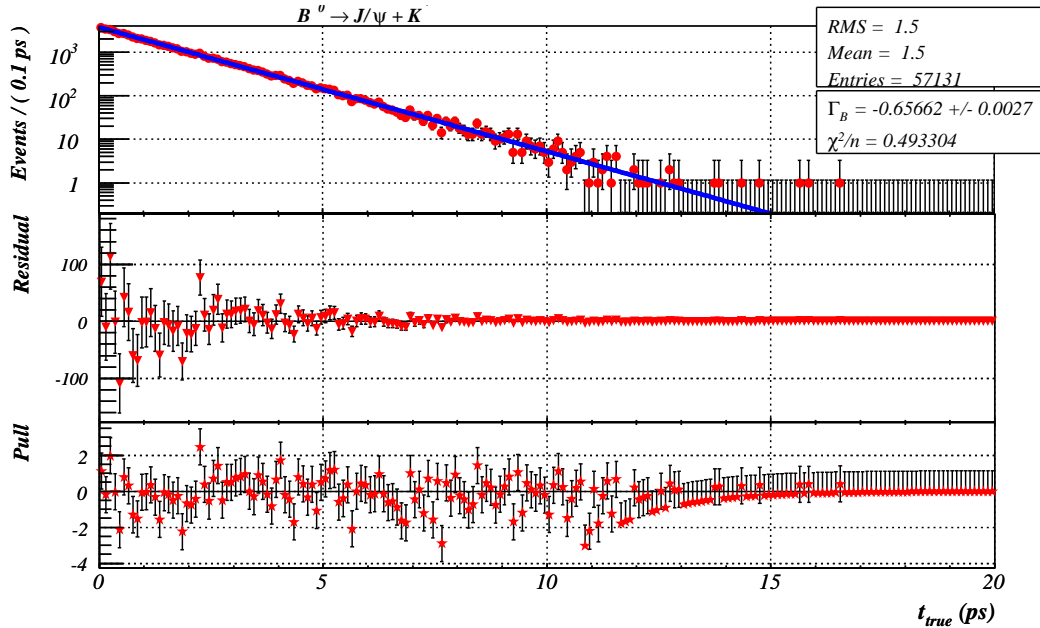


Figure 5.6. The MC true proper decay times fitted with an exponential function, the corresponding fit residuals and pulls for channel $B^0 \rightarrow J/\psi(1S)K^*$.

5.4 Resolution Model

The aim of this section is to describe in detail the ingredients of the resolution model. In Sec. 5.4.1 the reconstruction of the proper-time is presented. The basic resolution model is derived in Sec. 5.4.2. Section 5.4.3 shows how the proper-time per-event errors are included in this model. Next, the determination of how the parameters of the model depend on these per-event errors is explained in Sec. 5.4.4. Section 5.4.5 describes how the parameters of the resolution model are obtained with an unbinned maximum likelihood fit.

The main software packages used in the analysis are ROOFIT [76] - a tool for modeling the expected distribution of events in a physics analysis and ROOT [77] - a data analysis framework.

5.4.1 Proper-Time Reconstruction

The reconstructed proper-time t_{rec} of a B candidate, together with the estimated error, is obtained from a constrained χ^2 fit described in Ref. [78]. Ingredients of the fit are the measured primary vertex position \vec{x} (the production point), the measured decay vertex position \vec{v} and the measured momentum \vec{p} of the B meson. These nine observables, $\mathcal{O} = (\vec{v}, \vec{p}, \vec{x})$, are the input for the fit and, in the absence of detector resolution effects, are related by the following constraint,

$$\vec{x} = \vec{v} - t \frac{\vec{p}}{m} , \quad (5.3)$$

where t is the B proper-time.

As a result, seven parameters \mathcal{P} are needed to describe the system: the three components of the reconstructed decay point \vec{v} , the reconstructed momentum \vec{p} and the reconstructed proper-time t_{rec} , thus $\mathcal{P} = (\vec{v}, \vec{p}, t_{rec})$. It is assumed that the primary vertex and the particle are independent (i.e. that none of the daughters of the particle were used in the determination of the primary production vertex). The seven parameters \mathcal{P} are determined by minimizing the following χ^2 ,

$$\chi^2(\mathcal{P}) = \mathcal{R}^T W_{\mathcal{O}} \mathcal{R} , \quad (5.4)$$

where \mathcal{R} are the residuals between the measurements \mathcal{O} and their prediction based on the parameters \mathcal{P} , and $W_{\mathcal{O}}$ is the weight matrix corresponding to the observables \mathcal{O} . $W_{\mathcal{O}}$ takes into account the correlation between \vec{v} and \vec{p} provided the vertex algorithm that determined \vec{v} and \vec{p} has computed this correlation. It is assumed that there is no correlation between \vec{v} and \vec{p} on the one hand, and \vec{x} on the other. The errors on \mathcal{P} are given by the second order derivatives of the χ^2 with respect to \mathcal{P} at the minimum.

As the proper-time t_{rec} is one of the parameters \mathcal{P} , the fit, by construction, computes an error $\sigma_{t_{rec}}$ for each reconstructed B decay time - t_{rec} . As a result of this procedure, this error takes into account the specified correlations amongst the inputs.

This error is called the proper-time per-event-error or simply the per-event-error. The distributions of the per-event-errors for the channels of interest are shown in Fig. 5.7. The B^0 decay mode has a smaller mean $\sigma_{t_{rec}}$ than the B^+ mode, which is due to the fact that the B^0 vertex is reconstructed with four tracks, while the B^+ vertex is reconstructed with only three (see Fig. 5.2). As a result the position of the B^0 vertex is determined more precisely, hence the decay length is better defined and thus the proper-time uncertainty is smaller.

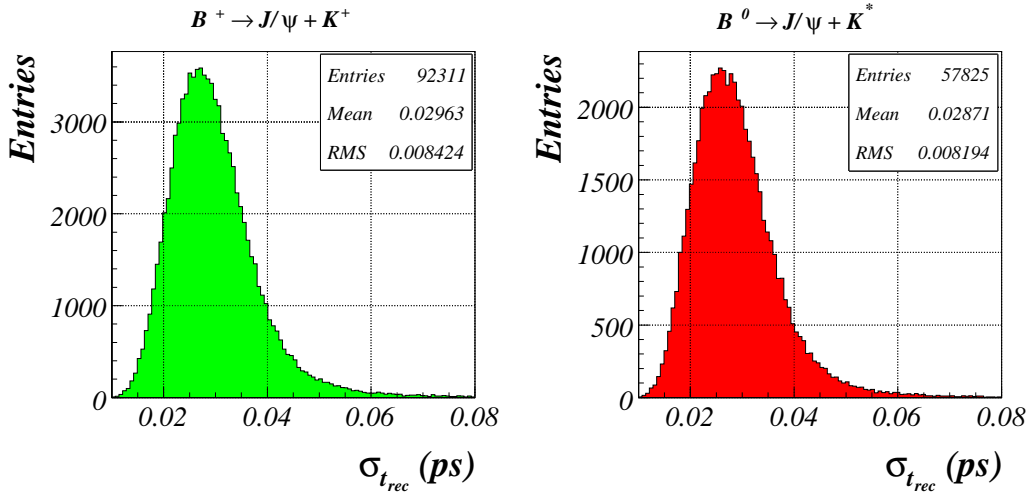


Figure 5.7. Proper-time per-event-error distributions.

In Sec. 5.6.3 we will refit the primary vertex, explicitly excluding the tracks originating from the B ³.

5.4.2 Resolution Model

A proper-time resolution model $R(x)$ is a mathematical construction which describes the distribution of the decay time residuals: $x^i = t_{rec}^i - t_{true}^i$, taking into account the per-event-errors. Ideally, with a perfectly described detector response, $R(x)$ is represented by a Gaussian,

$$R(t_{rec} - t_{true}, \sigma_{t_{rec}}) = \frac{e^{-\frac{1}{2}\left(\frac{t_{rec}-t_{true}}{\sigma_{t_{rec}}}\right)^2}}{\sqrt{2\pi}\sigma_{t_{rec}}} . \quad (5.5)$$

³The tracks from the tagging B , or any other long-lived resonances, cannot explicitly be excluded as they are not fully reconstructed. However, the bias introduced by the possible inclusion of these tracks is modeled and determined implicitly, and as a result does not bias the measurements. This is fundamentally different from the case where tracks from the signal are (re)used in the primary vertex, an effect that is more likely for short-lived B mesons. In this case, the bias depends on the true proper-time t_{true} , and this is *not* modeled as it is at this point unknown how one would determine such a bias without knowledge of t_{true} , *i.e.* for real data.

However, in real life, the function $R(x)$ typically takes a more complicated form. In order to understand the detector response, $R(x)$ needs to be determined. Knowledge of $R(x)$, in combination with sufficiently good resolution, is a necessary ingredient for time-dependent CP asymmetry measurements given that the oscillation amplitude decreases when the resolution degrades.

A natural suggestion for a realistic $R(x)$ function is a sum of Gaussians with different fractions,

$$R(x = t_{rec} - t_{true}) = \frac{N}{\sqrt{2\pi}} \left[(1 - f_1) \frac{e^{-\frac{1}{2}\left(\frac{x-M_1}{S_1}\right)^2}}{S_1} + f_1 \frac{e^{-\frac{1}{2}\left(\frac{x-M_2}{S_2}\right)^2}}{S_2} \right], \quad (5.6)$$

where M_1, M_2 represent biases to the reconstructed time.

Our first try was based on an analysis with the model described in Eq. (5.6). In due process we modified $R(x)$ into

$$R(x = t_{rec} - t_{true}) = \frac{N}{\sqrt{2\pi}} \left[(1 - f_1 - f_2) e^{-\frac{1}{2}\left(\frac{x-M}{S}\right)^2} + f_2 e^{-\frac{1}{2}\left(\frac{x}{S_{fixed}}\right)^2} + f_1 \left(e^{-\frac{1}{2}\left(\frac{x}{S}\right)^2} \otimes e^{-\left(\frac{x}{\tau}\right)} \right) \right], \quad (5.7)$$

which provides a better description of the observed residuals.

Now, $R(x)$ consists of three terms with different fractions defined by the fraction parameters f_1 and f_2 . The first term is a Gaussian of mean M and width S . The second term is a Gaussian of mean zero and width S_{fixed} , where S_{fixed} is not a free parameter but a fixed number, set to 10 ps, to describe the wide tails of the distribution. The third term is a Gaussian with mean 0 and sigma S convolved⁴ with an exponent with a base of $-\tau^{-1}$. This term is added to allow for a modified exponential decay time distribution. It describes the fact that there is a non negligible chance that the primary vertex position is biased in the downstream direction due to the inclusion of tracks from long(er) lived resonances, which causes a bias in the reconstructed proper-time towards smaller values. There are five free parameters in this model - $(M, S, f_1, f_2, \tau) = \vec{p}$. The question is how to determine these parameters.

5.4.3 The Per-Event-Errors

So far, constructing the resolution model we did not take into account the observed per-event-errors. In a perfect detector the width of the resolution function, for a given event, is expected to be determined by this per-event error. Accordingly, we

⁴The convolution, $C(x, a, b)$, of two functions $f(x, a)$ and $g(x, b)$ is written as $f(x, a) \otimes g(x, b)$.

By definition, $C(x, a, b) \equiv \int_{-\infty}^{+\infty} f(y, a)g(x - y, b)dy$.

make our model conditional on the per-event-error by substituting the width by the observed per-event error and by weighing it with a pdf describing the per-event-errors - $P(\sigma_{t_{rec}})$ [71],

$$\mathcal{R}(t_{rec} - t_{true}, \sigma_{t_{rec}}) = R(t_{rec} - t_{true} \mid \sigma_{t_{rec}}) \times P(\sigma_{t_{rec}}) . \quad (5.8)$$

The $P(\sigma_{t_{rec}})$ is constructed through a technique called *kernel estimation*, "KEYS". The best possible probability density function that aims to describe the $\sigma_{t_{rec}}$ parent distribution is obtained via a superposition of Gaussians, centered on the observed values. Note that this pdf does not have any free parameters. For more details see Ref. [79]. The implementation of this algorithm in a C++ program has been realized with the help of the ROOKEYSPDF class, which is a part of ROOFIT package.

The $\sigma_{t_{rec}}$ distributions are given in Fig. 5.8, superimposed with the pdf's $P(\sigma_{t_{rec}})$, as obtained with ROOKEYSPDF.

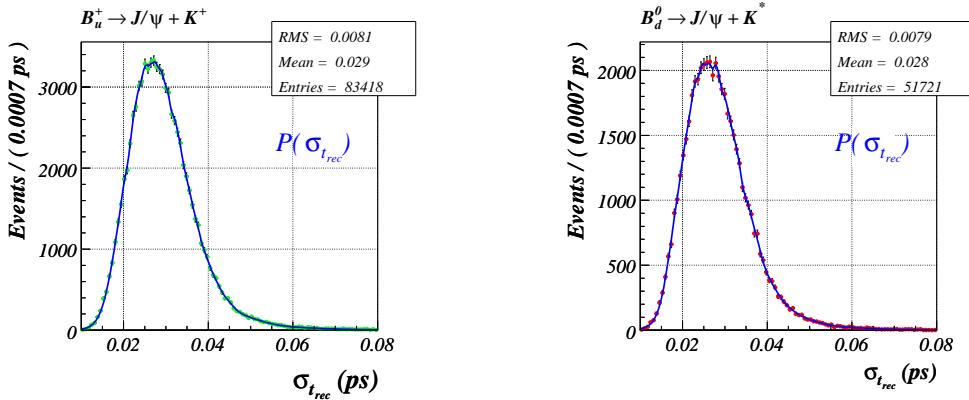


Figure 5.8. The $\sigma_{t_{rec}}$ distributions for both channels, as in Fig. 5.7, but now with superimposed RooKeysPdf's.

5.4.4 Determination of the Resolution Model Parameters

The method used for extracting the resolution model parameters is characterized by the following:

- ◊ 1) The per-event-error distribution $[\sigma_{t_{rec}}]$, shown in Fig. 5.7, is sliced into N bins. The bin interval is chosen such that an equal amount of entries fall inside each bin. For each slice k the average $\langle \sigma_{t_{rec}}(k) \rangle$ is calculated.
- ◊ 2) For each $\sigma_{t_{rec}}^i \in$ given bin k , the residual $x^i = t_{rec}^i - t_{true}^i$ is calculated, plotted and fitted with the function $R(x; \vec{p})$ given by Eq. (5.7). From the fits we get back $5 \times N$ different parameters, describing the residual distribution in each $\sigma_{t_{rec}}$ slice, as is shown in Fig. 5.9.

- ◊ 3) The N sets of parameters \vec{p}_k , extracted from the local slice fit, are expressed as a function of $\langle \sigma_{t_{rec}}(k) \rangle$, $\vec{p} = \vec{p}(\langle \sigma_{t_{rec}}(k) \rangle)$ and fitted in turn, see Fig. 5.10. The fitting functions are chosen to be $f(x) = p_0$ and $f(x) = p_0 + p_1 x$ ⁵:

$$M(\langle \sigma_{t_{rec}} \rangle) = p_1^M \langle \sigma_{t_{rec}} \rangle , \quad (5.9)$$

$$S(\langle \sigma_{t_{rec}} \rangle) = p_1^S \langle \sigma_{t_{rec}} \rangle , \quad (5.10)$$

$$f_1(\langle \sigma_{t_{rec}} \rangle) = p_0^{f_1} , \quad (5.11)$$

$$f_2(\langle \sigma_{t_{rec}} \rangle) = p_0^{f_2} , \quad (5.12)$$

$$\tau(\langle \sigma_{t_{rec}} \rangle) = p_1^\tau \langle \sigma_{t_{rec}} \rangle . \quad (5.13)$$

At the end of this step the parameters $p_1^M, p_1^S, p_0^{f_1}, p_0^{f_2}, p_1^\tau$ are determined (for example, we observe, as expected, that the Gaussian width S increases linearly with increasing $\langle \sigma_{t_{rec}} \rangle$).

- ◊ 4) Since \vec{p} depends on $\sigma_{t_{rec}}$ (more precisely on $\langle \sigma_{t_{rec}} \rangle$), Eq. (5.7) can be rewritten as

$$\begin{aligned} R(x) = \frac{N}{\sqrt{2\pi}} & \left[(1 - f_1(\sigma_{t_{rec}}) - f_2(\sigma_{t_{rec}})) e^{-\frac{1}{2} \left(\frac{x-M(\sigma_{t_{rec}})}{S(\sigma_{t_{rec}})} \right)^2} \right. \\ & + f_2(\sigma_{t_{rec}}) e^{-\frac{1}{2} \left(\frac{x}{S_{fixed}} \right)^2} \\ & \left. + f_1(\sigma_{t_{rec}}) \left(e^{-\frac{1}{2} \left(\frac{x}{S(\sigma_{t_{rec}})} \right)^2} \otimes e^{-\left(\frac{x}{\tau(\sigma_{t_{rec}})} \right)} \right) \right] . \end{aligned} \quad (5.14)$$

Next, we use relations Eq. (5.9) - Eq. (5.13), and find that $R(x)$ depends only on $p_1^M, p_1^S, p_0^{f_1}, p_0^{f_2}, p_1^\tau$ ⁶, which were determined in the previous step. That means that we now have a resolution model with a limited number of parameters.

- ◊ 5) Now that the dependence on $\sigma_{t_{rec}}$ is chosen and included into the model, the remaining few parameters can be determined in one single, two-dimensional, unbinned maximum likelihood fit to

$$(t_{rec}^1 - t_{true}^1, \sigma_{t_{rec}^1}), (t_{rec}^2 - t_{true}^2, \sigma_{t_{rec}^2}), \dots, (t_{rec}^N - t_{true}^N, \sigma_{t_{rec}^N}) , \quad (5.15)$$

where the suffix $1, 2, \dots N$ represents the i -th event, by maximizing:

$$\log \mathcal{L} = \sum_{i=1}^N \log R(t_{rec}^i - t_{true}^i, \sigma_{t_{rec}^i} | GM, GS, F1, F2, TAU) . \quad (5.16)$$

The parameters thus extracted are compared to the ones defined from the variation of the parameters determined on the various slices in the next section.

⁵Note that f_1 and f_2 were fitted with a function $f(x) = p_0$, while M , S and τ are fitted with $f(x) = p_0 + p_1 x$. In the latter case, the parameter p_0 was neglected in the subsequent analysis, since it was found to be close to 0.

⁶Further on, we use the notation $p_1^M \equiv GM$, $p_1^S \equiv GS$, $p_0^{f_1} \equiv F1$, $p_0^{f_2} \equiv F2$ and $p_1^\tau \equiv TAU$.

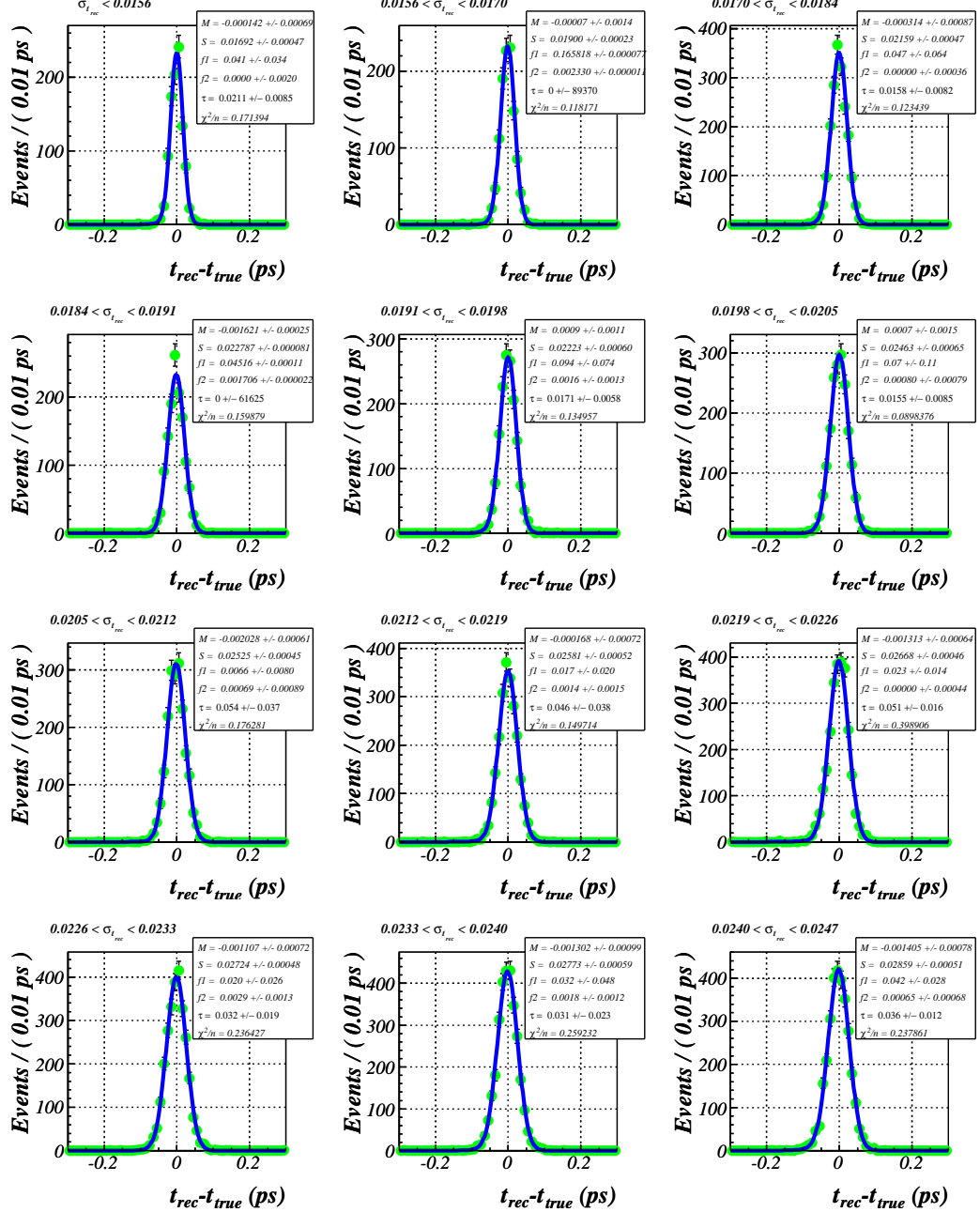


Figure 5.9. The $R(x)$ -fitted residual distributions for different slices of $\sigma_{t_{rec}}$. For each slice a different set of parameters is produced. The fit is based on Eq. (5.7), i.e. without using a $\sigma_{t_{rec}}$ dependence of the fit parameters. The decay channel is $B^+ \rightarrow J/\psi K^+$.

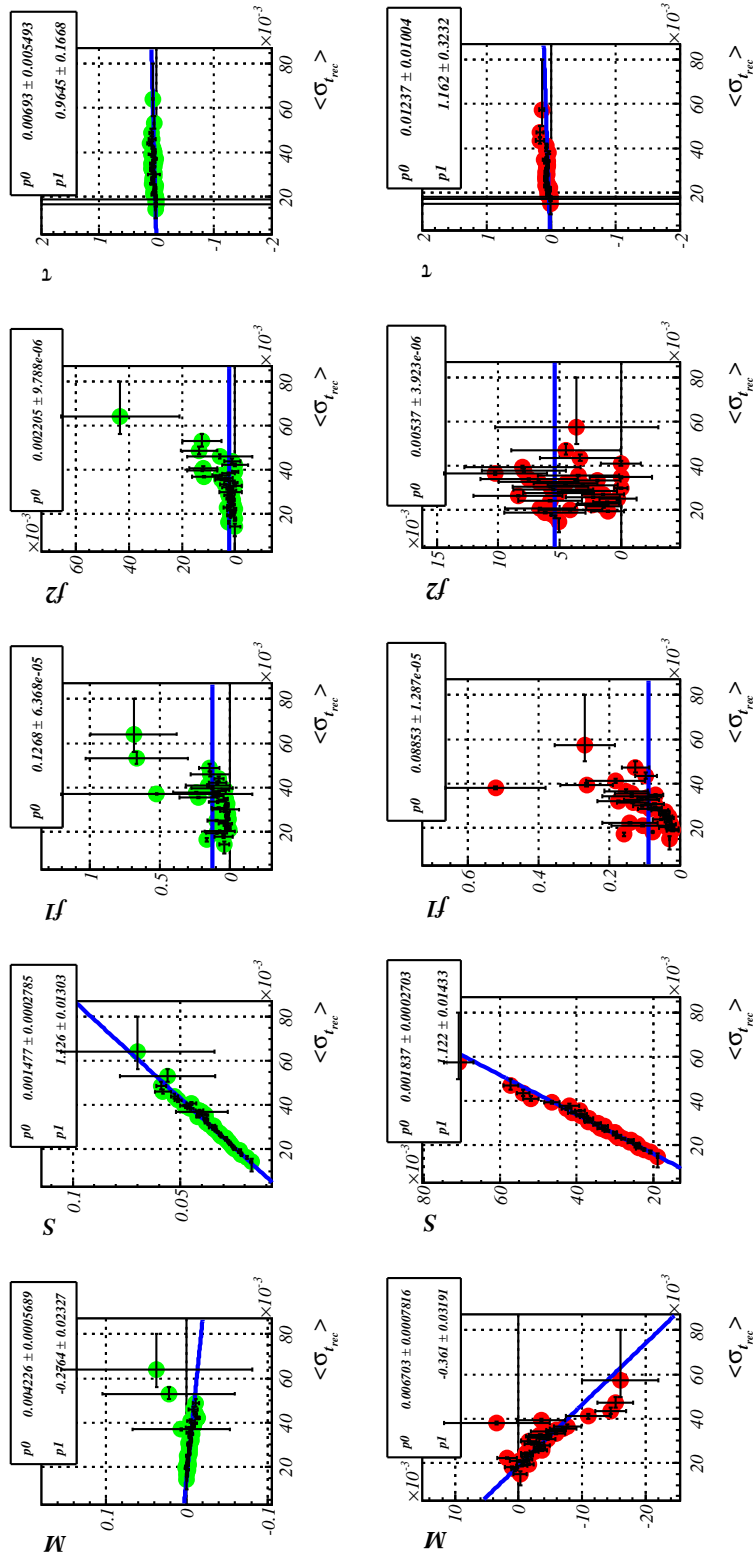


Figure 5.10. The extracted $R(x)$ parameters as a function of $\langle\sigma_{t_{rec}}\rangle$. Up: $B^+ \rightarrow J/\psi K^+$, Down: $B^0 \rightarrow J/\psi K^*$.

5.4.5 Validation of the Model

To validate the resolution model, an unbinned maximum likelihood fit to the data points in accordance with Eq. (5.15) is done. Plots in 2D and 3D revealing the $(t_{rec}^i - t_{true}^i)$ versus $\sigma_{t_{rec}^i}$ dependence are displayed in Fig. 5.11.

The projection of the fit on the $(t_{rec} - t_{true})$ axis can be expressed with

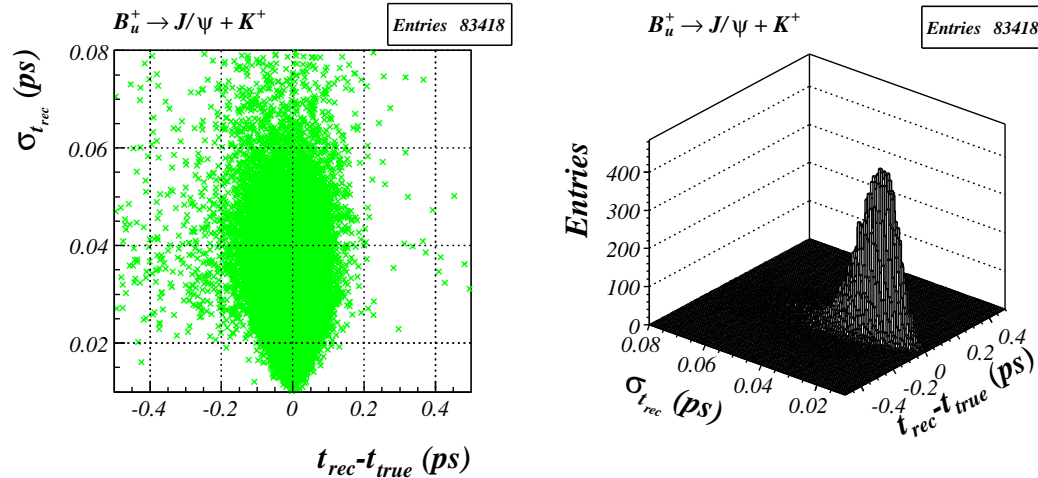
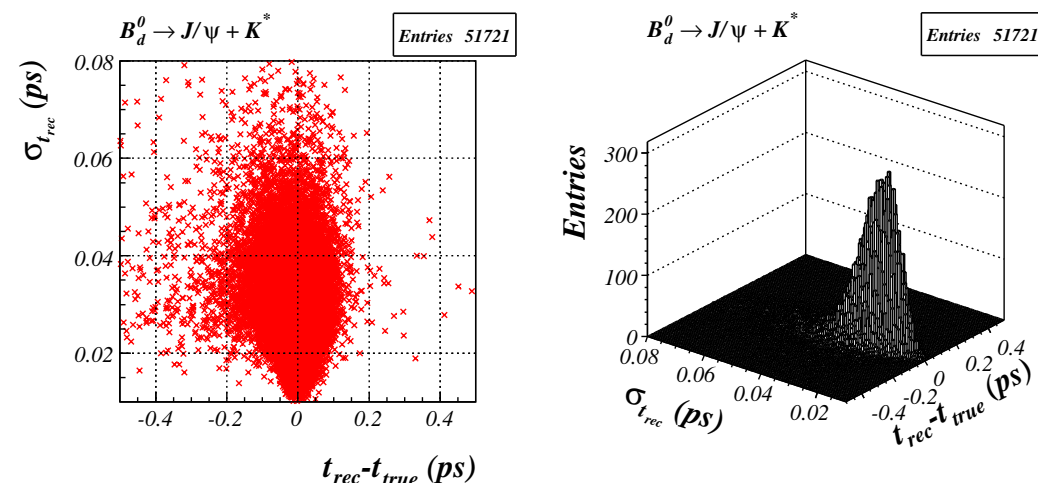
$$\mathcal{R}(t_{rec} - t_{true})_{proj} = \int_0^\infty d\sigma_{t_{rec}} R(t_{rec} - t_{true} | \sigma_{t_{rec}}) \times P(\sigma_{t_{rec}}) . \quad (5.17)$$

The results from the unbinned, *global* fit are presented in Fig. 5.12 and Fig. 5.13, where the fit projections on the $(t_{rec} - t_{true})$ axis are shown by the curve. The extracted values of the fit parameters are displayed in the statistics box. Note that the fractions $F1$ and $F2$ are relatively small, indicating that the resolution is mainly determined by the first term in Eq. (5.14), i.e. the simple Gaussian.

To see whether the unbinned fit correctly describes the time residual distributions in the various ranges of $\sigma_{t_{rec}}$, we have also projected $\mathcal{R}(x)$ in individual slices of $\sigma_{t_{rec}}$ and have examined the quality of the fit. These projections of the global fit on the residual distribution are shown in Fig. 5.14 for the different $\sigma_{t_{rec}}$ ranges, for the channel $B^+ \rightarrow J/\psi K^+$. Note that the fit parameters are the same for all the slices, since the curves shown are projections over different intervals of $\sigma_{t_{rec}}$ of the same global likelihood⁷.

Figure 5.15 and Fig. 5.16 illustrate the residuals and the pulls for the fits given in Fig. 5.14. Figure 5.17 shows that the pulls are nicely spread around zero.

⁷The curves *do* depend on the selected slice, as the projections differ because the interval over which $\sigma_{t_{rec}}$ is integrated in Eq. (5.17) varies. This is one of the reasons we have explicitly included the conditional pdf for $\sigma_{t_{rec}}$ in our likelihood.

(a) 2D (left) and 3D (right) plots of $[t_{rec} - t_{true}]$ versus $[\sigma_{t_{rec}}]$ for $B^+ \rightarrow J/\psi K^+$.(b) 2D (left) and 3D (right) plots of $[t_{rec} - t_{true}]$ versus $[\sigma_{t_{rec}}]$ for $B^0 \rightarrow J/\psi K^*$.**Figure 5.11.** 2D and 3D plots of $[t_{rec} - t_{true}]$ versus $[\sigma_{t_{rec}}]$ for both channels.

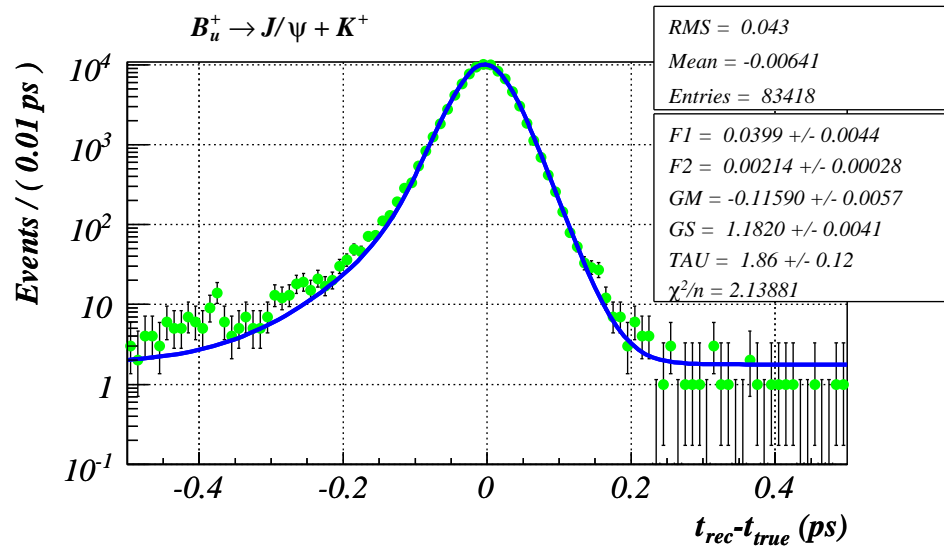


Figure 5.12. Projections of the global, unbinned fit onto the $[t_{rec} - t_{true}]$ axis for channel $B^+ \rightarrow J/\psi K^+$.

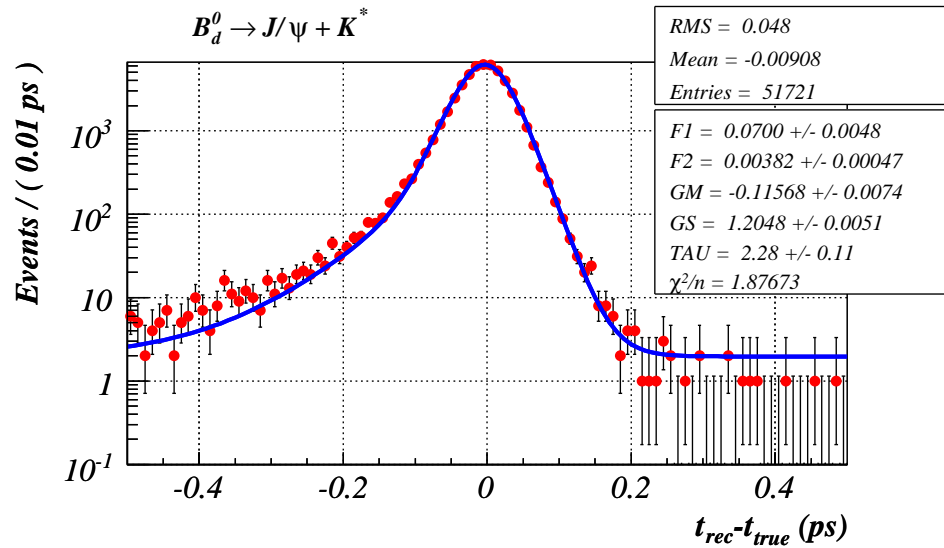


Figure 5.13. Projections of the global, unbinned fit onto the $[t_{rec} - t_{true}]$ axis for channel $B^0 \rightarrow J/\psi K^*$.

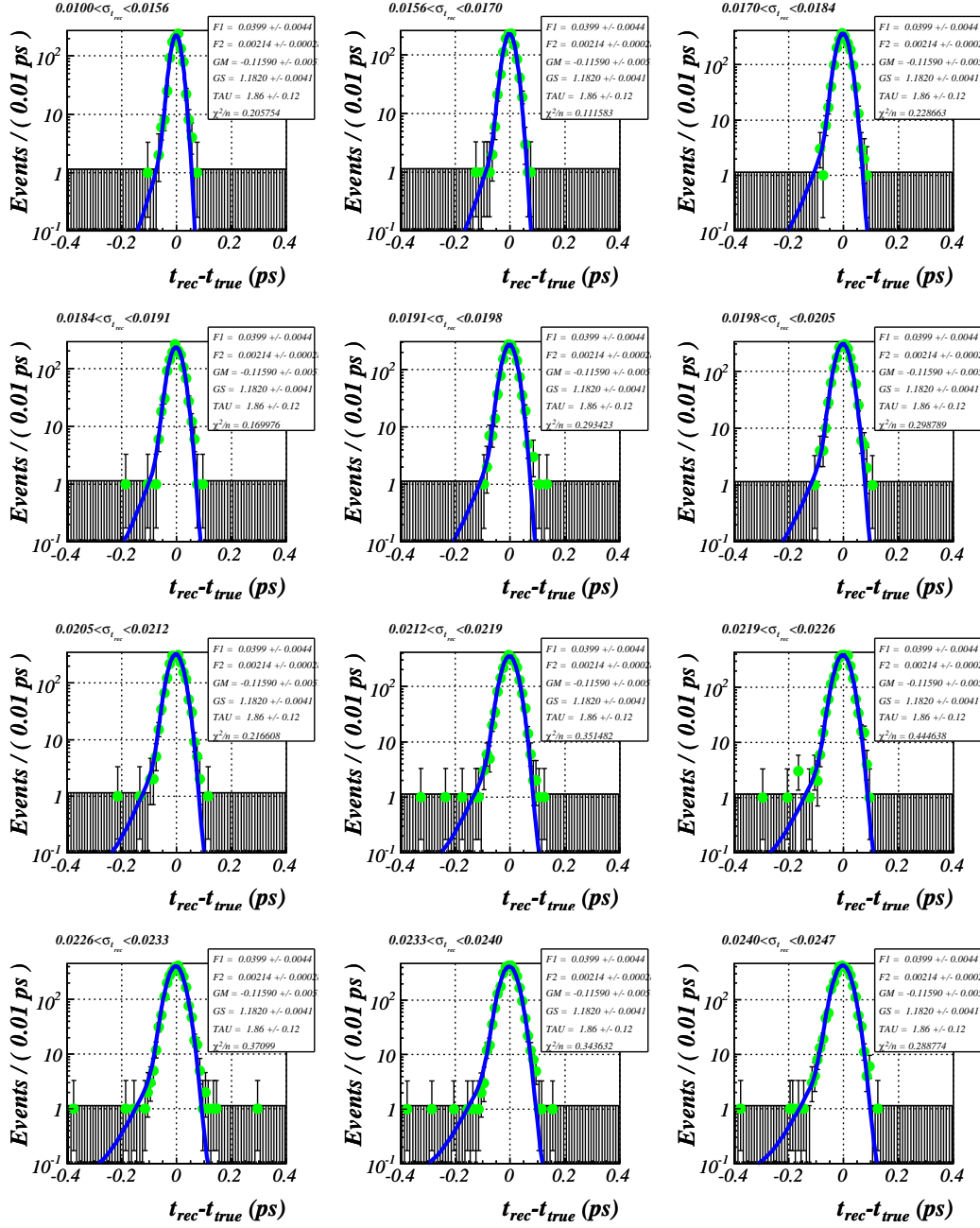


Figure 5.14. Projections of the global unbinned maximum likelihood fit, using Eq. (5.17), onto the $[t_{rec} - t_{true}]$ axis in intervals of $\sigma_{t_{rec}}$ for the channel $B^+ \rightarrow J/\psi K^+$.

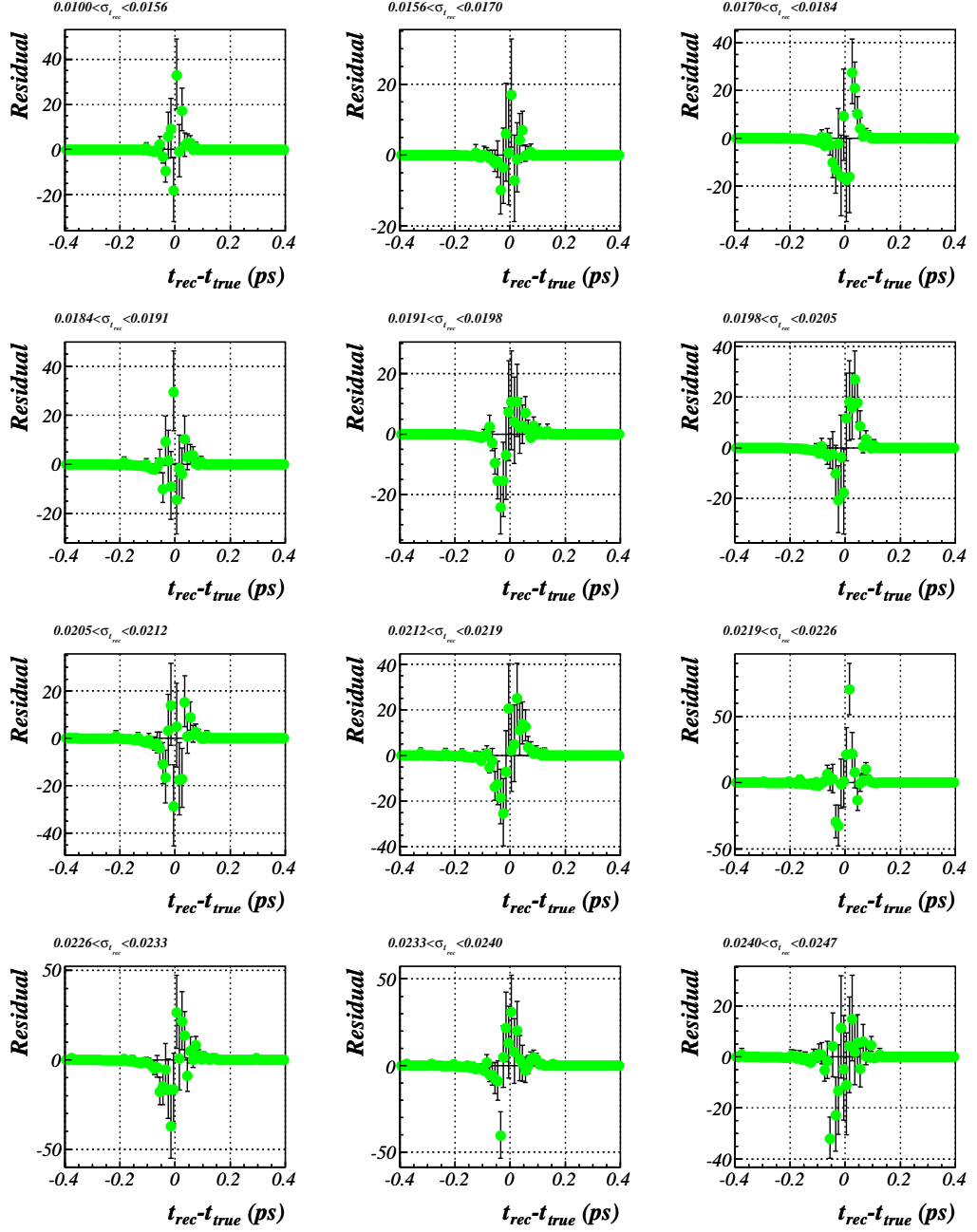


Figure 5.15. Fit residuals for the various projections of the global unbinned maximum likelihood fit onto $[t_{\text{rec}} - t_{\text{true}}]$ axis in different intervals of $\sigma_{t_{\text{rec}}}$ for the channel $B^+ \rightarrow J/\psi K^+$.

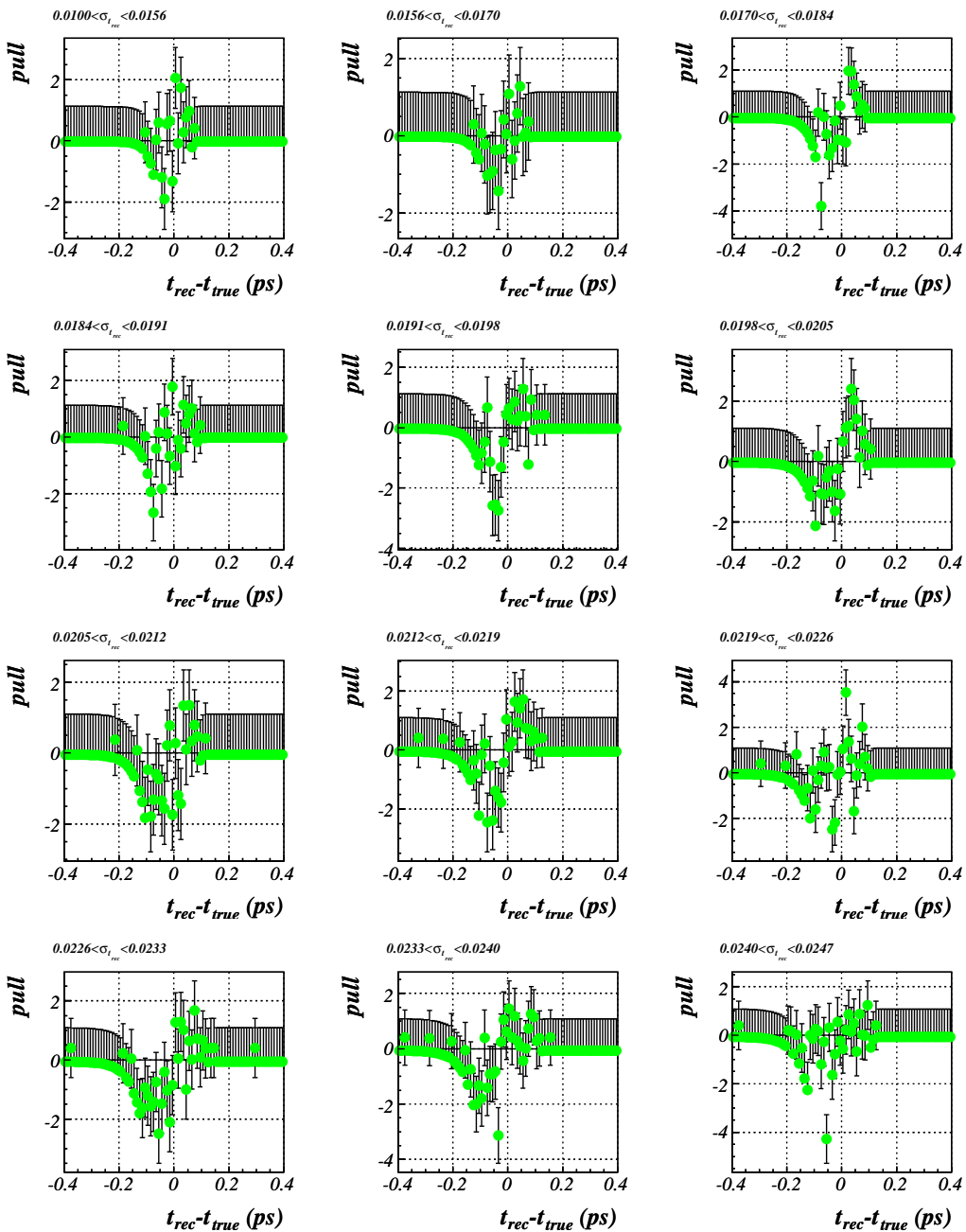


Figure 5.16. Pulls for the various projections of the global unbinned maximum likelihood fit onto $[t_{rec} - t_{true}]$ axis in different intervals of $\sigma_{t_{rec}}$ for the channel $B^+ \rightarrow J/\psi K^+$.

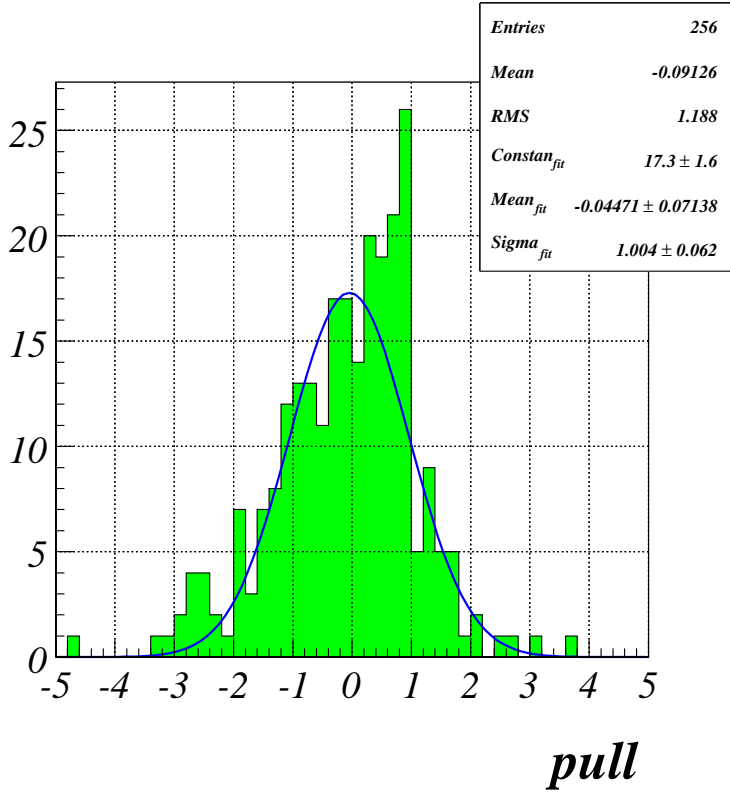


Figure 5.17. Distribution of the pulls for the projection of the global unbinned maximum likelihood fit onto the $[t_{rec} - t_{true}]$ axis for $B^+ \rightarrow J/\psi K^+$. Only the pulls for bins that contain more than 3 entries (Fig. 5.12) are plotted. The histogram is fitted with a Gaussian function.

5.5 Determination of the Parameters on Real Data

5.5.1 Method

At this point, we have obtained a resolution model with 5 parameters that attempts to describe the decay time residuals $t_{rec}^i - t_{true}^i$ for all values of $\sigma_{t_{rec}}$.

In reality, we will not have access to t_{true} . The only two available observables are t_{rec} and its uncertainty $\sigma_{t_{rec}}$. Here, we shall try to determine the resolution model parameters by using only these two observables. To do this, we must build an appropriate pdf describing the t_{rec} distribution. We know that for an ideal detector the distribution of the observed decay times t_{true} is a falling exponential distribution of type

$$E(t) = e^{-\frac{t}{\tau}}, \quad (5.18)$$

where τ is the mean lifetime of the B meson. Then, the reconstructed proper-time

pdf $F(t_{rec}, \sigma_{t_{rec}})$ is a falling exponent too, but smeared with the detector resolution. We can write $F(t_{rec}, \sigma_{t_{rec}})$ as a convolution between $E(t_{rec})$ and $\mathcal{R}(t_{rec} | \sigma_{t_{rec}})$ as [71]

$$F(t_{rec}, \sigma_{t_{rec}}) = E(t_{rec}) \otimes \mathcal{R}(t_{rec} | \sigma_{t_{rec}}) = \left[\int dt' e^{-\frac{t'}{\tau}} R(t-t' | \sigma_{t_{rec}}) \right] \times P(\sigma_{t_{rec}}) . \quad (5.19)$$

By performing an unbinned maximum likelihood fit with this pdf to the observed $[t_{rec}^i, \sigma_{t_{rec}}^i]$ pairs, we are able to determine the resolution model parameters. Note that now, we have six fit parameters - five from the resolution model plus the B lifetime τ_B , which is a free parameter and will be extracted from the global fit. Take into consideration that most information on the decay time resolution is obtained from the events with $t_{rec} \approx 0$, since in this region the distortion of the sharp rising edge of the exponential at $t = 0$ by the resolution is most pronounced. As a result it is important to test whether the resolution obtained from these events is representative of the entire sample, i.e. whether the resolution does *not* depend on the proper-time itself.

In the next subsection we will compare the resolution model parameters retrieved using $t_{rec} - t_{true}$, to the ones obtained with only t_{rec} .

5.5.2 Results

Figures 5.18 and 5.19 show the projection of the unbinned fit to the t_{rec} axis for both investigated decay modes. The corresponding fit residual and pull distributions are also given, indicating the quality of the fit.

The resolution model parameters extracted through a global fit (Eq. (5.19)) to the reconstructed simulation data are given in Table 5.3 (for $B^+ \rightarrow J/\psi K^+$) and Table 5.4 (for $B^0 \rightarrow J/\psi K^*$) together with the parameter values obtained from the global fit to the time residuals by using t_{true} .

Comparing the two sets of values we come to the following conclusions:

- * The mean lifetimes $\tau_{B^{+/0}}$ of the B^+ and B^0 respectively, are determined to a precision of 6 fs. The τ_B values match remarkably well with the ones received from the fit to t_{true} (the fit outputs in Table 5.2).
- * The fraction parameter $F1$, the fraction that allows for a modified decay time distribution, differs by a factor 0.1 and 4 for $B^+ \rightarrow J/\psi K^+$ and $B^0 \rightarrow J/\psi K^*$, respectively.
- * The scale factor for the bias, GM , for both channels, indicates that a larger bias in the decay time is observed in the data.
- * A smaller resolution scale factor GS , is seen in the data for both channels, compared to what is expected from Monte-Carlo simulation truth.

- * The values of TAU are not determined accurately from the data, which in the case of $B^+ \rightarrow J/\psi K^+$ can be attributed to the very small fraction $F1$.

Parameter	Fit to $(t_{rec} - t_{true})$	Error	Fit to t_{rec}	Error	Global Correlation
τ_{B^+}			1.6997	0.0057	0.1791
$F1$	0.0399	0.0042	0.0034	0.0009	0.8333
$F2$	0.0021	0.0003	0.0005	0.0003	0.6963
GM	-0.1159	0.0056	-0.4422	0.0289	0.4797
GS	1.1820	0.0039	0.8807	0.0280	0.5308
TAU	1.8561	0.1170	16.9820	4.7000	0.8849

Table 5.3. Resolution model parameters for channel $B^+ \rightarrow J/\psi K^+$.

Parameter	Fit to $(t_{rec} - t_{true})$	Error	Fit to t_{rec}	Error	Global Correlation
τ_{B^0}			1.5233	0.0065	0.1581
$F1$	0.0700	0.0048	0.2808	0.1480	0.9858
$F2$	0.0038	0.0005	0.0014	0.0003	0.1918
GM	-0.1157	0.0074	-0.4935	0.0559	0.7554
GS	1.2048	0.0051	0.4594	0.0761	0.8902
TAU	2.2831	0.1110	1.1098	0.2230	0.9759

Table 5.4. Resolution model parameters for channel $B^0 \rightarrow J/\psi K^*$.

Note that the difference between the decay channels can be explained by the fact that $F1$ and GS are correlated, given that a larger fraction $F1$ can be compensated by a smaller width GS .

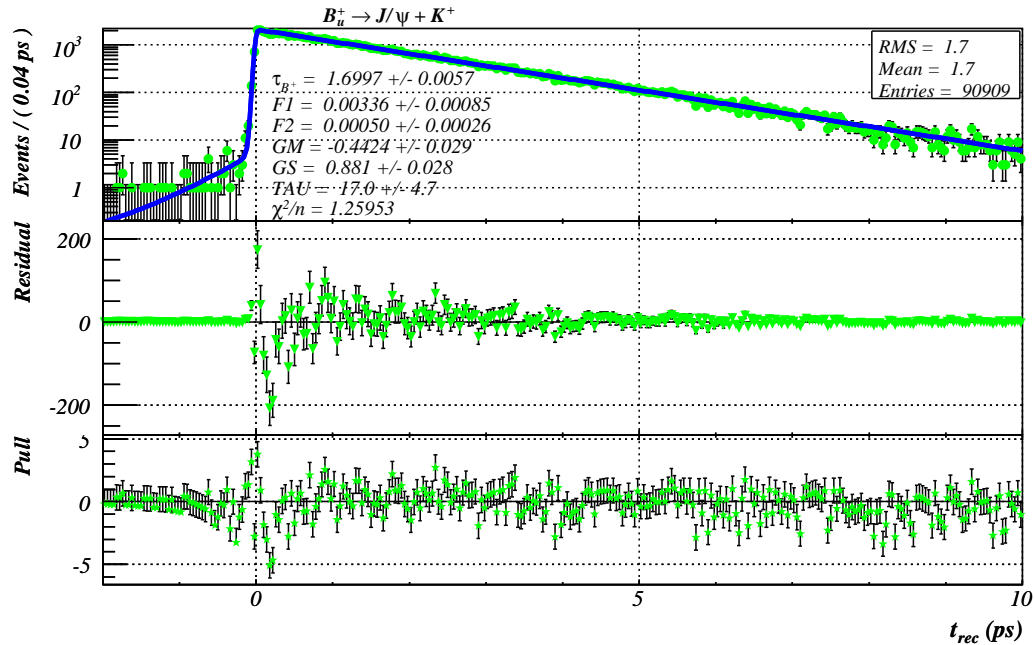


Figure 5.18. Projection of the global-unbinned fit to t_{rec} for channel $B_d^+ \rightarrow J/\psi(1S)K^+$. Fit residuals and pulls are given also.

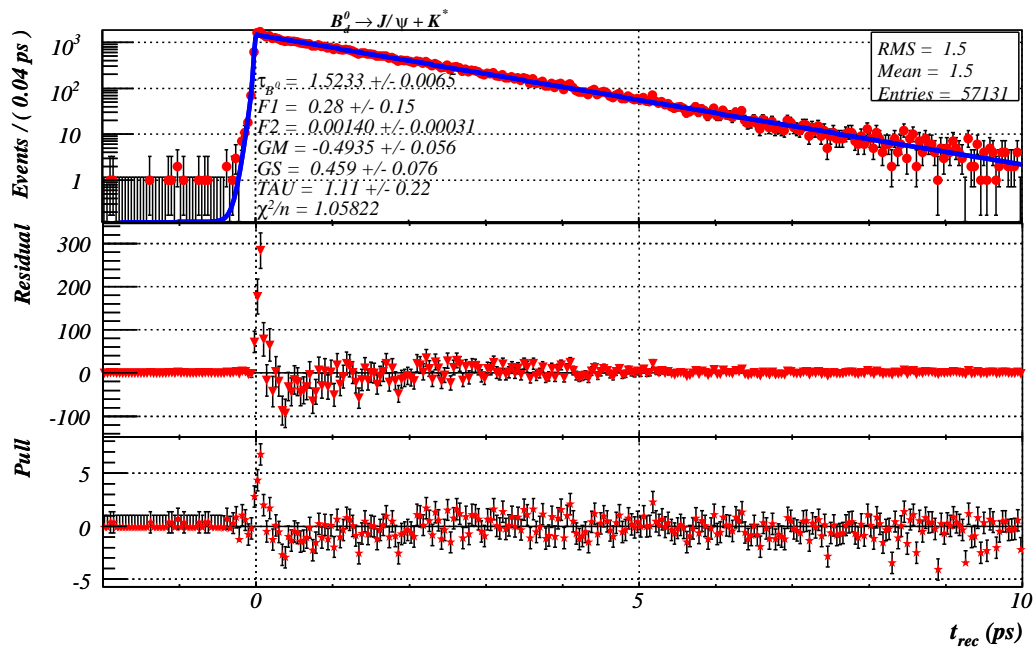


Figure 5.19. Projection of the global-unbinned fit to t_{rec} for channel $B_d^0 \rightarrow J/\psi(1S)K^*$. Fit residuals and pulls are given also.

5.6 Dependence on t_{true}

5.6.1 Test for Dependence on t_{true}

By construction, the resolution model does not explicitly depend on the true proper-time t_{true} of the B meson. It does depend on the difference $(t_{rec} - t_{true})$ but not on t_{true} . Any dependence on t_{true} is a sign of a bias.

To see whether there is a correlation between the true proper-time and the proper-time resolution, we sliced the t_{true} distributions, shown in Fig. 5.20, into bins and applied the resolution model (see Sec. 5.4) to the decay time residuals ($t_{rec} - t_{true}$) falling into each bin of t_{true} .

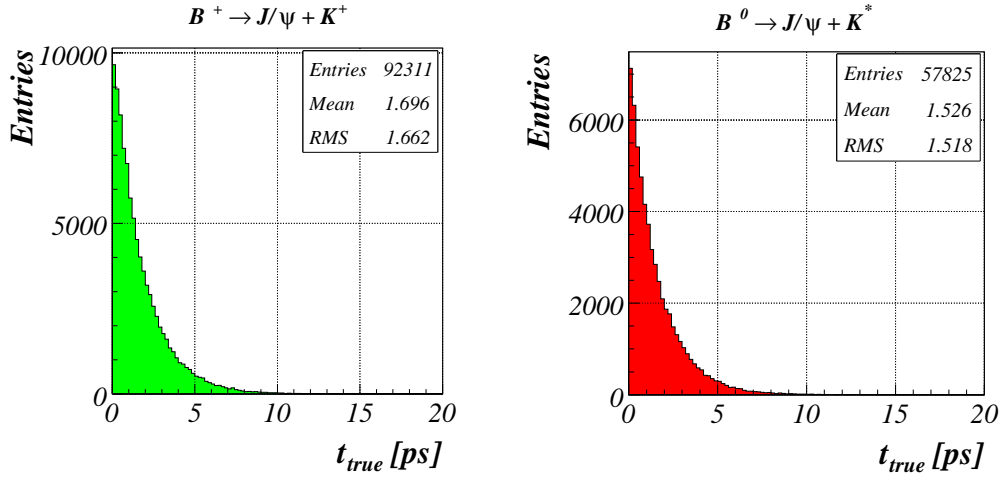


Figure 5.20. Distribution of t_{true} for $B^+ \rightarrow J/\psi K^+$ and $B^0 \rightarrow J/\psi K^*$.

The t_{true} slicing is done as follows:

- * The true proper-time distribution t_{true} , shown in Fig. 5.20, is sliced into N bins. The bin interval is chosen such that an equal amount of entries falls in each bin.
- * For each $t_{true}^i \in$ given bin k , the residual $x^i = t_{rec}^i - t_{true}^i$ is calculated, plotted and fitted with the function $R(x; \vec{p})$ given in Eq. (5.7).

In Fig. 5.21 and Fig. 5.22 the residual distributions are presented in slices of t_{true} fitted with $R(x)$ in each slice separately, for both studied channels.

Following the procedure described in Sec. 5.4.4, subsequently we include the per-event-error in the fit and perform an unbinned maximum likelihood fit for each t_{true} slice.

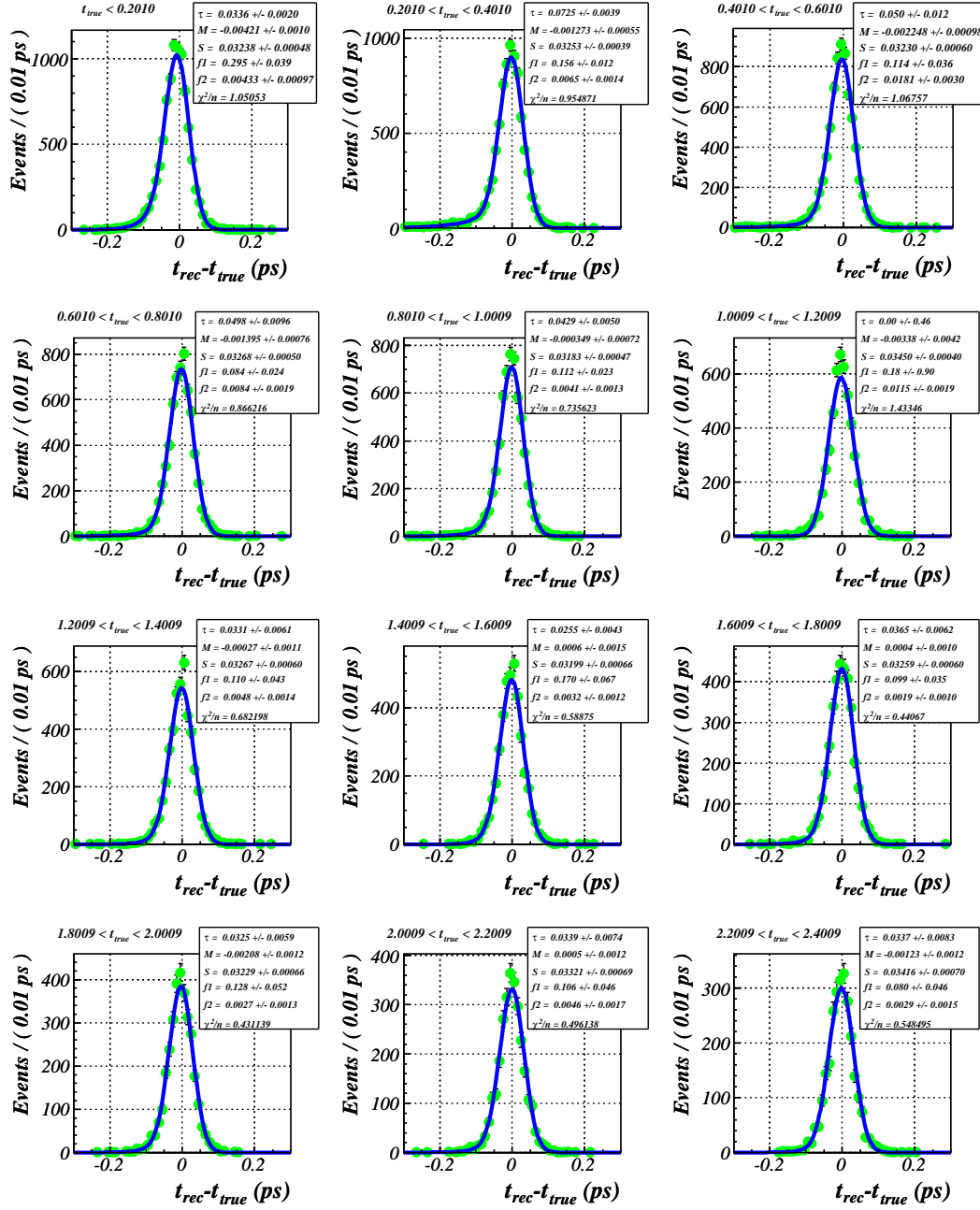


Figure 5.21. The $R(x)$ -fitted residual distributions for different slices of t_{true} , using Eq. (5.7). The decay channel is $B^+ \rightarrow J/\psi K^+$.

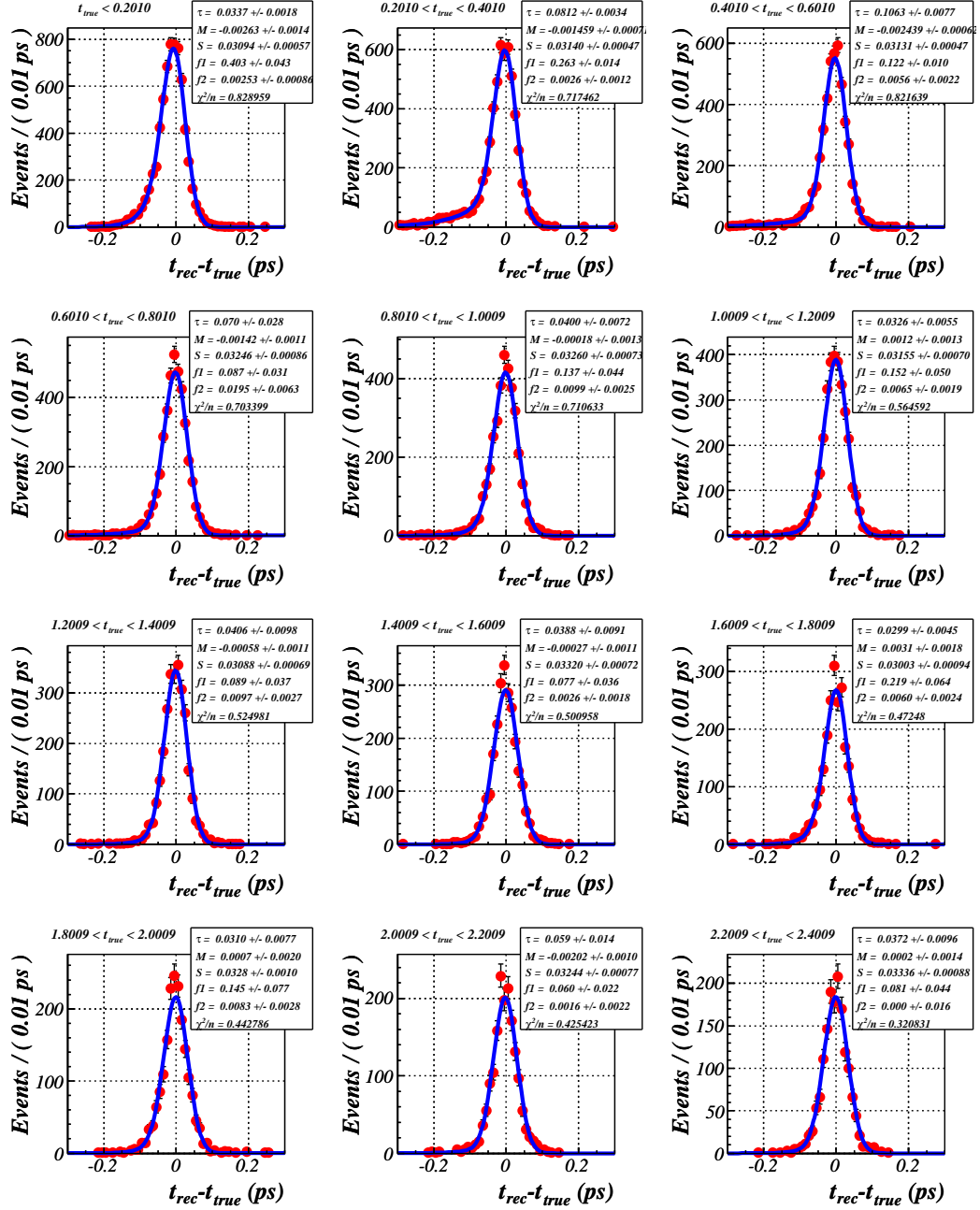


Figure 5.22. The $R(x)$ -fitted residual distributions for different slices of t_{true} , using Eq. (5.7). The decay channel is $B^0 \rightarrow J/\psi K^*$.

For each t_{true} interval, the $\sigma_{t_{rec}}$ errors are plotted with their pdf, obtained via the ROOKEYSPDF method [79]. Results are shown in Fig. 5.24.

The decay time residuals can be fitted with the unbinned maximum likelihood fit (Eq. (5.16)) separately, in each given t_{true} bin. The projections of that fit onto the $(t_{rec} - t_{true})$ axis for the slices of t_{true} for both channels is shown in Fig. 5.25 and Fig. 5.26. From these figures one can easily see that the behaviour of the residual distributions varies with the slices. The parameters of the global fit for each slice vary too. These parameters are quite different for the first several slices in comparison with the others (see *GS* and *TAU* for example). The conclusion is that we observe a clear evidence for a dependence of the resolution on the true proper-time.

5.6.2 Explanation of the t_{true} Dependence

A possible explanation for the resolution dependence on t_{true} is the hypothesis that the reconstruction of the primary vertex (PV) is biased. The PV could be biased when some of the B decay products are used in the PV reconstruction. If this is the case, then we would have a smaller reconstructed B meson travel path d_{rec} , which would lead to smaller reconstructed proper-time t_{rec} and hence to an abnormally smaller decay time residual $(t_{rec} - t_{true})$. This mechanism is illustrated in Fig. 5.23. According to that picture the primary vertex is attracted to the secondary (decay) vertex (SV).

Since the channel $B^0 \rightarrow J/\psi K^*$ has more associated tracks, the probability that one of them is used for the PV reconstruction is higher, and therefore the effect on the dependence of the resolution on t_{true} would be stronger. Indeed, e.g. *GS* varies between 1.15 and 1.22 for $B^+ \rightarrow J/\psi K^+$ and between 1.13 and 1.25 for $B^0 \rightarrow J/\psi K^*$. The t_{true} dependence is slightly stronger in the B^0 decay mode.

Again, note that the bias on the reconstructed proper-time due to other long-lived resonances is absorbed implicitly in the resolution model. As a result, as long as the bias is uncorrelated to the value of the proper-time, it is properly taken into account.

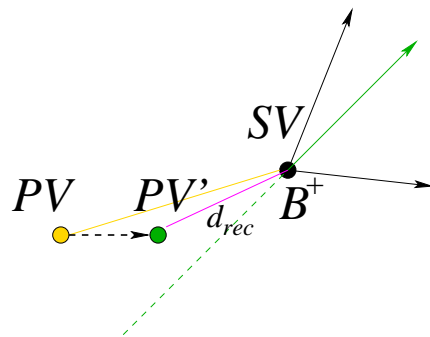


Figure 5.23. Illustration of a mechanism, which could lead to a bias in the reconstruction of the primary vertex. One of the B daughters is used in the definition of the PV. There is a PV to SV "attraction".

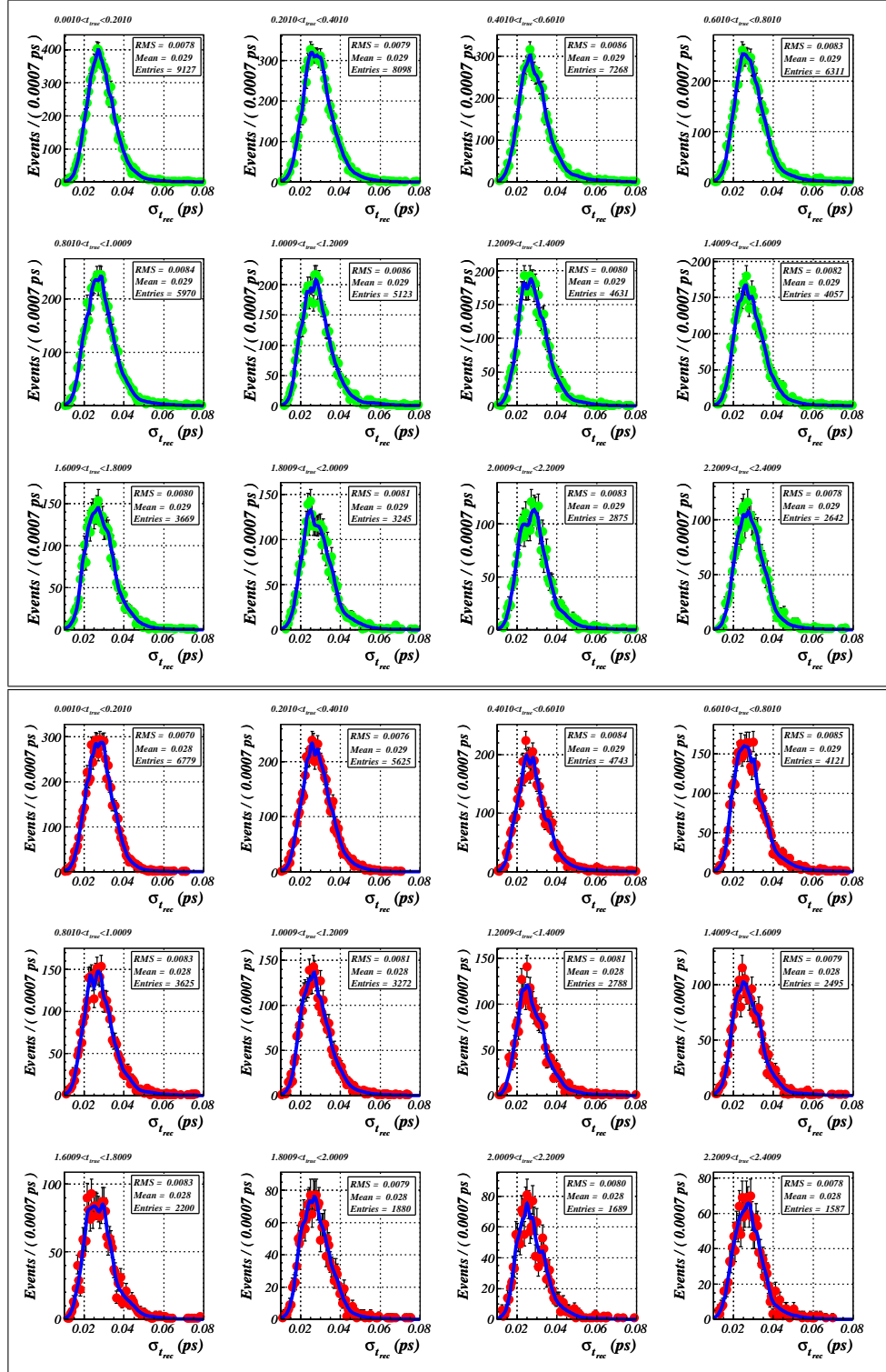


Figure 5.24. $\sigma_{t_{rec}}$ distribution per t_{true} slice, described by *RooKeysPdf*. Up: $B^+ \rightarrow J/\psi K^+$, Down: $B^0 \rightarrow J/\psi K^*$.

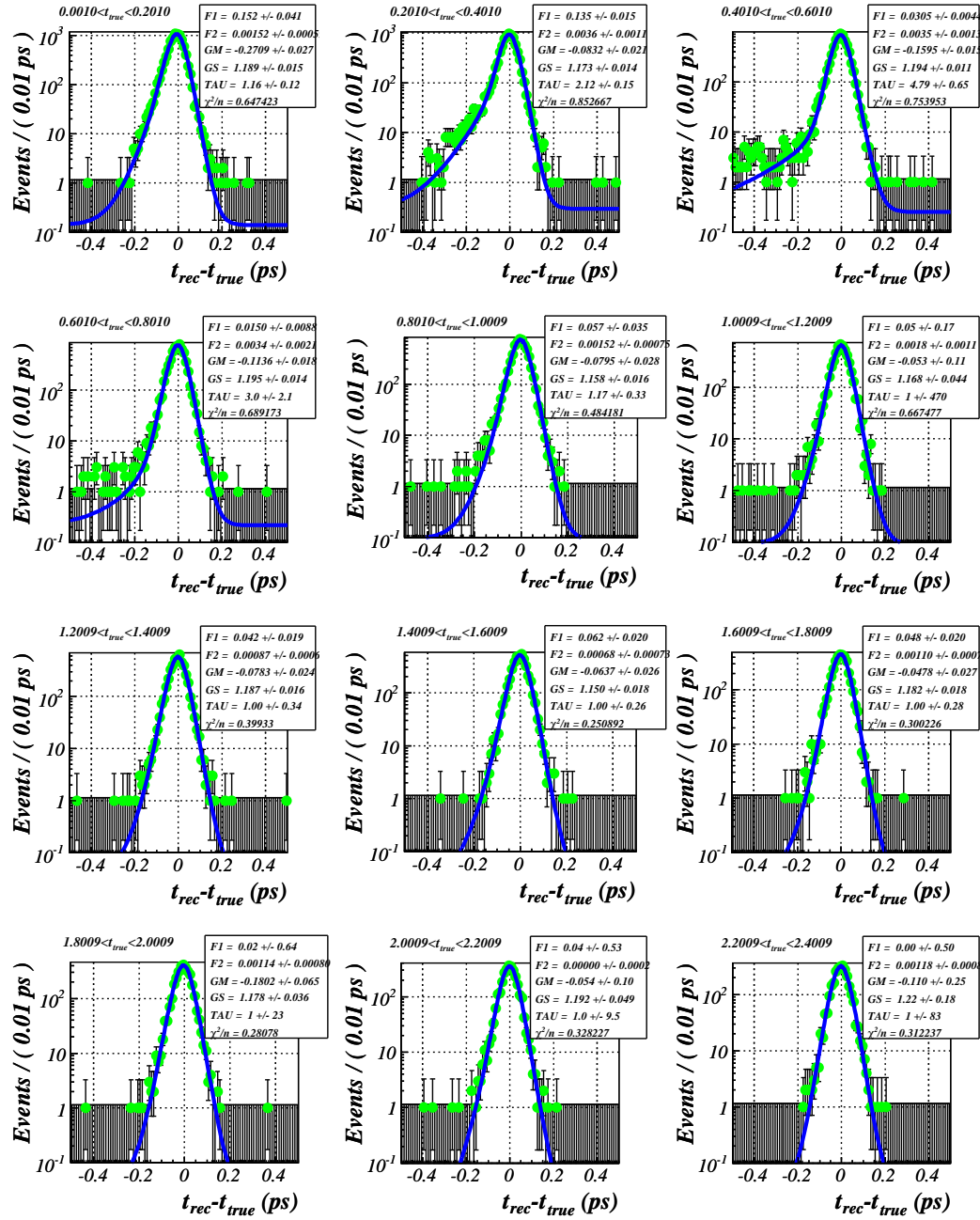


Figure 5.25. Projections of the unbinned maximum likelihood fits to the $[t_{rec} - t_{true}]$ axis for the corresponding slices of t_{true} for $B^+ \rightarrow J/\psi K^+$ using Eq. (5.17).

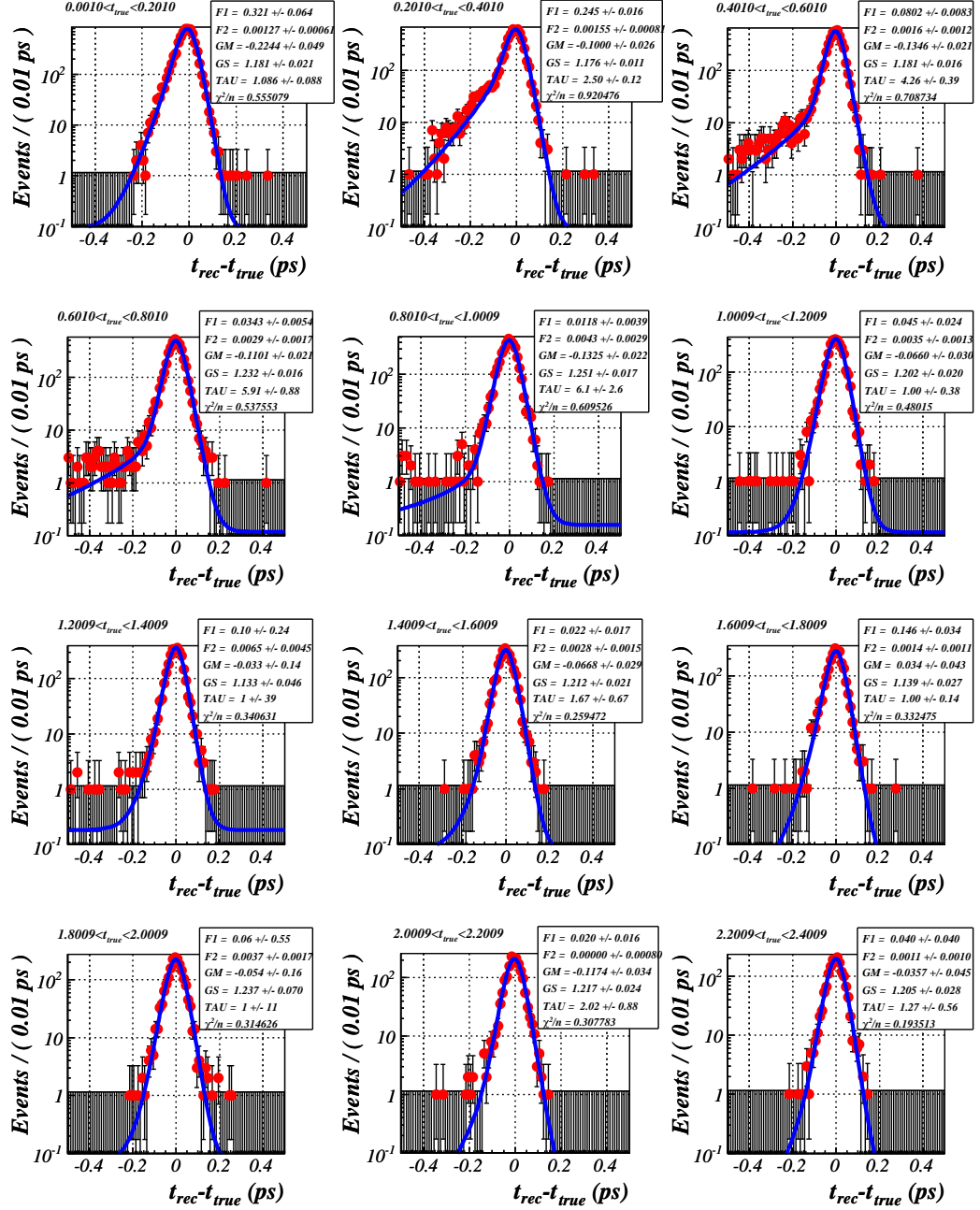


Figure 5.26. Projections of the unbinned maximum likelihood fits to the $[t_{rec} - t_{true}]$ axis for the corresponding slices of t_{true} for $B^0 \rightarrow J/\psi K^*$ using Eq. (5.17).

5.6.3 Primary Vertex Re-Definition

To check the hypothesis that the wrong reconstruction of the primary vertex is the cause for the dependence of the resolution on the true proper-time, we performed a separate study, in which we tried to re-define the PV position. The study was done with separate samples of $B^+ \rightarrow J/\psi(1S)(\mu^+\mu^-)K^+$ and $B^0 \rightarrow J/\psi(1S)(\mu^+\mu^-)K^*(K^+\pi^-)$ events. The selection procedure and the cuts applied were the same as those given in Sec. 5.3. The only difference is in the number of the processed events, which is now reduced (50000 selected B^+ candidates, and 29000 selected B^0 candidates).

We re-defined the primary vertex position in the following way⁸:

- * All tracks associated with the B particle are *removed* from the PV reconstruction list.
- * The PV is *refitted*.

In this manner, the reconstruction of the B particle is not affected, but the PV position is updated. We ran our event selections for the three possible cases, in order to be able to compare:

1. *Original PV* - The PV is nominally reconstructed.
2. *Refitted PV* - The PV is only refitted with an alternative approach.
3. *Removed B's and Refitted PV* - The B associates are removed from the tracks used for PV reconstruction and then the PV is refitted and updated.

In Fig. 5.27 the distributions of the primary vertex coordinates X , Y and Z are shown for the three cases that we considered. The mean Z coordinate of the PV is slightly shifted from 1.271 mm to 1.263 mm, once the PV is refitted with removed B associates. The "attraction" towards the secondary vertex is reduced. This can be seen more clearly in Fig. 5.28, where the differences in X , Y and Z are plotted for: $[PV_{orig} - PV_{rem\&refit}]$ (1st row on the graph); $[PV_{orig} - PV_{refit}]$ (2nd row) and $[PV_{rem\&refit} - PV_{refit}]$ (3rd row). The distribution of the Z differences now shows a clear shift to higher values, since Z_{orig} is bigger than $Z_{rem\&refit}$ by $\sim 8 \mu\text{m}$ on average.

We will now repeat the procedure as described in Sec. 5.6.1, to verify an improved t_{true} dependence. Applying slicing in t_{true} and then fitting each slice with an unbinned maximum likelihood (Eq. (5.17)) we get the results presented in Fig. 5.29 for the three cases of the PV position for $B^+ \rightarrow J/\psi K^+$ channel. For $B^0 \rightarrow J/\psi K^*$ channel the analogous plots are given in Fig. 5.30. Only the first four slices in t_{true} with the largest true proper-time dependence are shown. Comparing the figures one can see that there is an improvement, although a dependence on t_{true} is still

⁸The PVREFITTER DaVinci algorithm was used.

present. Both GM and the resolution scale factor GS , improve with improved PV reconstruction.

The projection of the global-unbinned fit to t_{rec} , the fit residuals and the fit pulls for both channels, when PV is updated, can be seen in Fig. 5.31 and Fig. 5.32.

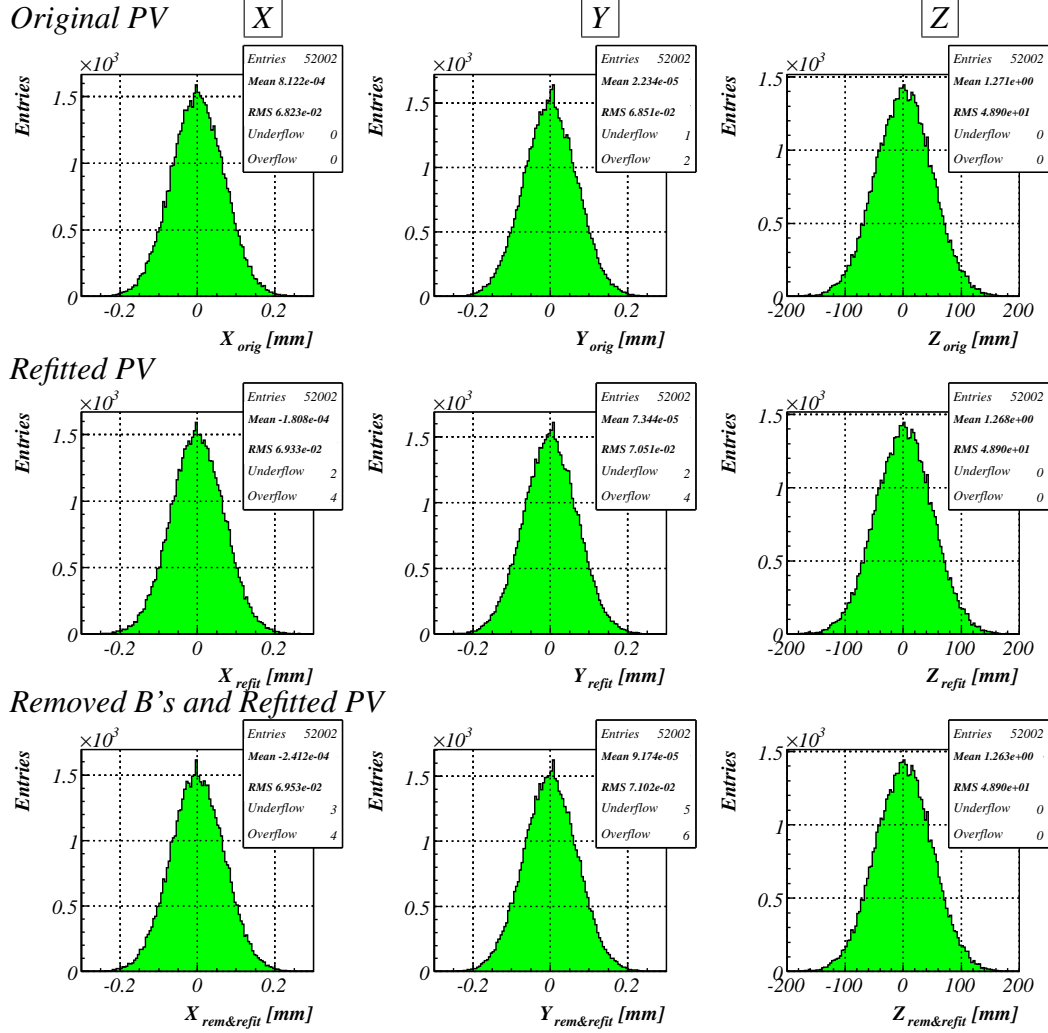


Figure 5.27. Distributions of the coordinates of the Primary Vertex, X , Y and Z for the 3 considered cases: Non-updated PV, Only refitted PV and Updated PV (removed B's and refitted). The decay channel is $B^+ \rightarrow J/\psi K^+$.

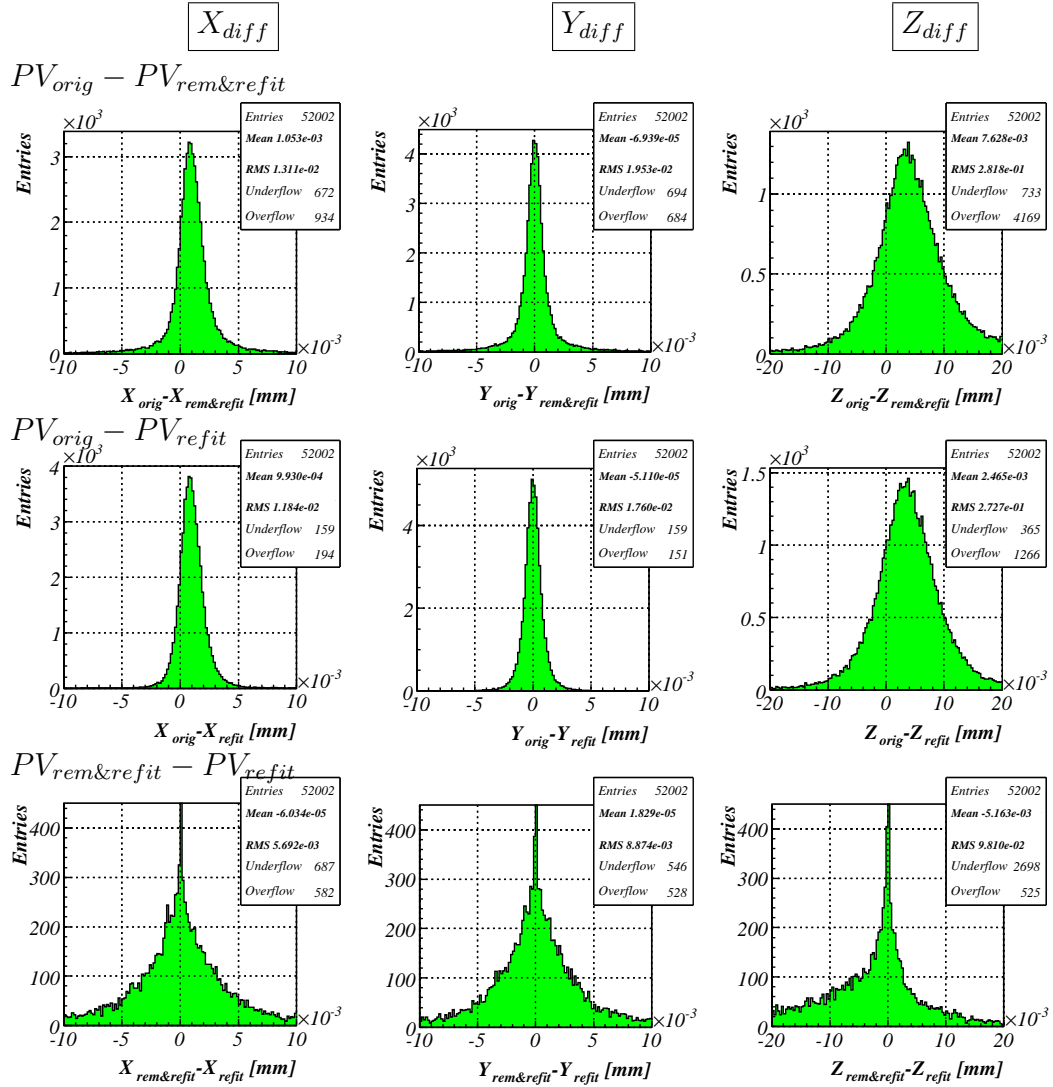


Figure 5.28. Distributions of the Primary Vertex X , Y and Z differences [$PV_{orig} - PV_{rem\&refit}$], [$PV_{orig} - PV_{refit}$] and [$PV_{rem\&refit} - PV_{refit}$]. The decay channel is $B^+ \rightarrow J/\psi K^+$. (The mean and RMS in the statistics box are not taken from the histogram, but were calculated on an event-by-event basis.)

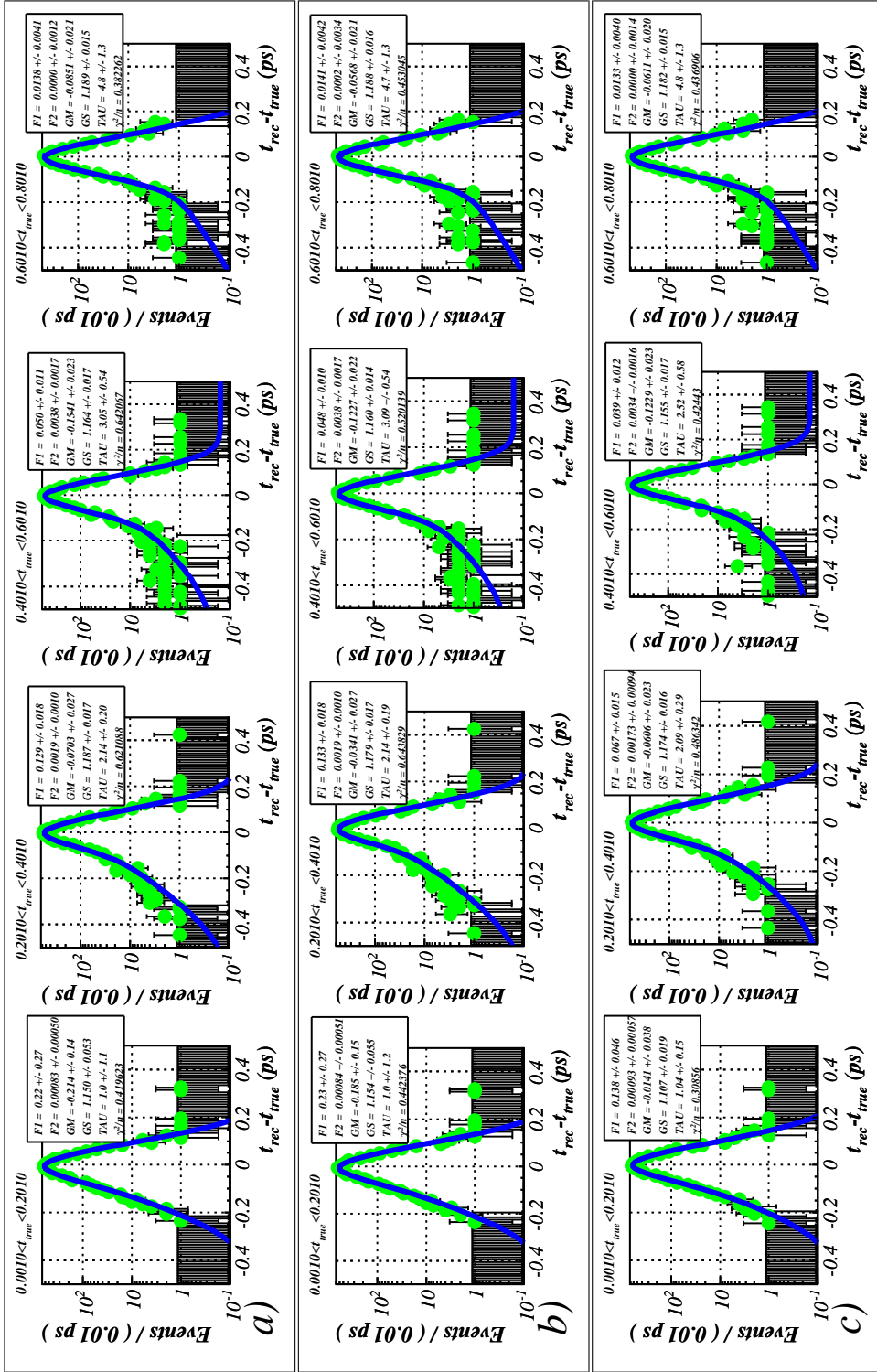


Figure 5.29. Projections of the unbinned maximum likelihood fits to the $[t_{\text{rec}} - t_{\text{true}}]$ axis for the corresponding slices of t_{true} for for a) Nominally reconstructed PV, b) Refitted only PV and c) Removed B associates and refitted PV. The decay mode is $B^+ \rightarrow J/\psi K^+$.

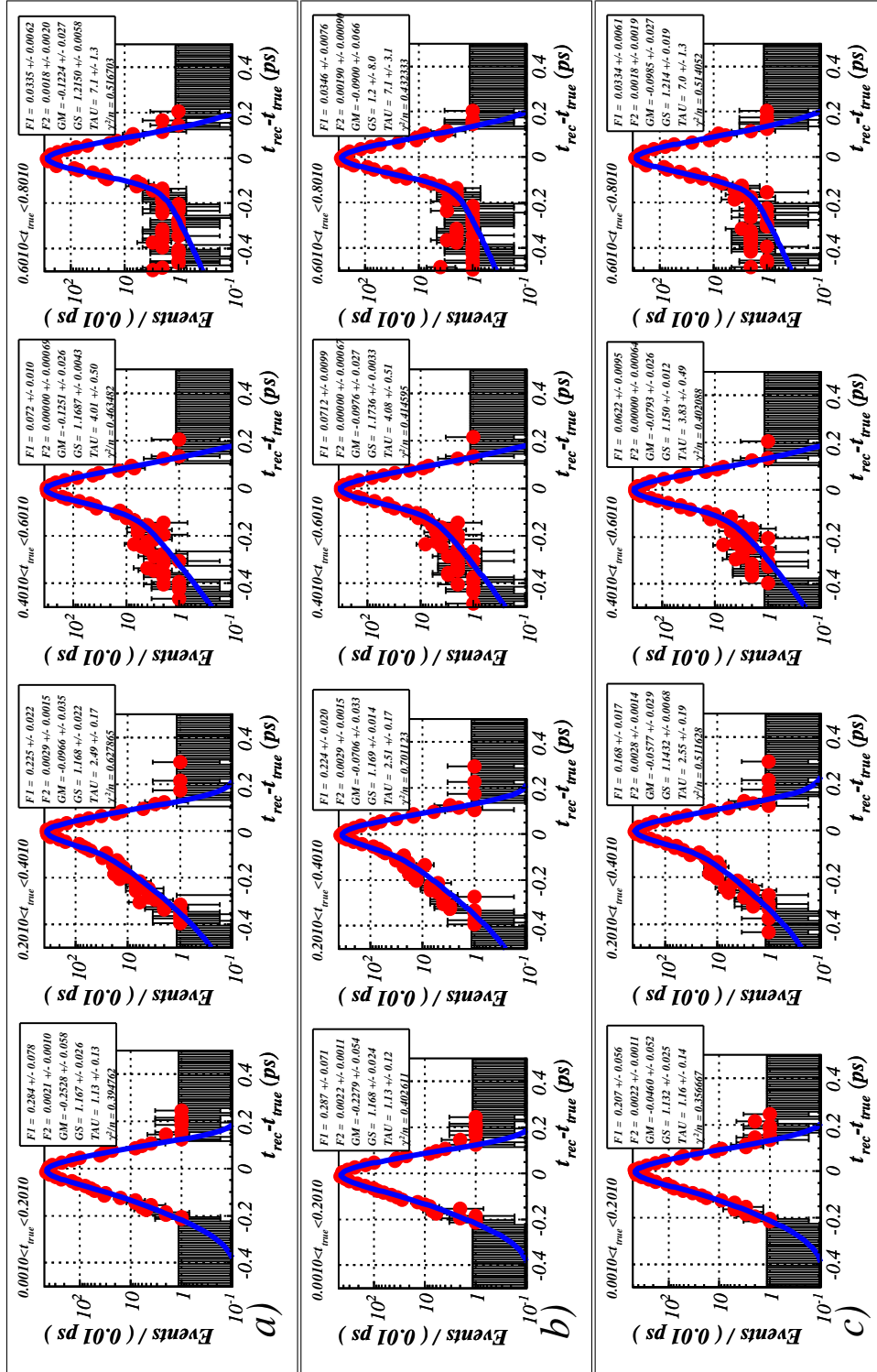


Figure 5.30. Projections of the unbinned maximum likelihood fits to the $[t_{rec} - t_{true}]$ axis for the corresponding slices of t_{true} for *a)* Nominally reconstructed PV, *b)* Removed B associates and refitted PV and *c)* Removed B associates and refitted PV. The decay mode is $B^0 \rightarrow J/\psi K^*$.

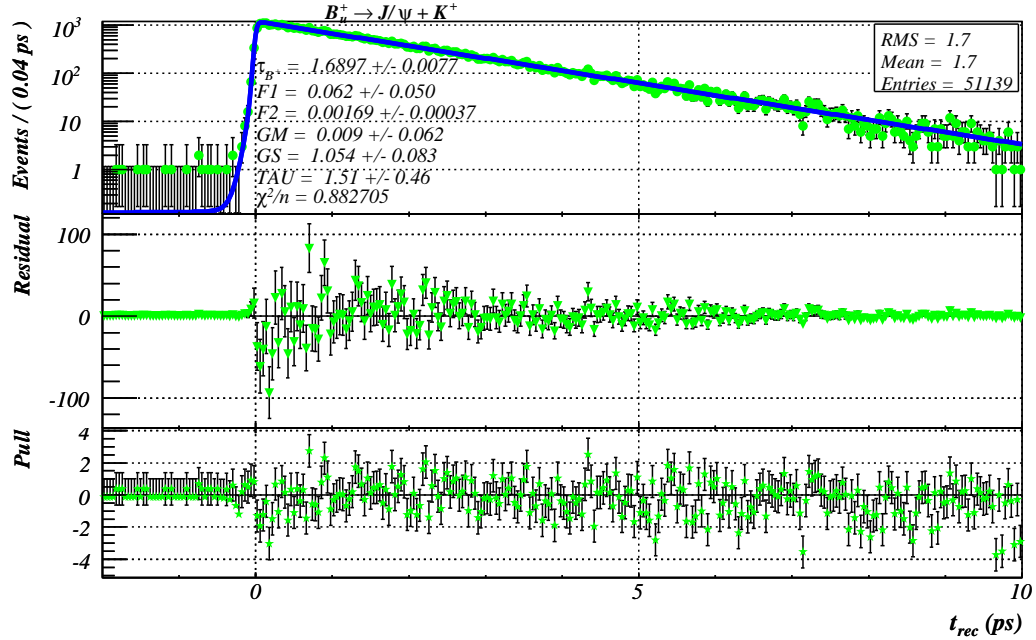


Figure 5.31. Projection of the global-unbinned fit to t_{rec} for channel $B^+ \rightarrow J/\psi(1S)K^+$ with updated PV. Fit residuals and pulls are given also.

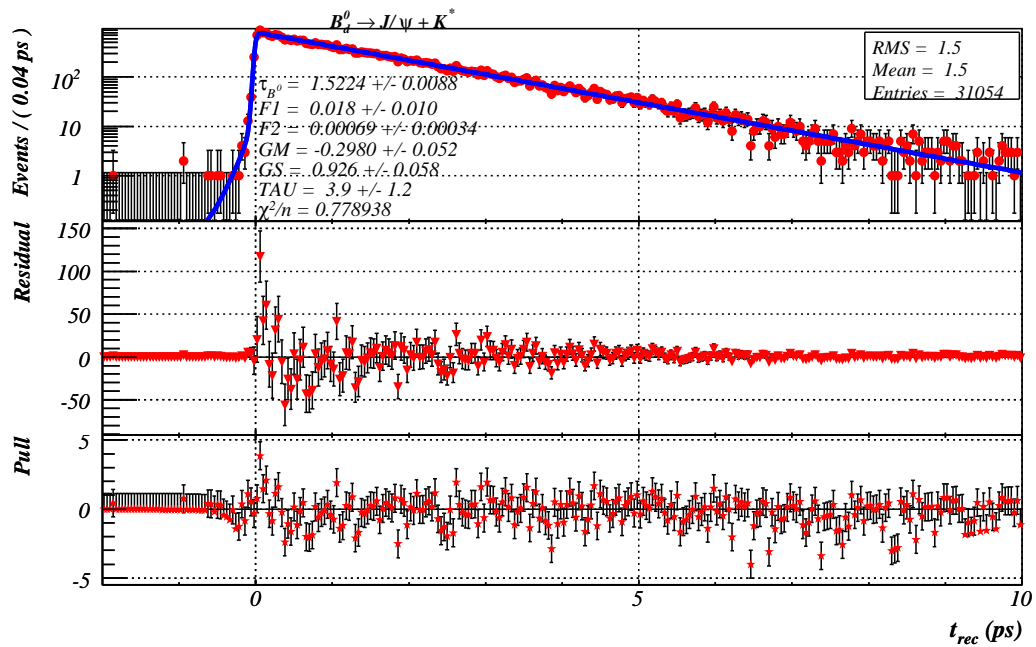


Figure 5.32. Projection of the global-unbinned fit to t_{rec} for channel $B_d^0 \rightarrow J/\psi(1S)K^*$ with updated PV. Fit residuals and pulls are given also.

The Resolution Model Parameters After the Update of the PV

In Table 5.5 and Table 5.6 the resolution model parameters are listed from the global unbinned maximum likelihood fits to the decay time residuals and to t_{rec} , given $\sigma_{t_{rec}}$ for a non-updated nominally reconstructed PV and for a re-defined PV with the B particles removed for the $B^+ \rightarrow J/\psi K^+$ decay mode. Note that Table 5.5 (5.7) gives similar results as Table 5.3 (5.4), with the only difference that the data set used in Table 5.5 (5.7) is a factor 2 smaller.

Parameter	Fit to $(t_{rec} - t_{true})$ [\vec{p}_{resid}]	Error	Fit to t_{rec} [$\vec{p}_{t_{rec}}$]	Error	Global Correlation Factor
τ_{B^+}			1.6945	0.0072	0.1761
$F1$	0.0434	0.0058	0.2537	0.3180	0.9978
$F2$	0.0015	0.0003	0.0015	0.0004	0.3920
GM	-0.1007	0.0076	-0.1509	0.1680	0.9683
GS	1.1700	0.0051	0.5988	0.0937	0.9024
TAU	1.7785	0.1390	1.0071	13.2000	0.9968

Table 5.5. Resolution model parameters with nominally reconstructed, original, PV for $B^+ \rightarrow J/\psi K^+$.

Parameter	Fit to $(t_{rec} - t_{true})$ [\vec{p}_{resid}]	Error	Fit to t_{rec} [$\vec{p}_{t_{rec}}$]	Error	Global Correlation Factor
τ_{B^+}			1.6897	0.0077	0.2172
$F1$	0.0381	0.0073	0.0617	0.0503	0.9714
$F2$	0.0015	0.0003	0.0017	0.0004	0.1201
GM	-0.0517	0.0082	0.0094	0.0620	0.7364
GS	1.1598	0.0054	1.0536	0.0827	0.8524
TAU	1.5330	0.1540	1.5117	0.0456	0.9453

Table 5.6. Resolution model parameters with updated PV for $B^+ \rightarrow J/\psi K^+$.

When the PV is updated, removing the B tracks from its reconstruction (Table 5.6), then the matching of the two sets of parameters (from the fit to $(t_{rec} - t_{true})$ and from the fit to t_{rec}) is significantly better in comparison with the case of using the nominal PV (Table 5.5). In fact all the parameters are in good agreement, with the exception of GM . A reason for this could be that the t_{true} dependence effect is not fully overcome and still partially present.

The results for the global parameters for a non-updated and updated primary vertex for channel $B^0 \rightarrow J/\psi K^*$ are summarized in Table 5.7 and Table 5.8. Here, we

do not observe as clear an improvement of the parameters values. The values of the most important parameters GS and TAU agree within the errors, but GM , $F1$ and $F2$ are not improved.

Parameter	Fit to $(t_{rec} - t_{true})$ [\vec{p}_{resid}]	Error	Fit to t_{rec} [$\vec{p}_{t_{rec}}$]	Error	Global Correlation Factor
τ_{B^0}			1.5224	0.0088	0.1709
$F1$	0.0575	0.0059	0.0305	0.0162	0.9326
$F2$	0.0032	0.0006	0.0007	0.0004	0.2907
GM	-0.1237	0.0094	-0.4398	0.0465	0.4703
GS	1.2054	0.0067	0.7214	0.0541	0.6637
TAU	2.5331	0.1700	3.1721	0.8970	0.9164

Table 5.7. Resolution model parameters with nominally reconstructed, original PV for $B^0 \rightarrow J/\psi K^*$.

Parameter	Fit to $(t_{rec} - t_{true})$ [\vec{p}_{resid}]	Error	Fit to t_{rec} [$\vec{p}_{t_{rec}}$]	Error	Global Correlation Factor
τ_{B^0}			1.5224	0.0088	0.1869
$F1$	0.0458	0.0043	0.0183	0.0101	0.9148
$F2$	0.0031	0.0006	0.0007	0.0003	0.2363
GM	-0.0744	0.0087	-0.2981	0.0515	0.4859
GS	1.1942	0.0063	0.9261	0.0579	0.6438
TAU	2.6206	0.1870	3.9468	1.1900	0.8989

Table 5.8. Resolution model parameters with updated PV for $B^0 \rightarrow J/\psi K^*$

To quantify the matching of the two sets of parameters (\vec{p}_{resid} and $\vec{p}_{t_{rec}}$), one can compute

$$\chi^2(\vec{\alpha}) = \vec{\alpha}^T (\text{Cov}_{\vec{\alpha}})^{-1} \vec{\alpha} , \quad (5.20)$$

where

$$\vec{\alpha} = \vec{p}_{resid} - \vec{p}_{t_{rec}} , \quad (5.21)$$

$$\text{Cov}_{\vec{\alpha}} = \text{Cov}_{\vec{p}_{resid}} + \text{Cov}_{\vec{p}_{t_{rec}}} , \quad (5.22)$$

with $\text{Cov}_{\vec{p}_{resid}}$ and $\text{Cov}_{\vec{p}_{t_{rec}}}$ the covariance matrices of \vec{p}_{resid} and $\vec{p}_{t_{rec}}$ respectively.

channel	Nominal PV		Updated PV	
	$\chi^2/\text{n.d.o.f.}$	<i>probability</i>	$\chi^2/\text{n.d.o.f.}$	<i>probability</i>
$B^+ \rightarrow J/\psi K^+$	128/5	0	5.67/5	0.34
$B^0 \rightarrow J/\psi K^*$	173/5	0	69/5	$2 \cdot 10^{-13}$

Table 5.9. χ^2 values, Eq. (5.20) and the corresponding probabilities, characterizing the goodness of matching of \vec{p}_{resid} and \vec{p}_{trec} for nominal and updated PV for both channels.

Table 5.9 presents the calculated values of $\chi^2/\text{n.d.o.f.}$ and the corresponding probabilities, for nominal and updated PV for both channels.

It is clear that the level of consistency of the parameters \vec{p}_{resid} and \vec{p}_{trec} is strongly increased when the PV is updated. In particular, for the B^+ decay mode, we achieve a $\chi^2/\text{n.d.o.f.} = 1.1$ corresponding to a χ^2 -probability of 34%.

For the B^0 channel the agreement between the determined parameter values is also improved. However, the agreement obtained is still not at the desired level.

5.7 Summary and Conclusions

A proper time resolution model was derived with simulated data. The parameters of this model have been extracted in two ways: by using the known residuals in the simulated data, and with the reconstructed proper time only. The latter can be used to determine the parameters of the model in real data. The parameter values obtained in both scenarios were compared.

A discrepancy was found in the values of the resolution model parameters obtained from these two techniques. This is explained as the result of a bias on the reconstructed proper-time which depends on the true proper-time. This bias can be decreased considerably when all final state tracks from the B meson under consideration are explicitly removed from the primary vertex. However, the issue is not fully resolved.

The method demonstrated here has two potential applications in LHCb: firstly, it could be used for tuning the Monte-Carlo itself; and secondly, for its principal intended purpose, of determining the proper-time resolution parameters on real data.

Chapter 6

Extraction of the Lifetime Ratio

$$\tau_{B^+}/\tau_{B^0}$$

Somewhere, something incredible is waiting to be known.

Carl Sagan (1934-1996)

The lifetime ratio, τ_{B^+}/τ_{B^0} , of B^+ and B^0 mesons can be used as a probe for validating of the Heavy Quark Expansion model (see Chapter 1).

In the previous chapter, a method for the precise determination of the proper lifetime resolutions of B^+ and B^0 mesons was described and applied. Here, the values of the lifetimes will be extracted, in the presence of backgrounds. The decay modes used are again $B^+ \rightarrow J/\psi(1S)K^+$ and $B^0 \rightarrow J/\psi(1S)K^*(892)$, with $J/\psi(1S) \rightarrow \mu^+\mu^-$, and $K^*(892) \rightarrow K^+\pi^{-}$ ¹. Subsequently, the ratio τ_{B^+}/τ_{B^0} is derived.

The outline of this chapter is as follows. The event selection is explained in Sec. 6.1. The modeling of the background, the signal and the total background plus signal data is discussed in Sec. 6.2. The extraction of the resolution model parameters is shown in Sec. 6.3. Finally, the results for the lifetime ratio, obtained from the maximum-likelihood fit, are presented and discussed in Sec. 6.4.

6.1 Event Selection

For the decays of interest, the $J/\psi(1S)$ resonance is reconstructed by its decay into two muons. Given the expected performance of the LHCb muon system [40], we assume that the dominant source of background will due to candidates containing the actual decay of a $J/\psi(1S)$ into muons. As a result, this study focuses on this type of background².

¹Charge-conjugate decays $B^- \rightarrow J/\psi(\mu^+\mu^-)K^-$ and $\overline{B^0} \rightarrow J/\psi(\mu^+\mu^-)\overline{K^*}(K^-\pi^+)$ are always implied throughout the chapter unless mentioned otherwise.

²The non- $J/\psi(1S)$ background can be treated in just the same way as the $J/\psi(1S)$ background and in practice it is basically the level of background that will deteriorate.

The inclusive $J/\psi(1S) \rightarrow \mu^+\mu^-$ events are generated with BRUNEL v23r7 [74], BOOLE v5r9 [73] and GAUSS v15r11 [72], as a part of the LHCb Data Challenge 2004 Monte Carlo dataset.

The background samples for the two B -decay modes are obtained by applying the selection procedure given in Sec. 5.3, but with ten times enlarged $B^+(B^0)$ invariant mass window, i.e. 500 MeV/c². The larger mass window is used to ensure a sufficient level of background events in the sidebands around the signal peak to properly describe the amount of background in the signal region.

To suppress the total level of background, an additional cut of 2000 MeV/c to the transverse momenta (p_t) of the K^+ and K^* particles is applied. Hence, for the $B^+ \rightarrow J/\psi K^+$ channel only those events with $p_t(K^+) > 2000$ MeV/c are accepted and for $B^* \rightarrow J/\psi K^*$ only those events with $p_t(K^*) > 2000$ MeV/c.

6.1.1 Background Scaling

Experimentally, the background and the signal event rates scale with the corresponding cross sections. In the simulation however, background and signal events are produced separately, with different corresponding "generation luminosities", $\mathcal{L}_{\text{Sig}}^{\text{gen}} \neq \mathcal{L}_{\text{Bkg}}^{\text{gen}}$. Therefore, the background events must be scaled by

$$\kappa = \frac{\mathcal{L}_{\text{Sig}}^{\text{gen}}}{\mathcal{L}_{\text{Bkg}}^{\text{gen}}} . \quad (6.1)$$

The integrated generation luminosities for the signal and the background can be calculated from the total number of generated events and the corresponding cross-sections for the processes to occur within a cone of 400 mrad³ as

$$\begin{aligned} \sigma_{\text{acc}}^{B^+ \rightarrow J/\psi(\mu^+\mu^-)K^+} &= \sigma_{b\bar{b}} \times \epsilon_{b\bar{b}}^{\text{acc}} \times f_B \times 2 \times \text{BR}(B^+ \rightarrow J/\psi K^+) \\ &\quad \times \text{BR}(J/\psi \rightarrow \mu^+\mu^-) , \\ \sigma_{\text{acc}}^{B^0 \rightarrow J/\psi(\mu^+\mu^-)K^*(K^+\pi^-)} &= \sigma_{b\bar{b}} \times \epsilon_{b\bar{b}}^{\text{acc}} \times f_B \times 2 \times \text{BR}(B^0 \rightarrow J/\psi K^*) \quad (6.2) \\ &\quad \times \text{BR}(J/\psi \rightarrow \mu^+\mu^-) \times \text{BR}(K^* \rightarrow K^+\pi^-) , \\ \sigma_{\text{acc}}^{J/\psi \rightarrow \mu^+\mu^-} &= \sigma_{J/\psi} \times \epsilon_{J/\psi}^{\text{acc}} \times \text{BR}(J/\psi \rightarrow \mu^+\mu^-) , \end{aligned}$$

where $\sigma_{b\bar{b}}$ is the $b\bar{b}$ inclusive cross-section, $\epsilon_{b\bar{b}}^{\text{acc}}$ is the angular cut efficiency for b (\bar{b}) to be produced within 400 mrad, f_B is the probability for a \bar{b} (b) to hadronize into B^+ (B^-) or B^0 (\bar{B}^0) meson, $\sigma_{J/\psi}$ is the J/ψ -inclusive cross section and $\epsilon_{J/\psi}^{\text{acc}}$ is the angular cut efficiency for J/ψ to be produced within the acceptance window of 400 mrad. The factor 2 accounts for the production of both \bar{b} and b hadrons. From

³In the Monte-Carlo event generator a cut of 400 mrad is applied to the polar angle of the generated b (\bar{b}) quarks.

Eq. (6.2), Table 6.1 and Table 6.2 it follows that

$$\begin{aligned}\sigma_{\text{acc}}^{B^+ \rightarrow J/\psi(\mu^+\mu^-)K^+} &= 12.51 \text{ nb} , \\ \sigma_{\text{acc}}^{B^0 \rightarrow J/\psi(\mu^+\mu^-)K^*(K^+\pi^-)} &= 10.93 \text{ nb} , \\ \sigma_{\text{acc}}^{J/\psi \rightarrow \mu^+\mu^-} &= 7.71 \mu\text{b} .\end{aligned}\quad (6.3)$$

The invariant mass spectra of the inclusive $J/\psi \rightarrow \mu^+\mu^-$ events that pass the selection criteria for $B^+ \rightarrow J/\psi(\mu^+\mu^-)K^+$ and $B^0 \rightarrow J/\psi(\mu^+\mu^-)K^*(K^+\pi^-)$ are shown in Figures 6.1 and 6.2. The peak around the B^+ , respectively B^0 mass, in these distributions is due to the presence of true signal decays and demonstrates that the selection can obtain a clear signal amongst the background. The two mass spectra are fitted with function

$$F(m) = (1-f) \left[\exp(\alpha m) \right] + f \left[\frac{1}{\sigma_{M_B} \sqrt{2\pi}} \exp \left(-\frac{(m-M_B)^2}{2\sigma_{M_B}^2} \right) \right], \quad (6.4)$$

with exponential and Gaussian terms for the background and signal components. The coefficient f stands for the fraction of signal events in the sample. The values of f obtained from the fit are $7.1\% \pm 1.2\%$ for the B^+ decay and $5.6\% \pm 1.2\%$ for the B^0 decay. Combined with the fact that the total number of selected inclusive $J/\psi \rightarrow \mu^+\mu^-$ events is 948, respectively 971, the estimated signal yield within these samples is

$$\begin{aligned}N_{\text{signal}}^{B^+ \rightarrow J/\psi(\mu^+\mu^-)K^+} &= (7.1\% \pm 1.2\%) \times 948 = 67.31 \pm 11.37 , \\ N_{\text{signal}}^{B^0 \rightarrow J/\psi(\mu^+\mu^-)K^*} &= (5.6\% \pm 1.2\%) \times 971 = 54.38 \pm 11.65 .\end{aligned}\quad (6.5)$$

The values of the integrated generation luminosities for the signal and background events for both channels of interest, together with the background scaling factor κ are listed in Table 6.3. Finally, in Tables 6.4 and 6.5 the event selection results are presented for the full (± 500 MeV/c 2) and reduced (± 30 MeV/c 2) invariant mass ranges. Note, that the number of selected background events is corrected for the estimated number of signal decays in the sample, see Eq. (6.5).

$b\bar{b}$		$B^+ \rightarrow J/\psi K^+$		$B^0 \rightarrow J/\psi K^*$	
$\sigma_{b\bar{b}}$	0.627 mb	$\text{BR}(B^+ \rightarrow J/\psi K^+)$	1.00%	$\text{BR}(B^0 \rightarrow J/\psi K^*)$	1.31%
$\epsilon_{b\bar{b}}^{\text{acc}}$	43.4%	$\text{BR}(J/\psi \rightarrow \mu^+\mu^-)$	5.88%	$\text{BR}(J/\psi \rightarrow \mu^+\mu^-)$	5.88%
f_B	39.1%			$\text{BR}(K^* \rightarrow K^+\pi^-)$	66.67%

Table 6.1. Values of the quantities used to calculate the cross-sections for signal events within a 400 mrad cone, $\sigma_{\text{acc}}^{B^+ \rightarrow J/\psi(\mu^+\mu^-)K^+}$ and $\sigma_{\text{acc}}^{B^0 \rightarrow J/\psi(\mu^+\mu^-)K^*(K^+\pi^-)}$, as given in Eq. (6.2) [27].

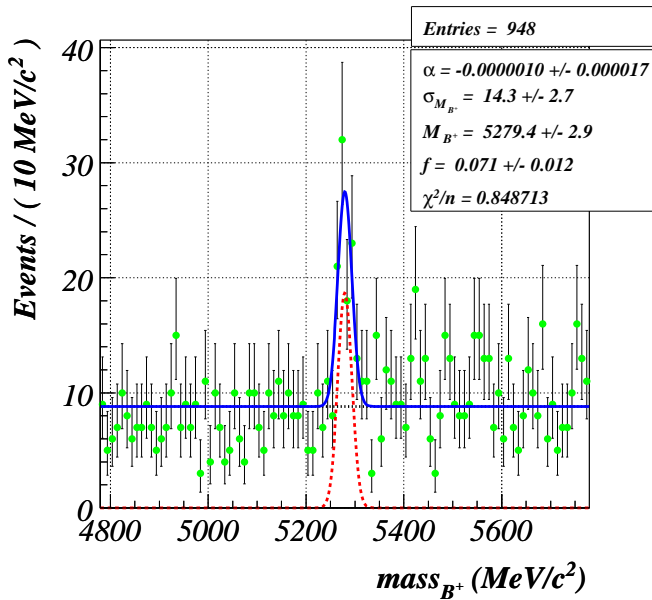


Figure 6.1. Invariant mass distribution of the $J/\psi \rightarrow \mu^+ \mu^-$ inclusive events, selected as $B^+ \rightarrow J/\psi(\mu^+ \mu^-) K^+$.

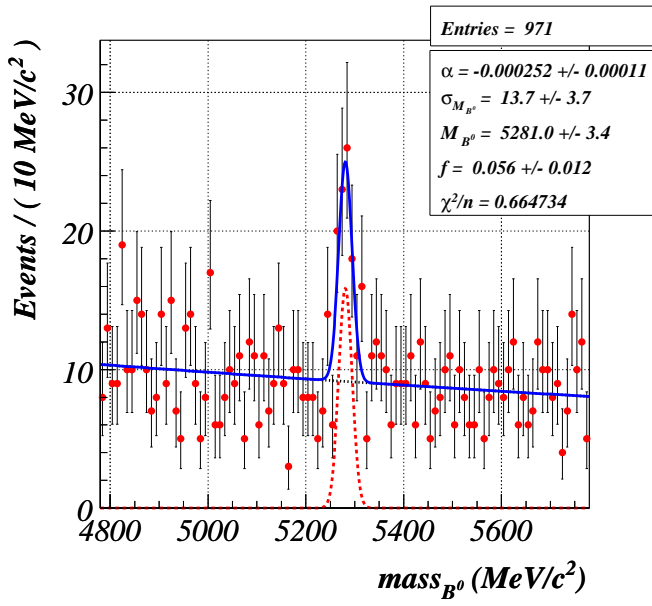


Figure 6.2. Invariant mass distribution of the $J/\psi \rightarrow \mu^+ \mu^-$ inclusive events, selected as $B^0 \rightarrow J/\psi(\mu^+ \mu^-) K^*(K^+ \pi^-)$.

inclusive $J/\psi \rightarrow \mu^+ \mu^-$	
$\sigma_{J/\psi}$	0.337 mb
$\epsilon_{J/\psi}^{\text{acc}}$	38.9%
$\text{BR}(J/\psi \rightarrow \mu^+ \mu^-)$	5.88%

Table 6.2. Values of the quantities used to calculate the cross-section for background events within a 400 mrad cone, $\sigma_{\text{acc}}^{J/\psi \rightarrow \mu^+ \mu^-}$, as given in Eq. (6.2) [27].

channel	# Gen. events (N^{gen})		$\mathcal{L}^{\text{gen}} = N^{\text{gen}} / \sigma_{\text{acc}}, [\text{pb}]^{-1}$		κ
	Signal	Backgr.	Signal	Backgr.	
$B^+ \rightarrow J/\psi K^+$	524000	1404000	41.8865	0.1821	230
$B^0 \rightarrow J/\psi K^*$	644000	1448000	58.9204	0.1878	314

Table 6.3. Generated events in the full invariant mass window of $\pm 500 \text{ MeV}/c^2$, the corresponding integrated generation luminosities and the background scaling factors (κ).

channel	# Sel. events (N^{sel})			Sel. eff. [%]	
	Signal	Backgr.	Backgr. (scaled)	Signal, ϵ_{sel}	Backgr.
$B^+ \rightarrow J/\psi K^+$	25514	881	202558	4.87	0.06
$B^0 \rightarrow J/\psi K^*$	20259	917	287818	3.15	0.06

Table 6.4. Results of the event selection in the full invariant mass window of $\pm 500 \text{ MeV}/c^2$.

channel	# Sel. events (N^{sel})		B/S
	Signal	Backgr. (scaled)	
$B^+ \rightarrow J/\psi K^+$	23951	5274	0.22
$B^0 \rightarrow J/\psi K^*$	18954	7221	0.38

Table 6.5. Results of the event selection in the signal invariant mass window of $\pm 30 \text{ MeV}/c^2$.

6.2 Background and Signal Modeling

6.2.1 Modeling the Background

The background model, $\mathcal{P}^{\text{Bkg}}(m, t_{rec}, \sigma_{t_{rec}})$, is the probability density function (pdf) which describes how background events are distributed as a function of the invariant mass m , the reconstructed lifetime t_{rec} and the error of the reconstructed lifetime $\sigma_{t_{rec}}$. It is constructed from the following components:

- $M^{\text{Bkg}}(m)$ - pdf describing the background mass distribution;
- $S^{\text{Bkg}}(\sigma_{t_{rec}}|m)$ - pdf describing the background proper-time per-event error distribution, given a value of the mass;
- $T^{\text{Bkg}}(t_{rec})$ - pdf describing the background proper-time distribution;

The pdf that describes the mass distribution is represented by a falling exponential function and has the following form,

$$M^{\text{Bkg}}(m) = \exp(\epsilon_m m) , \epsilon_m < 0 , \quad (6.6)$$

with ϵ_m a parameter to be determined from the sidebands.

For the description of the proper-time per-event-error distribution for the background, a Landau function, $L(\sigma_{t_{rec}}, m_L, w_L)$, is chosen with mean m_L and width w_L ,

$$S^{\text{Bkg}}(\sigma_{t_{rec}}|m) = L(\sigma_{t_{rec}}, m_L(m, m_{L0}, m_{L1}), w_L) , \quad (6.7)$$

where the Landau mean is chosen to vary with the mass as

$$m_L = m_{L0} + (m - m_B)m_{L1} , \quad (6.8)$$

with m_{L0} , m_{L1} and w_L free parameters.

Finally, to construct the pdf that describes the proper-time distribution of the background, the reconstructed invariant mass is divided into three ranges:

- ◊ left sideband, with $m_{\min} < m < m_{\min}^{\text{signal}}$,
- ◊ signal mass-range, with $m_{\min}^{\text{signal}} < m < m_{\max}^{\text{signal}}$,
- ◊ right sideband, with $m_{\max}^{\text{signal}} < m < m_{\max}$,

with m_{\min} (m_{\min}^{signal}) and m_{\max} (m_{\max}^{signal}) the minimal and the maximal value of the invariant mass window of 500 (100) MeV/c² around $m_{B^+} = 5279$ MeV/c² and $m_{B^0} = 5279.4$ MeV/c², respectively. Then, the t_{rec} distribution for background events is determined from the events in the sidebands, and is modeled by a ROOKEYSPDF (a functional form explained in Sec. 5.4.3), RKpdf,

$$T^{\text{Bkg}}(t_{\text{rec}}) \equiv \text{RKpdf}^{\text{Bkg}}(t_{\text{rec}}) . \quad (6.9)$$

With these three ingredients, the model of the background events becomes

$$\mathcal{P}^{\text{Bkg}}(m, \sigma_{t_{\text{rec}}}, t_{\text{rec}}) = M^{\text{Bkg}}(m) S^{\text{Bkg}}(\sigma_{t_{\text{rec}}} | m) T^{\text{Bkg}}(t_{\text{rec}}) . \quad (6.10)$$

6.2.2 Modeling the Signal

The probability density function of the signal events will be modeled from similar components,

$$\mathcal{P}^{\text{Sig}}(m, \sigma_{t_{\text{rec}}}, t_{\text{rec}}) = M^{\text{Sig}}(m) S^{\text{Sig}}(\sigma_{t_{\text{rec}}} | m) T^{\text{Sig}}(t_{\text{rec}} | \sigma_{t_{\text{rec}}}) . \quad (6.11)$$

In analogy to the background case, $M^{\text{Sig}}(m)$ describes the signal mass distribution, $S^{\text{Sig}}(\sigma_{t_{\text{rec}}})$ the signal $\sigma_{t_{\text{rec}}}$ distribution and $T^{\text{Sig}}(t_{\text{rec}} | \sigma_{t_{\text{rec}}})$ the signal t_{rec} distribution given a value of $\sigma_{t_{\text{rec}}}$.

The pdf that describes the mass distribution is now chosen to have a Gaussian functional form,

$$M^{\text{Sig}}(m) = \frac{1}{\sigma_{M_B} \sqrt{2\pi}} \exp(-(m - M_B)^2 / 2\sigma_{M_B}^2) . \quad (6.12)$$

The parameters M_B and σ_{M_B} represent the value of the mass of the $B^+(B^0)$ meson and its resolution respectively, and will be extracted from the fit.

The $S^{\text{Sig}}(\sigma_{t_{\text{rec}}})$ p.d.f. is characterized with ROOKeYSPDF,

$$S^{\text{Sig}}(\sigma_{t_{\text{rec}}}) \equiv \text{RKpdf}^{\text{Sig}}(\sigma_{t_{\text{rec}}}) . \quad (6.13)$$

The function $T^{\text{Sig}}(t_{\text{rec}})$ has the form

$$T^{\text{Sig}}(t_{\text{rec}} | \sigma_{t_{\text{rec}}}) = E(t_{\text{rec}}) \otimes R(t_{\text{rec}} | \sigma_{t_{\text{rec}}}) = \int dt' e^{-\frac{t'}{\tau_B}} R(t - t' | \sigma_{t_{\text{rec}}}) , \quad (6.14)$$

and depends on the five resolution model parameters plus the average lifetime $\tau_{B^+(B^0)}$ of the $B^+(B^0)$ mesons, as described in the previous chapter; see Eq. (5.18) and Eq. (5.7).

6.2.3 Modeling the Signal and Background Simultaneously

The total pdf, \mathcal{P}^{Tot} , describes the signal and background distributions together, and is composed from \mathcal{P}^{Sig} (see Eq. (6.11)) and \mathcal{P}^{Bkg} (see Eq. (6.10)) as follows

$$\mathcal{P}^{\text{Tot}}(m, \sigma_{t_{\text{rec}}}, t_{\text{rec}}) = f_{\text{sig}} \mathcal{P}^{\text{Sig}}(m, \sigma_{t_{\text{rec}}}, t_{\text{rec}}) + (1 - f_{\text{sig}}) \mathcal{P}^{\text{Bkg}}(m, \sigma_{t_{\text{rec}}}, t_{\text{rec}}) . \quad (6.15)$$

Here, f_{sig} is the fraction of the signal events over the sum of signal and background events in the entire mass interval, i.e. $\pm 500 \text{ MeV}/c^2$.

During the maximum-likelihood-fitting procedure that will be described in Sec. 6.4.1, we will determine ϵ_m , M_B , σ_{M_B} and f_{sig} solely based on the invariant mass distribution,

$$M^{\text{Tot}}(m) = f_{\text{sig}} M^{\text{Sig}}(m) + (1 - f_{\text{sig}}) M^{\text{Bkg}}(m) , \quad (6.16)$$

after which these four parameters will be fixed for the remaining fitting steps.

6.3 Determination of Lifetime with Signal Only

Ideally, looking only at the selected signal events (see Sec. 6.1) one can extract the resolution model parameters, \vec{p}_{resid} , from Monte-Carlo (MC) truth, as described in the previous chapter, by applying the developed resolution model for the time residuals ($t_{\text{rec}} - t_{\text{true}}$); see Fig. 6.3 (6.5) and Table 6.6 (6.7). (Note the difference between Fig. 6.3 (6.5) and Fig. 5.12 (5.13), expressed in reduced tails in the $(t_{\text{rec}} - t_{\text{true}})$ distribution. The tails are reduced because of the $K^+(K^*) p_t$ cut ($p_t > 2000 \text{ MeV}/c$) applied during the event selection (see Sec. 6.1) that decreases the selected event yield.) The same parameters, $\vec{p}_{t_{\text{rec}}}$, can be obtained from "real" data, i.e. without using t_{true} , but using solely the reconstructed signal $B^+(B^0)$ proper-time information, t_{rec} ; see the 3rd column of Table 6.6 (6.7). Fitting t_{rec} only, results in a decreased sensitivity to the resolution function parameters with respect to fitting $(t_{\text{rec}} - t_{\text{true}})$, because only events at short lifetimes can contribute. It is therefore important that these events are sufficiently representative for the entire sample.

Comparing the values of the two sets of parameters, \vec{p}_{resid} and $\vec{p}_{t_{\text{rec}}}$, a mismatch is observed, specially in $F1$ and TAU for $B^+ \rightarrow J/\psi K^+$ ⁴. The large uncertainty of $F1$ and TAU shows that the sensitivity to these parameters is limited due to the limited amount of available data.

To investigate the dependence of the fit on the parameters, the t_{rec} distribution is now fitted in two ways, once with a model with fixed resolution model parameters, determined from MC, and only τ_B left free (the solid curve), and once with the nominal resolution model with free resolution model parameters (the dashed curve); see Fig. 6.4 (6.6). The result obtained from the maximum-likelihood fit with fixed parameters is

$$\tau_{B^+} = 1.705 \pm 0.011 \text{ ps}, \quad \tau_{B^0} = 1.565 \pm 0.011 \text{ ps}. \quad (6.17)$$

The bottom plots of Fig. 6.4 (6.6) show the fit residuals (Eq. (5.1)) with fixed parameters, superimposed with the curves representing the differences if the fit parameters are left free. As expected, the largest difference between the fits is seen around

⁴Recall that the parameter $F1$ is the fraction of the pdf (see Eq. (5.14)) that describes the asymmetric form of the residual distribution, $(t_{\text{rec}} - t_{\text{true}})$, and TAU is the parameter that describes the size of this asymmetry.

$t_{rec} = 0$, which is the region where the resolution parameters are determined. However, the region of large t_{rec} is described equally well, which is the region where τ_B is determined. The value for τ_B obtained with free parameters, see the 4th column of Table 6.6 is indeed well within the error of Eq. (6.17).

Another aspect is that $F1$ and TAU are strongly correlated, because they are both related to the description of the asymmetry of the residual distribution ($t_{rec} - t_{true}$). If $F1 = 0$, then the likelihood does not depend on TAU . Hence, if there is no evidence for an asymmetric tail (as in the case with $B^+ \rightarrow J/\psi K^+$) in the data, $F1$ goes to 0 and TAU is undetermined. This is the reason to fix both $F1$ and TAU ($F1 = 0, TAU = 1$) during the fit for the channel $B^+ \rightarrow J/\psi K^+$. The resulting values for the rest of parameters are shown in the last two columns of Table 6.6. It can be seen that now (with fixed $F1$ and TAU), the error on τ_{B^+} is of the same order of magnitude as the one obtained with the fit with all parameters fixed but τ_{B^+} (see Eq. (6.17)).

With $B^0 \rightarrow J/\psi K^*$ it is not necessary to fix any of the parameters. Given that there are more negative t_{rec} events available in this mode, there is an evidence for an asymmetric tail, which can be fitted by the model.

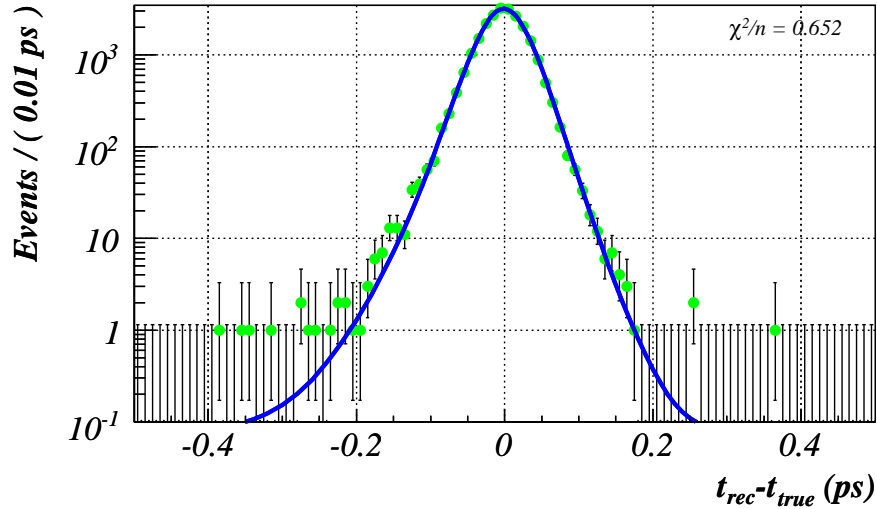


Figure 6.3. Projection of the unbinned maximum-likelihood fit to $(t_{rec} - t_{true})$ for the signal $B^+ \rightarrow J/\psi K^+$ events. Parameters of the fit are displayed in Table 6.6.

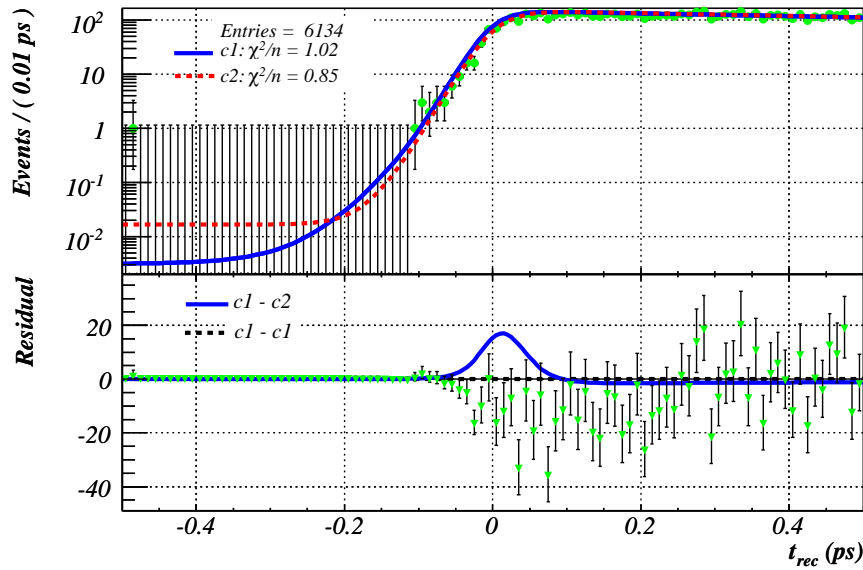


Figure 6.4. Top: Solid curve ($c1$) - projection of the unbinned maximum-likelihood fit with fixed $F1$, $F2$, GM , GS and TAU to t_{rec} of the signal $B^+ \rightarrow J/\psi K^+$ events. Dashed curve ($c2$) - projection of the fit with free resolution model parameters to t_{rec} . The parameter values obtained with $c2$ are listed in Table 6.6. Bottom: Fit residuals of $c1$, with superimposed curves ($c1-c1$) and ($c1-c2$).

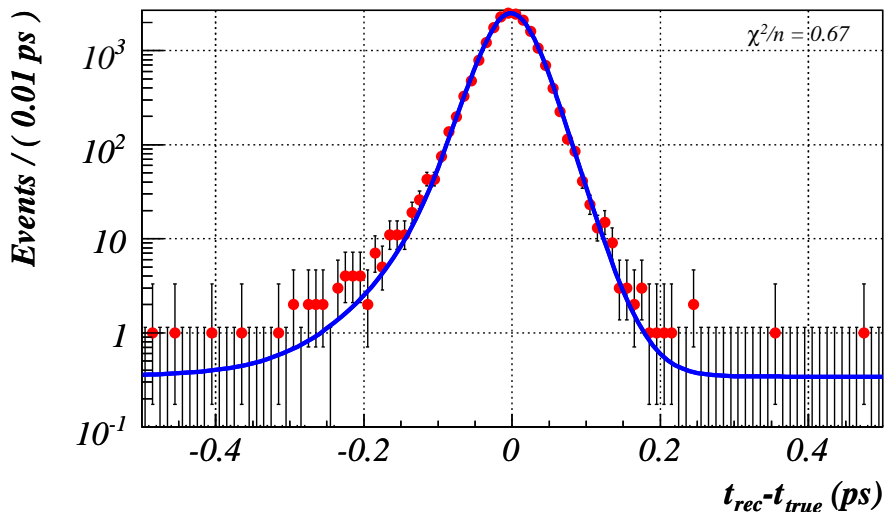


Figure 6.5. Projection of the unbinned maximum-likelihood fit to $(t_{rec} - t_{true})$ for the signal $B^* \rightarrow J/\psi K^0$ events. Parameters of the fit are displayed in Table 6.7.

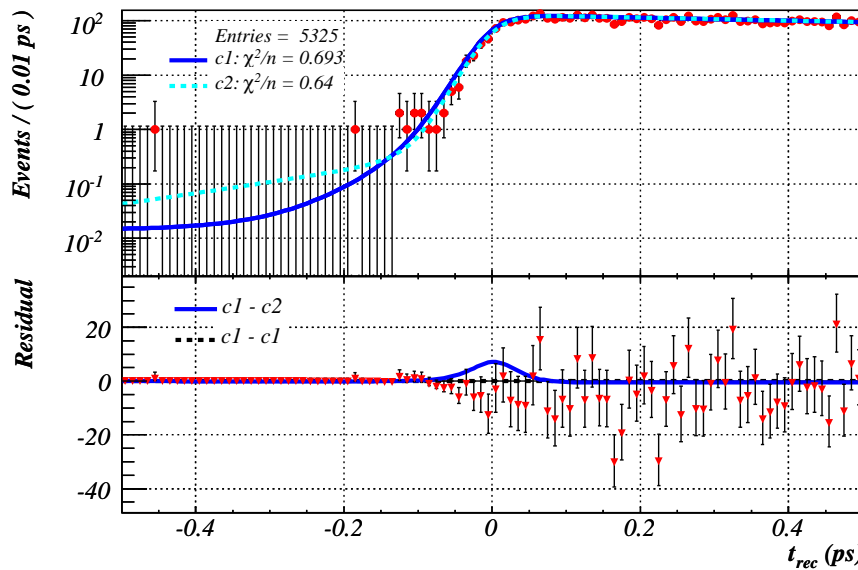


Figure 6.6. Top: Solid curve ($c1$) - projection of the unbinned maximum-likelihood fit with fixed $F1$, $F2$, GM , GS and TAU to t_{rec} of the signal $B^0 \rightarrow J/\psi K^*$ events. Dashed curve ($c2$) - projection of the fit with free resolution model parameters to t_{rec} . The parameter values obtained with $c2$ are listed in Table 6.7. Bottom: Fit residuals of $c1$, with superimposed curves ($c1-c1$) and ($c1-c2$).

Parameter	Fit to $(t_{rec} - t_{true})$ [\vec{p}_{resid}]	Error	Fit to t_{rec} [$\vec{p}_{t_{rec}}$]	Error	Fit to t_{rec}	Error
					fixed $F1$ and TAU	
τ_{B^+}			1.6927	0.0011	1.6930	0.011
$F1$	0.0403	0.0092	0.0000	0.1200		
$F2$	0.0003	0.0002	0.0017	0.0001	0.0017	0.0005
GM	-0.0301	0.0110	0.2919	0.0061	0.3170	0.0830
GS	1.1601	0.0070	1.3277	0.0057	1.2560	0.0790
TAU	1.0000	0.2700	1.0000	91169		

Table 6.6. Resolution model parameters obtained with fit to time residuals ($t_{rec} - t_{true}$) and with fit to t_{rec} for the signal $B^+ \rightarrow J/\psi K^+$ events.

Parameter	Fit to $(t_{rec} - t_{true})$ [\vec{p}_{resid}]	Error	Fit to t_{rec} [$\vec{p}_{t_{rec}}$]	Error
τ_{B^+}			1.5640	0.0110
$F1$	0.0259	0.0078	0.0043	0.0031
$F2$	0.0018	0.0005	0.0000	0.0001
GM	-0.0554	0.0110	0.1000	0.0790
GS	1.1901	0.0079	1.2150	0.0840
TAU	1.6900	0.2700	7.6000	3.1000

Table 6.7. Resolution model parameters obtained with fit to time residuals ($t_{rec} - t_{true}$) and with fit to t_{rec} for the signal $B^0 \rightarrow J/\psi K^*$ events.

6.4 Results

6.4.1 Maximum-Likelihood Fit including Background

As was stated in Sec. 6.1.1, the selected background events have to be scaled with a factor κ , given in Table 6.3, in order to get a coherent signal-plus-background picture. This scaling is performed by generating the estimated number of background events (see Table 6.4) according to the background model, $\mathcal{P}^{\text{Bkg}}(m, \sigma_{t_{\text{rec}}}, t_{\text{rec}})$ (see Eq. (6.10)), determined on the basis of the original, selected background sample. The ROOFIT toolkit for data modeling [76] is used to accomplish both the event generation and the subsequent maximum-likelihood fitting.

To create a realistic data sample, the selected signal events and the selected, scaled background events are merged, forming one data set containing the values for m , t_{rec} and $\sigma_{t_{\text{rec}}}$. This data set is then subject to the maximum-likelihood fit with the composite model given in Eq. (6.15). Since this is a 3-dimensional likelihood fit with 12 free parameters and because of the large amount of data ($\sim 300\,000$ events), a large amount of CPU is required. In order to minimize the required CPU power, the fit is performed in three consecutive steps, listed below. In addition, the parameters m_{L0} , m_{L1} and w_L of the Landau function describing the background proper-time per-event-errors, remain fixed to their nominal values during the fit. Their values are defined separately in a preliminary stage, and are set to $m_{L0} = 0.03$ ps, $m_{L1} = -0.01$ ps/[MeV/c²] and $w_L = 0.004$ ps.

Maximum-likelihood-fitting steps

1. The mass pdf M^{Tot} (see Eq. (6.16)) is fitted to the data.
2. The parameters M_B , σ_{M_B} , ϵ_m and f_{sig} , obtained from the M^{Tot} fit are fixed.
3. The total pdf \mathcal{P}^{Tot} is fitted to the data with only 6 free parameters - τ_B , $F1$, $F2$, GM , GS and TAU (in the case of $B^+ \rightarrow J/\psi K^+$, $F1$ and TAU are also fixed (see Sec. 6.3)).

The projections of the \mathcal{P}^{Tot} maximum-likelihood fit (the solid curves) on the m , t_{rec} and $\sigma_{t_{\text{rec}}}$ distributions for both decay channels, are shown in Fig. 6.7 and Fig. 6.9. The dashed curves in the same figures represent the background and the signal components of the model, respectively. In Fig. 6.8 and Fig. 6.10 the same projections are shown in the signal mass-range and in the two sideband mass-ranges (see Sec. 6.2.1).

The parameters extracted from the fit are listed in Tables 6.8 and 6.9.

M_{B^+}	5278.7000 ± 0.1190	[MeV/c ²]
$\sigma_{M_{B^+}}$	14.9500 ± 0.1080	[MeV/c ²]
ϵ_m	-0.0050 ± 0.0000	[MeV/c ²] ⁻¹
f_{sig}	0.1114 ± 0.0008	
τ_{B^+}	1.6913 ± 0.0109	[ps]
$F2$	0.0017 ± 0.0005	
GM	0.2935 ± 0.1660	
GS	1.4434 ± 0.1970	

Table 6.8. Values of the parameters obtained with maximum-likelihood fit to the total signal plus background data for the $B^+ \rightarrow J/\psi K^+$ decay channel.

M_{B^0}	5278.5000 ± 0.1400	[MeV/c ²]
$\sigma_{M_{B^0}}$	14.1230 ± 0.1350	[MeV/c ²]
ϵ_m	-0.0050 ± 0.0000	[MeV/c ²] ⁻¹
f_{sig}	0.0642 ± 0.0006	
τ_{B^0}	1.5622 ± 0.0116	[ps]
$F1$	0.0039 ± 0.0040	
$F2$	0.0000 ± 0.0001	
GM	0.3090 ± 0.1600	
GS	1.5518 ± 0.1800	
TAU	7.9454 ± 3.9700	

Table 6.9. Values of the parameters obtained with maximum-likelihood fit to the total signal plus background data for the $B^0 \rightarrow J/\psi K^*$ decay channel.

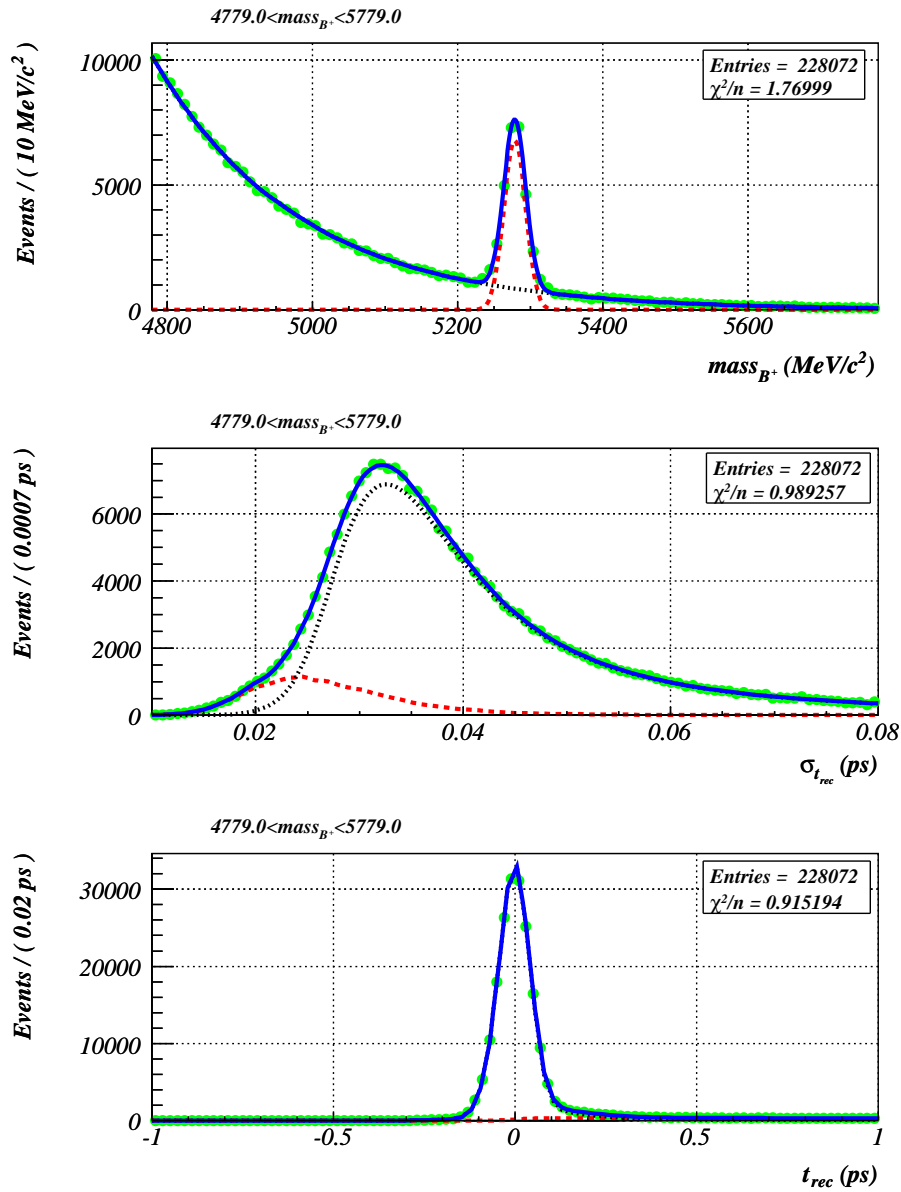


Figure 6.7. Projections of the \mathcal{P}^{Tot} maximum-likelihood fit (the solid curves) on m , $\sigma_{t_{\text{rec}}}$ and t_{rec} in the full invariant mass-range. The dashed curves represent the signal and background contributions to \mathcal{P}^{Tot} . The decay channel is $B^+ \rightarrow J/\psi K^+$.

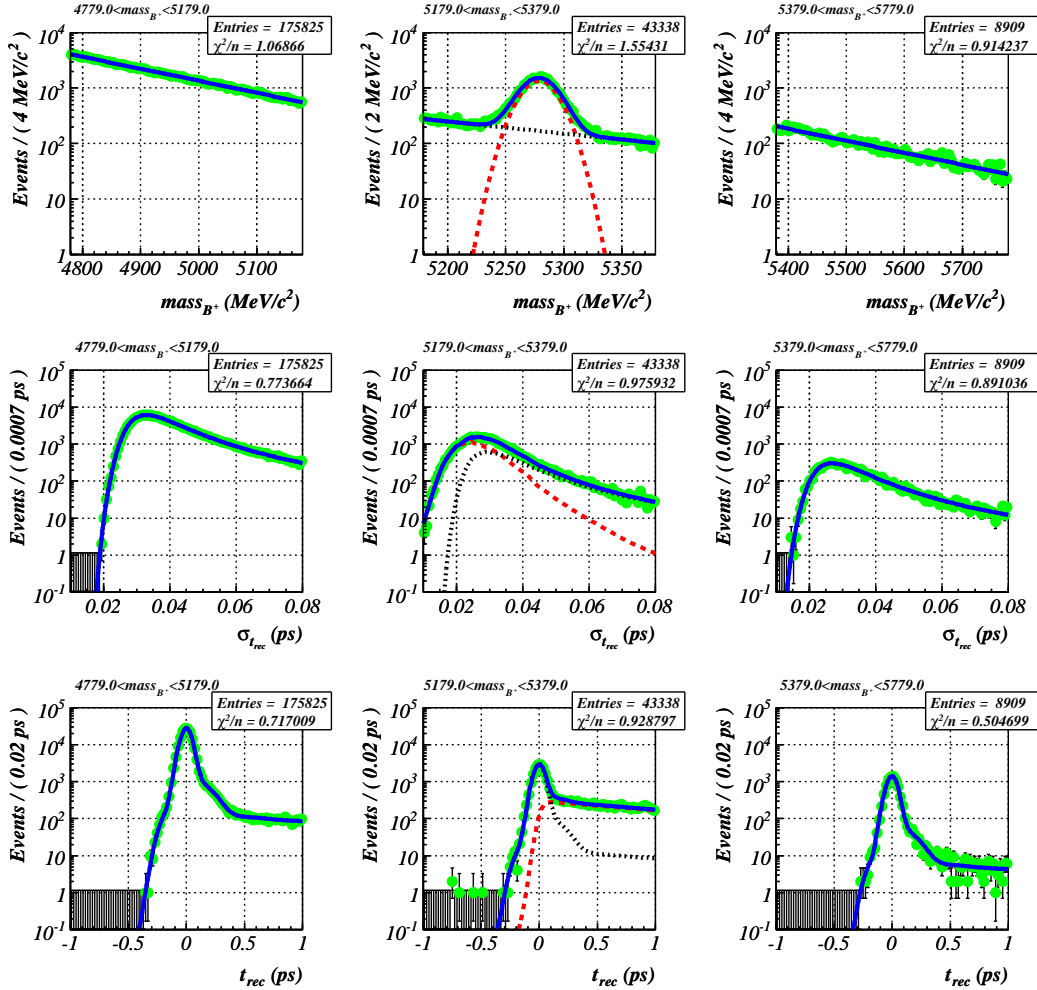


Figure 6.8. Projections of the \mathcal{P}^{Tot} maximum-likelihood fit (the solid curves) on m , $\sigma_{t_{rec}}$ and t_{rec} in the signal and in the sidebands mass-ranges. The dashed curves represent the signal and background contributions to \mathcal{P}^{Tot} . The decay channel is $B^+ \rightarrow J/\psi K^+$.

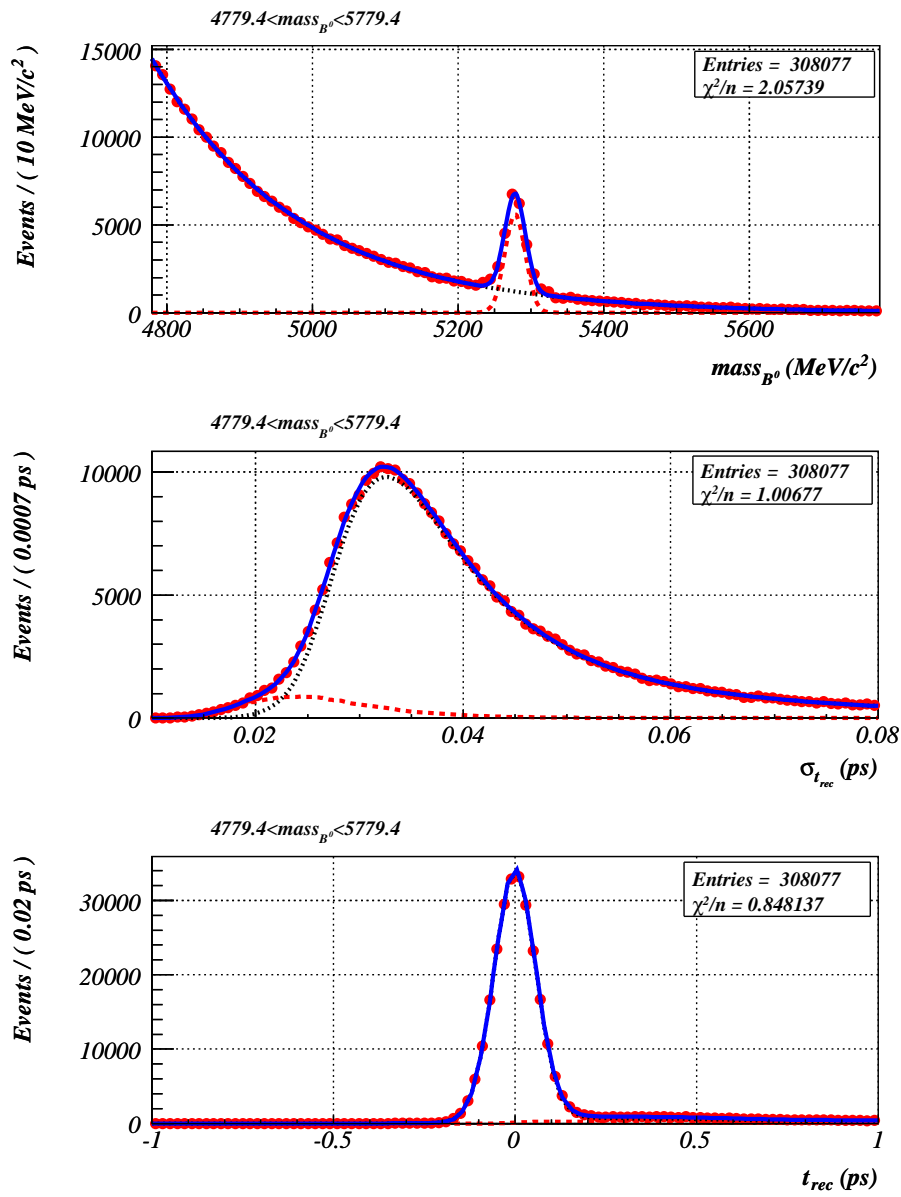


Figure 6.9. Projections of the \mathcal{P}^{Tot} maximum-likelihood fit (the solid curves) on m , $\sigma_{t_{\text{rec}}}$ and t_{rec} in the full invariant mass-range. The dashed curves represent the signal and background contributions to \mathcal{P}^{Tot} . The decay channel is $B^0 \rightarrow J/\psi K^*$.

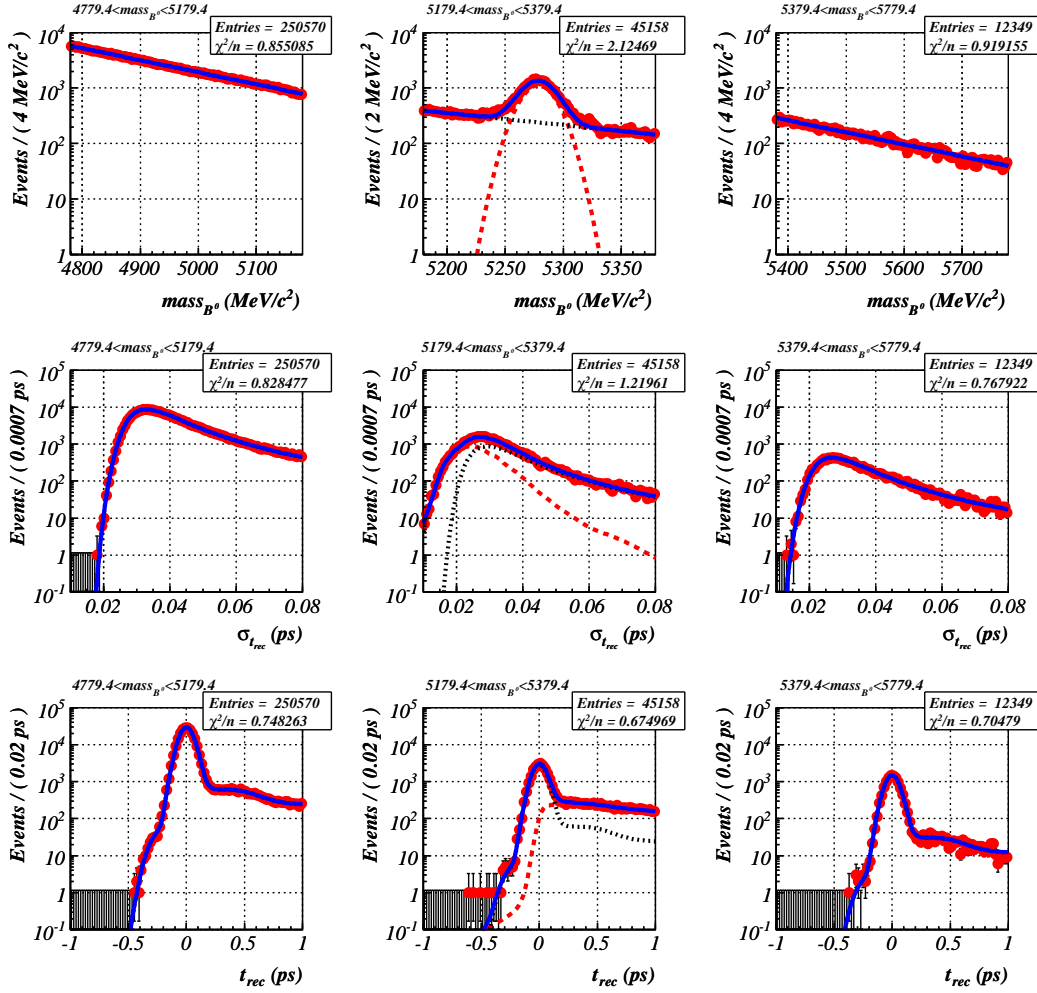


Figure 6.10. Projections of the P^{Tot} maximum-likelihood fit (the solid curves) on m , $\sigma_{t_{rec}}$ and t_{rec} in the signal and in the sidebands mass-ranges. The dashed curves represent the signal and background contributions to P^{Tot} . The decay channel is $B^0 \rightarrow J/\psi K^*$.

6.4.2 Dependence of the Resolution Model Parameters on the Background

The dependence of the resolution model parameters on the amount of background events has been studied. The results are shown in Fig. 6.11 and Fig. 6.12, where the parameters are plotted as a function of the fraction of the total amount of background. It can be seen that decreasing the background does not change the parameters values significantly. Their variation remains within their statistical error and no specific trend is observed.

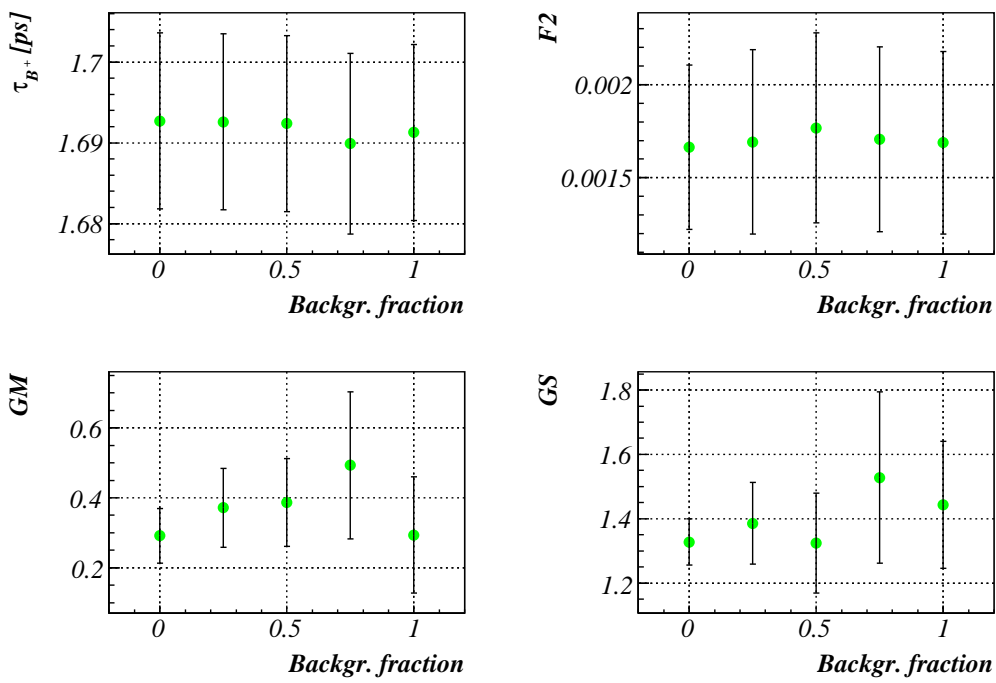


Figure 6.11. Resolution model parameters versus the background fraction for channel $B^+ \rightarrow J/\psi K^+$.

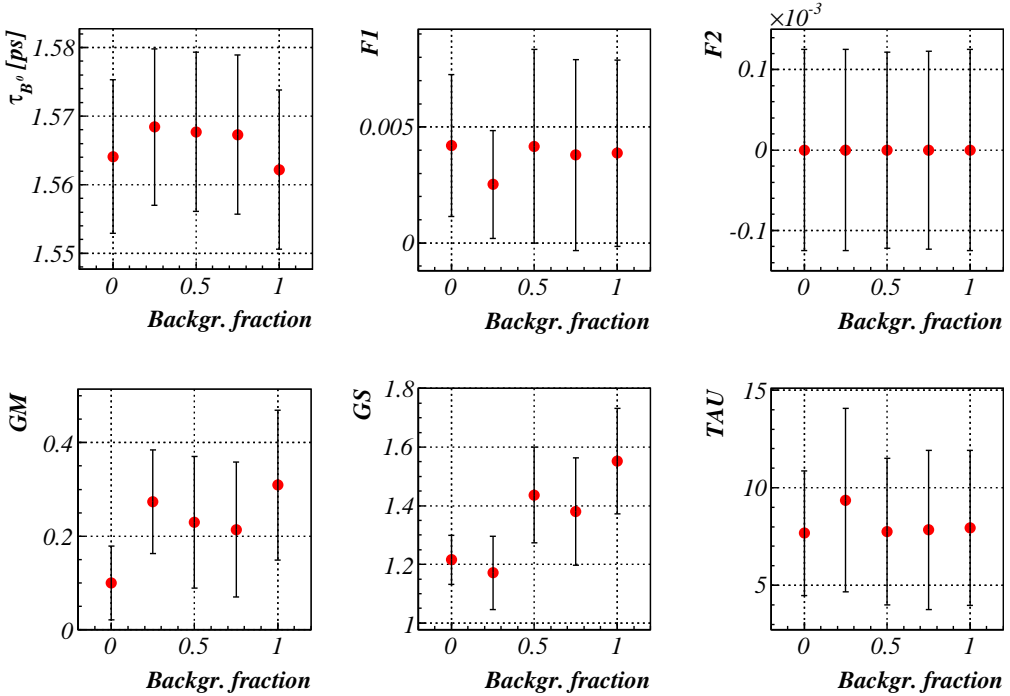


Figure 6.12. Resolution model parameters versus the background fraction for channel $B^0 \rightarrow J/\psi K^*$.

6.4.3 τ_{B^+}/τ_{B^0}

Based on the results reported in Table 6.8 and Table 6.9, the ratio of lifetimes of B^+ and B^0 mesons is evaluated, leading to the value

$$\frac{\tau_{B^+}}{\tau_{B^0}} = 1.0826 \pm 0.0106 . \quad (6.18)$$

This result roughly corresponds to about only 9 days of LHCb data taking. Note also that within its accuracy the result matches with the ratio of the input MC simulation values (see Table 5.2), which is 1.0879.

It is important to stress that the purpose of our study is mainly to obtain an estimation of the precision, $\Delta(\tau_{B^+}/\tau_{B^0})$, of the lifetime ratio at LHCb. The central value of the ratio will be interesting once LHCb takes real data.

In order to acquire an estimate of the resolution of (τ_{B^+}/τ_{B^0}) , equal amounts of data (integrated luminosity) for both decay channels are needed. Since the amounts differ in this study, the behavior of the τ_B error, σ_{τ_B} , as a function of the number of events is investigated. By extrapolation, σ_{τ_B} is predicted for an integrated luminosity of $2 [\text{fb}]^{-1}$ (1 year of LHCb data-taking at nominal luminosity) for both decays. In Fig. 6.13 and Fig. 6.14 the dependence of $\sigma_{\tau_{B^+/0}}$ on the number of signal events is presented.

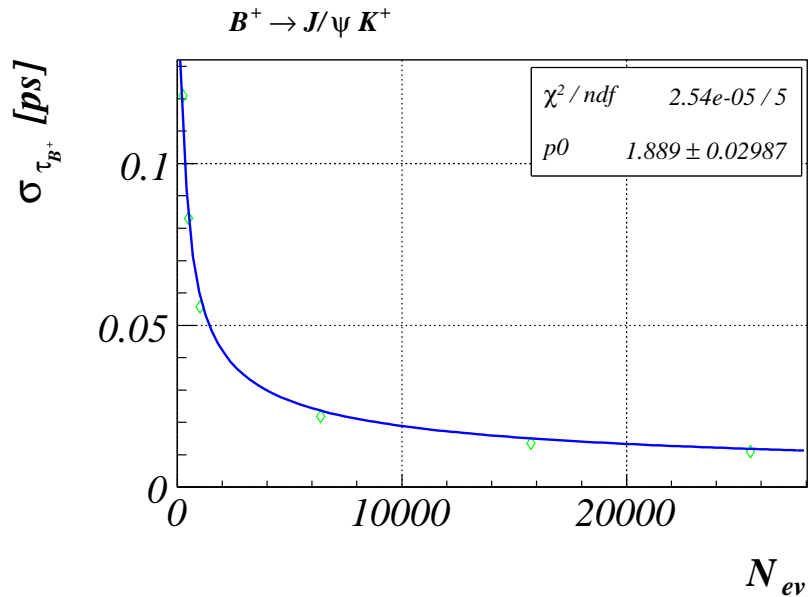


Figure 6.13. B^+ lifetime resolution as a function of the number of signal events. The data points are fitted with function $p0 / \sqrt{N_{ev}}$.

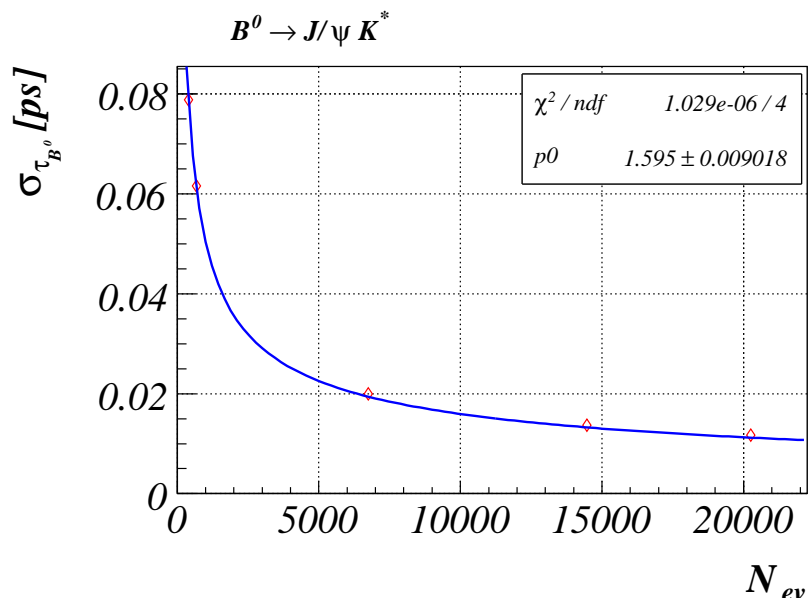


Figure 6.14. B^0 lifetime resolution as a function of the number of signal events. The data points are fitted with function $p0 / \sqrt{N_{ev}}$.

The data points are fitted with the following function

$$\sigma_\tau = p0/\sqrt{N_{\text{ev}}} , \quad (6.19)$$

where $p0$ is a parameter often referred to as a single event sensitivity, and is defined from the fit.

The number of signal events in 1 year of LHCb operation for both channels is calculated using the relation

$$N_{\text{ev}}^{1y} = 2[\text{fb}]^{-1} \times \sigma_{\text{acc}} \times \epsilon_{\text{sel}} , \quad (6.20)$$

with the cross-section σ_{acc} , and the selection efficiency ϵ_{sel} , taken from Eq (6.3) and Table (6.4). Thus, using Eq. (6.20) and the $p0$ fit, the values $\sigma_{\tau_{B^+}}(N_{\text{ev}}^{1y})$ and $\sigma_{\tau_{B^0}}(N_{\text{ev}}^{1y})$ are derived and listed in Table 6.10.

channel	N_{ev}^{1y}	$p0$ [ps]	$\sigma_{\tau_B}(N_{\text{ev}}^{1y})$ [fs]
$B^+ \rightarrow J/\psi(\mu^+\mu^-)K^+$	1.22×10^6	1.889 ± 0.030	1.71 ± 0.03
$B^0 \rightarrow J/\psi(\mu^+\mu^-)K^*(K^+\pi^-)$	6.89×10^5	1.595 ± 0.009	1.92 ± 0.01

Table 6.10. Number of selected signal events N_{ev}^{1y} , single event error $p0$, and lifetime error $\sigma_{\tau_B}(N_{\text{ev}}^{1y})$ in 1 year of LHCb operation, for both decay channels.

This demonstrates that in 1 year of data-taking at nominal luminosity, LHCb will improve the precision of the current experimental world-average $B^+(B^0)$ lifetime measurement significantly. The improvement of the measurement will be 7 (5) times (see Table 1.3 for comparison) neglecting the contribution of any possible systematics effects. However, it is quite possible that the measurement of $B^+(B^0)$ lifetime is systematics limited. Given that the LHCb B proper-time resolution is intrinsically so good, one can expect the systematic errors due to this to be smaller than what can be achieved in the current experiments.

Taking into account the obtained $\sigma_{\tau_{B^+}}(N_{\text{ev}}^{1y})$ and $\sigma_{\tau_{B^0}}(N_{\text{ev}}^{1y})$, the resolution on (τ_{B^+}/τ_{B^0}) in 1 year of LHCb data-taking amounts to a ‘statistical reach’⁵ of

$$\Delta\left(\frac{\tau_{B^+}}{\tau_{B^0}}\right) = 0.0017 . \quad (6.21)$$

The above result shows, that in 1 year of operation LHCb will achieve a sensitivity on τ_{B^+}/τ_{B^0} , which is significantly better than the current sensitivity, or neglecting the systematics, factor of 5.3 better.

This shows that LHCb experiment will be able to contribute significantly to scrutinize the Heavy Quark Effective model.

⁵Again, note that this result does not include the contribution of possible systematic effects.

6.4.4 Conclusion

A method for the determination of B^+ and B^0 lifetimes, and the corresponding resolution model parameters has been established. The method is applied on a data-set including signal and background events.

The results (that do not include the influence of possible systematic deviations) show that in 1 year of data-taking at nominal luminosity, the LHCb experiment will measure the lifetimes of the B^+ and B^0 mesons with a resolution of 1.71 ± 0.03 [fs] and 1.92 ± 0.01 [fs] respectively. This is an improvement of 7 (5) times over the present resolution on the B^+ (B^0) lifetime. Consequently, in 1 year of data-taking LHCb will measure the ratio τ_{B^+}/τ_{B^0} with a precision of 0.0017, improving the current experimental τ_{B^+}/τ_{B^0} precision with a factor of 5.3.

Bibliography

- [1] H. Diels and W. Kranz, *Die Fragmente der Vorsokratiker*, 6th ed., Berlin, 1951.
- [2] C.C.W. Taylor, *The Atomists: Leucippus and Democritus. Fragments, A Text and Translation with Commentary*, Toronto, 1999.
- [3] E. Komatsu *et al.*(WMAP Collaboration), *Five-Year Wilkinson Microwave Anisotropy Probe (WMAP) Observations: Cosmological Interpretation*, arXiv:astro-ph/0803.0547v1, (2008).
- [4] AMS-01 collaboration (M. Aguilar *et al.*), *The Alpha Magnetic Spectrometer (AMS) on the International Space Station, Part I, Results from the test flight on the Space Shuttle*, Physics Reports 366/6 (2002) 331.
- [5] A. D. Sakharov, *Violation of CP invariance, C asymmetry, and baryon asymmetry in the universe*, Pisma Zh. Eksp. Teor. Fiz. 5 (1967) 32-35.
- [6] J.H. Christenson, J.W. Cronin, V.L. Fitch, and R. Turlay, *Evidence for the 2π decay of the K_2^0 meson*, Phys. Rev. Lett. 13 (1964) 138.
- [7] Babar Collaboration (B. Aubert *et al.*), *Measurement of the CP asymmetry amplitude $\sin 2\beta$ with B^0 mesons*, Phys. Rev. Lett. 89, 201802 (2002).
- [8] Belle Collaboration (K. Abe *et al.*), *Measurement of CP violation parameter $\sin 2\phi$ with 152 million B anti- B pairs*, Belle-Conf-0353, (2003).
- [9] F. J. Botella, G. C. Branco, and M. Nebot, *CP violation and limits on New Physics including recent B_s measurements*, Nuclear Physics B 768, (2007).
- [10] G. Buchalla, *Heavy Quark Theory*, hep-ph/0202092, 2002.
- [11] M. Luke, *Bottom Quark Physics and the Heavy Quark Expansion*, Theoretical Advanced Study Institute in Elementary Particle Physics (TASI), Colorado, 2002.
- [12] W.N. Cottingham and D.A. Greenwood, *An Introduction to the Standard Model of Particle Physics*, Cambridge University Press, Cambridge, 1998.
- [13] W.-M.Yao *et al.*, *Review of Particle Physics*, Journal of Physics G 33, 1, (2006).
- [14] M.Kobayashi and T.Maskawa, *CP violation in the renormalizable theory of weak interaction*, Prog. Theor. Phys. 49 (1973) 652.
- [15] L. Wolfenstein, Phys. Rev. D 66, 010001-118 (2002).
- [16] J. Tilburg, *Track simulation and reconstruction in LHCb*, Ph.D. thesis, 2005.
- [17] C. Jarlskog, Phys. Rev. Lett. 55, 1039 (1985).
- [18] V. Gibson, *B physics*, Lecture notes at 57th Scottish Universities Summer School, St Andrew Scotland, 2003.

- [19] ARGUS Collaboration (H.Albrecht *et al.*), *Observation of $B^0 - \bar{B}^0$ mixing*, Phys. Lett. B192 (1987) 245).
- [20] CDF Collaboration, *Measurement of the $B_s^0 - \bar{B}_s^0$ Oscillation Frequency*, hep-ex/0606027v1, 2006.
- [21] BaBar Collaboration, *Search for T , CP and CPT Violation in $B^0 - \bar{B}^0$ Mixing with Inclusive Dilepton Events*, Phys.Rev.Lett.96:251802,2006.
- [22] L. Fernandez, *Exclusive Trigger Selections and Sensitivity to the $B_s - \bar{B}_s$ Mixing Phase at LHCb*, Ph.D. thesis, 2006.
- [23] D0 collaboration, *Measurement of B_s^0 mixing parameters from the flavor-tagged decay $B_s^0 \rightarrow J/\psi\phi$* , arXiv:hep-ex/0802.2255v1, 2008.
- [24] H.-G. Moser and A. Roussarie, *Mathematical methods for $B^0\bar{B}^0$ oscillation analyses*, Nucl. Instr. and Methods in Phys. Res. A 384 (1997) 491-505.
- [25] U. Nierste, *B_d and B_s mixing: mass and width differences and CP violation*, hep-ph/0612310v2, 2007.
- [26] J. P. Leveille, *Proceedings of the Ithaca B-decay Workshop, What Can We Hope To Learn From B Meson Decay*, University of Rochester, Ithaca, New York, 1981, UM HE 81-18.
- [27] S. Eidelman *et al.*, *Review of Particle Physics*, Physics Letters B 592, 1, (2004).
- [28] G. Bellini, I.I. Biggi, and P.J. Dorgan, *Lifetimes of Charm and Beauty Hadrons*, Phys. Rep. 289, 1 (1997).
- [29] CDF Collaboration, *Measurement of Exclusive B Lifetimes in the modes $B^+ \rightarrow J/\psi K^+$, $B^0 \rightarrow J/\psi K^{*0}$, $B^0 \rightarrow J/\psi K^0_s$, $B_s^0 \rightarrow J/\psi\phi$ and $\Lambda_b \rightarrow J/\psi\Lambda$, and measurement of the B^+/B^0 , B_s^0/B^0 and Λ_b/B^0 lifetime ratios*, CDF note 8524, 2007.
- [30] C. Tarantino, *Beauty Hadron Lifetimes and B-Meson CP-Violation Parameters from Lattice QCD*, arXiv:hep-ph/0310241v2, 2003.
- [31] LHC Study Group, P. Lefevre, and T. Pettersson, *The Large Hadron Collider: Conceptual design*, CERN/AC/95-05(LHC), 1995.
- [32] ATLAS Collaboration, *ATLAS: Technical Proposal for a General-Purpose pp Experiment at the Large Hadron Collider at CERN*, CERN-LHCC/94-43, 1994.
- [33] CMS Collaboration, *Technical Proposal*, CERN-LHCC/94-38, 1994.
- [34] ALICE Collaboration, *A Large Ion Collider Experiment - Technical Proposal*, CERN-LHCC/95-71, 1995.
- [35] R. Eijk, *Track reconstruction in the LHCb experiment*, Ph.D. thesis, 2002.
- [36] T. Sjstrand *et al.*, *High-Energy-Physics Event Generation with Pythia 6.1*, hep-ph/0010017, 2001.
- [37] LHCb Collaboration, *LHCb - Technical Proposal*, CERN-LHCC/98-4, 1998.
- [38] LHCb collaboration, *LHCb Magnet - Technical Design Report*, CERN/LHCC/2000-007, 1999.
- [39] LHCb collaboration, *LHCb Vertex Locator - Technical Design Report*, CERN/LHCC/2001-011, 2001.
- [40] LHCb Collaboration, *LHCb Reoptimized Detector Design and Performance - Technical Proposal*, CERN-LHCC/2003-030, 2003.

- [41] G. Baumann *et al.*, *Quality assurance of 100 CMS-OB2 sensors*, CERN-LHCb-2004-105, 2004.
- [42] J. Gassner, F. Lehner, and S. Steiner, *The Mechanical Design of the LHCb Silicon Trigger Tracker*, CERN-LHCb-2004-110, 2005.
- [43] M. Needham, *Silicon Tracker simulation performance*, CERN-LHCb-2003-015, 2003.
- [44] LHCb collaboration, *LHCb Trigger System - Technical Design Report*, CERN/LHCC/2003-31, 2003.
- [45] LHCb collaboration, *LHCb Inner Tracker - Technical Design Report*, CERN/LHCC/2002-029, 2002.
- [46] B. Adeva *et al.*, *Design and Production of Detector Modules for the LHCb Silicon Tracker*, CERN-LHCb-2007-009, 2007.
- [47] LHCb collaboration, *LHCb RICH - Technical Design Report*, CERN/LHCC/2000-0037, 2000.
- [48] LHCb collaboration, *LHCb Calorimeters - Technical Design Report*, CERN/LHCC/2000-0036, 2000.
- [49] LHCb collaboration, *LHCb Muon System - Technical Design Report*, CERN/LHCC/2001-010, 2001.
- [50] E. Rodrigues, *The LHCb Trigger System*, CERN-LHCb-2006-065, 2006.
- [51] E. Rodrigues, *Private Communication*.
- [52] LHCb collaboration, *LHCb Outer Tracker - Technical Design Report*, CERN/LHCC 2001-024, 2001.
- [53] F. Sauli, *Principles of Operation of Multiwire Proportional and Drift Chambers*, CERN-1977-9, p.9, 1977.
- [54] G. Van Apeldoorn *et al.*, *Outer Tracker Module Production at NIKHEF - Quality Assurance*, CERN-LHCb-2004-078.
- [55] B. Hommels, *The Tracker in the Trigger of LHCb*, Ph.D. thesis, 2006.
- [56] <http://www.calfinewire.com/>.
- [57] P. Vankov *et al.*, *Wire Tension Meter for the Production of the LHCb Outer Tracker - Commissioning and Calibration*, CERN-LHCb-2004-034.
- [58] http://www.nikhef.nl/pub/experiments/bfys/lhcb/outerTracker/Mechanics/Drawings/Tools/WireTension/wire_tension_meter.htm.
- [59] S. Bachmann, *Specifications for the drift gas quality of the outer tracking system*, CERN-LHCb-2002-031.
- [60] <http://www.ionscience.com/>.
- [61] P. Vankov *et al.*, *Gas Tightness Tests of the LHCb Outer Tracker Modules Produced at NIKHEF*, CERN-LHCb-2004-092.
- [62] M. Walter, *Results from ageing tests with Ar/CO₂/CF₄ (75:10:15) and Ar/CO₂ (70:30) and varying water contents*, LHCb collaboration week, September 2003.
- [63] I. Mous, *The Dependence of the Signal Strength on the Applied Voltage and Gas Mixture of the LHCb Outer Tracker Detector*, CERN-LHCb-2005-093.
- [64] G. Van Apeldoorn, *Private Communication*.
- [65] G.W. van Apeldoorn *et al.*, *Beam Tests of Final Modules and Electronics of the LHCb Outer Tracker in 2005*, CERN-LHCb-2005-076.

- [66] M. Milite, *Tests of the ZEUS Microvertex Silicon Sensors*, Ph.D. thesis, desy-thesis-01-050, 2001.
- [67] M. Moritz, *Measurement of the High Q^2 Neutral Current DIS Cross Section at HERA*, Ph.D. thesis, desy-thesis-02-009, 2001.
- [68] I.R. Fernandez, *Charm Electroproduction at HERA*, Ph.D. thesis, desy-thesis-01-037, 2001.
- [69] M. Needham, *Tracking Performance and Robustness Tests*, CERN-LHCb-2003-020.
- [70] T. Haas, *Ageing and performance studies of the outer tracker of the LHCb detector*, Ph.D. thesis, Heidelberg University, 2007.
- [71] P. Vankov and G. Raven, *Proper-Time Resolution Modelling*, CERN-LHCb-2007-055.
- [72] I. Belyaev *et al.*, *Simulation for the LHCb experiment*, arXiv:physics/0306035, 2003.
- [73] *The BOOLE Project*, <http://lhcb-release-area.web.cern.ch/LHCb-release-area/DOC/bole/>.
- [74] *The BRUNEL Project*, <http://lhcb-release-area.web.cern.ch/LHCb-release-area/DOC/brunel/>.
- [75] *The DAVINCI Project*, <http://lhcb-release-area.web.cern.ch/LHCb-release-area/DOC/davinci/>.
- [76] W. Verkerke and D. Kirkby, *The RooFit ToolKit for Data Modelling*, <http://roofit.sourceforge.net/>.
- [77] R. Burn and F. Rademakers, *An Object-Oriented Data Analysis Framework*, <http://root.cern.ch/>.
- [78] G. Raven, *Selection of $B_s \rightarrow J/\psi\phi$ and $B^+ \rightarrow J/\psi K^+$* , CERN-LHCb-2003-118, 2003.
- [79] K. Cranmer, *Kernel estimation in High-Energy Physics*, hep-ex/0011057.

Summary

The Large Hadron Collider (LHC), scheduled to start operations this year at CERN, will accelerate and collide proton beams at 14 TeV center-of-mass energy at luminosities up to $10^{34} \text{ cm}^{-2}\text{s}^{-1}$. In these collisions the heavy B mesons (bound states of a b quark and a light antiquark) will be produced at high rate, thus allowing precise measurements of the violation of the combined Charge-Parity (CP) symmetry in the B system and the study of rare B decays. A dedicated experiment, LHCb, will operate with LHC to exploit this possibility.

The research in this dissertation addresses two issues: the overall performance of the LHCb Outer Tracker (OT) detectors as shown during quality checks and beam tests; the study of the lifetimes of B^+ and B^0 mesons at LHCb.

The OT system of LHCb comprises three stations consisting of layers of straw tubes in vertical and non-vertical (± 5 deg) orientation. The basic element of the OT stations is the module, a self-contained gas-detector unit, built of arrays of straw-tube drift cells and filled with a mixture of Ar (70%) and CO₂ (30%).

The quality of the OT modules was strictly checked during their construction (Chapter 3). To make sure that no deviations from the design specifications [52] were present, a variety of quality assurance tests were carried out: inspection of the anode wire quality, control of the friction force of the wire locators with the straw, control of the position of the wire inside the straw, systematic measurement of the wire tension, systematic measurement of the current of each wire in air at high voltage (HV), systematic measurement of the gas tightness of each OT module, HV training of the channels of the module in a counting gas and final validation of the module with a radioactive source with counting gas. The results of these tests, presented in this dissertation, showed that the performance of the OT detector fulfills the requirements. The final validation of the OT modules with a ⁹⁰Sr radioactive source showed homogeneous responses of the modules over their active surface within $\pm 10\%$.

In 2005, beam tests of the OT modules were performed at the DESY laboratory. Four OT modules, equipped with front-end electronics, were irradiated with an electron beam of 6 GeV. The analysis of the beam test data (Chapter 4), showed a high detector efficiency ($\sim 98\%$), a coordinate resolution better than $200 \mu\text{m}$, acceptable noise level $\leq 10 \text{ kHz/wire}$ and modest cross talk ($< 5\%$).

To perform the studies described in the second part of this dissertation simulated data, produced as part of LHCb 2004 data challenge, were used.

The first part of these studies (Chapter 5) was devoted to the modeling of the behavior of the resolution of the B -mesons proper time. This resolution is an important ingredient in the measurement of the time-dependent (CP) asymmetries. The study was performed with B^+ and B^0 mesons, using the decay modes $B^+ \rightarrow J/\psi(\mu^+\mu^-)K^+$ and $B^0 \rightarrow J/\psi(\mu^+\mu^-)K^*(K^+\pi^-)$ and their conjugates. The resolution model is based on the proper-time residuals and the corresponding per-event errors. The parameters of the model were extracted in two ways: by using the known residuals from the simulated data and by using the proper time only (i.e. data that will be experimentally accessible). In addition to the precise determination of the resolution-model parameters, the method can be used to tune the LHCb Monte-Carlo (MC) algorithms.

The measurement of the B -meson lifetimes is a crucial element for the test of the theory. In particular, the Heavy Quark Expansion model (HQE) predicts a difference in the B^+ and B^0 lifetimes. According to the HQE $\tau_{B^+}/\tau_{B^0} = 1.06 \pm 0.02$ [30]. The final chapter of the dissertation (Chapter 6) focused on the extraction of the lifetime ratio τ_{B^+}/τ_{B^0} in the presence of backgrounds. The same B^+ and B^0 decay modes were used and the developed resolution model was applied. The ratio $\tau_{B^+}/\tau_{B^0} = 1.0826 \pm 0.0106$ has been determined, in good agreement with the input MC simulation value of 1.0879. It has also been found that in 1 year of data-taking at nominal luminosity and in the absence of other systematic errors, the LHCb experiment will measure the lifetimes of B^+ and B^0 mesons with a resolution of 1.71 ± 0.03 fs and 1.92 ± 0.01 fs, respectively, resulting in a sensitivity to τ_{B^+}/τ_{B^0} of 0.0017.

Samenvatting

Studie van de B -meson levensduur en van de eigenschappen van de LHCb Outer Tracker

De "Large Hadron Collider" (LHC) proton versneller, gebaseerd in CERN, zal dit jaar naar verwachting voor het eerst proton-proton botsingen produceren met een energie van 14 TeV in het zwaartepuntssysteem en met een luminositeit van $10^{34} \text{ cm}^{-2}\text{s}^{-1}$. In deze botsingen zullen met hoge frequentie zware B -mesonen (gebonden toestanden van een b -quark en een licht antiquark) geproduceerd worden. Dit staat toe met hoge precisie metingen te doen van lading-pariteitsschending ("charge-parity", CP) in B toestanden, alsmede zeldzame vervallen van B -mesonen te bestuderen. Het LHCb experiment is specifiek ontworpen om deze mogelijkheid te exploiteren.

Het onderzoek in dit proefschrift behandeld twee vraagstukken: de overall performance van de LHCb buitenste sporen-detectoren ("Outer Tracker", OT), bepaald in kwaliteitscontroles en tijdens test bundel metingen; de studie van de levensduur van B^+ en B^0 mesonen in LHCb.

Het OT detectorsysteem van LHCb bestaat uit drie stations, die op hun beurt zijn opgebouwd uit lagen strootjes detectoren ("straw-tubes") met verticale en niet-verticale (± 5 graden) oriëntatie. Het basisonderdeel van de OT stations is de module, een onafhankelijke gas-detectoreenheid, opgebouwd uit een reeks straw-tube drift cellen, gevuld met een mengsel van Ar (70%) en CO₂ (30%).

De kwaliteit van de OT modules werd tijdens de productie strikt gecontroleerd (Hoofdstuk 3). Om te garanderen dat er geen afwijkingen van de ontwerpspecificaties waren [52], werden verschillende kwaliteitscontroles uitgevoerd: inspectie van de anodedraadkwaliteit, controle van de wrijvingsparameters van de draad fixaties in de straw-tube, controle van de positie van de draad in de straw-tube, systematische meting van de draadspanning, systematische meting van de stroom in elke draad in lucht onder hoogspanning (HV), systematische meting van de gasdichtheid van elke OT module, HV training van alle kanalen van de module in een telgas ("counting gas") en de uiteindelijke validatie van de module met een radioactieve bron en met telgas. De resultaten van deze tests, gepresenteerd in deze dissertatie, demonstreerden dat de performance van de OT detector aan de vereisten voldoet. De uiteindelijke validatie van de OT modules met een ⁹⁰Sr radioactieve

bron demonstreerden een homogene respons binnen $\pm 10\%$ van de modules over het gehele actieve oppervlak.

In 2005 werden de OT modules getest in de bundelfaciliteit aan het DESY laboratorium. Vier OT modules, uitgerust met uitleeselektronica, werden met een elektronenbundel van 6 GeV bestraald. De analyse van de bundeltest data (Hoofdstuk 4), toonde een hoge detector efficiëntie ($\sim 98\%$), een coördinaat resolutie beter dan $200 \mu\text{m}$, aanvaardbare hoeveelheden detector ruis $\leq 10 \text{ kHz/draad}$ en een bescheiden signaal overspraak ("cross talk") ($< 5\%$).

Ter verrichting van de studies beschreven in het tweede deel van deze dissertatie werden gesimuleerde data gebruikt. De laatste werden geproduceerd als onderdeel van de LHCb 2004 data uitdaging ("data challenge").

Het eerste deel van deze studies (Hoofdstuk 5) werd gewijd aan het modeleren van het gedrag van de resolutie van de "proper time" van de B -mesonen. Deze resolutie is een belangrijk ingrediënt in de meting van de tijd-afhankelijke (CP) asymmetrieën. De studie werd verricht met B^+ en B^0 mesonen en maakte gebruik van de $B^+ \rightarrow J/\psi(\mu^+\mu^-)K^+$, de $B^0 \rightarrow J/\psi(\mu^+\mu^-)K^*(K^+\pi^-)$, zowel als de corresponderende geconjugeerde vervalskanalen. Het resolutiemodel is gebaseerd op de "proper-time" residuen en de corresponderende "per-event" fouten. De parameters van het model werden op twee manieren bepaald: met gebruik van de kennis van de residuen in de gesimuleerde data en met enkel het gebruik van de "proper-time" (m.a.w. met enkel het gebruik van experimenteel toegankelijke data). Naast de nauwkeurige bepaling van de parameters van het resolutiemodel, kan de methode tevens gebruikt worden voor de optimalisatie van de LHCb Monte-Carlo (MC) algoritmen.

De meting van B -meson levensduren is een cruciaal onderdeel in het testen van de theorie. Het Zware Quark Uitbreidingsmodel (Heavy Quark Expansion model, HQE) met name, voorspelt een verschil in de B^+ en B^0 levensduren. Volgens het HQE model $\tau_{B^+}/\tau_{B^0} = 1.06 \pm 0.02$ [30]. Het laatste hoofdstuk van deze dissertatie (Hoofdstuk 6) concentreerde zich op de bepaling van de verhouding τ_{B^+}/τ_{B^0} met aanwezigheid van achtergronds processen. Dezelfde B^+ en B^0 vervalskanalen werden gebruikt, zowel als het ontwikkelde resolutiemodel. De verhouding $\tau_{B^+}/\tau_{B^0} = 1.0826 \pm 0.0106$ werd bepaald, in goede overeenkomst met de invoerwaarde van 1.0879, gebruikt in de simulatie. Er werd tevens gedemonstreerd dat met de data genomen in 1 jaar, bij nominale luminositeit en in de afwezigheid van andere systematische fouten, het LHCb experiment de levensduur van B^+ en B^0 mesonen kan bepalen met een resolutie van $1.71 \pm 0.03 \text{ fs}$ en $1.92 \pm 0.01 \text{ fs}$, respectievelijk. Dit resulteert in een gevoeligheid van 0.0017 in de meting van de verhouding τ_{B^+}/τ_{B^0} .

Acknowledgements

This work was carried out at the Dutch National Institute for Subatomic Physics, Nikhef. It was a privilege and honor for me to work in this world-class research center, surrounded by highly skilled, experienced and motivated colleagues in a dynamic and international environment.

I am most grateful to my two supervisors - Antonio Pellegrino and Gerhard Raven. Antonio, who discovered me for Nikhef, not only guided my work but continuously supported and encouraged my progress. During the 4.5 years of my PhD I could always rely on him for any help and advice.

Gerhard supervised the physics analysis part of the dissertation. I profited a lot from his enormous expertise in the field of B physics, data-analysis techniques and computer programming. I would like to thank him also for his patience.

I owe my warmest gratitude to Niels Tuning with whom I have shared a common office in Nikhef during all these years. I have spent many inspiring moments with Niels. We talked, discussed and argued a lot (Niels, I apologize for my annoying stubbornness, sometimes). Besides his friendly assistance whenever I had a need, both in-work and out-of-work, Niels rendered me a tremendous help in improving the dissertation.

I am also very thankful to Gras van Apeldoorn, who showed me the spirit of experimental physics.

I want to express my sincere gratitude to Marcel Merk for his useful advices and for his responsiveness to all my questions and concerns.

In this years I also benefited a lot from the knowledge and experience of Thomas Bauer, Wouter Verkerke, Bart Hommels, Eduardo Rodrigues, Jeroen van Tilburg, Ivo van Vulpen, Jan Spelt, Gabriel Ybeles Smit and Jan Amoraal.

I would like to gratefully acknowledge the help on various occasions of Marco Zupan, Jacopo Nardulli, Eduard Simioni, Edwin Boss, Hella Snoek, Max Baak, Aras Papadelis, Tristan du Pree, Besma M'Charek, Fabian Jansen as well as of all other members of the B -physics group. Here is the place to mention that I enjoyed very much the time spent in our weekly Friday LHCb out-of-work meetings.

I deeply appreciate the help of Jo van den Brand, who made every endeavor to improve the dissertation. I am also very thankful to Uli Uwer and Tjeerd Ketel for their useful comments and suggestions and to Joost Vossebeld for the dutch translation of the summary.

В заключение, бих искал да благодаря на цялото си семейство без чиито обич, разбиране и подкрепа този труд би бил невъзможен.